

A NEW APPROACH TO OBTAIN FORMING LIMITS
OF SHEET MATERIALS

A NEW APPROACH TO OBTAIN FORMING LIMITS
OF SHEET MATERIALS

By

QUAN SITU, M. A. Sc. (Mechanical Engineering)

McMaster University, Hamilton, Ontario

A Thesis

Submitted to the School of Graduate Studies

in Partial Fulfillment of the Requirements

for the Degree of

Doctor of Philosophy

McMaster University

© Copyright by Quan Situ, January 2008

Philosophy of Doctoral (2008)

McMaster University

(Mechanical Engineering)

Hamilton, Ontario

TITLE: A New Approach To Obtain Forming Limits Of Sheet Materials

AUTHOR: Quan Situ, M. A. Sc. (Mechanical Engineering)

McMaster University, Hamilton, Ontario

SUPERVISOR: Dr. Mukesh K. Jain, Dr. Donald R. Metzger

Department of Mechanical Engineering

McMaster University

NUMBER OF PAGES: CCXXX, 230

Abstract

A new methodology is proposed to obtain the forming limit diagram (or FLD) of sheet materials by utilizing routinely obtained experimental load versus displacement traces and incorporating finite element (FE) analysis of strain history to extract the characteristic points of diffuse and localized necking and further the limit strains. The experimental data from hemispherical punch stretching test such as limit dome height, maximum load and location of inflection point are utilized to adjust the load curves in the FE simulations. An optimization procedure to obtain various parameters in material definition has been established to obtain a good agreement between the FE-based and experimental punch load versus displacement curves. An analysis of FE model based strain history is then carried out to determine the limit strains. This approach avoids using experimental strain measurement in the vicinity of the neck on the dome specimens. The materials tested with the new methodology include automotive sheets AA6111-T4, AA6181-T4 and DP600. The one utilized for optimization of FE inputs was AA6111-T4.

The proposed method for FLD determination considers out-of-plane displacement, punch-sheet contact and friction, and avoids the use of a rather arbitrary inhomogeneity factor to trigger localization such as in the Marciniak-Kuczynski method.

A new criterion to determine the localized necking is proposed by seeking an inflection point in the major strain rate curve, or, maximum point in the second order of derivative of major strain, $(\dot{\epsilon}_1)_{\max}$. The proposed localized necking criterion is compared with other two methods to determine the onset of localized necking. These are (i) Bragard

criterion for post-test of deformation, and (ii) critical major strain $(\epsilon_1)_{cr}$ based on comparison of strain of material inside the localized site and its vicinity in the un-necked site. The new criterion of $(\dot{\epsilon}_1)_{max}$ exhibits a more definite physical meaning towards developing an understanding of flow localization, formability and fracture.

This new approach for obtaining FLDs is rapid and accurate and could be implemented easily for routine FLD generation in a lab setting with little user input and subjectivity.

Acknowledgements

I would first express my gratitude to my supervisors, Dr. M. K. Jain and Dr. D. R. Metzger, for giving me a chance to complete this interesting and challenging research. Their instructive guidance and support benefited me from the very first day and throughout the research.

I would specially thank Dr. M. Bruhis for the invaluable and painstaking laboratory assistance on some tests and image processing.

I would thank my thesis supervisory committee members Dr. J. R. McDermid and Dr. M. P. Sklad, for their comments and suggestions from time to time.

I would express my gratitude to Dr. P. D. Wu and Dr. E. Ng, for technical discussions and interesting ideas in plasticity and finite element analysis.

I would also like to thank Ms. Janet Murphy, Ms. BettyAnne Bedell-Ryc and all the academic staff in Department of Mechanical Engineering, who helped me in manuscript preparation, presentation rehearsal and meeting coordination.

I would thank Dr. W. Hotz from Novelis Canada for giving me an opportunity to participate the Round Robin Contest of material test of AA6181-T4. I would also thank Dr. P. Martin from NRC for giving advice in specimen design and rig setup of punch test.

I would also like to thank my friends and colleagues, Young Suk Kim, Diaa Elkott, Elisabeth Azhikannickal, Mohamed Elnagmi, Lathan Arasaratnam for their timely help.

I am forever indebted to my parents for their understanding, endless patience and encouragement.

Finally, I would heartily thank my wife Huiwen and my children Xuan and Yuan for their commitment, support and everlasting love.

Contents

	Page
Abstract.....	iii
Acknowledgements.....	v
Contents.....	vii
List Of Figures.....	xii
List Of Tables.....	xxiv
Nomenclature.....	xxv
Chapter 1 Introduction.....	1
1.1 Definition And Application Of Forming Limit Diagram (FLD).....	1
1.2 Objectives Of Present Research.....	3
1.3 System Of Units.....	4
Chapter 2 Literature Review.....	5
2.1 Significant Studies In FLD Research (Prediction Of Localized Necking Behaviour).....	5
2.1.1 Marciniak-Kuczynski Model To Predict FLD.....	6
2.1.2 Approaches Other Than M-K Model To Predict FLD.....	8
2.2 Yield Criteria Of Material Modelling (Continuum And Crystalline Plasticity Based Criteria).....	8
2.3 Determining Onset Of Localized Necking.....	15
2.3.1 Theoretical Determination Of Instability.....	15

2.3.2	Experimental Limitations Of Existing FLD Test Methods, Associated Test Variables And Their Determination.....	19
2.4	Failure.....	27
2.5	Inflection And Instability Characteristics Of Punch Based Load- Displacement Curve.....	30
2.6	Strain Hardening At Large Strain And Optimization On Stress-Strain Input.....	34
2.7	Stain-Rate Sensitivity And Thickness Effect.....	37
2.8	Additional Strain Paths Of Forming Characteristics.....	38
2.9	Finite Element Prediction Of FLD.....	39
2.10	Shear Band Failure.....	42
Chapter 3	A Proposed Localized Necking Criterion.....	44
3.1	Application Of Localized Necking Criterion For FE Output Data.....	45
3.2	Analysis Of Strain History From FE Simulation.....	47
3.3	Experimental FLD Determination With Strain History Data From ARAMIS.....	51
Chapter 4	Experimental And Numerical Procedure For FLD Determination.....	61
4.1	Procedure For Obtaining FLDs.....	62
4.2	Experiment Details.....	66
4.2.1	Formability Test Setup.....	66
4.2.2	Test Conditions.....	71
4.2.2.1	Uniaxial Tensile Tests And Analysis Of Data.....	71

	4.2.2.2 Hemispherical Punch Stretching And Other Tests.....	77
	4.2.3 Characterization Of Load Curves For Inflection.....	81
	4.2.4 Procedure For Data Processing Of Strain History.....	86
4.3	FE Modelling.....	87
	4.3.1 Solution Convergence In FE Simulations.....	89
	4.3.2 Influence Of Damage Model On Strain Analysis.....	91
4.4	Validation of Formability Characteristics.....	92
Chapter 5	Optimization Of Material And Friction Input Data For FE Simulations Of Forming Tests.....	94
	5.1 Optimization Of $\sigma - \epsilon$ Input For AA6111-T4.....	97
	5.2 Optimization Of μ Input For AA6111-T4.....	116
	5.3 Further Optimization Of $\sigma - \epsilon$ And μ Input For Other Materials.....	120
	5.4 General Procedure Of Optimization Of $\sigma - \epsilon$ And μ Input	120
Chapter 6	Results.....	122
	6.1 Material Properties From Uniaxial Tensile Tests.....	122
	6.2 Characteristics Of Load Curve From Experiments.....	124
	6.3 FE Output Of Load Curves.....	126
	6.4 Using FE Results Of Strain History To Obtain FLD.....	128
	6.5 Experimental Data From ARAMIS / ARGUS Systems.....	132
	6.5.1 ARAMIS Results For AA6111-T4.....	133
	6.5.2 ARAMIS And ARGUS Results For AA6181-T4.....	139

6.6	Further Experimental Examinations Of The Proposed Localized Necking Criterion.....	144
6.6.1	Thickness And Strain Rate Effects.....	144
6.6.2	Additional Strain Paths.....	149
6.6.2.1	High Friction Interface Characteristics.....	149
6.6.2.2	Specimen With A Central Hole.....	152
6.6.2.3	In-plane Shear Tests.....	155
Chapter 7	Discussion.....	158
7.1	Strain Evaluation In And Around Neck Region And Validity Of Bragard Criterion	159
7.2	Assessment Of Various Localized Necking Criteria To Determine The Limit Strains.....	163
7.3	General Definition Of Inflection Point In Forming Process.....	169
7.4	Physical Significance Of The Proposed Localized Necking Criterion...	172
7.5	Punch Size Effect On Prediction Of FLD.....	174
7.6	Expanding Optimization Work.....	174
Chapter 8	Conclusions.....	179
	References.....	182
	Appendices.....	194
Appendix 1	Analytical Model Of Hemispherical Punch Test.....	194
Appendix 2	MATLAB Code For Re-sample Process.....	206
Appendix 3	MATLAB Code For Moving Average Method.....	207

Appendix 4	Instability Criteria Of Uniaxial And Biaxial Tensile Tests.....	208
Appendix 5	FE Code For Uniaxial Tensile Path.....	210
Appendix 6	Optimized Material Input For AA6111-T4 Of 1 mm And 2 mm Sheet Thickness.....	222
Appendix 7	Material Properties From Uniaxial Tensile Tests Of AA6111-T4 Of 1 mm And 2 mm Sheet Thickness.....	224

List Of Figures

		Page
Figure 1-1	A photograph of a dome specimen showing a ring of localized neck	2
Figure 1-2	A typical FLD showing various forming modes	2
Figure 2-1	Schematic yield loci for anisotropic materials	10
Figure 2-2	Sensitivity of FLD predictions based on M-K theory on the choice of yield criterion	16
Figure 2-3	Schematic of strain gradient as function of strain as per Kocks et al.	18
Figure 2-4	Identifying deformed specimen as per different status of grids as safe, unnecked, partially necked and necked	20
Figure 2-5	Typical result of FLD construction	20
Figure 2-6	Strain distribution across a neck in a test specimen	23
Figure 2-7	Gradient of major strain as an indicator for the onset of necking	24
Figure 2-8	Development of strain distribution and gradient of major strain as a function of time	25
Figure 2-9	Thinning as a function of time for the critical node	26
Figure 2-10	Significant peak of second time derivation of the thickness strain and corresponding nodes on the formed specimen	26
Figure 2-11	Punch load as a function of displacement from hemispherical punch stretching tests for four different materials	31

Figure 2-12	Punch load versus displacement curves from hemispherical punch tests indicating the location of inflection point	32
Figure 2-13	Punch-to-sheet interface pressure as a function of radial distance from pole of a dome specimen for four stages of punch displacement	33
Figure 2-14	Diameter of the boundary of punch contact as function of punch displacement	33
Figure 2-15	Schematic of hydraulic bulge test system	36
Figure 2-16	Specimen for Miyauchi shear test	37
Figure 3-1	Procedure to obtain the limit strains from the strain history for AA6111-T4, 5” wide specimen, 2” diameter punch, dry condition	45
Figure 3-2	FE result of a deformed band A – B with localized zone in a 0.5” wide dome test specimen	46
Figure 3-3	Extracted strain history from FE simulations shown in Figure 3-2 of selected band from pole to edge	47
Figure 3-4	Processed major and minor strain, strain rate and strain acceleration histories from a 0.5” wide dome specimen of AA6111-T4 sheet	49
Figure 3-5	Processed major and minor strain, strain rate and strain acceleration histories from a 5” wide dome specimen of AA6111-T4 sheet under dry contact	50
Figure 3-6	Specimen with major strain overlay calculated from ARAMIS system showing localized site <i>B</i> and its vicinity <i>A</i>	52

Figure 3-7	Temporal and spatial major and minor strains calculated from ARAMIS system showing localized site <i>B</i> and its vicinity <i>A</i>	53
Figure 3-8	Analysis of strain history based on ARAMIS results showing limit strains and difference between localized site and its vicinity	54
Figure 3-9	Different stages of strain overlay on a deformed 0.5” uniaxial tensile specimen obtained from ARAMIS post-processing	55
Figure 3-10	Spatial and temporal strains (major and minor) of 0.5” uniaxial tensile specimen in ARAMIS post-processing	55
Figure 3-11	Analysis of major and minor strain histories of 0.5” wide uniaxial tensile specimen based on ARAMIS data	56
Figure 3-12	Analysis of major and minor strain histories of 0.5” wide biaxial tensile specimen based on ARAMIS data	57
Figure 3-13	Major strain history of 4” wide specimen in ARAMIS post-processing	58
Figure 3-14	Minor strain history of 4” wide specimen in ARAMIS post-processing	59
Figure 4-1	Punch load-displacement traces from experiments and FE simulations identifying diffuse necking, localized necking and fracture stages	62
Figure 4-2	Main block for FLD construction	63
Figure 4-3	A schematic representation of strain paths from different specimen geometry and lubrication conditions	64
Figure 4-4	Limit strain determination for each strain path	65

Figure 4-5	Hemispherical punch test rig (4" diameter punch) with universal test system MTS with Interlaken data acquisition and control system (top right console) and strain imaging system ARAMIS (bottom right console)	66
Figure 4-6	Specimens designed for 4" diameter punch tests	68
Figure 4-7	Hemispherical punch test rig (2" diameter punch) with Interlaken hydraulic test system (console not shown) and strain imaging system ARAMIS using cameras	69
Figure 4-8	Specimens designed for 2" diameter punch tests	70
Figure 4-9	Obtaining parameters for power law fitting from post-processing of experimental uniaxial tensile data	72
Figure 4-10	Obtaining parameters for Voce law fitting from post-processing of experimental uniaxial tensile data (AA6111-T4, 1 mm thickness, 0.25 mm/s test speed) using trial value 420 MPa for B value	74
Figure 4-11	Relationship between trial value of B and linear fitting result of A for AA6111-T4	75
Figure 4-12	Relationship between trial value of B and linear fitting result of m for AA6111-T4	76
Figure 4-13	Obtaining parameters for Voce law fitting from post-processing of experimental uniaxial tensile data (AA6111-T4, 1 mm thickness, 0.25 mm/s test speed) using trial value 435 MPa for B value	76
Figure 4-14	Profile of a specimen with a central hole	79

Figure 4-15	Specimen designed for shear test	80
Figure 4-16	Raw data of load-displacement curve showing raw data (column <i>D, E</i>), re-sampled data (column <i>G, H</i>) and processed data with moving average (column <i>J, K</i>)	83
Figure 4-17	Expanded plot of Figure 4-16 showing raw data, re-sampled data and processed data with moving average	83
Figure 4-18	Load rate data for Figure 4-16	86
Figure 4-19	FE results of various mesh sizes for sheet compared with experimental data	90
Figure 4-20	Actual errors of FE simulations with different mesh sizes for a study of convergence (based on Figure 4-11)	90
Figure 4-21	Application of damage model in FE modelling	91
Figure 5-1	Strain history from ARAMIS result indicating diffuse necking and localized necking for 0.5” wide uniaxial tensile test specimen	95
Figure 5-2	Strain history from ARAMIS result indicating diffuse necking and localized necking for 0.5” wide punch test specimen	96
Figure 5-3	Stress-strain relationship of 1 mm thickness specimen of AA6111-T4 (1 mm thickness) from uniaxial tensile test and fitted with power law and Voce law	98
Figure 5-4	True stress – true strain relationship of AA6111-T4 specimen showing a band of $\pm 2\%$ variation	99

Figure 5-5	A comparison of experimental load-displacement data and those based on power law in the FE simulation	101
Figure 5-6	A comparison of experimental load-displacement curve and those based on Voce law in the FE simulation	103
Figure 5-7	Influence of Voce law parameter A on the hardening behaviour shown in $\frac{1}{\sigma} \frac{d\sigma}{d\varepsilon}$ versus ε curve	105
Figure 5-8	Influence of Voce law parameter B on the hardening behaviour shown in $\frac{1}{\sigma} \frac{d\sigma}{d\varepsilon}$ versus ε curve	106
Figure 5-9	Influence of Voce law parameter m on the hardening behaviour shown in $\frac{1}{\sigma} \frac{d\sigma}{d\varepsilon}$ versus ε curve	107
Figure 5-10	Stress-strain curves for different hardening laws	109
Figure 5-11	Hardening behaviour as per Considère criterion of four laws	110
Figure 5-12	Weight functions for power law part of hybrid laws (1), (2) and (3)	112
Figure 5-13	Weight functions for Voce law part of hybrid laws (1), (2) and (3)	112
Figure 5-14	Stress-strain relationship of 1 mm thickness specimen of AA6111-T4 from uniaxial tensile test and fitted with power law, Voce law and hybrid law (3)	114
Figure 5-15	Hardening behaviour as per Considère criterion of four laws	115
Figure 5-16	FE results of load curves with different constant friction inputs	117
Figure 5-17	Friction input as a function of punch displacement	118

Figure 6-1	True stress – true strain relationship of AA6111-T4 sheets in 1 mm and 2 mm thickness at different test speeds	123
Figure 6-2	Experimental punch load versus displacement curves from hemispherical punch tests. Solid circles indicate inflection points	124
Figure 6-3	Inflection points in processed experimental load versus displacement curves, 1 st order of derivative of load curve, or, the load rate dF/dh versus punch displacement for AA6111-T4, 1 mm thickness, 2” punch diameter	125
Figure 6-4	Comparison of FE and experimental load traces for AA6111-T4	127
Figure 6-5	Comparison of FE and experimental load traces for AA6111-T4	127
Figure 6-6	Comparison of FE and experimental load traces for AA6111-T4	128
Figure 6-7	Typical deformed specimen shapes (a, c, e, g) and corresponding FE results (b, d, f, h) showing localized necking	129
Figure 6-8	Histories of major/minor strain, strain rate and strain acceleration of 0.5” wide specimen of AA6111-T4	131
Figure 6-9	Histories of major/minor strain, strain rate and strain acceleration of 5” wide specimen (dry contact) of AA6111-T4	131
Figure 6-10	FE prediction of FLD for AA6111-T4	132
Figure 6-11	Typical test specimen with corresponding major strain map for AA6111-T4 over the specimen surface from ARAMIS strain measurement system	133

Figure 6-12	Typical test specimen with corresponding major strain map for AA6111-T4 over the specimen surface from ARAMIS strain measurement system	134
Figure 6-13	Typical test specimen with corresponding major strain map for AA6111-T4 over the specimen surface from ARAMIS strain measurement system	134
Figure 6-14	Typical test specimen with corresponding major strain map for AA6111-T4 over the specimen surface from ARAMIS strain measurement system	135
Figure 6-15	Typical test specimen with corresponding major strain map for AA6111-T4 over the specimen surface from ARAMIS strain measurement system	135
Figure 6-16	Typical test specimen with corresponding major strain map for AA6111-T4 over the specimen surface from ARAMIS strain measurement system	136
Figure 6-17	Analysis of strain history showing evolution of strain, strain rate and strain acceleration at the localization and its vicinity for 2" wide specimen	137
Figure 6-18	Analysis of strain history showing evolution of strain, strain rate and strain acceleration at the localization and its vicinity for 5" wide specimen	137

Figure 6-19	FLDs obtained from FE simulation using $(\dot{\epsilon}_i)_{\max}$ criterion compared with experimental values from ARAMIS for AA6111-T4	138
Figure 6-20	FLDs from FE results using $(\dot{\epsilon}_i)_{\max}$ and $(\epsilon_i)_{cr}$ criteria for AA6111-T4	139
Figure 6-21	Strain history from ARAMIS result indicating localized necking at $(\dot{\epsilon}_i)_{\max}$ for 0.5" wide specimen	140
Figure 6-22	Strain history from ARAMIS result indicating localized necking at $(\dot{\epsilon}_i)_{\max}$ for 7" wide specimen	141
Figure 6-23	Post-test strain assessment with ARGUS 3D for 4" wide specimen using Bragard criterion	142
Figure 6-24	Comparison of limit strains of AA6181-T4 using various criteria	143
Figure 6-25	Load versus displacement curves for 1 mm sheets of AA6111-T4 at different speeds with different lubrication conditions	145
Figure 6-26	Load versus displacement curves for 2 mm sheets of AA6111-T4 at different speeds with different lubrication conditions	145
Figure 6-27	Comparison of load versus displacement curves of 1 mm and 2 mm sheets of AA6111-T4 at difference speeds and lubrication conditions	146
Figure 6-28	Comparison of FLDs of 1 mm and 2 mm sheets of AA6111-T4 at different speeds	147
Figure 6-29	Experimental load versus displacement curves at different punch speeds for DP600, 1.88 mm sheet	148
Figure 6-30	A comparison of experimental FLDs of 1.88 mm sheets of DP600 steel at two different punch speeds	149

Figure 6-31	Punch load-displacement curves under various lubrication conditions	150
Figure 6-32	Strain map and strain history of test with sand paper interface between the punch and sheet	151
Figure 6-33	FLD of AA6111-T4 obtained with $(\dot{\epsilon}_i)_{\max}$ criterion	152
Figure 6-34	Strain map of specimen and strain paths from different locations along the edge of the specimen with central hole in Nakajima test	153
Figure 6-35	Strain map of specimen and strain paths from different locations along the edge of the specimen with central hole in Marciniak test	154
Figure 6-36	FLD of AA6111-T4 obtained with $(\dot{\epsilon}_i)_{\max}$ criterion	155
Figure 6-37	Strain paths of shear specimens with non-symmetric notches	156
Figure 6-38	Curves of strain rate from a notched specimen showing inflection point as onset of shearing process	156
Figure 7-1	Strain contours for 4" wide specimen from ARGUS 3D post-processing	160
Figure 7-2	Strain path A-A from Figure 7-1	161
Figure 7-3	Strain paths C-C, D-D from Figure 7-1	161
Figure 7-4	Using the post-test strains to trace the strain evolution from ARGUS 3D post-processing	162
Figure 7-5	Bifurcation behaviour of major strain	166
Figure 7-6	Strain histories of major, minor and thickness for 0.5" wide specimen of AA6111-T4 in 2" diameter punch test	168

Figure 7-7	Strain history, rate and acceleration of thickness strain for Figure 7-6 specimen	168
Figure 7-8	Major strain rate curves of various paths showing inflection point and different curvature	171
Figure 7-9	Comparison strain acceleration curves of in-plane and out-of-plane test	173
Figure 7-10	Ratios of thickness, width and area with respect to the original values obtained from strain imaging system	176
Figure 7-11	Stress versus time curves for uniaxial tests on AA6111-T4 sheet	176
Figure 7-12	Engineering stress-strain curve and two different corresponding true stress-strain curves from (i) conventional method, and (ii) based on local strain measurements	177
Figure 7-13	Plot of hardening behaviour with various hardening laws	178
Figure A1-1	Schematic of full dome specimen with rigs	194
Figure A1-2	Expanded surface of truncated cone of area S_2	200
Figure A1-3	Analytical model to obtain characteristic points in load curve	205
Figure A7-1	Proposed curve fitting for AA6111-T4, 1 mm thickness, 0.25 mm/s test speed	225
Figure A7-2	Proposed curve fitting for AA6111-T4, 1 mm thickness, 0.025 mm/s test speed	226
Figure A7-3	Proposed curve fitting for AA6111-T4, 1 mm thickness, 1.25 mm/s test speed	227

Figure A7-4	Proposed curve fitting for AA6111-T4, 2 mm thickness, 0.25 mm/s test speed	228
Figure A7-5	Proposed curve fitting for AA6111-T4, 2 mm thickness, 0.025 mm/s test speed	229
Figure A7-6	Proposed curve fitting for AA6111-T4, 2 mm thickness, 1.25 mm/s test speed	230

List Of Tables

		Page
Table 2-1	Representative fracture criteria of uncoupled damage model	29
Table 2-2	Selected FE investigations on punch test to obtain FLD	41
Table 4-1	Configuration of shear test specimens with notches	80
Table 4-2	Excel data sheet showing raw and processed punch load versus displacement data for plots in Figures 4-16 to 4-18	81
Table 5-1	Power law parameters for trial-and-error tests in FE simulation	100
Table 5-2	Voce law parameters for trial-and-error tests in FE simulation	102
Table 5-3	Influence of power law and Voce law parameters on the hardening behaviour in Considère curve	108
Table 5-4	Weight functions for proposed hybrid laws	113
Table 6-1	Uniaxial tensile material parameters in the longitudinal direction (with respect to rolling) for AA6111-T4 at different sheet thickness and test speeds	123
Table A4-1	Comparison of criteria to determine instability in uniaxial and biaxial tension	207

Nomenclature

A	Material constant in Voce law, the initial stress	
A_0	Base value of material constant A	
a	Inner diameter of die	(Figure A1-1)
a	Anisotropic parameter [Barlat et al., 1989]	(Eq 2-10)
B	Material constant in Voce law, the saturation stress	
B_0	Base value of material constant B	
C	Clearance for shear specimen	
C	Constant in [Oyane et al., 1980]	(Table 2-1)
C_i	$i = 1 \sim 9$, constants in [Gotoh, 1977]	(Eq 2-6)
C_{ij}	$i = 1 \sim 3, j = 1 \sim 3$, constants in [Jones-Gillis, 1984]	(Eq 2-7)
c	Weight function in [Karafillis-Boyce, 1993]	(Eq 2-18)
D	Damage parameter	
dF	Force increment	
dh	Displacement increment	
dP	Force (punch load) increment	
dp	Pressure increment	
dt	Time increment	
F	Force	
F	Anisotropic parameter [Hill 1948, Hill 1979]	(Eq 2-3, 2-4)
f_0	Material imperfection (surface roughness factor)	

f	Volumetric fraction of voids	(Eq 2-29)
f^*	Effective void volume fraction	(Eq 2-29)
f_F	Volume fraction at final failure	(Eq 2-29)
f_c, f_U	Material constants describing void coalescence	(Eq 2-29)
G	Anisotropic parameter [Hill 1948, Hill 1979]	(Eq 2-3, 2-4)
H	Anisotropic parameter [Hill 1948, Hill 1979]	(Eq 2-3, 2-4)
h	Punch displacement	
h	Punch height	
h	Material constant [Barlat et al., 1989]	
h_0	Material constant from [Savoie et al., 1998]	(Table 2-2)
J_2	Second invariant of stress deviator tensor	
K	Material constant for power law	
K_0	Reference value of material constant K	
k	Anisotropic parameter [Hill, 1979]	(Eq 2-5)
k	Anisotropic parameter [Bassani, 1977]	(Eq 2-9)
L	Notch length	
L	Anisotropic parameter [Hill, 1979]	(Eq 2-4)
M	Anisotropic parameter [Hill, 1979]	(Eq 2-4)
m	Strain rate sensitivity	
m	Material constant in Voce law, exponential coefficient	
m	Index parameter in [Hosford, 1979]	(Eq 2-8)
m	Index parameter in [Bassani, 1977]	(Eq 2-9)

m	Index parameter [Barlat et al., 1989]	(Eq 2-10)
m_0	Base value of material constant m	
max	Maximum	
min	Minimum	
N	Anisotropic parameter [Hill, 1979]	(Eq 2-4)
n	Strain-hardening exponent	
n	Notch width	
n	Index parameter in [Bassani, 1977]	(Eq 2-9)
n_0	Reference value of strain-hardening exponent n	
P	Load or force	
P_{max}	Maximum punch load	
p	Variable for Considère criterion, $\frac{1}{\sigma} \frac{d\sigma}{d\varepsilon} = p$	
p	Pressure	
p	Material constant [Barlat et al., 1989]	(Eq 2-10)
q_1, q_2, q_3	Material constants	(Eq 2-28)
R	External radius	
R	Punch radius	
R	Anisotropic ratio	
R_d	Die edge radius	(Figure A1-1)
R_p	Punch radius	(Figure A1-1)
r	Internal radius	
r	Anisotropic ratio	

r_0	Strain ratio along 0° to the rolling direction	
r_1	Contact radius of punch (to punch axis)	(Figure A1-1)
r_2	Contact radius of die (to punch axis)	(Figure A1-1)
r_{90}	Strain ratio along 90° to the rolling direction	
r_{RD}	Strain ratio in the transverse direction	
r_{TD}	Strain ratio in the rolling direction	
S	Notch spacing for shear specimen	(Figure A1-1)
S_1	Surface area of contact in punch	(Figure A1-1)
S_2	Surface area of straight section	(Figure A1-1)
S_3	Surface area of contact in die	(Figure A1-1)
S_i	$i = 1 \sim 3$, principal stress in symmetric matrix $S_{\alpha\beta}$ [Barlat et al., 1989]	
S_{xx}, S_{yy}, S_{zz}	Stresses in x, y and z orthogonal axes in [Barlat et al., 1989]	(Eq 2-10)
S_{xy}, S_{yz}, S_{zx}	Stresses in [Barlat et al., 1989]	(Eq 2-10)
t	Time	
t	Thickness	
t_0	Initial thickness	(Figure A1-1)
V	Volume	
v	Velocity	
W	Width for shear specimen	
x_1	Contact height of punch	(Figure A1-1)
x_2	Contact height of die	(Figure A1-1)

α	Stress ratio ($\alpha = \sigma_2 / \sigma_1$)
β	Strain ratio ($\beta = \varepsilon_2 / \varepsilon_1$)
Δ	Increment
$\Delta\varepsilon_1$	Increment in major principal strain ε_1
$\Delta\varepsilon_2$	Increment in minor principal strain ε_2
$\Delta\varepsilon_3$	Increment in minimum principal strain ε_3
ε	True strain
ε_1	Major principal strain
ε_2	Minor principal strain
ε_3	Through thickness principal strain
ε_B	Bending strain
ε_{Br}	Limit strain obtained with Bragard criterion
ε_D	Strain at diffuse necking
ε_L	Strain at localized necking
ε_{S1}	Solution for strain value in (Eq 5-11), the small value
ε_{S2}	Solution for strain value in (Eq 5-11), the large value
ε_t	Thickness strain
$\dot{\varepsilon}$	Strain rate
$\dot{\varepsilon}_1, \dot{\varepsilon}_2, \dot{\varepsilon}_3$	Principal strain rates
$\ddot{\varepsilon}_1, \ddot{\varepsilon}_2, \ddot{\varepsilon}_3$	Pseudo strain acceleration
$(\ddot{\varepsilon}_1)_{\max}$	Maximum major strain acceleration

$(\ddot{\epsilon}_2)_{\max}$	Maximum minor strain acceleration	
$(\ddot{\epsilon}_2)_{\min}$	Minimum minor strain acceleration	
$(\epsilon_1)_{cr}$	Critical major strain	
$\bar{\epsilon}$	Equivalent or effective strain	
$\bar{\epsilon}^p$	Effective plastic strain	
$d\bar{\epsilon}^p$	Increment in equivalent or effective plastic strain	
ϕ	Total stress function [Karafillis-Boyce, 1993]	(Eq 2-18)
ϕ_1	Stress function representing (Barlat 1991) in [Karafillis-Boyce, 1993]	
ϕ_2	Adjusted stress function in [Karafillis-Boyce, 1993]	(Eq 2-19)
ϕ_s	Thickness strain in [Pepelnjak et al, 2005]	(Eq 2-26)
$\ddot{\phi}_s$	Second derivative of thickness strain in [Pepelnjak et al, 2005]	(Eq 2-26)
γ	Stress ratio $(\gamma = \sigma_3 / \sigma_1)$	
μ	Coulomb friction coefficient between tools and sheet	
θ	Contact angle	
σ	True stress	
σ_0	Yield stress in uniaxial tension	
σ_1	Major principal stress	
σ_2	Minor principal stress	
σ_3	Through thickness principal stress	
σ_{H1}	Flow stress, hybrid law (1)	

σ_{H2}	Flow stress, hybrid law (2)	
σ_{H3}	Flow stress, hybrid law (3)	
σ_h	Hydrostatic stress	
σ_p	Flow stress, power law	
σ_V	Flow stress, Voce law	
σ_x	Rolling direction stress [Barlat et al., 1989]	(Eq 2-10)
σ_y	Transverse direction stress [Barlat et al., 1989]	(Eq 2-10)
σ_i	Flow stress	(Eq 2-28)
$\bar{\sigma}$	Equivalent or effective stress	

Chapter 1

Introduction

1.1 Definition And Application Of Forming Limit Diagram (FLD)

Sheet forming is an important process to produce automotive components. Formability or the ability to make a part without a failure is often assessed using a forming limit diagram (or FLD) prior to a forming operation. The FLD is a measure of formability of a sheet material [Keeler et al., 1963, Goodwin, 1968]. Sheet specimens are subjected to a variety of strain paths by a punch stretching process. The minor-major strain pairs (ϵ_2 , ϵ_1) that are closest to the neck on multiple specimens are utilized to construct a boundary between safe and unsafe zones (Figure 1-1). The resulting curve is defined as a forming limit diagram (thick solid line in Figure 1-2). Beyond the forming limit curve, as the strain path changes towards the plane strain state ($\epsilon_2 \approx 0$), the neck deepens, which leads to fracture as shown by the dashed line in Figure 1-2.

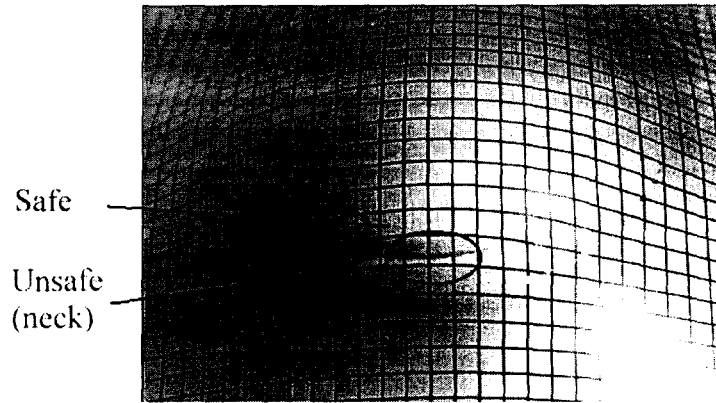


FIGURE 1-1. A photograph of a dome specimen showing a ring of localized neck.

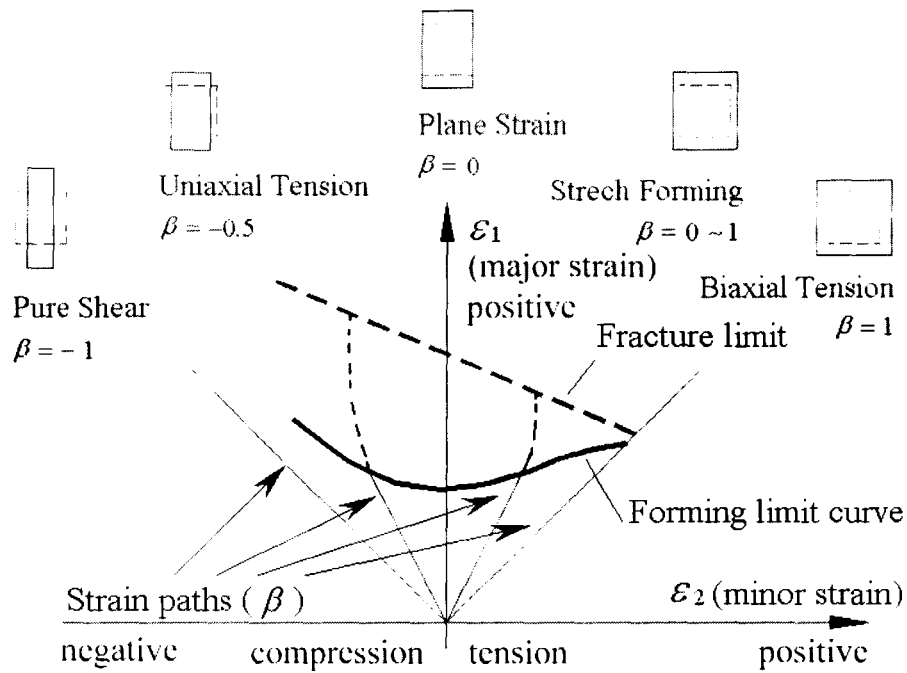


FIGURE 1-2. A typical FLD showing various forming modes.

The concept of FLD has been widely accepted in metal forming industry to identify the limit strains of stretched sheets or to evaluate the formability of different

metals. An important challenge in FLD determination, both theoretically and experimentally, involves determination of the onset of localization. Many attempts have been made in the past towards force, stress and strain based localization criteria. A review of the literature is present in Chapter 2.

1.2 Objectives Of Present Research

This research is aimed at developing a rapid and accurate experimental and analytical methodology to obtain FLDs by utilizing experimental load versus displacement traces and by incorporating FE analysis of strain localization in a hemispherical punch test. Limit strains are traditionally obtained using laborious and time-consuming surface grid based strain measurements on multiple samples. The proposed approach avoids using experimental strain measurement in the vicinity of the neck on the dome specimens. The formability data (or limit strains) is to be collected from the FE simulations of punch tests in which various combinations of specimen geometry and friction produce different strain paths, and then assembled to construct a FLD. The methodology is explained in detail in Chapter 3. Specific objectives are to:

- Develop a criterion to determine the onset of localization from an integrated method of load analysis and strain evolution.
- Reveal and integrate the characteristics of load and strain evolution during the hemispherical punch stretching tests in order to apply the proposed criterion towards determination of FLD.

- Demonstrate and analyze the effectiveness of the new method for several automotive sheet materials and a range of test conditions by comparing with other available experimental and numerical approaches, as well as the effectiveness of optical on-line strain measurement system for analyzing the localized strains.

1.3 System Of Units

The imperial units (inch) are used for punch diameter, sheet diameter and width. All the other units, such as test speed and sheet thickness, are in metric system.

Chapter 2

Literature Review

In this chapter, major studies and the associated parameters that influence the FLD determination are reviewed. In particular, Marciniak-Kuczynski model and its subsequent development are reviewed. Various continuum yield criteria are compared for the influence on the prediction of FLD. Determinations of forming limit are discussed both theoretically and experimentally. Also, failure modes in sheet forming processes and various fracture criteria applied to sheet forming are compared. In addition, evidence and analysis of inflection point in load versus displacement curve during hemispherical punch test is reviewed. Stress-strain behaviour at large strain, its uncertainty and aspects of optimization of material input are reviewed. In terms of specific material behaviour, research on thickness and strain rate effect on aluminum alloys is investigated. Past efforts to obtain additional strain paths to enhance the FLD determination are discussed. Finally, some of the recent studies on finite element simulation of hemispherical punch test to obtain FLD are reviewed.

2.1 Significant Studies In FLD Research (Prediction Of Localized Necking Behaviour)

Many attempts have been made to obtain the FLDs experimentally and theoretically, such as the theory of localized necking [Hill, 1948], theory of diffuse

necking for biaxial loading [Swift, 1952]. More recently, Marciniak and Kuczynski analysis assumes an existence of an initial thickness imperfection in the sheet and involves a comparison of strain paths of material point in and outside of the imperfection to obtain limit strains [Marciniak and Kuczynski, 1967, 1973]. In this analysis and subsequent researches, it has been found that FLD is affected by many factors such as r -value, material imperfection, yield criteria, hardening laws, grain size, etc. This complexity has made the existing approaches for predicting FLD often unsatisfactory and less robust.

2.1.1 Marciniak-Kuczynski Model To Predict FLD

The prediction of FLDs has been further developed in recent years by incorporating various enhancements, such as the effects of stress state (bending and out-of-plane deformation), the intrinsic factors of strain-hardening exponent n , strain rate sensitivity m , anisotropic ratio r -value, material imperfection based on surface roughness f_0 , thickness effects, hardening laws, yield criteria and grain size. The influences of parameters n , m have been extensively studied by many researchers and are clearly understood, whereas the role of strain ratio r -value and yield criterion is often debatable. The selection of material imperfection parameter f_0 in M-K analysis is often arbitrary and in many studies this parameter is adjusted to match the experimental data. Although effort has continued for the past three decades to improve the predictions of FLDs by M-K method, it is still difficult to consistently reproduce the experimental FLDs for a range

of materials and test conditions. Extension of M-K analysis as mentioned above can be found in the following references, which are presented more or less chronologically.

- * Anisotropic ratio, r -value, material imperfection, f_0 [Parmar et al., 1977] [Rasmussen, 1982];
- * Effects of stress state (bending and out-of-plane deformation) [Marciniak Kuczynski, 1979] [Barata da Rocha, 1995], strain path changes on work hardening [Barata da Rocha, 1989]
- * Sheet thickness effects [Wilson et al., 1982]
- * Grain size and surface roughness effects [Wilson et al., 1983]
- * FE models of basic M-K specimen geometry including finite groove models [Bate et al., 1984] [Zhao et al., 1996]
- * Incorporation of new continuum and crystallographic yield criteria [Barata Da Rocha et al., 1984] [Barlat et al., 1989] [Toth et al., 1996]
- * Temperature effects by incorporating temperature sensitive models [Ferron, et al., 1985]
- * Incorporation of realistic material dependent hardening laws [Barata Da Rocha, 1989] [Jain et al., 1996] [Barlat et al., 2002]
- * Strain rate, strain rate sensitivity effects [Barata da Rocha, 1989] [Nie et al., 1991]
- * Intrinsic factors of strain-hardening exponent n , strain rate sensitivity m [Barata Da Rocha, 1989] [Nie et al., 1991];
- * Non-proportional strain paths [Nie et al., 1991]

2.1.2 Approaches Other Than M-K Model To Predict FLD

Approaches other than the M-K model of FLD prediction mainly includes the vertex theory [Lin, 1971]. This theory assumes a vertex or corner at the loading point on the yield surface and has received both theoretical and experimental support [Storen and Rice, 1975] [Hecker, 1976]. However, the singular point in the yield surface or sharp vertex makes the differentiation of the yield function needed in the analysis impossible. Storen and Rice incorporated the J_2 deformation theory into a bifurcation analysis to predict FLD. The occurrence of localized necking is attributed to the formation of a vertex. The approach was inadequate to predict the negative strain ratios and received minor improvement [Hutchinson et al., 1975] [Chu, 1983]. The vertex theory was recently simplified by incorporating Hosford's high-order yield criterion, Hill's quadratic yield criterion and the von Mises yield criterion [Zhu et al., 2001]. Hill's zero-extension criterion can be implemented for LHS whereas the RHS of FLD is largely influenced by the order of yield function [Chow et al., 2001] [Yang et al., 2001].

2.2 Yield Criteria Of Material Modelling (Continuum And Crystalline Plasticity Based Criteria)

Various yield criteria that depict the yield behaviour of aluminum sheet materials in forming process are presented in this section. Two fundamental yield criteria that assume isotropic material behaviour are von Mises [von Mises et al., 1928] and Tresca

[Tresca, 1964]. The von Mises criterion indicates that material yields if the three principal stress components (σ_1 , σ_2 and σ_3) in the following form reach their uniaxial elastic limit:

$$f(\sigma_0) = (\sigma_1 - \sigma_2)^2 + (\sigma_1 - \sigma_3)^2 + (\sigma_2 - \sigma_3)^2 \quad (\text{Eq 2-1})$$

where $f(\sigma_0)$ is the uniaxial yield stress only.

According to Tresca yield criterion, yielding occurs when the maximum shear stresses reaches a critical value. In terms of the three principal stress components the criterion can be expressed as three separate expressions depending upon the order of maximum, intermediate and minimum stress component as follows:

$$|\sigma_1 - \sigma_2| = \sigma_0, \text{ or, } |\sigma_2 - \sigma_3| = \sigma_0, \text{ or, } |\sigma_3 - \sigma_1| = \sigma_0 \quad (\text{Eq 2-2})$$

Rolled metallic sheet materials are inherently anisotropic. The most well-known anisotropic yield function is Hill's quadratic (also referred to as Hill's 1948 criterion) [Hill, 1948] (Eq 2-3).

$$f(\sigma) = F(\sigma_2 - \sigma_3)^2 + G(\sigma_1 - \sigma_3)^2 + H(\sigma_1 - \sigma_2)^2 \quad (\text{Eq 2-3})$$

where F , G , H are material constants related to anisotropic parameters, namely $F = r_{RD} = r_0$ (rolling direction), $G = r_{TD} = r_{90}$ (transverse direction) and $H = r_{RD}r_{TD}$ (thickness direction). The symbols r_0 and r_{90} refer to plastic strain ratios along 0° and 90° to the rolling direction of the sheet.

As later verified by other researchers, Hill's quadratic yield criterion does not fit the f.c.c material, such as the aluminum alloys (or metals with r -values less than unity) [Pearce, 1968]. In particular, the proposed theory does not accurately fit the yielding in

plane strain or biaxial tension. Figure 2-1 shows the yield loci for anisotropic materials. As per Hill's 1948 criterion, aluminum alloys are assumed to exhibit lower yield stress in biaxial loading than uniaxial. However, experiments demonstrated the opposite behaviour for aluminum sheet under biaxial loading. This was termed as "anomalous behaviour" [Pearce, 1968].

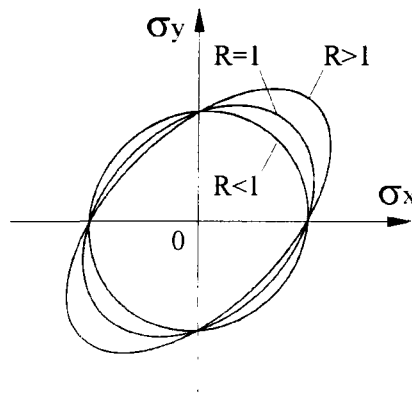


FIGURE 2-1. Schematic yield loci for anisotropic materials.

In order to account for this "anomalous behaviour", especially for aluminum alloys, a new criterion of nonquadratic yield criterion was subsequently proposed by Hill [Hill, 1979].

$$f(\sigma) = F|\sigma_2 - \sigma_3|^m + G|\sigma_1 - \sigma_3|^m + H|\sigma_1 - \sigma_2|^m \\ + L|2\sigma_1 - \sigma_2 - \sigma_3|^m + M|2\sigma_2 - \sigma_3 - \sigma_1|^m + N|2\sigma_3 - \sigma_1 - \sigma_2|^m \quad (\text{Eq 2-4})$$

where F , G , H , L , M , N and m are all material constants. Four cases of the new theory have been proposed. However, since the outward concavity violates the normality principle as per Drucker [Drucker, 1951], only the case of plane stress (case IV, Eq 2-5

below) has received significant interest since it can be utilized to deal with the FLD prediction.

$$f(\sigma) = k(|\sigma_1 - \sigma_2|^m + |\sigma_1 + \sigma_2|^m) \quad (\text{Eq 2-5})$$

where k is constant. The limitation of the nonquadratic theory (Hill 1979) is the non-coaxial problem of principal stress axes (orthotropic) and anisotropy axes and the insufficient representation of shear stress in orthotropic axes [Barlat, 1986].

Criterion that accommodates the stress for non-principal axes was proposed using the form of fourth order of polynomial function [Gotoh, 1977] (Eq 2-6, $\sigma_3 = 0$).

$$\begin{aligned} \sigma^4 = & C_1 \sigma_{xx}^4 + C_2 \sigma_{xx}^3 \sigma_{yy} + C_3 \sigma_{xx}^2 \sigma_{yy}^2 + C_4 \sigma_{xx} \sigma_{yy}^3 + C_5 \sigma_{yy}^4 \\ & + \sigma_{xy}^2 (C_6 \sigma_{xx}^2 + C_7 \sigma_{xx} \sigma_{yy} + C_8 \sigma_{yy}^2) + C_9 \sigma_{xy}^4 \end{aligned} \quad (\text{Eq 2-6})$$

where C_i are constants. Similar polynomial yield function that neglects shear strain was proposed by Jones and Gillis, assuming $\sigma_3 = 0$ [Jones-Gillis, 1984] (Eq 2-7).

$$f(\sigma) = C_{11} \sigma_x^2 + C_{11} \sigma_x \sigma_y + C_{13} \sigma_{xx} \sigma_{xy} + C_{22} \sigma_y^2 + C_{23} \sigma_y \sigma_{xy} + C_{33} \sigma_{xy}^2 \quad (\text{Eq 2-7})$$

where C_{ij} are constants. These modified Hill's quadratic yield functions still cannot fully represent the yielding in pure shear and equi-biaxial tension [Barlat, 1986]. Also, the constants involved in the above expressions have rather tenuous connection to fundamental material parameters and have not been experimentally verified.

Based on polycrystalline yield functions, Hosford proposed a modified Hill quadratic yield criterion [Hosford, 1979] (Eq 2-8).

$$\sigma^m = \frac{1}{1+r} (|\sigma_1|^m + |\sigma_2|^m + r|\sigma_1 - \sigma_2|^m) \quad (\text{Eq 2-8})$$

where $m = 6$ is for metals with b.c.c. and $m = 8$ is for metals with f.c.c. crystal structures. However, the Hosford criterion still leads to “anomalous behaviour”. Bassani proposed a nonquadratic equation as a solution to the “anomalous behaviour” problem [Bassani, 1977] (Eq 2-9).

$$|\sigma|^n + k|\sigma|^m = |\sigma_1 + \sigma_2|^n + k|\sigma_1 - \sigma_2|^m \quad (\text{Eq 2-9})$$

where n and m are two different constants. The major deficiency of this criterion is the lack of explicit solution to obtain the n , m and k values.

Barlat and coworkers proposed a series of nonquadratic criteria. In 1989, a tri-component criterion (two normal and one shear stress) for rolled sheet materials was proposed [Barlat, Lian, 1989] (Eq 2-10).

$$2\sigma^m = a_1 K_1 + K_2 + a_1 K_1 - K_2 + (2 - a) 2K_2,$$

$$\text{with } K_1 = \frac{\sigma_{xx} + h\sigma_{yy}}{2}, K_2 = \sqrt{\left[\frac{\sigma_{xx} - h\sigma_{yy}}{2}\right]^2 + p^2 \tau_{xy}^2} \quad (\text{Eq 2-10})$$

where a , h , p and m are parameters that characterize the material anisotropy, and x and y represent the rolling and transverse directions in the sheet respectively.

A six-stress component anisotropic yield criterion was proposed in 1991 [Barlat et al., 1991] (Eq 2-11).

$$2\sigma^M = |S_1 - S_2|^M + |S_2 - S_3|^M + |S_3 - S_1|^M \quad (\text{Eq 2-11})$$

where σ is the effective stress, $S_{i=1,2,3}$ are the principal values of a symmetric matrix $S_{\alpha\beta}$, defined with the components of the stress σ as:

$$S_{xx} = \frac{c(\sigma_{xx} - \sigma_{yy}) - b(\sigma_{zz} - \sigma_{xx})}{3} \quad (\text{Eq 2-12})$$

$$S_{yy} = \frac{a(\sigma_{yy} - \sigma_{zz}) - c(\sigma_{xx} - \sigma_{yy})}{3} \quad (\text{Eq 2-13})$$

$$S_{zz} = \frac{b(\sigma_{zz} - \sigma_{xx}) - a(\sigma_{yy} - \sigma_{zz})}{3} \quad (\text{Eq 2-14})$$

$$S_{yz} = f\sigma_{yz} \quad (\text{Eq 2-15})$$

$$S_{zx} = g\sigma_{zx} \quad (\text{Eq 2-16})$$

$$S_{xy} = h\sigma_{xy} \quad (\text{Eq 2-17})$$

The subscripts x , y and z in equations (Eq 2-12 to 2-17) represent the mutually orthogonal axes. The coefficients of a , b , c , f , g and h represent the anisotropic material properties. This approximation of yield surfaces leads to Hosford's criterion when M equals to 6 and 8. Also, this function reduces to von Mises criterion for $M = 2$ or 4 and Tresca for $M = 1$. As Barlat's 1991 criterion is the generalized version of Hill's 1948 and Hosford's criterion, it also has the disadvantage such as the "anomalous behaviour" of aluminum.

The Barlat's 1991 criterion was further extended by Karaffilis and Boyce using weight function [Karaffilis-Boyce, 1993].

$$\phi = (1 - c)\phi_1 + c\phi_2 \quad (\text{Eq 2-18})$$

where ϕ_1 is the same yield function as Barlat 1991 (Eq 2-11) and ϕ_2 is defined by:

$$\phi_2 = 2\sigma^M = \frac{3^M}{2^{M-1} + 1} \left(|S_1|^M + |S_2|^M + |S_3|^M \right) \quad (\text{Eq 2-19})$$

c is a weight factor. When c is zero, the above yield function reduces to Barlat's 1991 criterion. As reviewed by Barlat, the c value accounts for isotropic behaviour, so that c does not help to improve the prediction in ϕ_1 [Barlat et al., 1997].

In summary, a number of yield criteria for anisotropic sheet materials have been proposed since the first one from Hill in 1948. However, many of these yield functions have not been fully and properly verified by suitable experiments, although some parameters were generalized as phenomenological models [Inal et al., 2000]. Theoretical analysis has shown that although the Hill and Barlat yield criteria to some extent produce improvement to the FLD prediction compared to the Mises for aluminum alloys, many of the parameters are expensive to justify.

Since theoretical and FE based investigations to obtain FLDs have mainly focused on the exploration and implementation of yield criterion of plastic anisotropy with increasing complexity, more inputs are often required from the experiments. This has made the FE prediction rather expensive and far from practical. Some modelling works and associated assumptions are still not justifiable in the context of experimental FLD test procedures.

Theoretical predictions of FLD using M-K analysis have shown that the limitation of M-K method mainly lies in its many assumptions some of which are not fully justifiable. For example, the selection of the yield criterion itself can provide significantly different prediction of FLD (Figure 2-2). The closest agreement with experimental data is the result calculated with CMTP (continuum mechanics of textured polycrystals, a crystal plasticity based yield criterion) [Montheillet et al., 1985]. The significant difference in the predicted results between the continuum model and crystal plasticity model is probably attributed to the microstructural and textural changes in aluminum sheet during forming processes that are accounted in the CMTP model [Zhou et al., 1993].

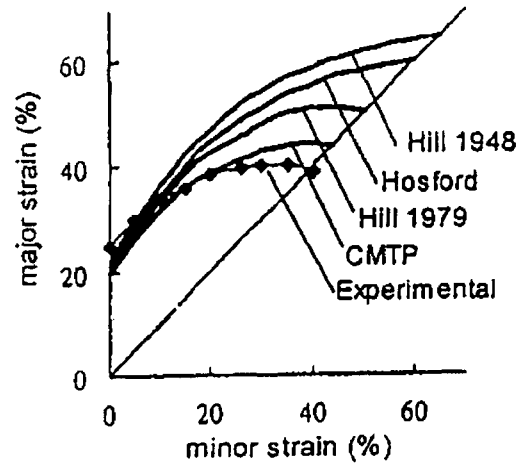


FIGURE 2-2. Sensitivity of FLD predictions based on M-K theory on the choice of yield criterion [Tai et al., 1996].

A detailed discussion of crystal plasticity based yield criterion is beyond the scope of the present work and will not be reviewed.

2.3 Determining Onset Of Localized Necking

2.3.1 Theoretical Determination Of Instability

An important factor in determining forming limits is the theoretical determination of the onset of strain localization. The plastic instability was first studied by subjecting materials to uniaxial tension (homogeneous tensile specimens at constant strain rate) by Considère in 1885 [Considère, 1885]. A maximum loading condition ($dF = 0$) was proposed as an instability criterion. For a material that follows power law as a stress-strain relationship ($\sigma = K\epsilon^n$) this criterion leads to the following expression for instability:

$$\frac{1}{\sigma} \frac{d\sigma}{d\varepsilon} = 1 \quad (\text{Eq 2-20})$$

where n is the hardening index. The following condition for localized necking was derived [Hart, 1967]:

$$\frac{1}{\sigma} \frac{d\sigma}{d\varepsilon} = \frac{1}{2} \quad (\text{Eq 2-21})$$

Early researches to obtain the FLDs include the theory of localized necking for tension-compression region [Hill, 1948]:

$$\varepsilon_1 = \frac{n}{1+\beta}, \quad (\beta = \varepsilon_2 / \varepsilon_1, -1/2 < \beta < 0) \quad (\text{Eq 2-22})$$

A criterion of critical major strain to predict the onset of diffuse necking, based on the assumption that a maximum load leads to a plastic instability under proportional loading, was developed by Swift [Swift, 1952].

$$\varepsilon_1 = \frac{2n(1+\beta+\beta^2)}{(1+\beta)(2\beta^2-\beta+2)} \quad (\text{Eq 2-23})$$

However, the strain of interest in forming is significantly underestimated from this criterion to be useful in practice since the occurrence of localized necking (but not the diffuse necking) is of more practical relevance.

The quantification of thickness reduction in diffuse necking is made by utilizing the two in-plane strain rates $\dot{\varepsilon}_1$ and $\dot{\varepsilon}_2$ while localized necking utilizes only $\dot{\varepsilon}_1$. The strain rate $\dot{\varepsilon}_2$ along the necking band is assumed to be zero [Lian et al., 1989].

The instability of plane stress has been extended with Hollomon's law by taking the through thickness stress component σ_3 into account [Gotoh, 1995].

$$\varepsilon_1 = \frac{2n(1 + \alpha + \alpha^2)(1 - \gamma)}{(1 + \alpha)(2\alpha^2 - \alpha + 2) + \gamma\alpha^2(1 - \alpha)} \quad (\text{diffuse necking}) \quad (\text{Eq 2-24})$$

$$\varepsilon_1 = \frac{n}{(1 + \alpha) \left(1 + \frac{\frac{\gamma}{2}(1 + \alpha - 2\gamma)}{(1 + \alpha + \alpha^2) - \gamma(1 + \alpha - \gamma)} \right)} \quad (\text{localized necking}) \quad (\text{Eq 2-25})$$

where $\gamma = \sigma_3 / \sigma_1$, $\alpha = \sigma_2 / \sigma_1$ (ratio of in-plane minor stress to in-plane major stress).

Although this model has considered the out-of-plane deformation, and the σ_3 stress component enhances the formability of sheet materials, it has been found that it is only valid for the strain rate insensitive materials, such as some aluminum alloys [Smith et al., 2003].

The concept of plastic instability or strain localization based on an increasing strain gradient was analyzed by considering three different types of defects [Kocks et al., 1979]. The defects included (i) a “geometric” defect similar to the one considered in the initial M-K analysis, (ii) a “deformation” defect (possible origin includes pre-strained region in a material), and (iii) a “material heterogeneity” defect arising from compositional and / or microstructural differences. The analysis was carried out for a strain hardening and strain rate hardening material with a constitutive law in the form of $\sigma = K\varepsilon^n \dot{\varepsilon}^m$. A detailed analysis of an axisymmetric bar under uniaxial tension led to a second order differential equation in terms of the cross-section area gradient of the test specimen. This differential equation was solved for each of the above defect types (and their mathematical descriptions) to gain an insight into the evolution of area (or strain) gradient with increasing strain. Three hypothetical sets of material parameters were

considered in this analysis corresponding to different levels of work hardening, strain rate and uniform strain for each of the defect types. The results from this analysis typically revealed a characteristic saddle shape curves in area rate gradient (strain gradient) as a function of macroscopic axial strain (see Figure 2-3 for a schematic description). The lowest point in the curves has been attributed to the onset of plastic instability (point *I* in Figure 2-3). However, as concluded by the authors, severe neck growth characteristic of localized necking, is usually delayed very considerably past this point (for example, point *N* in Figure 2-3).

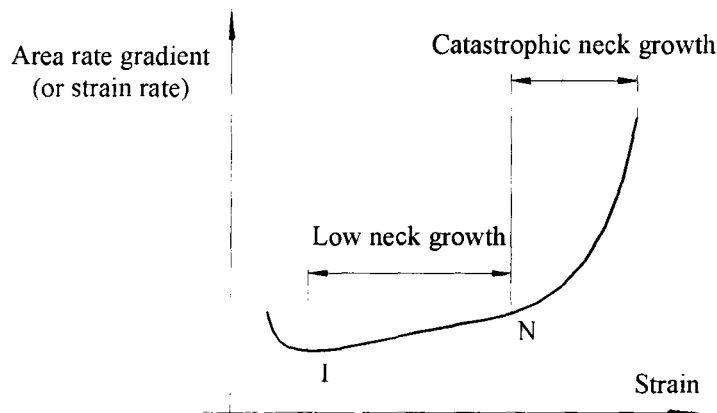


FIGURE 2-3. Schematic of strain gradient as function of strain [Kocks et al., 1979].

The plastic flow beyond unstable deformation is influenced by the strain increment in the necking region [Barata Da Rocha et al., 1984]. The change in the strain path to plane strain is still considered a necessary condition for onset of localized necking. It is assumed in all cases that plane strain state is reached in the localized neck region. The plane strain state is assumed to prevail in the neck until fracture occurs often largely

due to the inability to experimentally capture the strain evolution in the neck. The final stage of deformation has been studied with an empirical method to obtain the critical effective strain values to determine the strain paths [Muschenborn et al., 1975].

2.3.2 Experimental Limitations Of Existing FLD Test Methods, Associated Test Variables And Their Determination

Experimental procedure to determine the FLDs has been further developed since the first hemispherical punch test by Hecker [Hecker, 1972]. Two major experimental methods for FLD tests based on Marciniak and Nakajima punch tests are widely used. The Marciniak type of punch is an axisymmetric cylinder with a flat bottom and a central cut out region to allow unsupported deformation of the sheet, i.e. in-plane test of sheet, for limit strain. Nakajima type of punch is a hemispherical punch that allows out-of-plane deformation. Specimen with imprinted grid on its exposed surface is clamped in a test rig typically mounted on a specially designed mechanical test system is utilized to stretch the specimen to fracture. During the test, localized necking behaviour of test material occurs prior to fracture. The imprinted grids on specimen typically include periodic square or circular pattern that are subsequently processed using square grid analysis (SGA) and circle grid analysis (CGA) methods to obtain principal strains on the surface of the sheet and in the vicinity of neck or fracture. Hecker proposed a method to determine the limit strains by identifying the status of the grid as fractured, necked and unnecked (Figure 2-4). The major and minor strains of different types are calculated and plotted in the FLD

strain space. The limit curve is constructed by linking the points between the necked and unnecked regions (Figure 2-5). This approach has been utilized widely for its simplicity.

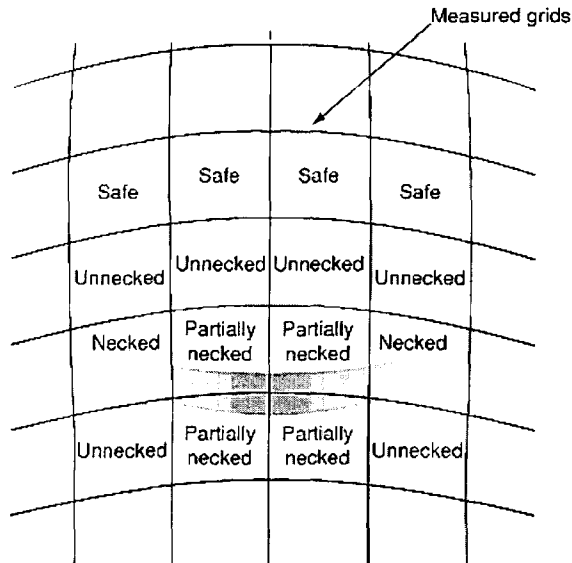


FIGURE 2-4. Identifying deformed specimen as per different status of grids as safe, unnecked, partially necked and necked (area colored in gray representing a localized region).

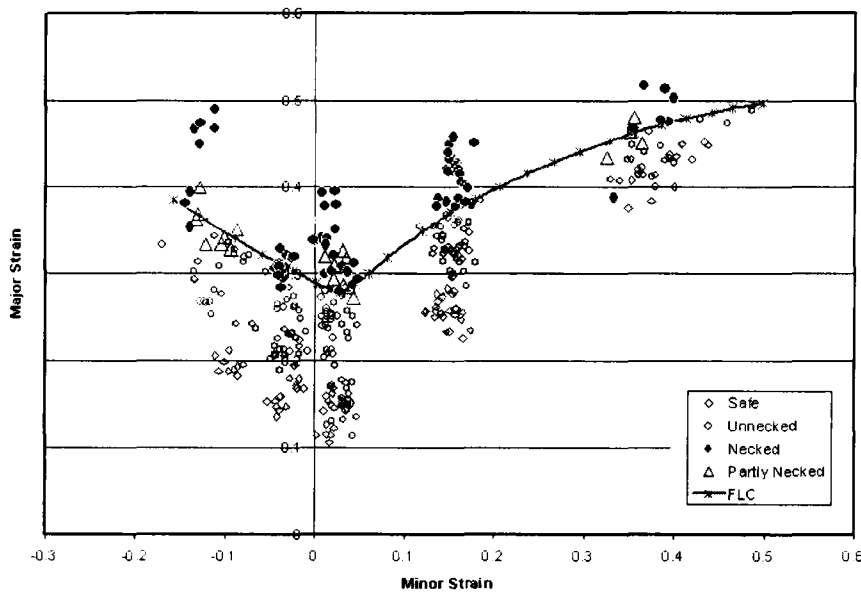


FIGURE 2-5. Typical result of FLD construction (material: AA5754-O, 2mm).

FLD is generally considered as a material property and it is often compared for different materials to assess their relative forming performance. However, the profile and location of the FLD curve is highly sensitive to the experimental procedure, tool dimension, grid type and strain measurement technique. Extensive investigation on experimental variability such as punch diameter, test speed, grid size and analysis method have been reported [Story, 1982] [Jain et al., 1994]. The clamp force and draw bead design were investigated for their influence on FLD [Schey et al., 1991]. Increased clamp force resulted in decreased limit dome height. Increased punch force was obtained from wider specimen (draw bead with greater radius). It was also noted that prestrains are introduced in the specimen during the clamp process with a lock bead. Material movement and deformation at the lock bead causes specimen to have some straining in the region outside of the lock-bead prior to the punch contact. The amount of “pre-straining” depends on the size of the draw bead, radius of lock ring and magnitude of clamp height. The prestrained specimens generally result in strain path changes and affect the FLD. This has been noted in several studies [Graf et al., 1993]. Biaxially prestrained specimens tend to lower the overall FLD. On the other hand, uniaxially prestrained specimens exhibit increased forming limits on the tension-tension side and only a minor change on the tension-compression side. The lowest limits, generally under a plane strain path, in prestrained specimen, also shifted depending on prestrain loading path. These results have implication in the test rig design and process control to avoid deviation in the FLD from an “as received” state of material.

Industrial applications such as sheet stamping require a simple, accurate and rapid approach to evaluate the FLD. Experimental methodology using grid measurement in the neck region tends to be laborious and time consuming. To experimentally obtain the limit strains, various techniques to measure the surface strains such as grid (periodic) pattern have been widely employed. More recently, a speckle (stochastic) pattern has also been used with success [Galanulis et al., 1999]. The major-minor strain pairs from grids or speckle pattern that are closest to the neck on multiple specimens are then utilized to construct a boundary between safe and unsafe zones.

The strains from selected grids on the deformed specimens can be analyzed in a position plot and interpolated with Bragard criterion [Bragard et al, 1972]. A quadratic curve fitting is often utilized to obtain the vertex in major strain (ϵ_{Br}) and corresponding minor strain as the limit strain (Figure 2-6, the symbols shown in the graph are for a later discussion). This criterion applies well when the maximum value of measured strain is at the very centre of the specimen and a well-established strain gradient is present in the data. Subjectivity exists since a different selection of measured points may produce errors in the shape and position of the resulting limit curves. Most importantly, this so-called “maximum” value does not physically exist (or physically measured). In fact, to address subjectivity associated with this type of interpolation, ISO standard TC164/SC for FLD determination has been recommended.

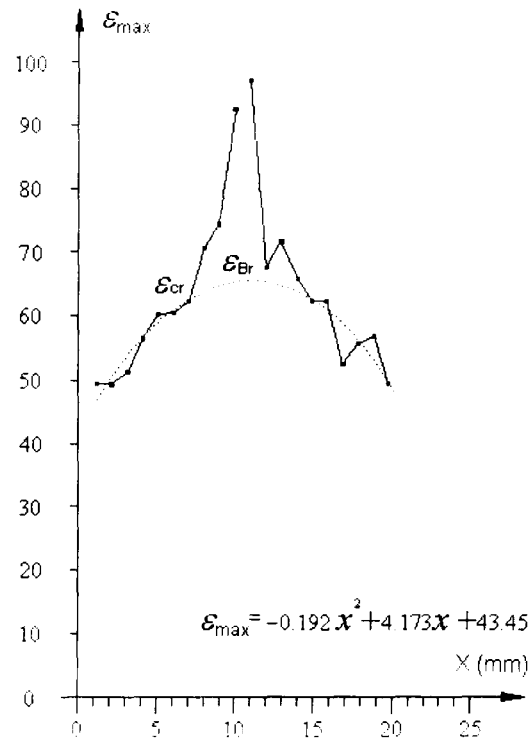


FIGURE 2-6. Strain distribution across a neck in a test specimen. Scheme by Bragard criterion is used to obtain limit strain (major strain). Dashed curve indicates an interpolation.

Speckle pattern can be analyzed using automated strain measurement system and has less limitation on grid size since it can be produced in the micron level [Galanulis et al., 1999]. On-line imaging with a speckle pattern has been employed in some tests in conjunction with Bragard criterion to obtain the limit strains. The advantage of the on-line imaging and speckle-based strain analysis system is that the entire deformation process can be captured and calculated to obtain history of a forming process. However, there is no commonly accepted criterion for the analysis of strain history to obtain the limit strains.

One method to compare the strain gradient of neighboring patterns at a given instance was proposed to obtain the limit strains [Geiger et al., 2003]. The major strain distribution of a localized neck and its vicinity from a deformed specimen is obtained and plotted as a function of coordinate. The gradient, the first derivative, is calculated. By observation of a rapid increase of the gradient, the onset of localized necking is located (Figure 2-7).

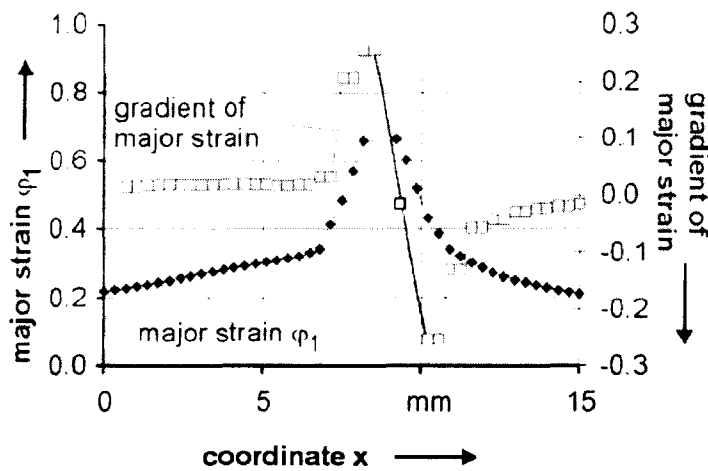


FIGURE 2-7. Gradient of major strain as an indicator for the onset of necking, H360LA, sheet thickness $s = 1.5$ mm, plain strain [Geiger et al., 2003].

Figure 2-8 shows a plot of temporal and spatial distribution of strains from a deformed specimen. In each curve of a recorded strain history, the gradient is obtained. From the comparison of the gradient curves, the strain value corresponding to the gradient showing rapid increase is verified as limit strain.

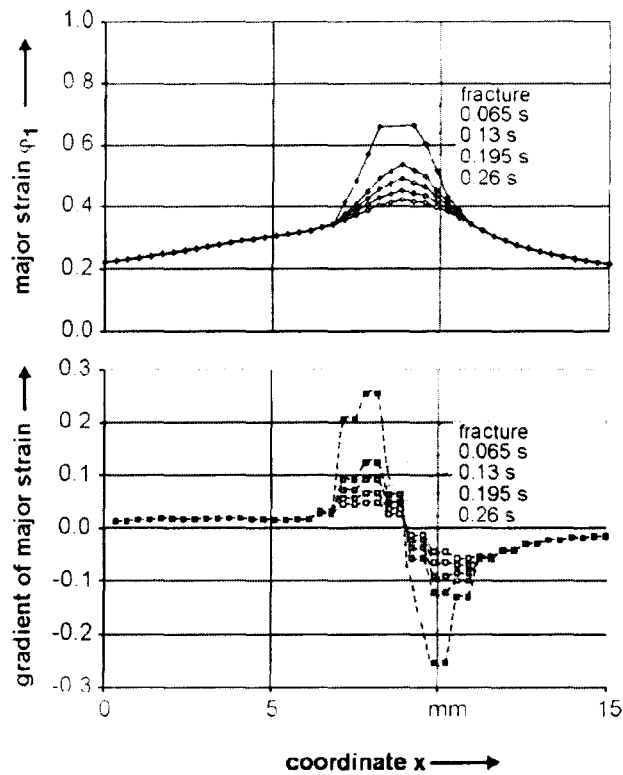


FIGURE 2-8. Development of strain distribution and gradient of major strain as a function of time, H360LA, sheet thickness $s = 1.5$ mm, plain strain [Geiger et al., 2003].

The question arises as to when a material point in its deformation history becomes the site of a neck. The selection of the instance after the failure requires a definite criterion but was not discussed. In other words, the strain history is not fully utilized. The basis of this method is still a comparison of the localized neck and its vicinity, i.e., an analysis of spatial output of strain. In such a condition, comparison of strain gradients of neck and its neighbor is always pattern size dependent. Therefore, the presented results are still a study of the relationship between the neck and its vicinity but not the neck itself.

Strain history was considered and a concept of “acceleration” was proposed for processing the thickness strain [Pepelnjak et al., 2005].

$$\ddot{\varphi}_s = \frac{d^2\varphi_s}{dt^2} \quad (\text{Eq 2-26})$$

where φ_s , $\dot{\varphi}_s$ and t are the thickness strain, strain acceleration and simulation time respectively. The procedure to obtain the limit strain is demonstrated in Figures 2-9 and 2-10. The necking point is assumed to be present in the circled area (Figure 2-9), which is obtained from post-processing by taking the first and second derivatives of thickness strain (Figure 2-10).

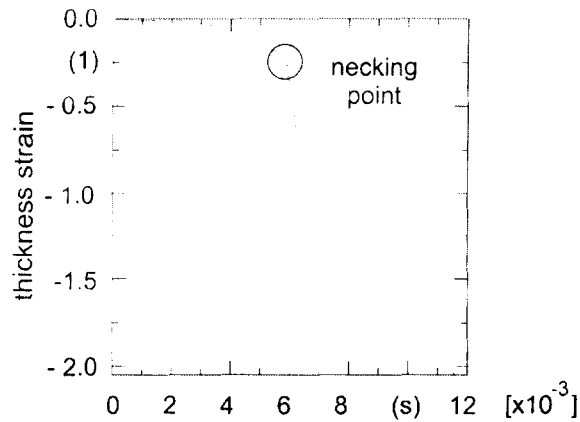


FIGURE 2-9. Thinning as a function of time for the critical node [Pepelnjak et al., 2005].

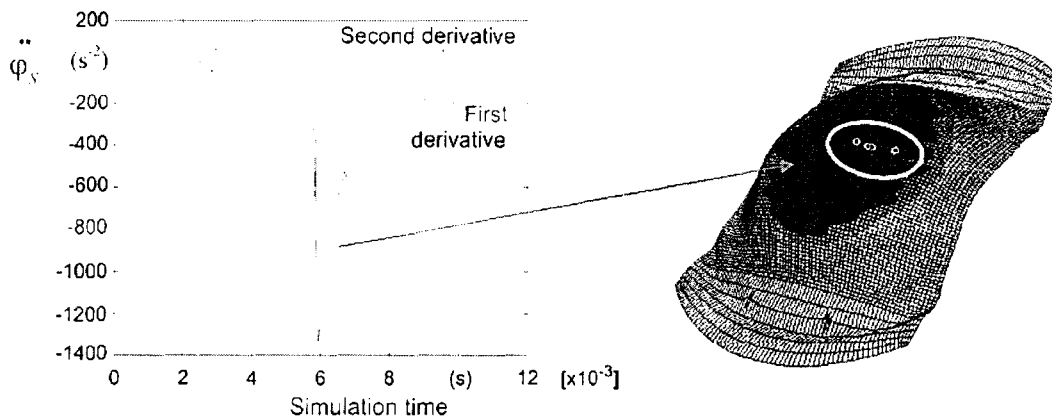


FIGURE 2-10. Significant peak of second time derivation of the thickness strain and corresponding nodes on the formed specimen [Pepelnjak et al., 2005].

Pepelnjak's research directly associated the thickness reduction with limit strain by considering that necking occurs because the work hardening can no longer overcome the thickness reduction. A procedure to obtain the limit strain was proposed. However, a physical meaning to thickness based "acceleration" was not extensively revealed. There was no experimental support to the FE approach of obtaining the strain history and derivatives, although this is actually not a major deficiency, as thickness strain is generally not directly examined from experiment. Also, only the thickness was considered but not the commonly obtained experimental major and minor strain component and their derivatives.

A more suitable criterion to determine the forming limit from the strain history was earlier proposed by this author [Situ et al., 2006]. In this research, a criterion to locate the inflection point in the major strain rate curve has been examined with ARAMIS on-line imaging and strain analysis system. Also, routinely obtained experimental load versus displacement curves were utilized to adjust the input to the FE models. The combination of these conventional methods has never been employed to predict the limit strains of sheet materials. This approach is presented in detail in Chapter 4.

2.4 Failure

Failure during sheet forming process reflects not only the capacity of work hardening of aluminum alloys but also the development of different ductile damage processes. Based on the initiation and propagation of a crack, the failure mode can be

sorted into ductile fracture and localized shear fracture. Ductile fracture, caused by hydrostatic or mean stresses, involves nucleation, propagation and coalescence of microvoids, whereas the localized shear fracture forms a macroscopic shear band due to the insufficient work hardening rate [Teirlinck et al., 1987]. Theoretical models for the failure modes are accordingly established as uncoupled damage and coupled damage.

Uncoupled damage assumes that the constitutive law is not affected by the damage development. The occurrence of fracture depends on a threshold value obtained from an integral of a certain stress function over the strain range as shown in (Eq 2-27).

$$D = \int_0^{\bar{\epsilon}^p} f(\sigma) d\bar{\epsilon}^p \quad (\text{Eq 2-27})$$

where D is a normalized damage parameter, $\bar{\epsilon}^p$ is the effective plastic strain, $d\bar{\epsilon}^p$ is an increment in equivalent or effective plastic strain. Studies of uncoupled damage models are often obtained empirically, such as the early studies using effective stress [Freudenthal, 1950] and maximum principal stress (σ_I) as a fracture criterion [Cockcroft-Latham, 1968]. Principal stress components as well as hydrostatic stress (σ_h) at large plastic strains permit the voids to grow and coalesce. This justifies the integration over effective plastic strain. Triaxiality (or hydrostatic stress) was subsequently added to account for the growth of damage (for example voids) [Rice-Tracey, 1969] [Oyane et al. 1980]. A summary of some of the continuum fracture criteria applied to sheet forming is presented in Table 2-1.

TABLE 2-1. Representative fracture criteria of uncoupled damage model.

Author and year	Fracture Criterion
Freudenthal, 1950	$D = \int_0^{\bar{\epsilon}^p} \bar{\sigma} d\bar{\epsilon}^p$
Cockcroft and Latham, 1968	$D = \int_0^{\bar{\epsilon}^p} \sigma_1 d\bar{\epsilon}^p$
McClintock, 1968	$D = \int_0^{\bar{\epsilon}^p} \left(\frac{2}{\sqrt{3}(1+n)} \sin\left(\frac{\sqrt{3}(1-n)}{2}\right) \frac{\sigma_1 + \sigma_2}{\bar{\sigma}} \right) d\bar{\epsilon}^p$
Rice and Tracy, 1969	$D = \int_0^{\bar{\epsilon}^p} \exp\left(c \frac{\sigma_h}{\bar{\sigma}}\right) d\bar{\epsilon}^p$
Oyane et al., 1980	$D = \int_0^{\bar{\epsilon}^p} \left(1 + C \frac{\sigma_h}{\bar{\sigma}}\right) d\bar{\epsilon}^p$

Since a threshold value for crack initiation is utilized, uncoupled damage models are convenient for implementation in FE modelling as they are often based on one or two experimentally measured parameters. However, the models are not realistic because influence of fracture evolution on material properties is neglected. Insufficient representation of crack propagation still remains to be a problem.

Coupled damage models involve constitutive laws that incorporate damage characteristics of the materials as intrinsic parameters. As the damage evolves the constitutive softening of the material occurs. A widely used constitutive softening model applicable to ductile fracture was proposed by Gurson [Gurson, 1977] and modified later by Needleman and Tvergaard [Needleman-Tvergaard, 1984]. The Gurson model is a pressure sensitive yield function for a porous solid, Φ , which is defined as:

$$\Phi = \left(\frac{\bar{\sigma}}{\sigma_y}\right)^2 + 2f^* q_1 \cos\left(-\frac{3}{2} q_2 \frac{\sigma_h}{\sigma_y}\right) - (1 + f^* q_3) = 0 \quad (\text{Eq 2-28})$$

where $\bar{\sigma}$ is the equivalent stress, σ_y the flow stress, σ_h the hydrostatic stress, q_1, q_2 and q_3 are material constants and f is the volumetric fraction of voids in the material as shown in (Eq 2-29):

$$f^*(f) = \begin{cases} f, & \text{for } f \leq f_c \\ f_c - \frac{f_U - f_c}{f_F - f_c}(f - f_c), & \text{for } f > f_c \end{cases} \quad (\text{Eq 2-29})$$

where $f^*(f)$ is effective void volume fraction, f_F is the volume fraction at final failure, f_c and f_U are material constants describing void coalescence. The limitation of modified Gurson model and its modification by Needleman and Tvergaard mainly lies in determination of parameters. The selection of various parameters with definite physical meanings is often arbitrary due to the lack of experimental data for specific materials. Unlike the uncoupled damage models, the implementation of coupled damage models in FE analysis is more complex and remains unrealistic in terms of material specific microstructural damage characteristics [Samuel et al., 1998].

2.5 Inflection And Instability Characteristics Of Punch Based Load-Displacement Curve

The theoretical support of this research comes from the findings of Hecker [Hecker, 1977] and Ghosh [Ghosh, 1977]. Hecker has published the following important observation regarding the inflection point:

“...diffuse necking begins just beyond step 5 in steel and step 8 in brass, which correspond to the inflection points in the load-deflection curves...” (Figure 2-11).

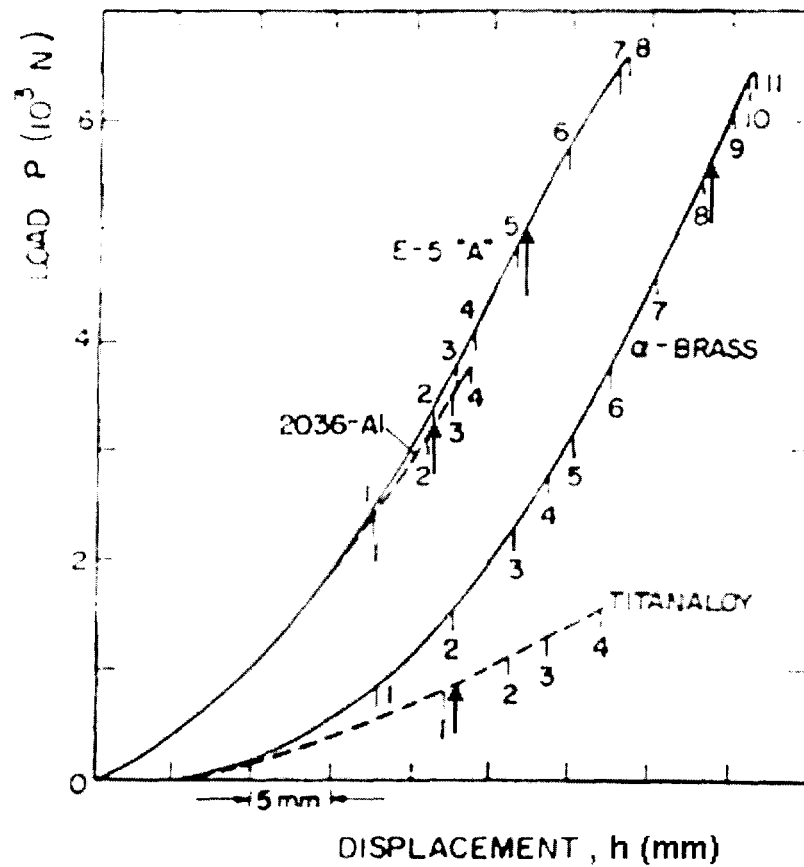


FIGURE 2-11. Punch load as a function of displacement from hemispherical punch stretching tests for four different materials. Arrow indicates the onset of diffuse instability $d^2P/dh^2 = 0$, for each of the materials [Hecker, 1977].

Ghosh also reported that “the inflection points in the load-displacement plots (Figure 2-12, indicated by arrows) correspond to the attainment of maximum crown load”.

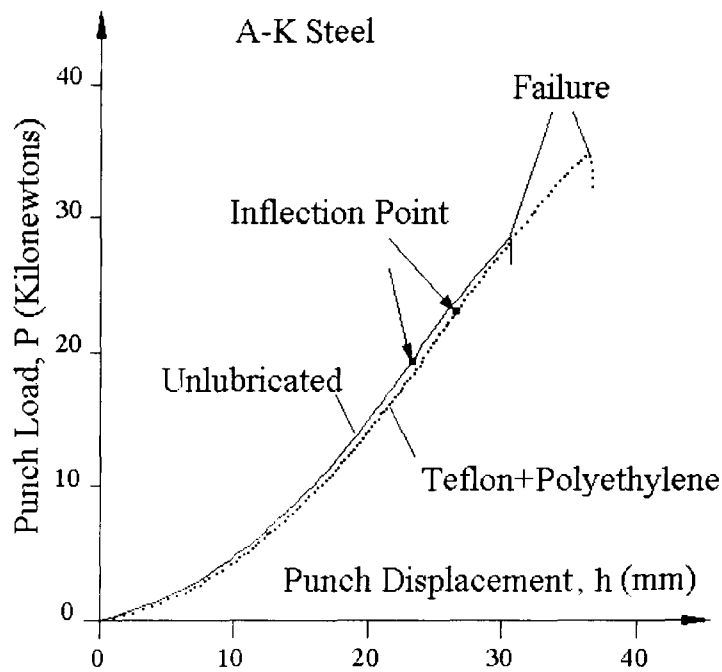


FIGURE 2-12. Punch load versus displacement curves from hemispherical punch tests indicating the location of inflection point [Ghosh, 1977].

Ghosh presented two other important experimental observations. Firstly, it was stated that “*the interface pressure is uniform at any stage of deformation*” (Figure 2-13). Secondly, it was observed that the contact radius of the punch-sheet interface is independent of material property, and is a function of punch displacement only (Figure 2-14).

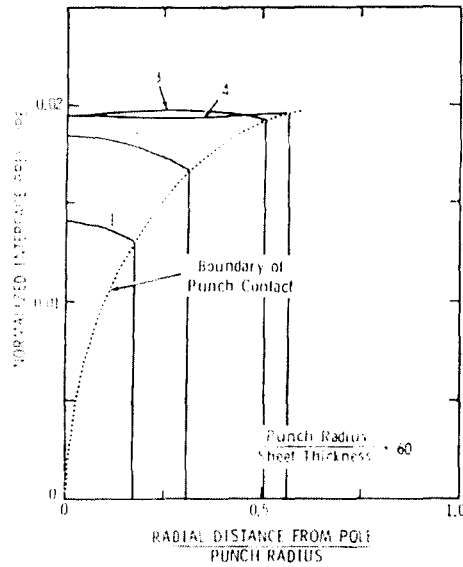


FIGURE 2-13. Punch-to-sheet interface pressure as a function of radial distance from pole of a dome specimen for four stages of punch displacement [Ghosh, 1977].

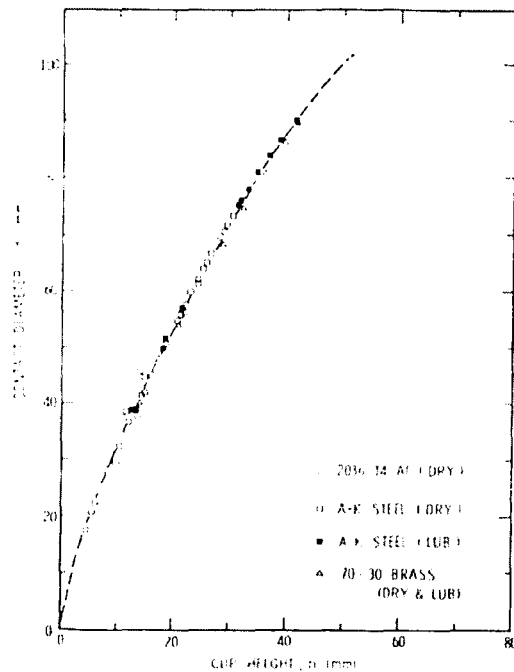


FIGURE 2-14. Diameter of the boundary of punch contact as function of punch displacement [Ghosh, 1977].

An analytical model of the hemispherical punch stretching process that demonstrates the usefulness of the above observation of Ghosh in analyzing instability is presented in Appendix 1. The model enables a quick and easy approach to obtain the inflection point.

2.6 Strain Hardening At Large Strain And Optimization On Stress-Strain Input

Uniaxial tensile test of aluminum alloys typically provide effective strain values not greater than 0.25, whereas for most forming processes the strain value can reach 0.5 and higher when localized necking occurs. Therefore, extrapolation of uniaxial stress-strain curve to large strains is required. Since empirical hardening laws such as Hollomon (or power) law, Voce law, etc, are utilized to fit the uniaxial tensile data, the same laws are also employed to extrapolate the curves beyond the experimental range.

The power law is represented as:

$$\sigma = K \varepsilon_p^n \quad (\text{Eq 2-30})$$

where σ is the flow stress, ε_p the plastic strain, and K and n are the material constants referred to as strength coefficient and strain hardening exponent respectively. The Voce law is represented as:

$$\sigma = B - (B - A)e^{-m\varepsilon} \quad (\text{Eq 2-31})$$

where the A and B are threshold stress and saturation stress respectively, and m is the hardening parameter. The power law does not depict the stress-strain relationship well for

aluminum alloys such as 5xxx and 6xxx especially at large strain values. The true stress versus true strain relationship from hydraulic bulge test for aluminum alloys has demonstrated that a fit to Voce-type saturation-stress constitutive equations exhibits better representation of material behaviour [Voce, 1955]. This indicates that at large strains, the Voce-type hardening law gives a better prediction than the power law for aluminum alloys. The advantage of employing these hardening laws is the simplicity of implementation for material modelling.

The common problem with extrapolation of uniaxial tensile $\sigma - \epsilon$ curve is the lack of direct experimental support to validate the proposed extrapolation. Also, introducing more parameters into consideration would lead to a complicated form and a poor justification for its selection.

There are experimental methods that can directly obtain stress-strain curves up to large strains (0.50 ~ 0.80), such as hydraulic bulge test, in-plane shear test and in-plane biaxial tension test of cruciform specimens. However, all these tests require specialized and expensive equipment and / or specimen preparation method.

Hydraulic bulge test is an important approach to determine the $\sigma - \epsilon$ behaviour of sheet metals. In hydraulic bulge test, sheet metals are deformed frictionless under oil pressure, as shown in Figure 2-15. There is inevitable prestraining from clamping mechanism as well as the bending of the sheet during the test.

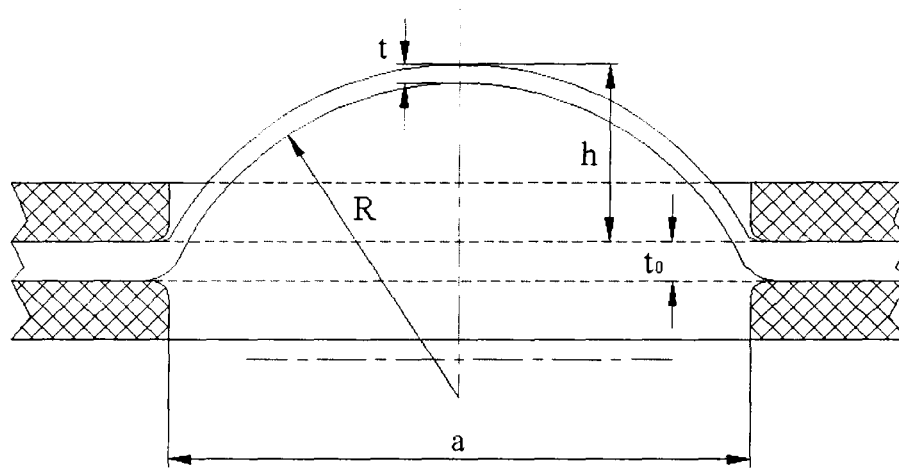


FIGURE 2-15. Schematic of hydraulic bulge test system.

The in-plane pure shear test (Miyachi shear test) was originally proposed by Miyachi [Miyachi, 1985] and later improved by Boogaard [Boogaard, 2002]. The profile of specimen and the pulling force direction is shown in Figure 2-16. The material colored in gray is subjected to pure shear loading. The problem with the specimen design is mainly in terms of attainment of a well-confined shear zone. To overcome this problem, a region of reduced sheet thickness in the shear zone is obtained by high accuracy machining. However, machining introduces sharp corners as well as modifies the original surface characteristics of the sheet in the shear region.

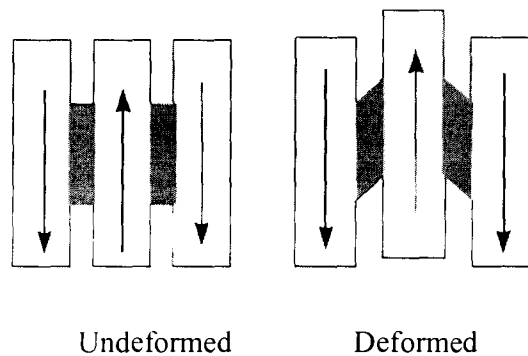


FIGURE 2-16 Specimen for Miyauchi shear test.

In-plane biaxial tests with cruciform specimen geometry have had limited success in terms of attaining uniform deformation of the gauge region up to large strains.

2.7 Stain-Rate Sensitivity And Thickness Effect

The behaviour of formable materials at large strain is highly influenced by the strain, strain rate, temperature and microstructure. For materials with a positive strain rate sensitivity parameter (or m -value), the flow stress increases as the strain rate increases, i.e. strain rate hardening. A typical metal cutting process can reach a strain rate of 10^6 /s, accompanied with adiabatic heating, whereas the typical forming processes are carried out in the strain rate range of 1~10 /s and at room temperature. Strain rate hardening can be important to material modelling at large strain when strain localization occurs.

The influence of strain rate sensitivity (m -value) on the FLD of some materials has been experimentally investigated [Hosford et al., 1999]. During the stage of uniform deformation in uniaxial tension, the deformation is over the length of specimen. As

diffuse necking occurs, the deformation is within the length that is almost equal to width of specimen, which increases the length to width ratio and can be regarded as an increased strain rate. As localized necking occurs, the width of neck is approximately equal to the thickness of specimen, i.e. length to thickness ratio (or the strain rate) is increased significantly. With a positive m -value, the stress in the neck where strain rate is higher increases which resists further deformation of the neck and distributes the strain to neighboring material, leading to an increased limit strain. There is general agreement that a higher m -value delays the development of neck, comparing steel and aluminum. Aluminum sheet materials in general exhibit a low and sometimes a negative m -value. The latter tends to lead to a quick fracture once localization has occurred.

The thickness effect on FLD seems to be more direct in that a thicker sheet exhibits higher forming limits since compensation from more neighboring material volume accounts for some resistance to localized necking. The results, however, need to be analyzed carefully since the same type and size of surface grid is used for sheets of different thicknesses. The strain is overestimated if the size of the neck is greater than the grid. The solution is to enlarge the grid size for thicker specimen to accommodate the size of the necked zone within one grid. In this regard, more area should be averaged to ensure the result is not exaggerated [Hosford et al., 1999].

2.8 Additional Strain Paths Of Forming Characteristics

Classical approach to FLD determination is to employ different geometries of specimens for the tension-compression side of FLD and different lubrication conditions

for a full size clamped specimen for the tension-tension side. The limit strains along different proportional paths such as uniaxial tensile, plane-strain test and balance-biaxial are conveniently obtained. However, specimen design varies significantly since there is no widely accepted standard available. Stretching of a specimen with a hole in the centre (hole-flanging) was proposed for the tests to obtain the limit drawing ratio (LDR) [Yamada et al., 1968]. By varying the hole size, different limit heights can be achieved, which reflects the formability of a certain material. However, the strain paths corresponding to different geometries (hole sizes) were not investigated.

Similarly, a range of lubrication conditions between punch and sheet are often utilized and there are no commonly accepted lubrication procedures in use for FLD determination. Other than the widely utilized oil and grease based lubricant in industrial practice, various lubricants such as the transmission fluid, combination of boric acid and oil, and volatile lubricant, have been investigated [Lovella et al., 2006]. Although reduced friction effect was obtained with the above lubricants, whether these lubrication conditions produce different strain paths from well-studied paths such as Teflon and Polyurethane was not reported. Although the dry contact inevitably results in poor forming limits, the property of liquid lubricant is also highly influenced by the surface texture of sheet materials.

2.9 Finite Element Prediction Of FLD

The FE analysis has been employed to implement the complex constitutive material models of yield, flow and fracture, to simulate the sheet forming processes. The

rapid development of computer hardware allows the iterations of the advanced material models of yield, hardening and fracture to predict the material behaviour. Also, it is the strength of FE method that the test conditions, such as various specimen and tooling geometries, test velocity, loading and friction between tool-sheet interfaces, can be easily included in the analysis. Therefore, formability investigations, especially the punch tests to obtain the limit strains for FLD construction, are often carried out via FE analysis. Some representative FE researches on FLD prediction through punch test simulations are reviewed in this section.

Earlier in Section 2.1, substantial researches dealing with FLD prediction based on M-K method were presented. In the last two decades, FE method has also been used for FLD prediction. In the work of Toh et al., Hill's 1948 anisotropy yield function and power law hardening behaviour have been employed [Toh et al., 1986]. Load curves of interrupted punch tests for different lubrications were reported. The influence of specimen design and friction involvement on the forming process was considered. However, the comparison between the FE results of load and the experimental values, in the view of limit dome height, maximum load, and inflection point in load, were not explained. The influence of hardening law on FE prediction was not discussed. A criterion to determine the onset of localized necking was not given. Although different yield criterion (Hill's 1979) and strain rate effect on work hardening were considered in the work of Burford [Burford et al., 1989], it suffered from the same limitation as the work of Toh et al. No criterion on determination of localized necking was presented. Some aspects, such as the thickness effect, fracture mode and strain path change, were

studied in the work of Horsetemeyer [Horsetemeyer et al., 1994]. In particular, the formation of localized necking was associated with the void fraction. The details of yield criterion, hardening law and friction were not presented. The reason of thickness reduction was studied to a rather limited extent. In-depth explanation of how void growth initiated the localization was not provided. A comparison of various yield criteria and hardening laws was carried out in the work of Savoie [Savoie et al., 1998]. Three yield criteria, namely von Mises, Hill's 1990 and Barlat's 1989, and three hardening laws, namely power law, Voce law and modified Voce law (in a form of $d\sigma = h_0(1 - \sigma / \sigma_c)^n d\varepsilon$), were investigated in the simulations. An important conclusion from the authors was that the hardening law influences the results of limit strains from FE simulation more than the yield criterion.

Some other researches dealing with FE based prediction of FLD are summarized in Table 2-2 as shown below.

TABLE 2-2. Selected FE investigations on punch test to obtain FLD.

Author year	FE code	Yield	Friction	Hardening Law	Punch test	Failure	Localization	FLD
Toh, 1986	N/A 3D	Hill 1948	Coulomb	Power law $\sigma = K\varepsilon^n$	Out-of-plane	N/A	M-K No criterion	Yes
Burford et al., 1989	N/A 2D	Hill 1979	N/A	Prestrained $\sigma = K(\varepsilon_0 + \varepsilon)^n (\dot{\varepsilon} / \dot{\varepsilon}_0)^m$	In-plane	N/A	M-K No criterion	Yes
Goglio et al., 1989	MARC Axisymmetry	Mises	N/A	N/A	Out-of-plane	N/A	N/A	N/A
Horsetemeyer et al., 1994	Dyna3D Explicit Implicit	N/A	N/A	N/A	In-plane	Void formation	M-K Void No criterion	N/A
Kim et al., 1997	PAM-STAMP 3D	Hill 1948	Coulomb	Swift's law $\sigma = K(\varepsilon_0 + \varepsilon)^n$	Plane strain	N/A	N/A	N/A
Takuda et al., 1998	N/A Axisymmetry	Hill 1948	N/A	Power law $\sigma = K\varepsilon^n$	In-plane	Oyane	N/A	N/A
Savoie et al., 1998	ABAQUS Standard	Mises Hill 1990 Barlat 1989	Coulomb	Power law Voce law Modified Voce law	Out-of-plane	N/A	N/A	Yes

Overall, the FE simulations of punch test (in-plane and out-of-plane) in the past did not utilize a definite criterion for the determination of limit strains. The experimental punch load versus displacement traces received very little attention in FE modelling work. In particular, the characteristics of forming process, such as the inflection point representing the onset of diffuse necking and its significance for calibration of FE curves was not exploited. Also, the thickness reduction was not extensively investigated, although it is closely related to forming limit. Although the thickness reduction in punch test is hard to capture due to the geometric limitation, the influence of major and minor strains on the thickness reduction was not revealed. Further, the determination of a suitable hardening law applicable at large strain and providing a suitable extrapolation to uniaxial stress-strain input for FE simulation was not considered.

2.10 Shear Band Failure

As often seen in forming processes, shear band formation is a main failure type for automotive sheet materials. Investigation was carried out to distinguish the shear bands from other microscopic features such as Portevin-Le Chatelier, PLC bands, over specimen surface under uniaxial tensile and plane strain tensile paths [Kang et al., 2007]. Multiple inclined bands for AA5754 automotive aluminum sheet have been observed in the through thickness direction when localization occurs. However, only one develops into a localized necking band, or shear band, which further propagates through the thickness. For in-plane plane strain tensile tests, shear bands are formed horizontally and perpendicular to the loading direction in the middle of the specimen, suggesting that the

orientation of the band is perhaps related to the specimen geometry. Shear bands for plane strain mode also propagate through the thickness direction. No results have been obtained for biaxial tensile strain paths. Also, it is not clear as to what the role of in-plane versus out-of-plane deformation is on the extent, shape and orientation of the through thickness shear bands under various loading paths.

Although effort has continued for the past three decades to improve the predictions of FLDs, there are unrealistic assumptions that make it quite difficult to accurately reproduce the experimental FLDs. Therefore, a new method to predict the FLD from punch test load-displacement data and strain analysis is proposed. A new method that incorporates results from both experimental and FE analysis is presented and verified in this research. A material model with von Mises yield criterion that associates with an optimized hybrid hardening law and fracture model has been employed. A novel criterion to determine the limit strains by locating the inflection point in the major strain rate history has been proposed and examined. The routinely obtained load versus displacement curves of punch test have been utilized to adjust the FE model to largely represent the forming process. The limit strains for FLD construction are obtained from FE analysis and verified by experimental work. The details of the necking criterion, methodology and optimization procedure are presented in the following Chapters 3 ~ 5.

Chapter 3

A Proposed Localized Necking Criterion

A new criterion to determine the onset of localized necking is proposed to obtain the limit strains for each strain path and subsequently the FLD. The procedure to locate the limit strain is to process the history of major strain by taking the 1st and 2nd order of derivatives, the strain rate $\dot{\epsilon}$ and the “pseudo” strain acceleration $\ddot{\epsilon}$. In this research, the word “pseudo” refers to the use of only the magnitude of strain acceleration and not the direction. The limit strain for a given strain path is obtained at the inflection point in the major strain rate, or, a corresponding value of maximum “strain acceleration”, $(\dot{\epsilon}_1)_{\max}$, (Figure 3-1). The processing of major and minor strains, strain rates and strain accelerations are presented in detail in Sections 3.1 and 3.2 below. Temporal and spatial strain data is collected from FE simulations of hemispherical punch tests of particular strain paths. This process is repeated for all specimen geometries to obtain a locus of the limit strains, i.e., FLD for a given material.

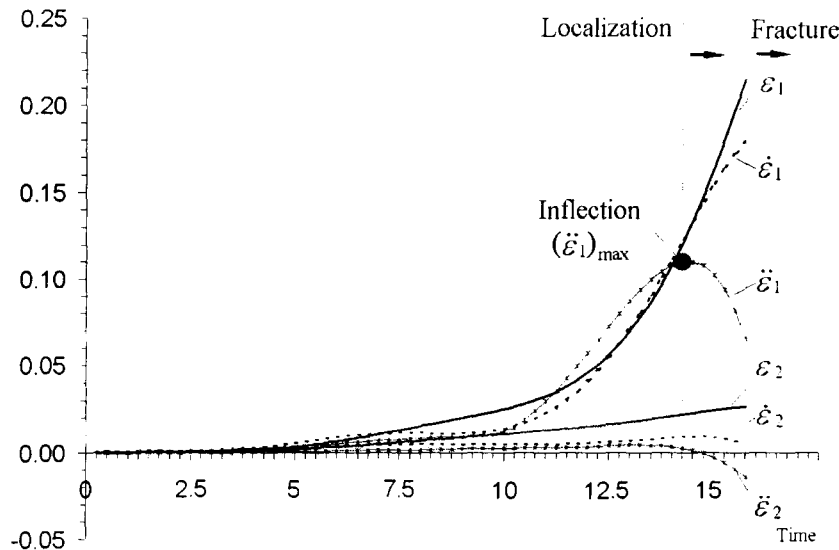


FIGURE 3-1. Procedure to obtain the limit strains from the strain history for AA6111-T4, 5" wide specimen, 2" diameter punch, dry condition.

3.1 Application Of Localized Necking Criterion For FE Output Data

Present work is based on the assumption that an equivalence in the FE and experimental load-displacement curves is sufficient to represent the experimental process by the FE model. A strain history analysis of FE output data based on the proposed necking criterion is then used to obtain the limit strain. Once the localized necking site is visually identified, a band of elements from the pole to the edge of the dome including those at the localization are selected (Figure 3-2). The histories from the beginning of the deformation process to the fracture of all the elements are extracted (Figure 3-3). The major and minor strain histories of the element inside the neck are further processed for the onset of localized necking. The localized necking is determined from an analysis of

strain history by taking 1st and 2nd order of derivatives of major and minor strains to obtain strain rate ($\dot{\epsilon}$) and pseudo “strain acceleration”, $\ddot{\epsilon}$. It is to be noted that only the magnitude of major strain acceleration is considered and not its direction, in the analysis. The time when an inflection point occurs in the major strain rate curve, or a peak in the major strain acceleration, i.e. $(\ddot{\epsilon}_1)_{\max}$, is considered as the onset of localized necking. The strain rates and pseudo strain accelerations are expressed as follows:

$$\dot{\epsilon}_1 = d\epsilon_1/dt, \quad \dot{\epsilon}_2 = d\epsilon_2/dt, \quad \ddot{\epsilon}_1 = d\dot{\epsilon}_1/dt, \quad \ddot{\epsilon}_2 = d\dot{\epsilon}_2/dt \quad (\text{Eq 3-1})$$

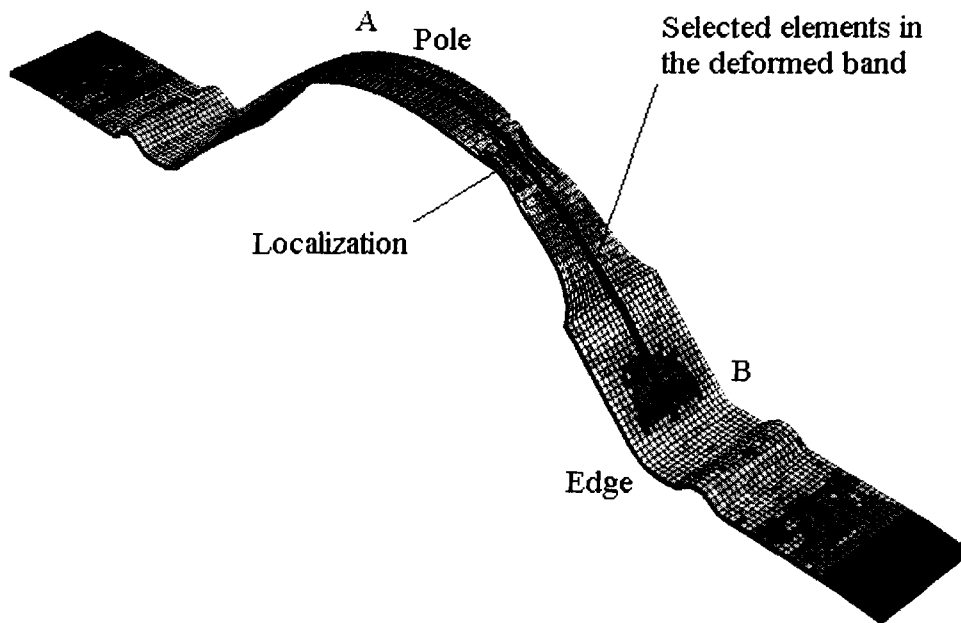


FIGURE 3-2. FE result of a deformed band A – B with localized zone in a 0.5” wide dome test specimen.

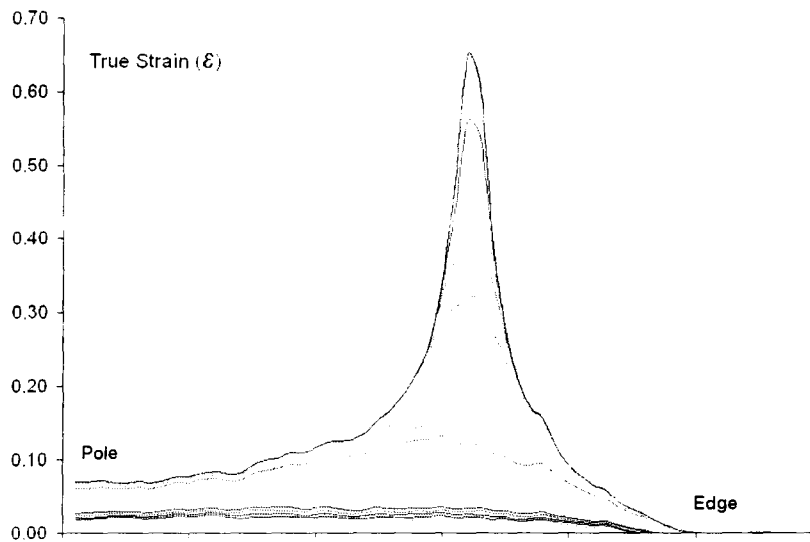


FIGURE 3-3. Extracted strain history from FE simulations shown in Figure 3-2 of selected band from pole to edge.

3.2 Analysis Of Strain History From FE Simulation

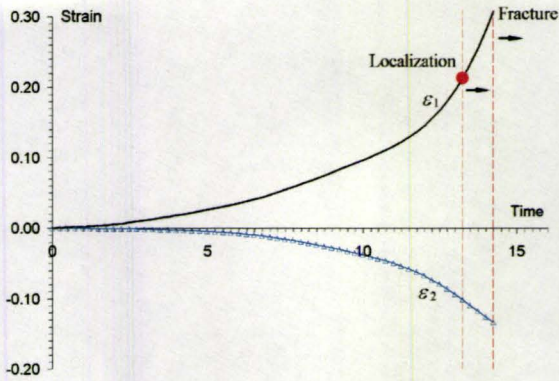
For the specimens that lead to left side strain paths on FLD ($-1/2 \leq \beta < 0$), such as narrow strip specimens (Figure 3-4 specifically Figure 3-4e), the sequence of the characteristic points includes $(\dot{\epsilon}_2)_{\min} \rightarrow (\dot{\epsilon}_1)_{\max} \rightarrow \dot{\epsilon}_1 \approx 0$. The latter two correspond to the occurrence of localized necking and fracture respectively. In both of the cases, the $(\dot{\epsilon}_2)_{\min}$ is searched earlier than $(\dot{\epsilon}_1)_{\max}$, although these two events are quite close.

Four different lubrication conditions: a sand paper interface between the punch and sheet (silica paper of grit 320 applied on the punch surface), dry (direct contact between cleaned punch and sheet surface), Teflon (Teflon film applied on the punch surface) and Polyurethane (Polyurethane pad applied under the sheet surface) were considered for the full dome specimens of AA6111-T4, which provide strain paths on the

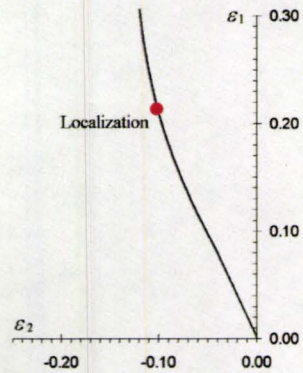
RHS of FLD space ($0 < \beta \leq 1$). Figure 3-5 presents results for a low friction (i.e. for polyurethane) case. Figure 3-5e shows the major and minor strain acceleration evolution sequence: $(\ddot{\epsilon}_2)_{\max} \rightarrow (\dot{\epsilon}_1)_{\max} \rightarrow \ddot{\epsilon}_1 \approx 0$. The latter two correspond to localized necking and fracture.

Specimens with widths close to punch radii resulted in strain paths near plane strain but on either left or right side of the plane strain path respectively. Accordingly, the occurrence of characteristic events shows $(\ddot{\epsilon}_2)_{\min}$ or $(\ddot{\epsilon}_2)_{\max} \rightarrow (\dot{\epsilon}_1)_{\max} \rightarrow \ddot{\epsilon}_1 \approx 0$. The latter two are localized necking and fracture respectively.

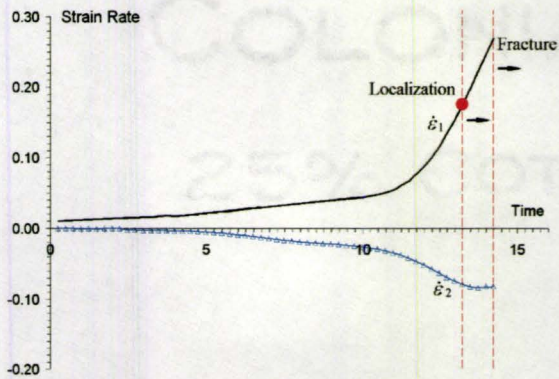
The $(\ddot{\epsilon}_2)_{\min}$ for tension-compression side, and the $(\ddot{\epsilon}_2)_{\max}$ for tension-tension side, occur earlier than the $(\dot{\epsilon}_1)_{\max}$. The attainment of limits in minor strain acceleration cannot occur after or at the same time as the occurrence of maximum in major strain acceleration, since the minor strain acceleration signifies a strain path change towards plane strain, although plane strain is not necessarily a condition of localization, as investigated and discussed in Section 3.3 and Chapter 6.



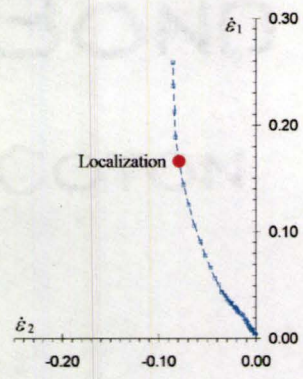
a. major / minor strain.



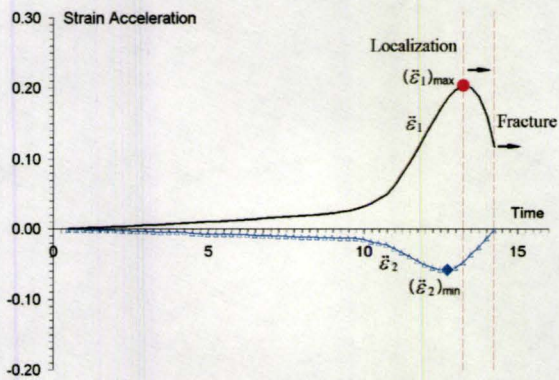
b. $\epsilon_2 - \epsilon_1$ plot.



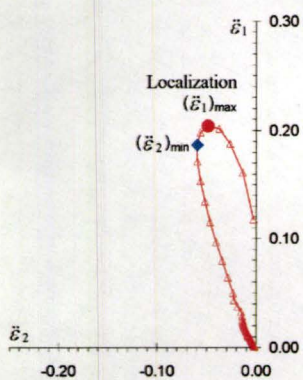
c. major / minor strain rate.



d. $\dot{\epsilon}_2 - \dot{\epsilon}_1$ plot.

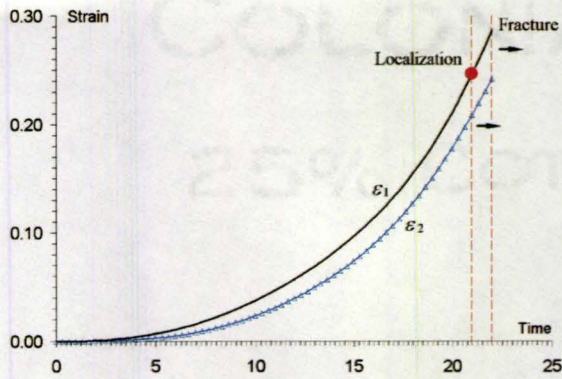


d. major / minor strain acceleration.

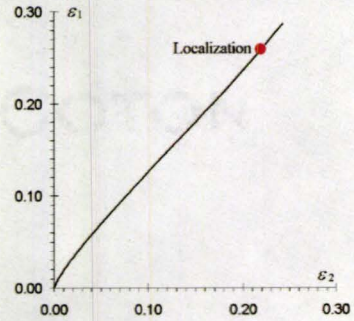


e. $\ddot{\epsilon}_2 - \ddot{\epsilon}_1$ plot.

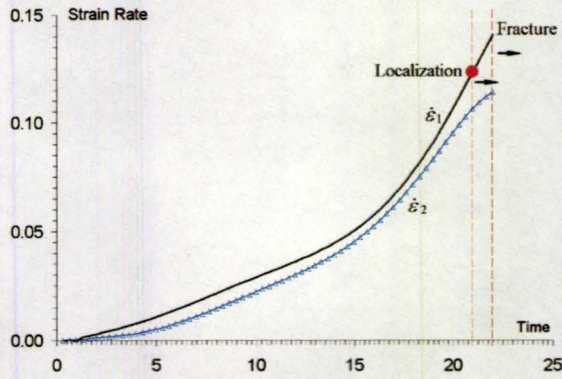
FIGURE 3-4. Processed major and minor strain, strain rate and strain acceleration histories from a 0.5" wide dome specimen of AA6111-T4 sheet (solid circle in these graphs indicating a peak in $(\dot{\epsilon}_1)_{\max}$ at the onset of localized necking).



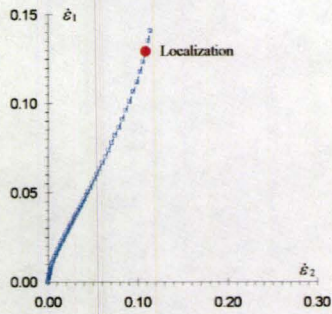
a. major / minor strain.



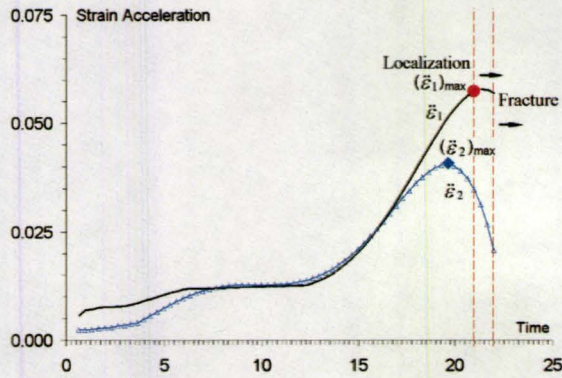
b. $\epsilon_2 - \epsilon_1$ plot.



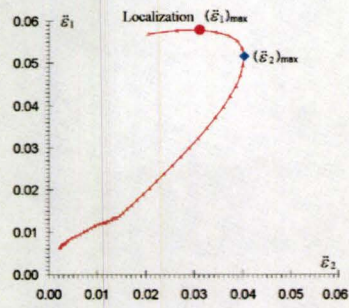
c. major / minor strain rate.



d. $\dot{\epsilon}_2 - \dot{\epsilon}_1$ plot.



d. major / minor strain acceleration.



e. $\ddot{\epsilon}_2 - \ddot{\epsilon}_1$ plot.

FIGURE 3-5. Processed major and minor strain, strain rate and strain acceleration histories from a 5" wide dome specimen of AA6111-T4 sheet under dry contact (solid circle in these graphs indicating a peak in $(\dot{\epsilon}_1)_{max}$ at the onset of localized necking).

A generalization of the characteristics of the different strain paths produced the common condition that the occurrence of maximum major strain $(\dot{\epsilon}_1)_{\max}$ represents the onset of localization. The method to determine the limit strains by locating the occurrence of $(\dot{\epsilon}_1)_{\max}$ is thus referred to as the criterion of maximum major strain acceleration $(\ddot{\epsilon}_1)_{\max}$.

3.3 Experimental FLD Determination With Strain History Data From ARAMIS

The ARAMIS system utilizes a technique called digital image correlation (DIC), which effectively analyzes consecutive deformation patterns from the surface of a specimen throughout its deformation process. This non-contact technique uses high-resolution digital cameras to track the gray level change of the speckles in small facets during deformation at regular intervals. By analyzing the displacement of the patterns within the entire image, the maximum correlation corresponds to the displacement. Further, by comparing the facets in the current image with reference to the initial image, or the previous image, the shift, rotation, distortion of the facets can be calculated, so that the incremental and total strain can be obtained.

For in-plane deformation (two-dimensional) single camera can be used whereas for out-of-plane deformation (three-dimensional) two cameras positioned at a fixed angle to each other are required to simultaneously record the images of a pre-selected region of the specimen. If the deformation of the specimen is recorded by two cameras from different angles, then the position of each object point is focused on an overlapping of

the two cameras, all coordinates in three-dimensions of any surface point in space can be calculated. The spatial contour of the specimen can be determined if the specimen surface exhibits sufficient features to allow the DIC to correlate the identical points for calculation.

Some typical results of strain distribution calculated from ARAMIS strain imaging system are shown in Figure 3-6.

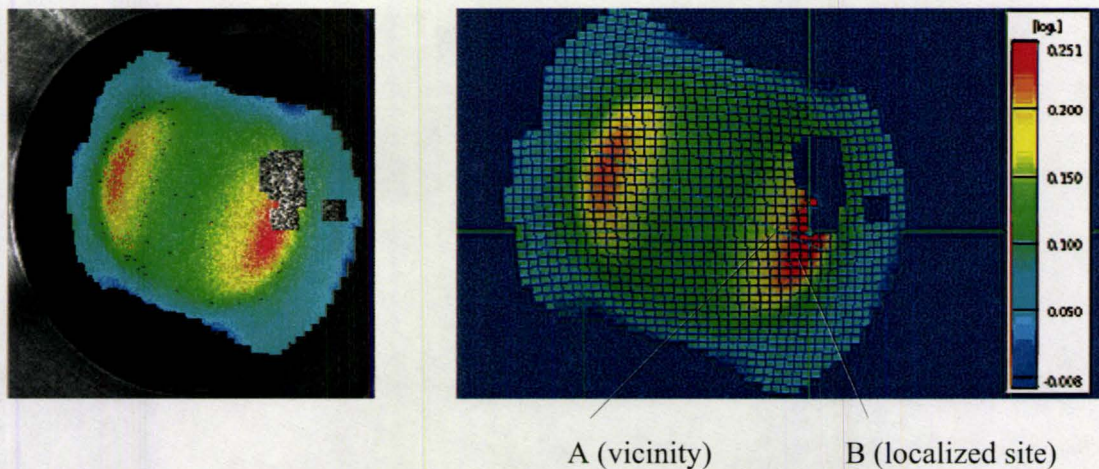


FIGURE 3-6. Specimen with major strain overlay calculated from ARAMIS system showing localized site *B* and its vicinity *A* (AA6111-T4, 2” wide specimen, 2” diameter punch).

The spatial and temporal strains calculated from ARAMIS were plotted in terms of time and location to show the relationship between localized site and its vicinity (region *A* and *B* in Figure 3-7). The localized necking behaviour was observed in the region *B* where plane strain did not occur, whereas in the vicinity of region *A*, where plane strain has occurred, there was no obvious localization. Based on the strain history results calculated from ARAMIS, proposed necking criterion was employed to determine

the limit strains and the difference between localized site and its vicinity was studied. The result is given in Figure 3-8 and is further discussed in Chapter 7.

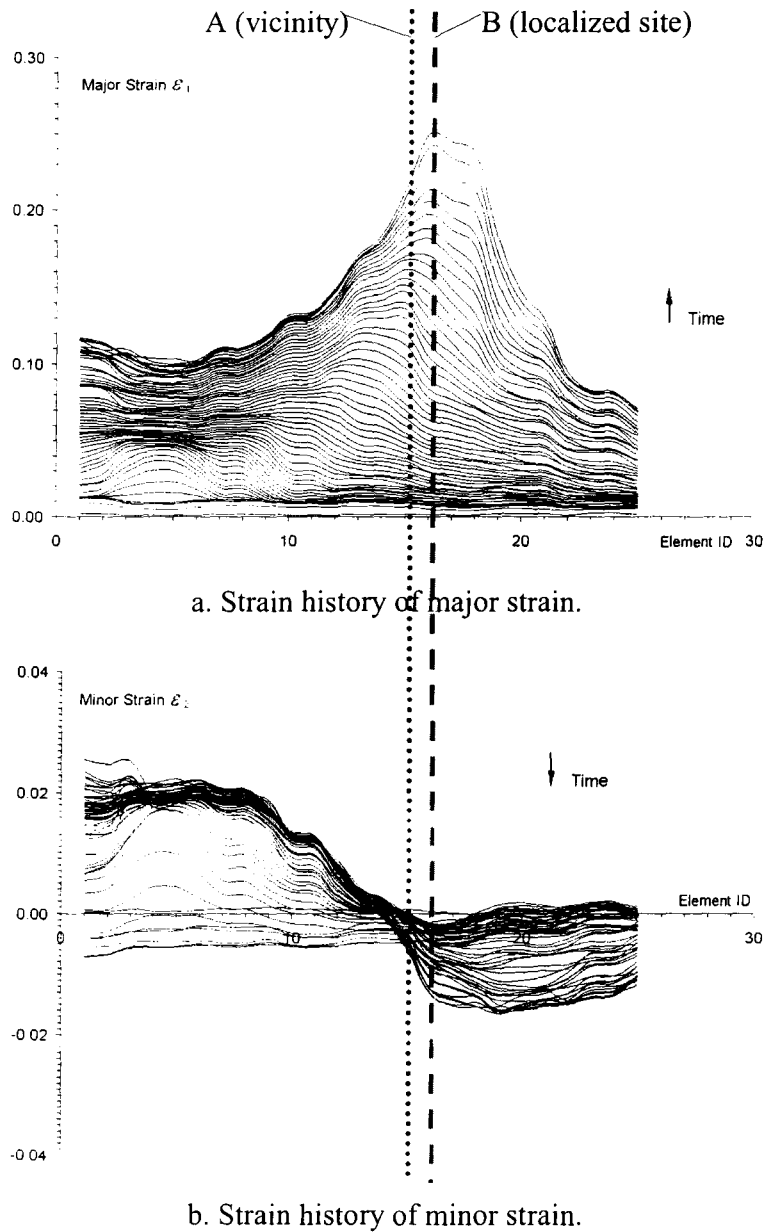


FIGURE 3-7. Temporal and spatial major and minor strains calculated from ARAMIS system showing localized site *B* and its vicinity *A* (based on Figure 3-6).

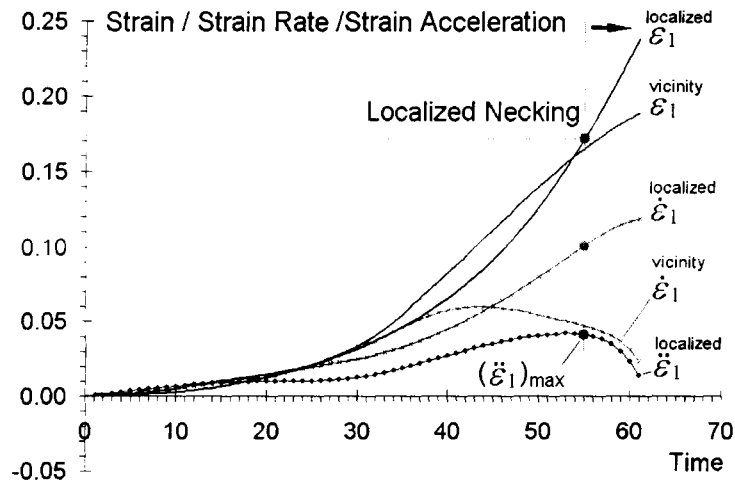


FIGURE 3-8. Analysis of strain history based on ARAMIS results showing limit strains and difference between localized site and its vicinity (AA6111-T4, 2" wide specimen, 2" diameter punch).

The proposed localized necking criterion was also assessed for in-plane uniaxial tension test. ARAMIS analysis produced both the strain overlay on the specimens and spatial and temporal strains. It is to be noted that by visual check on the presence of localized neck (Figure 3-9), there would be inevitable subjectivity to determine when is the onset of localized necking. Even from the data of strain history (Figure 3-10), it is difficult to determine the limit strains without a definite criterion for localized necking.

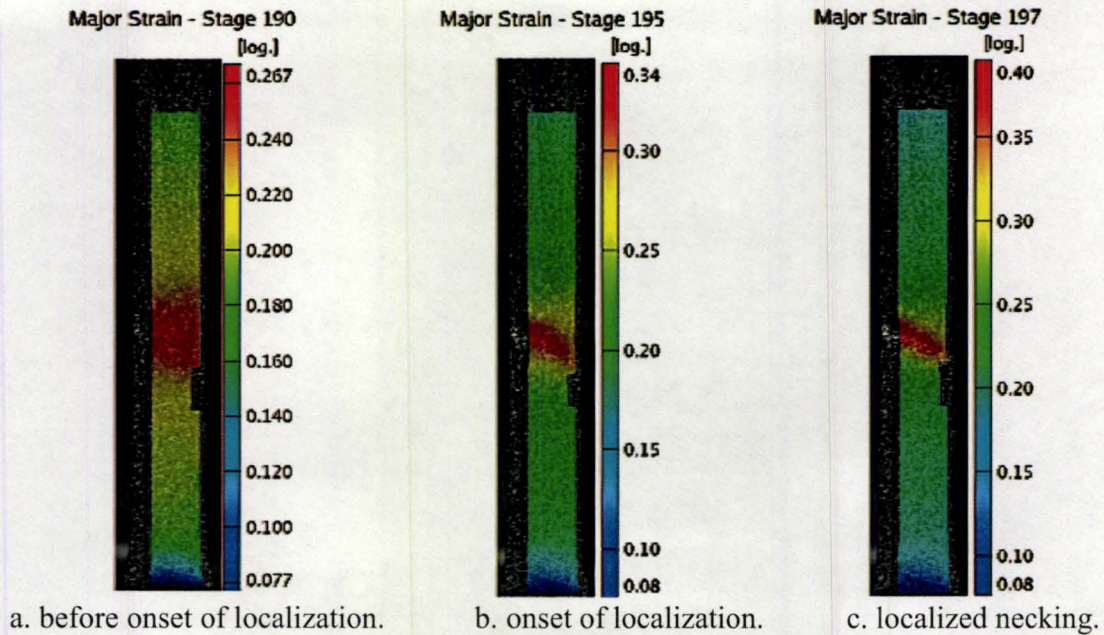


FIGURE 3-9. Different stages of strain overlay on a deformed 0.5” uniaxial tensile specimen obtained from ARAMIS post-processing (AA6111-T4, 1 mm thickness, 0.25 mm/s test speed).

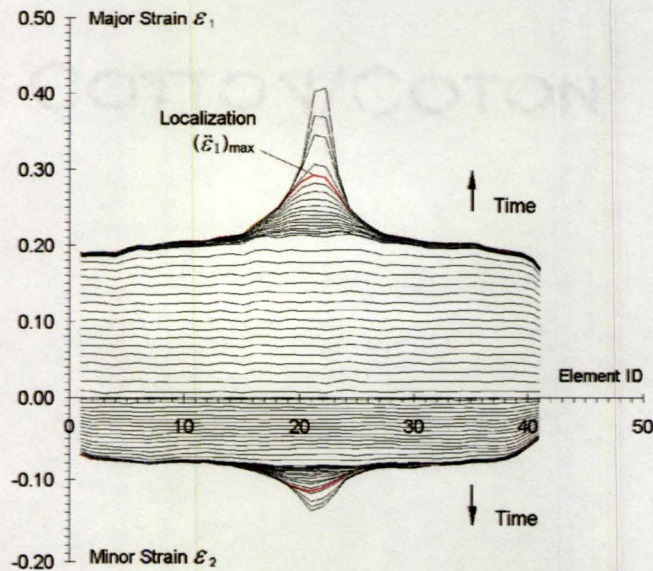


FIGURE 3-10. Spatial and temporal strains (major and minor) of 0.5” uniaxial tensile specimen in ARAMIS post-processing (AA6111-T4, 1 mm thickness, 0.25 mm/s test speed).

The proposed localized necking criterion by seeking the maximum in the major strain acceleration curve was utilized to determine the limit strains in the in-plane uniaxial tensile tests. The result in Figure 3-11 demonstrates the unique characteristic point, the peak, in the major strain acceleration curve. The limit strains of at the instance can be quickly obtained in the strain curves.

Another characteristic point, the onset of diffuse necking, was also easily obtained from Figure 3-11. The major strain rate curve exhibits quite linear shape until the onset of diffuse necking. This exists in the uniaxial tensile results, but not the biaxial loading tests, since material behaves differently in uniaxial tensile and biaxial loading (Figures 3-11 and 3-12).

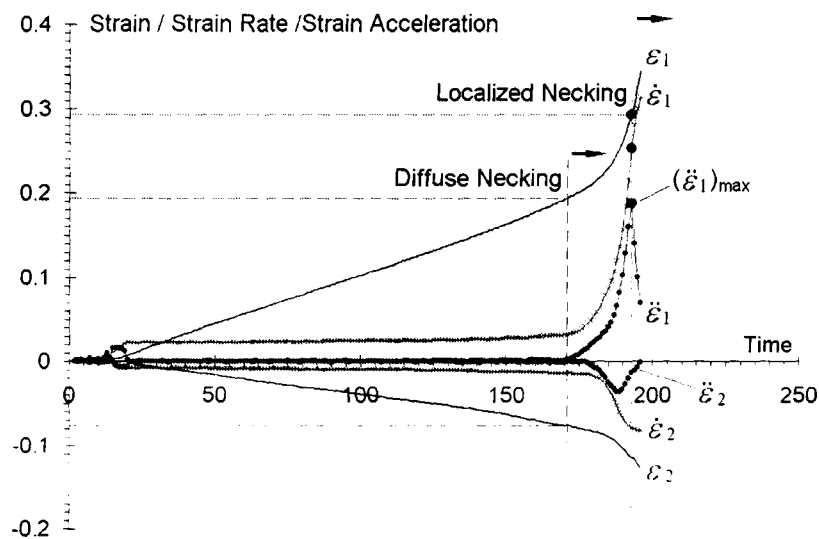


FIGURE 3-11. Analysis of major and minor strain histories of 0.5” wide uniaxial tensile specimen based on ARAMIS data (AA6111-T4, 1 mm thickness, 0.25 mm/s test speed).

Note: Strain rate and strain acceleration curves have been amplified 10 times.

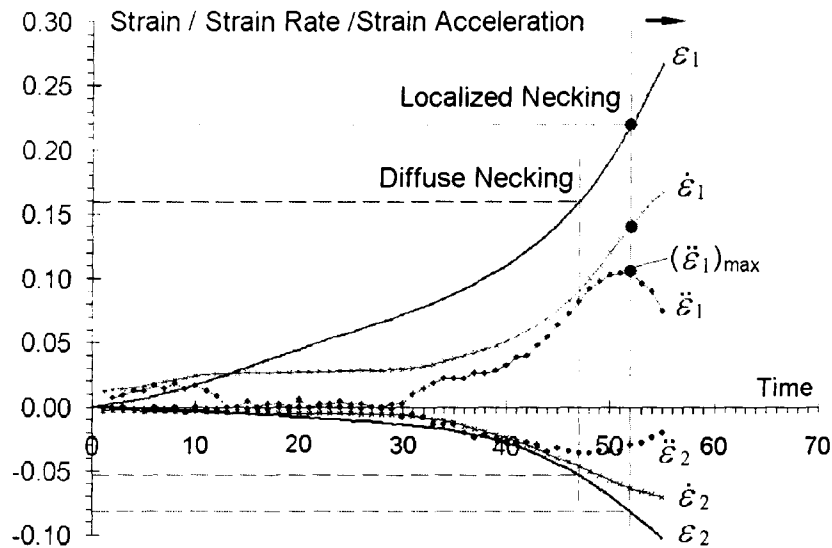


FIGURE 3-12. Analysis of major and minor strain histories of 0.5” wide biaxial tensile specimen based on ARAMIS data (AA6111-T4, 1 mm thickness, 2” diameter punch).

Note: Strain rate and strain acceleration curves have been amplified 10 times.

The above out-of-plane (dome) tests and in-plane uniaxial tests with AA6111-T4 demonstrate the effectiveness of the proposed $(\dot{\epsilon}_1)_{\max}$ localized necking criterion. This is further discussed in Chapter 7.

In summary, the conventional approach did not accurately predict the localization behaviour whereas the proposed criterion demonstrated its effectiveness with good experimental support. Another material, AA6181-T4, was also examined to further investigate if strain path change towards plane strain leads to strain localization.

The method to measure the strain in the vicinity of the localized neck as the limit strains is defined as the criterion of critical major strain $(\epsilon_1)_{cr}$. Generally before the occurrence of localization, the elements towards the pole of the specimen are subjected to

a larger strain than the element near the pole side. However, when localization occurs, the major strain in the localized element (point *A*, towards the edge or the clamped region of the sheet) shows a rapid growth in strain exceeding the one adjacent to it (point *B*, towards the pole), the previously larger one (Figure 3-13).

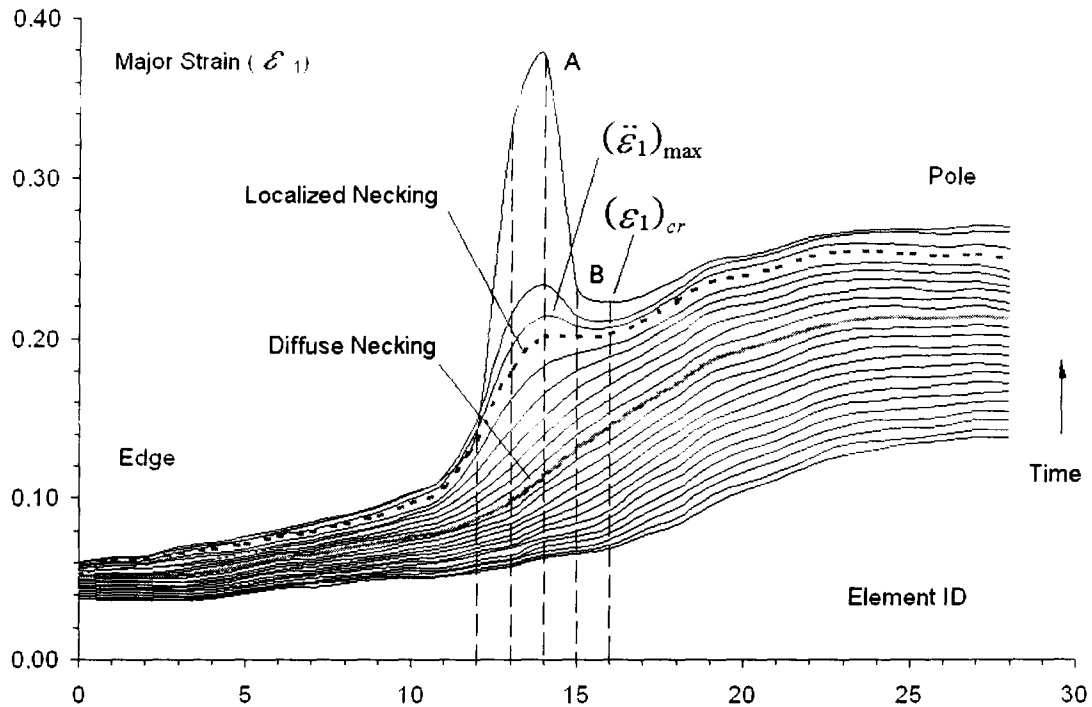


FIGURE 3-13. Major strain history of 4" wide specimen in ARAMIS post-processing (AA6181-T4, 1 mm thickness, 4" diameter punch).

The time step corresponding to the instance when major strain at point *A* and point *B* are equal indicates the onset of the localization. The pair of major and minor strain obtained at such moment is defined as the limit strain. The method to determine the limit strains by observing the major strain history to locate the localized element that exceeds the previously larger one is defined as the criterion of critical major strain $(\epsilon_1)_{cr}$.

Critical major strain $(\epsilon_1)_{cr}$ and the proposed maximum major strain acceleration $(\dot{\epsilon}_1)_{max}$ are discussed further in Chapter 7.

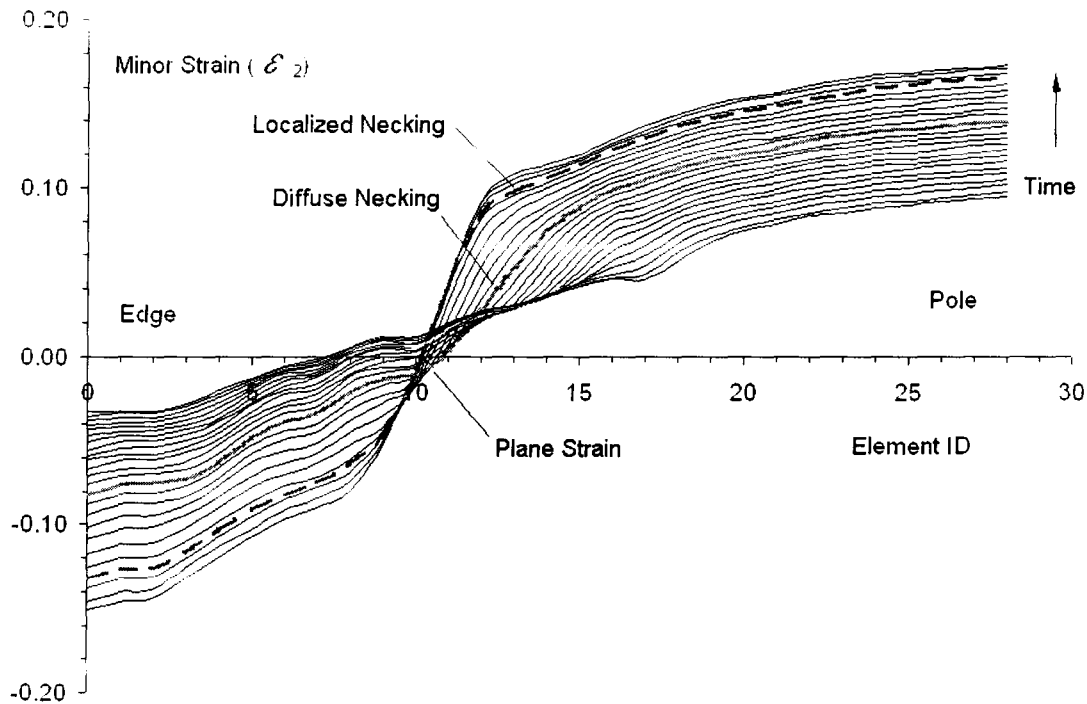


FIGURE 3-14. Minor strain history of 4" wide specimen in ARAMIS post-processing (AA6181-T4, 1 mm thickness, 4" diameter punch).

The results given in Figure 3-14 indicate that plane strain may not be the necessary condition for the localization to occur. The minor strain history of the localized element still shows a slow but steady increment. On the contrary, the major strain is rapidly rising and becomes the site of localization. This observation indicates that the trigger of localization does not necessarily require $\Delta\epsilon_2 \approx 0$. This is a rather surprising and new observation that deviates from all previous work on the subject.

Another approach to obtain the limit strains experimentally in the present work was based on post-test strain measurement using the ARGUS system. The results from this system are presented and discussed in Chapter 6.

The procedure to conduct the research utilizing the proposed criterion to obtain forming limit diagram is presented in detail in the Chapter 4.

Chapter 4

Experimental And Numerical Procedure For FLD Determination

The methodology presented here integrates the experimental load versus displacement traces with FE modelling of localization behaviour for the formability prediction. To determine the limit strain of each strain path, the specimens were stretched to obtain the load versus displacement curves in the hemispherical punch tests for various widths and lubrication conditions, which produce different strain paths. An inflection point in the load-displacement trace has been observed experimentally, depending on strain path (and hence the test specimen geometry or the friction between the punch and the sheet). The location of inflection point, limit dome height and corresponding maximum load at fracture from experiments is utilized to adjust the load curves in FE modelling (Figure 4-1). By varying the parameter of stress-strain input $\sigma - \epsilon$, coefficient of friction at the punch-sheet interface μ , a close agreement between the experimental and FE predicted load-displacement curve may be obtained.

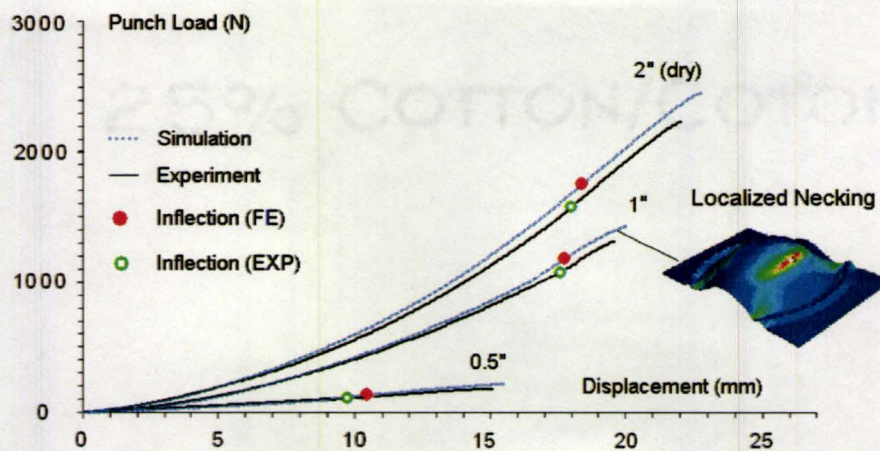


FIGURE 4-1. Punch load-displacement traces from experiments and FE simulations identifying diffuse necking, localized necking and fracture stages (2" diameter Nakajima punch tests for AA6111-T4).

Once the FE modelling produces load curves in good agreement with experimental data, an analysis of strain history is carried out to locate the characteristic points or limit strains in the strain history.

The limit strains can also be obtained from the experimental in-situ strain measurement system ARAMIS, and separately from post-test grid based strain measurement system ARGUS, for validation. The FE based FLDs are then compared with those obtained experimentally.

4.1 Procedure For Obtaining FLDs

The trace of load versus punch displacement from punch stretching test exhibits an inflection in the curve (Figure 2-4) [Ghosh, 1977]. The characteristic points can be obtained by taking the derivatives of 1st and 2nd order of load traces since for a given

material, geometry and lubrication condition, the limit dome height and punch load and the location of inflection are stable. Experimental methodology in terms of the integration of the previous steps such as load curve analysis and necking criterion as well as experimental and FE modeling steps is summarized in Figures 4-2 to 4-4. The procedure essentially consists of 3 parts as shown in Figure 4-2. Various specimen geometries and lubrications between the specimen and punch are utilized to obtain different strain paths (Figure 4-3).

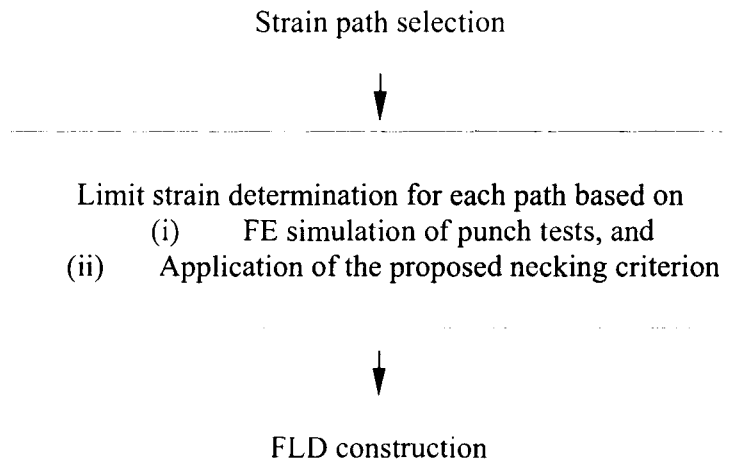


FIGURE 4-2. Main block for FLD construction.

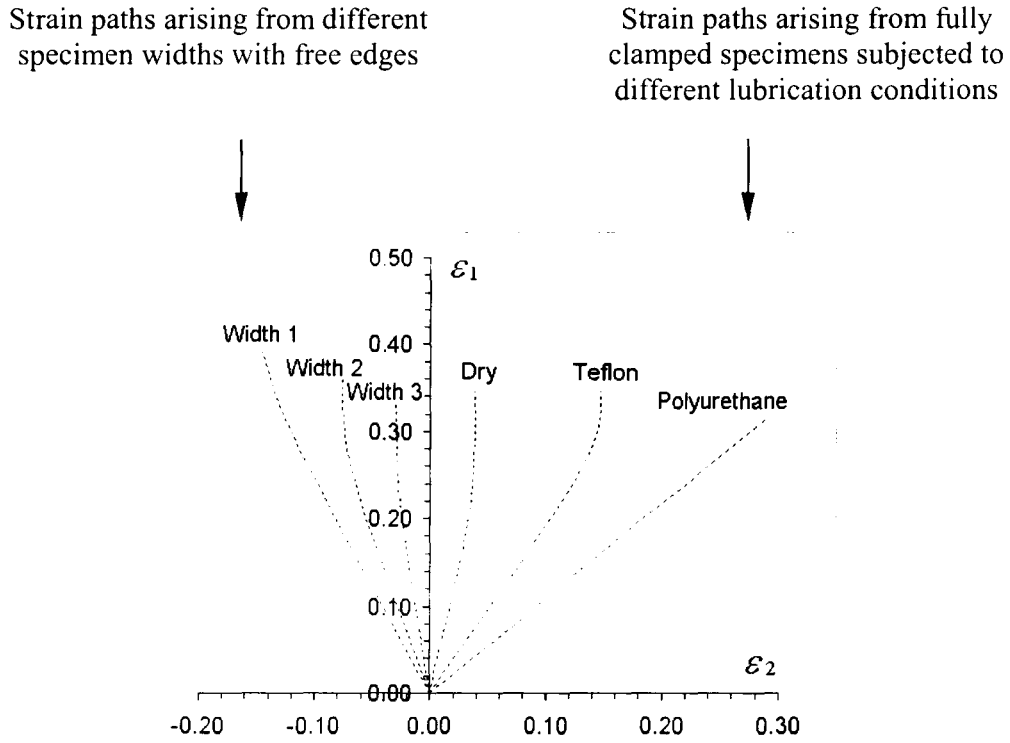


FIGURE 4-3. A schematic representation of strain paths from different specimen geometry and lubrication conditions.

For each strain path, the specimen is stretched in the punch test to obtain continuous raw load and displacement data. The load analysis of experimental data provides accurate results of limit dome height, magnitude of load and stable location of inflection (diffuse necking), which are utilized to adjust the load curve in the FE analysis (Figure 4-4). An optimization process, presented in detail in Chapter 5, essentially involves carrying out a number of FE simulations of each test geometry by varying $\sigma - \epsilon$ input and frictional coefficient μ within the range of experimental scatter in order to

obtain a close agreement between the FE based and experimental load versus displacement curves.

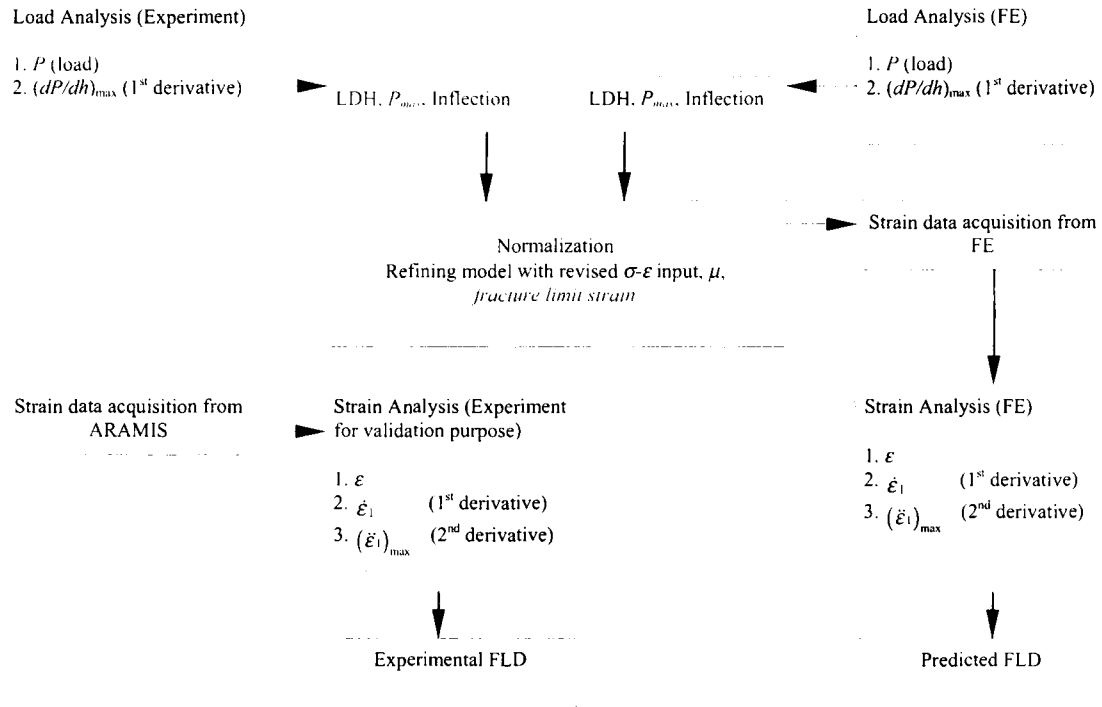


FIGURE 4-4. Limit strain determination for each strain path.

The predicted limit strains from FE can also be obtained from the experimental in-situ strain measurement system ARAMIS, and separately from the post-test strain measurement system ARGUS. The experimental and predicted FLDs are compared to assess the overall methodology for FLD prediction.

4.2 Experiment Details

4.2.1 Formability Test Setup

Formability testing was carried out using a hemispherical punch test (Nakajima) utilizing a universal mechanical test system MTS and an online strain imaging system ARAMIS (Figure 4-5).

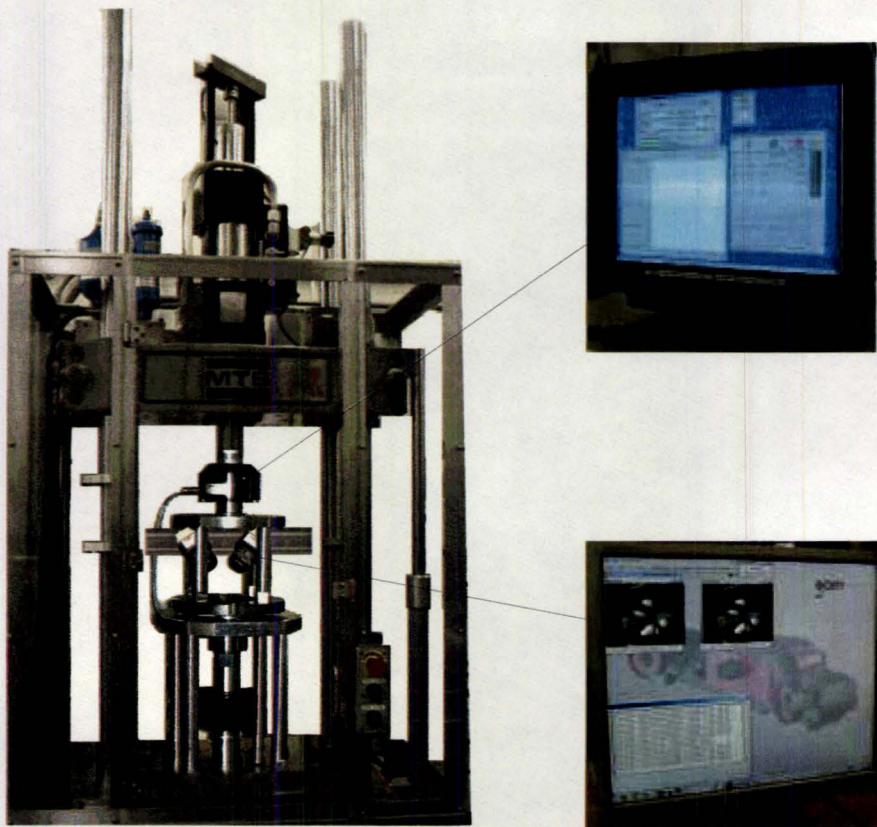


FIGURE 4-5. Hemispherical punch test rig (4" diameter punch) with universal test system MTS with Interlaken data acquisition and control system (top right console) and strain imaging system ARAMIS (bottom right console).

A test rig with a standard 4” diameter hemispherical punch was employed and mounted in an instrumented and controlled two-actuator mechanical test system, MTS. Two hydraulic actuators were used to enable the clamping and punching process. The stretching experiments were performed at a constant speed of 0.25 mm/s. The load versus displacement data from hemispherical dome tests was transferred to the Interlaken console through the load cells and LVDT in the MTS test system.

The material tested in this system was an automotive sheet material AA6181-T4 at a thickness of 1 mm. The specimen profiles are shown in Figure 4-6. The 0.5” and 2” wide specimens resulted in strain paths on left-hand-side of FLD (LHS, the strain ratio, $\beta = \varepsilon_2 / \varepsilon_1 = -1/2 \sim 0$). The 4” and 5” specimens were tested for the plane strain path (PS, $\beta \approx 0$). Full round 7” specimens were tested to obtain the right-hand-side strain paths (RHS, $\beta = 0 \sim 1$) with different lubrication conditions, such as direct dry contact, lubricated with Teflon film, polyurethane pad between punch and sheet. A circular dot pattern was deposited on the sheet and the centres of the dots formed a pattern that was a “square” of 2 mm spacing. The sheet was further coated using a fine jet of water-based ink to create white and black speckles on the surface.

The camera captured the deformation of specimens for strain analysis via ARAMIS system. A variation in strain distribution from the speckle pattern during the deformation were continuously captured using an online optical strain mapping system ARAMIS.

The water-based ink is subsequently washed away from the deformed samples after the test and the periodic dot pattern is revealed for measurements with ARGUS 3D

system, the latter being the conventional method to obtain the limit strains. This was done to compare results from the speckle-based ARAMIS system and the ARGUS system for FLD determination.

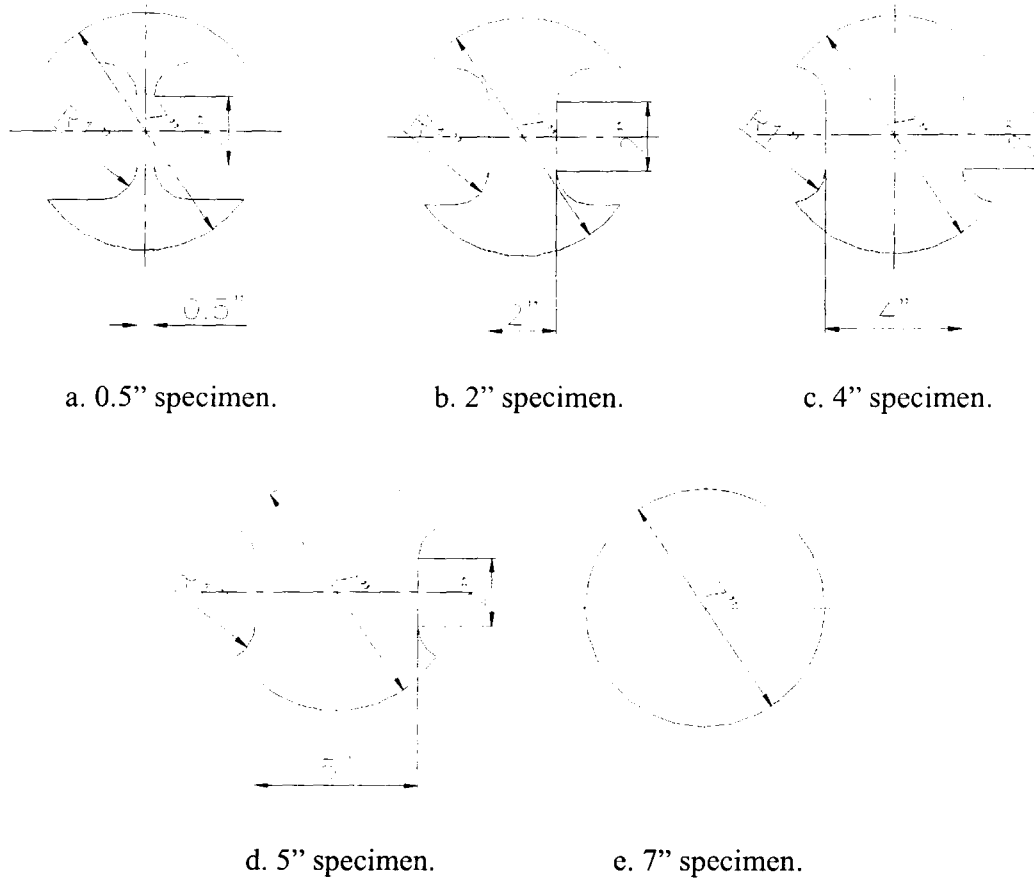


FIGURE 4-6. Specimens designed for 4" diameter punch tests (material: AA6181-T4, 1 mm thickness).

Another sheet material AA6111-T4 was tested on Interlaken hydraulic test system using a 2" hemispherical punch (Figure 4-7). This test setup was mounted on the test bed, which moves upward towards the stationary upper plate mounted on the four posts to clamp the sheet.

The specimens shown in Figure 4-8 were designed for 2” Nakajima punch test system, in which 0.5” and 1” width specimens were used to attain tension-compression strain paths, 2” and 3” width specimens for close-to-plane-strain paths and 5” width specimens for tension-tension paths.

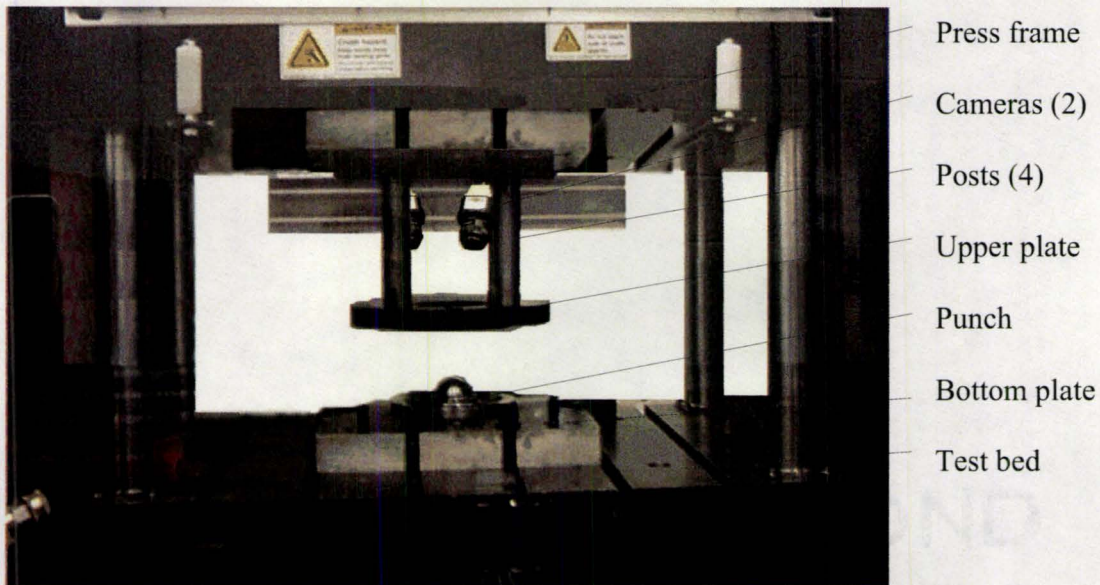


FIGURE 4-7. Hemispherical punch test rig (2” diameter punch) with Interlaken hydraulic test system (console not shown) and strain imaging system ARAMIS using cameras.

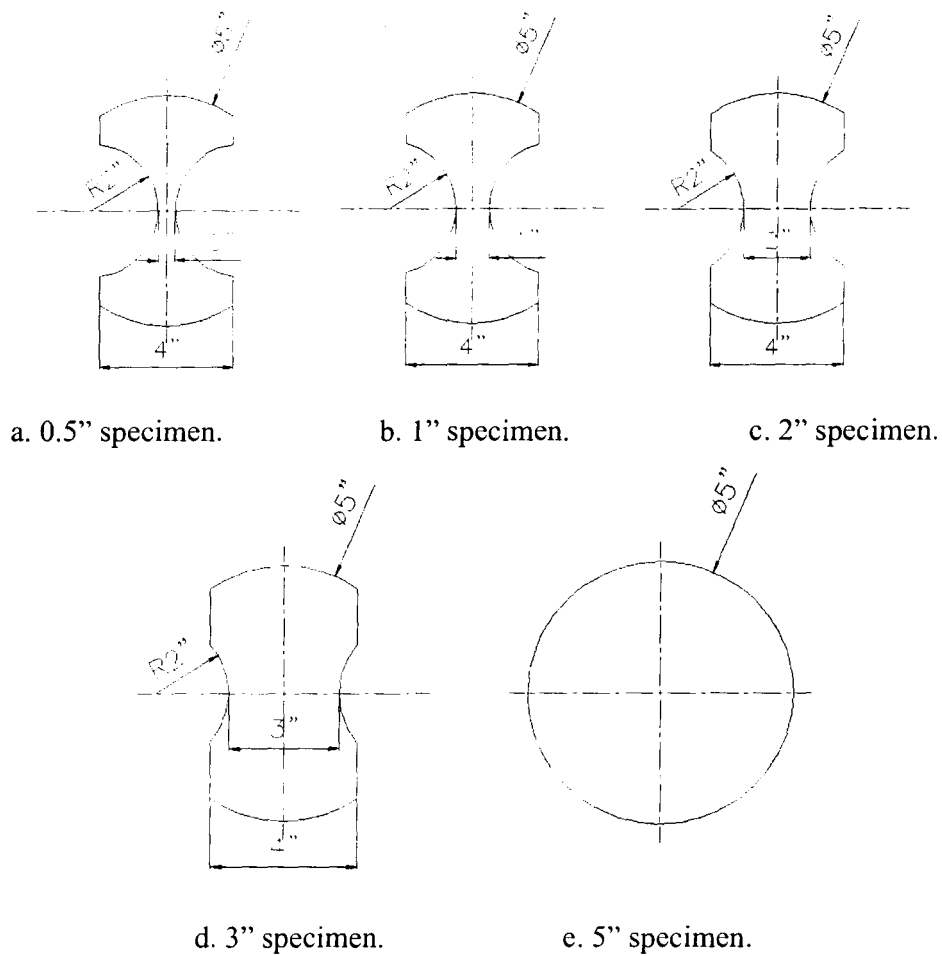


FIGURE 4-8. Specimens designed for 2" diameter punch tests (material: AA6111-T4, 1 mm thickness).

Two different set-ups and punches were utilized in this work research, a 4" test set-up for AA6181-T4 and 2" test set-up for AA6111-T4 respectively. The small set-up of 2" Nakajima punch was designed in proportion to the 4" Nakajima in all aspects of dimensions that the results from the two test systems were considered equivalent. Also, the small punch set-up uses less material, and is preferable when the material available for testing is limited.

4.2.2 Test Conditions

4.2.2.1 Uniaxial Tensile Tests And Analysis Of Data

Uniaxial tensile tests were conducted to obtain material parameters for the 3 materials utilized in this study, namely AA6111-T4 of 1 mm and 2 mm sheet thickness, AA6181-T4 at 1 mm, and DP600 at 1.88 mm. In this sub-section, experimental conditions and analysis of test data for AA6111-T4 are presented as an example. True stress – true strain curves from AA6111-T4 uniaxial tensile specimens were obtained using a screw driven electromechanical test system under constant crosshead velocities of 1.25, 0.25 and 0.025 mm/sec to failure. The strains were measured using a clip-on extensometer. The specimens were prepared according to the ASTM B-557M-94 standard. Yield strength, ultimate tensile strength and elongations were obtained using standard ASTM procedures.

The experimental load versus displacement data was first processed to obtain engineering stress versus strain curves and then the true stress versus true strain curves. The true values of stress and strain were further fitted to power and Voce material hardening laws. The power law can be expressed in a logarithmic form as follows:

$$\ln \sigma = \ln(K \varepsilon^n) = \ln K + n \ln \varepsilon \quad (\text{Eq 4-1})$$

When the experimental data σ - ε was plotted in logarithm coordinates, i.e. $\ln \sigma$ - $\ln \varepsilon$, linear fitting was employed to obtain the slope and the intersection with $\ln \sigma$ axis. The n -value was obtained directly from the slope of the fitted lines. The intersection of the

fitted line with $\ln \sigma$ axis produced $\ln K$ and subsequently the K value from the following expression:

$$K = \exp(\ln \sigma |_{\ln \epsilon = 0}) \quad (\text{Eq 4-2})$$

An example of AA6111-T4 (1 mm thickness, 0.25 mm/s test speed) is given in Figure 4-9 to demonstrate the procedure. A hardening index value (or n -value) of 0.2152 and a K value of 549.88 MPa for AA6111-T4 of 1 mm thickness at test speed of 0.25 mm/s, i.e. $\sigma = K \epsilon^n = 550 \epsilon^{0.215}$ MPa.

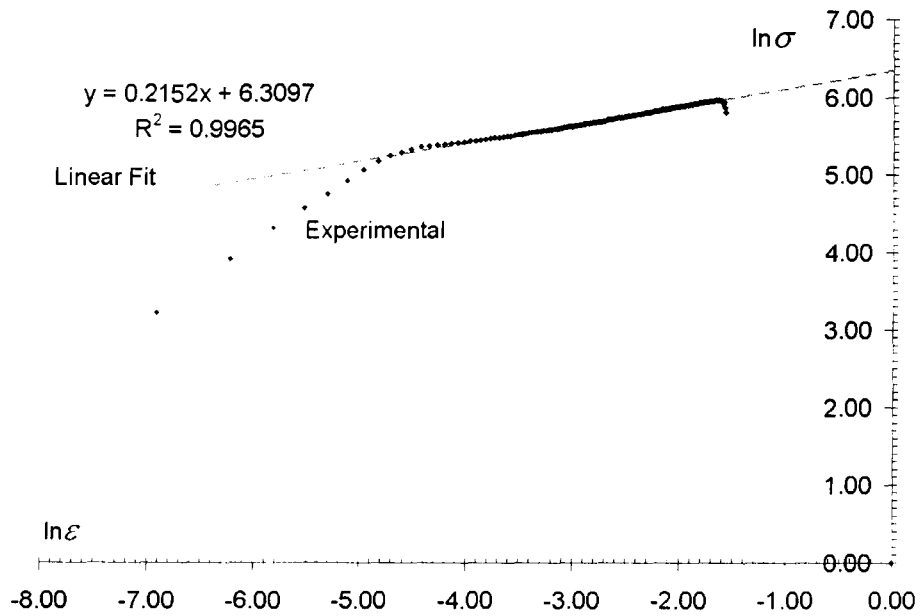


FIGURE 4-9. Obtaining parameters for power law fitting from post-processing of experimental uniaxial tensile data (AA6111-T4, 1 mm thickness, 0.25 mm/s test speed).

A similar method was utilized in the post-processing of experimental data for parameters of Voce law. The Voce law in its logarithmic form as be expressed as:

$$m \epsilon = \ln(B - \sigma) - \ln(B - A) \quad (\text{Eq 4-3})$$

The determination of the parameters A , B and m in Voce law is described below. The threshold stress A was obtained by finding the initial yield stress using the following expression:

$$\varepsilon_p = \varepsilon - \sigma_{y0}/E = \varepsilon - A/E \quad (\text{Eq 4-4})$$

where E , ε_p , ε , σ_{y0} are Young's modulus, plastic equivalent strain, total strain and initial yield stress respectively. For AA6111-T4 of 1 mm thickness with 0.25 mm/s test speed, an A value of 195 MPa was obtained. The Eq (4-3) still remains unsolved, even after receiving the A value, since the term $\ln(B - A)$ is unknown. Alternatively, if the saturation stress B is known, with linear fitting for intersection and slope, threshold stress A and hardening parameter m can be obtained. However, for materials that continue to work harden up to large strains, it is not possible to determine the saturation stress parameter B .

As reported by other researchers, for materials that are insensitive to strain rate, the threshold stress A and hardening parameter m are the same for any strain rate [Wagoner, 1981]. Also, the saturation stress is influenced by various factors such as temperature effect and work hardening rate [Lloyd, 2006]. Therefore, the saturation stress is subjected to change. Torsion test may be necessary to obtain the B value.

However, using trial values of B for Eq (4-3), relationship of B and A can be associated. With a given value of B in Eq (4-3) with linear fitting, there are determined A and m values accordingly. A range of B values with regular increment as input produces A and m values as a continuous function of B . Once an A value that is closest to the one calculated with Eq (4-4) was obtained, the corresponding B value was taken as the

saturation stress value. Using this B value in Eq (4-3), an m value was obtained. For example, a trial value of 420 MPa for B was utilized in Eq (4-3). The $\ln(B - \sigma)$ was plotted as function of ϵ (Figure 4-10). Using a linear fitting to the data, a slope (or m -value) of -10.565 was obtained. The intersection of the fitted line with the $\ln(B - \sigma)$ axis was first obtained and then using the following expression:

$$A = B - \exp[\ln(B - \sigma)_{\epsilon=0}] \quad (\text{Eq 4-5})$$

a value of $A = 420 - \exp(5.5021) = 420 - 245.21 = 174.79$ MPa was obtained.

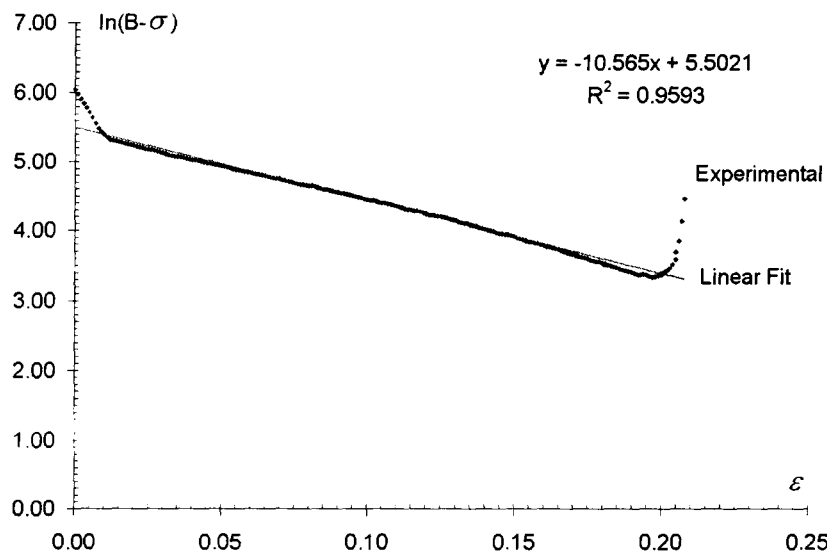


FIGURE 4-10. Obtaining parameters for Voce law fitting from post-processing of experimental uniaxial tensile data (AA6111-T4, 1 mm thickness, 0.25 mm/s test speed) using trial value 420 MPa for B value.

Using more trial values of B , for example, from 400 MPa to 500 MPa, with increment of 1, the relationship of B - A was established, which is plotted in Figure 4-11.

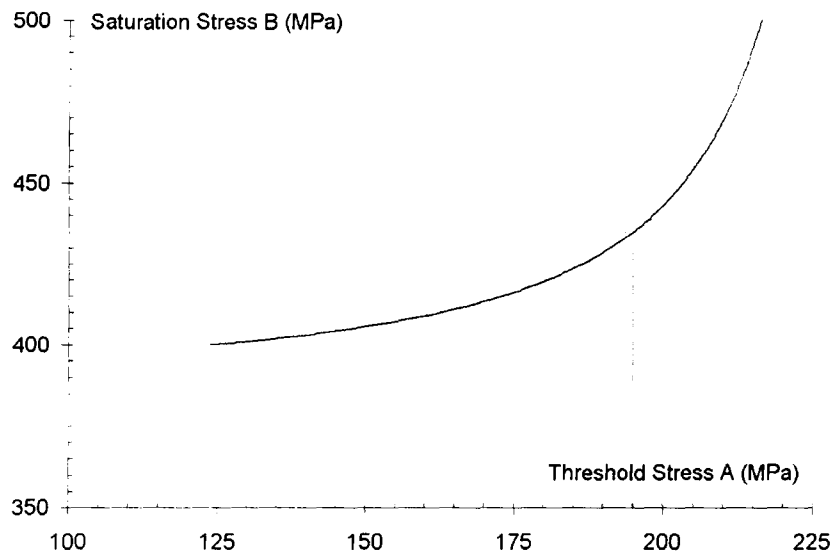


FIGURE 4-11. Relationship between trial value of B and linear fitting result of A for AA6111-T4 (1 mm thickness, 0.25 mm/s).

The relationship of B - A is monotonic, which means if either B or A is known, the other one can be determined. For AA6111-T4 of 1 mm thickness at a test speed of 0.25 mm/s, the A value is 195 MPa using Eq (4-4). Accordingly, from Figure 4-11, a B value of 435 MPa is obtained. The relationship of B - m was also established as plotted in Figure 4-12. At $B = 435$ MPa, the corresponding m value is -8.206 .

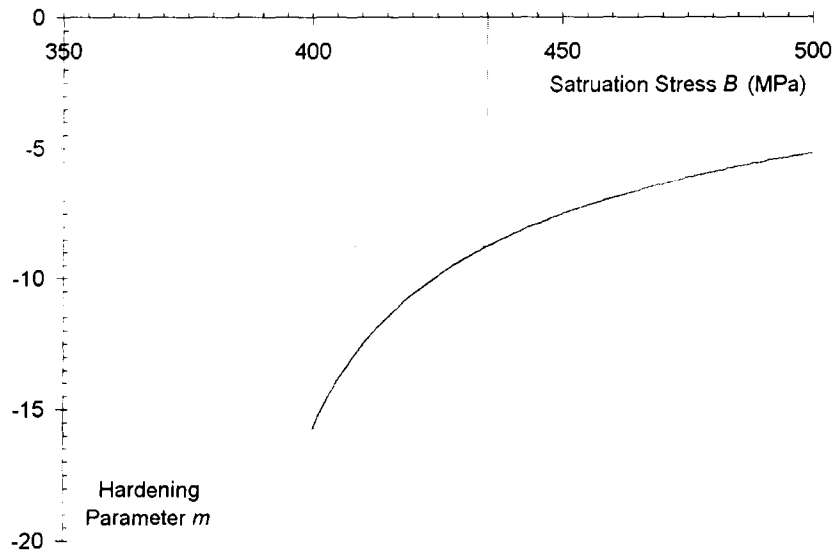


FIGURE 4-12. Relationship between trial value of B and linear fitting result of m for AA6111-T4 (1 mm thickness, 0.25 mm/s).

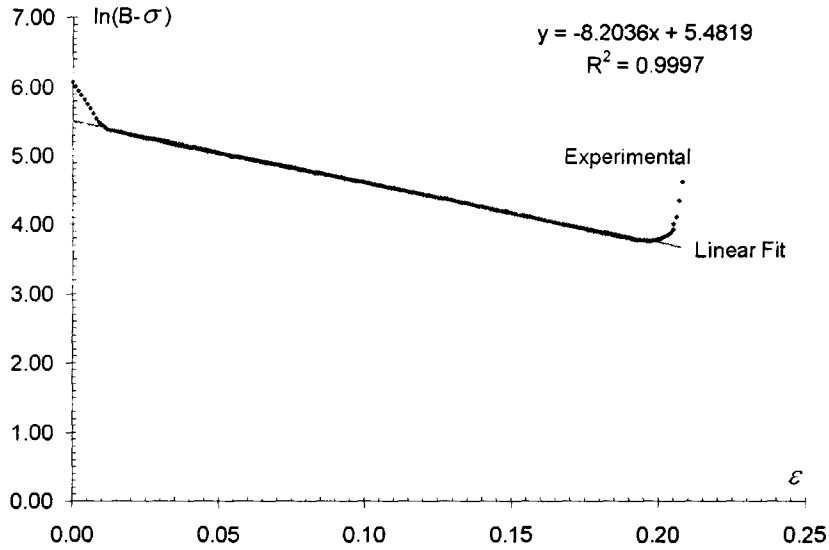


FIGURE 4-13. Obtaining parameters for Voce law fitting from post-processing of experimental uniaxial tensile data (AA6111-T4, 1 mm thickness, 0.25 mm/s test speed) using trial value 435 MPa for B value.

For the purpose of examining the quality of the fit, the results of linear fitting for obtaining A and m at $B = 435$ MPa is plotted in Figure 4-13. The Voce law parameters were calculated as:

$$\sigma = B - (B - A)\exp(m\varepsilon) = 435 - (435 - 195)\exp(-8.206\varepsilon) = 435 - 240\exp(-8.206\varepsilon).$$

The results of the analysis of the uniaxial tensile true stress – strain data for all materials used in the study are presented in Chapter 6.

4.2.2.2 Hemispherical Punch Stretching And Other Tests

The proposed approach to predict the localized necking behaviour of aluminum sheet material is to seek an inflection point in the major strain rate, or, a maximum in pseudo strain acceleration. Since the aluminum sheet materials in general are insensitive to the strain rate, the proposed method would be more powerful if it could also apply to the material that is rate sensitive. Therefore, the strain rate effect was investigated using not only AA6111-T4 but also a high strength steel DP600.

Also, current punch tests were mainly carried out on 1 mm sheet materials. It would be more useful if it can be utilized for formability determination of materials with a range of thicknesses. Therefore, two different sheet thickness values were tested to further verify the proposed criterion.

The influence of strain rate was investigated in AA6111-T4 by changing the punch speed. The specimens were tested with 0.25 mm/s (regular speed), 1.25 mm/s (system maximum limit) and 0.025 mm/s (low speed). For each test at different speeds,

both dry condition and polyurethane were utilized. This type of test was carried out for both 1 mm thickness and 2 mm thickness specimens.

Other than the conventional tests of various widths of specimens for the draw side and different lubrication conditions for the stretch side, it was felt that the proposed localized necking criterion should be further verified for other strain paths to assess its general applicability. The additional tests included a sand paper interface between the punch and sheet, a specimen geometry with a hole in the center, and a specimen with non-symmetric notches perpendicular to the loading axis (a “shear” test).

Traditional approach for biaxial tensile limit strain determination is to use a full dome specimen test and vary the lubricants between the sheet and punch. A range of lubrication conditions such as dry (direct contact between punch and sheet, $\mu = 0.3$), grease ($\mu = 0.1\sim 0.15$), Teflon (Teflon film applied on punch surface, $\mu = 0.05$) and polyurethane pad ($\mu = 0.015$) can be utilized. A high friction condition was introduced in one of the tests by applying a silica sand paper of grit 320 between the punch and sheet. The procedure resulted in a strain path in between the strain paths for direct dry contact and plane strain. Further by changing the grit size of the sand paper, various strain paths were produced, since this strain path was expected to be closer to the plane strain condition. These tests were carried out using AA6111-T4 at 1 mm sheet thickness.

Specimen with a central hole was tested to investigate whether strain paths to the left-hand-side of traditional FLD paths could be attained and especially to the left of the uniaxial tensile path. The strain paths were varied by changing the inner radius r of the central hole (Figure 4-14). Both 2” Nakajima punch (hemispherical) and 2” Marciniak

punch (cylindrical punch with flat head) were employed. Again, the material tested was AA6111-T4.

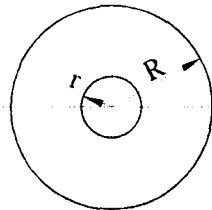


FIGURE 4-14. Profile of a specimen with a central hole ($R = 50$ mm, $r = 5$ mm, 10 mm, 12.5 mm, 20 mm, material: AA6111-T4, 1 mm thickness).

A specimen profile with two non-symmetric rectangular notches of 1 mm width with an offset was designed for shear test by modifying the ISO 11004-2 (ASTM D 3984-81) to obtain a strain path that approaches $\beta = -1$ as close as possible (Figure 4-15). It was assumed that both the clearance (C , length between the notch tips) and spacing (S , length between the notch body) influence the strain ratio β . Although strain path of pure shear is practically impossible in a hemispherical punch test due to the out-of-plane deformation, configurations of different notch length and spacing were chosen to obtain various strain paths that approach $\beta = -1$ as close as possible for the in-plane shear test specimens subjected to uniaxial loading (Figure 4-15 and Table 4-1).

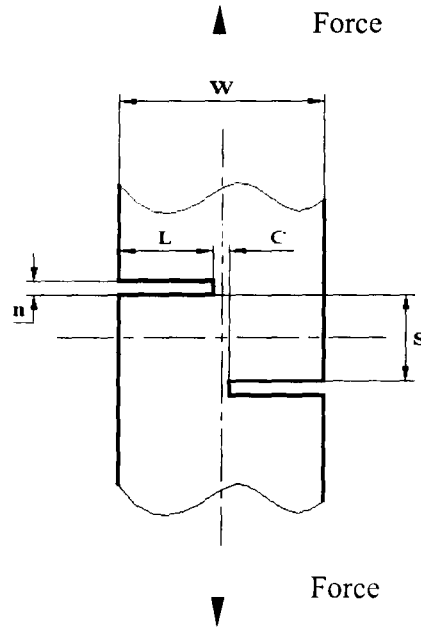


FIGURE 4-15. Specimen designed for shear test (material: AA6111-T4, 1 mm thickness).

TABLE 4-1. Configuration of shear test specimens with notches.

No.	Notch Length L	Clearance C	Notch Spacing S	Notch Ratio C/S
<i>1a</i>	$W/2-t/2$	t	$10t$	0.1
<i>1b</i>	$W/2$	0	$10t$	0
<i>1c</i>	$W/2+t/2$	$-t$	$10t$	-0.1
<i>2</i>	$W/2+t/2$	$-t$	$5t$	-0.2
<i>3</i>	$W/2+t/2$	$-t$	$2t$	-0.5
<i>4</i>	$W/2+t/2$	$-t$	T	-1
<i>5</i>	$W/2-t/2$	t	T	1
<i>6</i>	$W/2-3t/2$	$3t$	T	3

Note: t , thickness of the sheet, 1 mm, n , width of the notch, 1 mm, and W , width of the specimen, 12.5 mm.

4.2.3 Characterization Of Load Curves For Inflection

In current research on punch test experiment, the frequency of data acquisition of the load cell from MTS system is 10 points/second. For a test on AA6111-T4 specimen (dry condition) on biaxial side, the duration (till fracture occurs) is around 60 seconds at a speed of 0.25 mm/s. Therefore, approximately 600 data points are recorded.

The process was implemented in a spreadsheet based program (Microsoft Excel) to quickly obtain increments of load and displacement for the quotient as rate data, and further the acceleration data. Table 4-2 shows the procedure of numerical processing of the raw data. Column *A* is the punch displacement (inch) and column *B* is the punch load (pound). Column *D* is the conversion of column *A* into millimeter, whereas the column *E* is the conversion of column *B* into Newton. Column *G* is punch displacement in regular interval, i.e. 0.1 mm increment. Column *H* is re-sampled load point according to the value in *G*. For example, there are four collected load points in *E* at the value range of 0.4 in *D*. An average is taken ($\frac{16.8 + 16.8 + 21.34 + 21.34}{4} = 19.07$). The re-sample process is actually an average process of the raw load data into regular interval of displacement (Appendix 2).

The column *J* is the same as column *G*. The column *K* is the result of each column *H* element minus the load value when punch travel is zero, in order to remove the initial error. Column *L* is the derivative of column *K* element with regard to its previous record, e.g. $L_i = (K_i - K_{i-1}) / (J_i - J_{i-1})$.

TABLE 4-2. Excel data sheet showing raw and processed punch load versus displacement data for plots in Figures 4-16 to 4-18.

	A	B	C	D	E	F	G	H	I	J	K	L	M	N	O	P	Q	R	S	
1	Raw	recorded		Raw	converted		Raw	re-sample	Re-sample	initialized	1st diff	Moved	1st diff	Fitted	Diff_Fit					
2	(mm)	(N)		(mm)	(N)		(mm)	(N)	(mm)	(N)	(N/mm)	(mm)	(N/mm)	(N/mm)	(N/mm)	(N/mm)	(N/mm)	(N/mm)	(N/mm)	(N/mm)
3	-1.562	8		0.0	0.00		0.0	1.59	0.0	0.00		0.00		0.00		0.00				
4	-1.561	15		0.0	3.18		0.1	4.99	0.1	3.40		34.03		4.31		43.13		3.71		37.08
5	-1.56	18		0.1	4.54		0.2	11.13	0.2	9.54		61.32		8.22		39.05		7.54		38.32
6	-1.559	21		0.1	5.90		0.3	12.26	0.3	10.67		11.35		12.42		42.00		11.50		39.55
7	-1.557	18		0.1	4.54		0.4	19.07	0.4	17.48		68.10		16.89		44.72		15.57		40.79
8	-1.556	25		0.2	7.72		0.5	22.59	0.5	21.00		35.20		20.97		40.84		19.77		42.00
9	-1.555	35		0.2	12.26		0.6	27.35	0.6	25.76		47.60		25.83		48.58		24.10		43.23
10	-1.554	38		0.2	13.62		0.7	31.55	0.7	29.96		42.03		29.92		40.86		28.54		44.44
11	-1.553	32		0.2	10.90		0.8	36.55	0.8	34.96		49.93		34.48		45.62		33.11		45.67
12	-1.552	35		0.3	12.26		0.9	39.50	0.9	37.91		29.50		39.00		45.18		37.80		46.89
13	-1.551	35		0.3	12.26		1.0	45.40	1.0	43.81		59.05		43.31		43.14		42.61		48.11
14	-1.549	32		0.3	10.90		1.1	49.94	1.1	48.35		45.40		47.78		44.72		47.54		49.34
15	-1.549	38		0.3	13.62		1.2	53.12	1.2	51.53		31.80		52.76		49.76		52.60		50.58
16	-1.548	45		0.4	16.80		1.3	58.91	1.3	57.32		57.88		57.46		47.00		57.78		51.82
17	-1.547	45		0.4	16.80		1.4	64.38	1.4	62.79		54.71		62.50		50.40		63.09		53.06
18	-1.546	55		0.4	21.34		1.5	68.90	1.5	67.31		45.17		68.17		56.74		68.52		54.32
19	-1.545	55		0.4	21.34		1.6	75.14	1.6	73.55		62.40		73.87		56.98		74.08		55.58
20	-1.544	55		0.5	21.34		1.7	81.49	1.7	79.90		63.55		79.25		53.76		79.76		56.85
21	-1.543	52		0.5	19.98		1.8	87.40	1.8	85.81		59.05		84.95		57.06		85.58		58.13
22	-1.542	62		0.5	24.52		1.9	91.26	1.9	89.67		38.60		90.88		59.24		91.52		59.42
23	-1.541	62		0.5	24.52		2.0	97.43	2.0	95.84		61.75		97.05		61.76		97.59		60.71
24	-1.54	66		0.6	26.33		2.1	104.76	2.1	103.17		73.32		103.20		61.46		103.79		62.01
25	-1.539	59		0.6	23.15		2.2	112.37	2.2	110.78		76.05		109.58		63.80		110.12		63.30
26	-1.538	69		0.6	27.69		2.3	118.13	2.3	116.54		57.63		116.36		67.80		116.59		64.70
27	-1.537	79		0.6	32.23		2.4	123.18	2.4	121.59		50.53		123.17		68.10		123.19		66.00
28	-1.536	72		0.7	29.06		2.5	131.30	2.5	129.71		81.15		130.03		68.60		129.92		67.30
29	-1.535	76		0.7	30.87		2.6	138.83	2.6	137.24		75.36		136.98		69.50		136.78		68.60
30	-1.534	83		0.7	34.05		2.7	146.65	2.7	145.06		78.11		144.77		77.90		143.78		70.00
31	-1.533	79		0.7	32.23		2.8	152.89	2.8	151.30		62.40		153.11		83.40		150.92		71.40
32	-1.532	86		0.8	35.41		2.9	162.15	2.9	160.56		92.68		160.87		77.60		158.20		72.80
33	-1.531	86		0.8	35.41		3.0	172.98	3.0	171.39		108.22		168.68		78.10		165.61		74.10

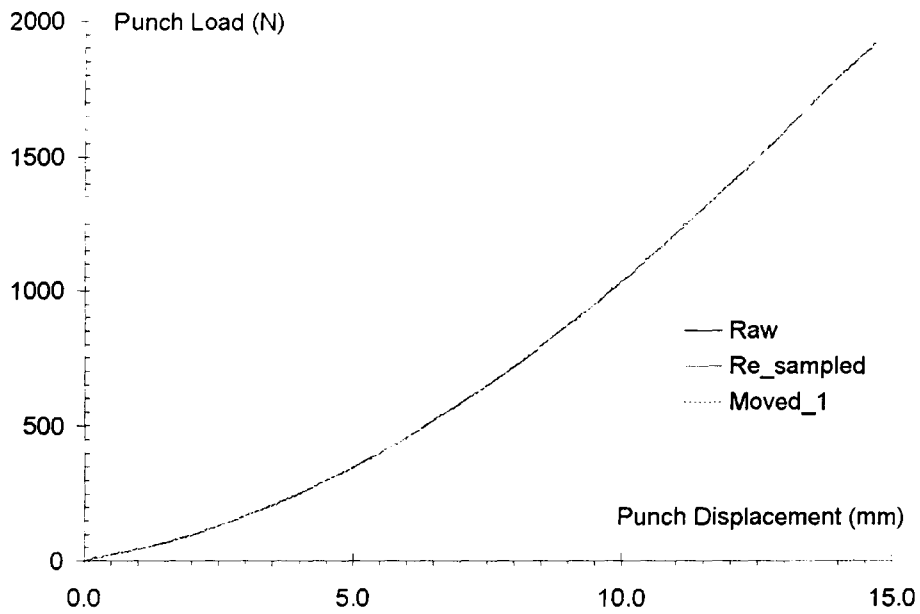


FIGURE 4-16. Raw data of load-displacement curve showing raw data (columns *D* and *E*), re-sampled data (columns *G* and *H*) and processed data with moving average (column *N*) (AA6111-T4, 1 mm thickness, test speed 0.25 mm/s).

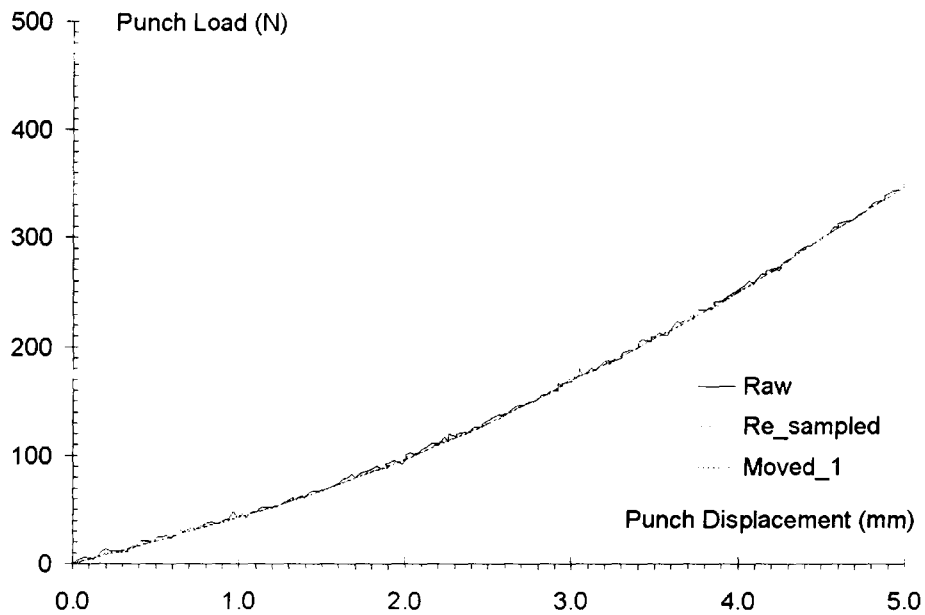


FIGURE 4-17. Expanded plot of Figure 4-16 showing raw data, re-sampled data and processed data with moving average.

The noise in the processed data was further smoothed using the running average method with only one iteration in MATLAB (Appendix 3). The window size was “2”, the minimum, i.e. in each step only 2 records were averaged (Column N in Table 4-2, termed as “Moved_1” in Figures 4-16 and 4-17). Under these conditions, the least amount of error was introduced. A monotonic increase in the magnitude of load has been obtained, although curve is not smooth. The mean square error of punch load between re-sampled curve and moved curve is 1.40 N, acceptable compared to the maximum punch load of 1912 N. As the iteration proceeds, this error is further decreased. If the processed data is further processed with the same parameter setting for more than one time, the curve looks smoother. However, the deviation from the original data is increased.

Post-processing of load-displacement data was carried out to obtain the 1st order of derivative of load curve, or, the load rate dF/dh . The inflection point, which represents the onset of diffuse necking, is located at $(d^2P/dh^2)=0$, or, $(dP/dh)_{max}$. Since the tests were conducted at a constant punch velocity, the functions of load rate and load acceleration in terms of time were converted into functions with regard to displacement. A theoretical basis for existence of inflection point in the load curve corresponding to the onset of diffuse necking is given in Appendix 4.

Since the tests were conducted at a constant punch velocity, the functions of load rate and load acceleration in term of time were converted into functions with respect to displacement as follows:

$$\frac{dP}{dt} = \frac{dP}{\frac{dh}{v}} = v \frac{dP}{dh} \quad (\text{Eq 4-6})$$

$$\frac{d^2P}{dt^2} = \frac{d^2P}{dh^2} = v^2 \frac{d^2P}{dh^2} \quad (\text{Eq 4-7})$$

where P , h , t , v are punch load, punch displacement, test time and punch speed respectively.

Three load curves, namely re-sampled data, processed with moving average, fitted with 6th order polynomial, were processed to obtain the load rate curves (columns L , O and R in Table 4-2).

The re-sampled data and the processed data with moving average were fitted with 6th order polynomial. The previously fitted load curve was directly calculated to obtain load rate curve without fitting. ‘Re-sampled’ in Figure 4-18 refers to the load rate of raw data (column L in Table 4-2). ‘Moved_1’ refers to processed raw data of load rate with moving average (column O in Table 4-2). ‘Fitted’ data refers to load rate of fitted load curve with 6th order of polynomial (column R in Table 4-2). ‘Poly.(Re-sampled)’ refers to trend line with 6th order polynomial fitting to ‘Re-sampled’ load rate data. ‘Poly.(Moved_1)’ refers to trend line with 6th order of polynomial fitting to ‘Moved_1’ load rate data.

The major interest here is to find the location of the inflection point. Both the raw data and the fitted curve produce peak point at the same location. No further iteration is necessary since 6th order of fitting has been employed. The trend lines exhibit very similar characteristics, which proves that the previously fitted load curve is sufficient to represent the raw data curve.

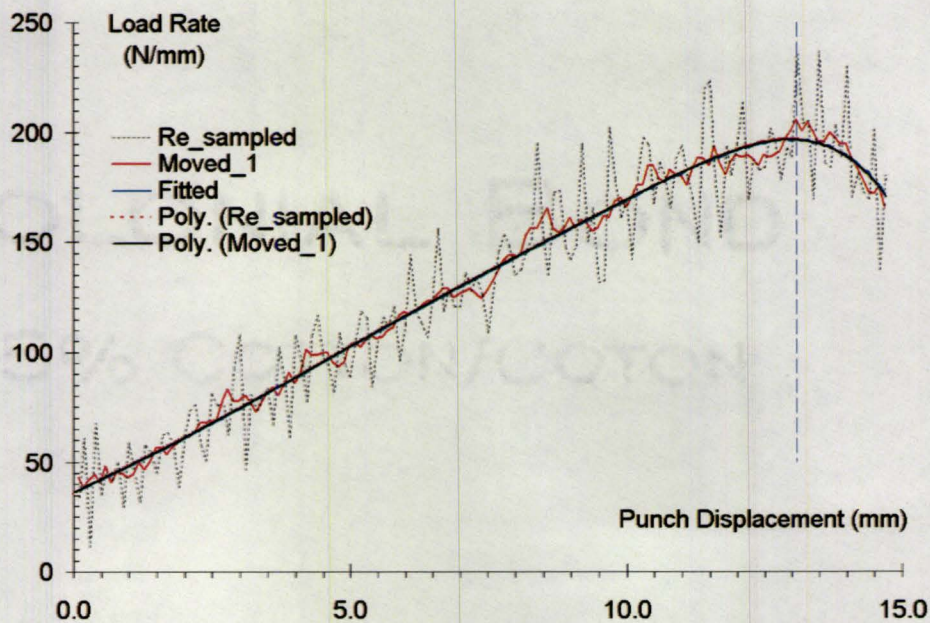


FIGURE 4-18. Load rate data for Figure 4-16 (raw data of re-sampled load curve, load curve processed with moving average, trend lines of 6th order for the two curves of raw data).

This analysis has demonstrated that the curve fitting for load curves is not absolutely necessary to obtain the required parameter, i.e. the location of inflection point. A moving average method yield a result very similar to those obtained from the curve fitting.

4.2.4 Procedure For Data Processing Of Strain History

The strain history data from experiment and FE simulation should first be extracted and examined for the relevant part, e.g. from punch contact to fracture. This can be easily implemented in experimental data (ARAMIS), since there are images showing

cracking in the specimen. The determination of valid range for FE data is discussed in Section 4.3.2.

The major / minor strain histories should then be constructed as a function of time or step (data entry in Excel). Moving average method has been utilized to remove the initial irregular scatter of data to obtain a monotonic increasing or decreasing curves.

Since a second derivative of strain is required to obtain the maximum value in major strain acceleration, the strain rate curve should be smooth. Based on the strain rate curve the calculation to obtain the characteristic points, such as inflection point in major strain rate curve is carried out. Both moving average and polynomial curve fitting can improve the visual recognition of the trend in the first derivative of strain, i.e. the strain rate curve. However, it may take a number of iterations in the moving average if minimum window size is employed to reduce the introduced error. As analyzed earlier, 6th order polynomial and moving average exhibit similar results. In Excel program, trend lines of 6th order of polynomial can be created automatically and have been utilized in this research.

4.3 FE Modelling

FE models of the hemispherical dome test were developed to investigate the strain development on the specimen surface to study aspects of strain localization in the form of a neck. Temporal and spatial strains were characterized in an extensive FE investigation and compared with the conventional grid measurement and analysis in an attempt to assess the FE methodology for FLD prediction.

Since the formability data was collected from the FE simulations of hemispherical punch tests in order to obtain limit strains from various strain paths, the proposed localized necking criterion was utilized in conjunction with the simulation data.

The load curves obtained from FE investigation were normalized with the experimental data of load magnitude, limit dome height and location of inflection. This normalization procedure was followed for each specimen geometry and lubrication (or friction) condition. An optimization process was undertaken for each strain path and obtained parameters were used as experimental input into the FE models. This is discussed in more detail in Chapter 5.

ABAQUS/Explicit FE program was utilized to simulate the punch tests and predict the FLDs. The material has been modelled as homogenous, and rate-independent and as following the von Mises yield criterion. A strain-based uncoupled damage model based on a critical effective plastic strain as a fracture criterion has been implemented in the simulations. Critical effective plastic strain is used as a criterion for element deletion in the simulations and has no bearing on the occurrence of localization. This is further discussed in Section 4.3.2.

For the process modelling, the entire experimental dome test procedure, as followed in the laboratory, including the clamping with draw bead and stretching with punch, has been modelled. A constant punch speed was implemented. Colomb friction coefficients are also included to account for different “lubrication” conditions in the experiments. Frictional coefficients at various tool-sheet interfaces were utilized in the simulations and the details are given in Chapter 5. Eight-node brick element (C3D8) in

ABAQUS of various mesh sizes were selected for FE modeling. The aspects of FE mesh and damage model are discussed in the context of solution convergence and mesh dependency in Sections 4.3.1 and 4.3.2 below.

4.3.1 Solution Convergence In FE Simulations

From the analysis of strain evolution of the localized element in FE, the occurrence of maximum major strain $(\dot{\epsilon}_1)_{\max}$ can be established. By comparing the strain history of the localized element with its neighbor, the time when the major strain of the localized element $(\epsilon_1)_{cr}$ exceeds the previously larger element can also be determined by post-processing of FE results.

However, the study of instability is highly mesh dependent because it does not follow the general rule that a finer mesh is always more accurate and therefore better. Enhancements of the modeling, such as various mesh sizes and re-mesh technique are necessary because the range of “localized area” (width) is more than 1 mm (thickness). Various mesh sizes, such as 2 x 2, 1 x 1 and 0.5 x 0.5 (mm x mm) were utilized in a case study to investigate the convergence problem for a 2” wide specimen geometry (Figure 4-19). The normalized FE curves from the three models were compared with the experimental punch load curves. The deviation in load values is plotted in Figure 4-20 to show that the trend with respect to the mesh size is not always consistent. An optimal value close to the regular 1 x 1 (mm x mm) configuration is suggested by these

simulations. Other geometries of specimens were also studied for the convergence problem more extensively.

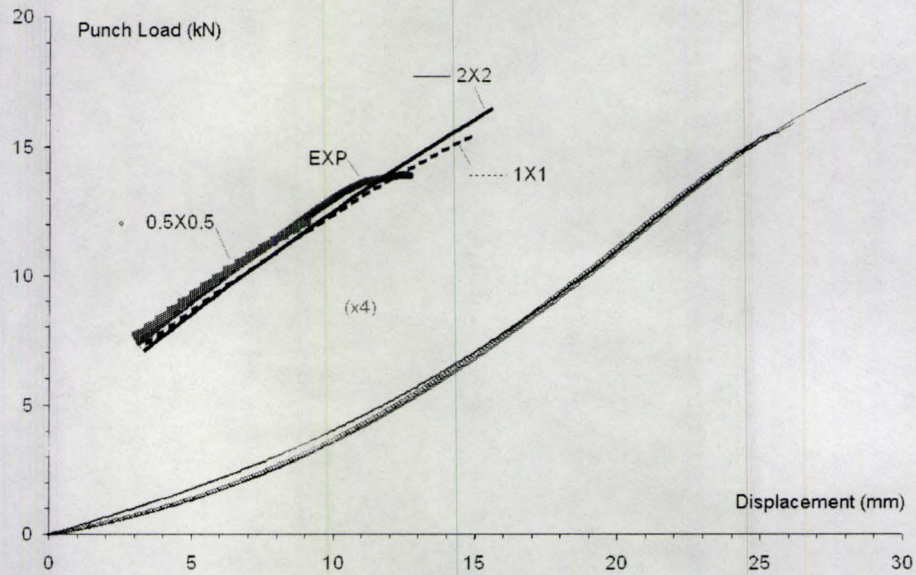


FIGURE 4-19. FE results of various mesh sizes for sheet compared with experimental data (AA6181-T4, 2" wide specimen, 1 mm thickness, 4" diameter punch).

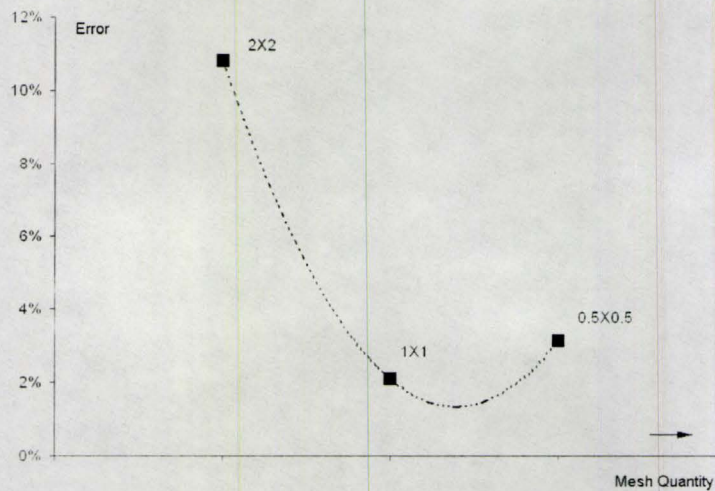


FIGURE 4-20. Actual errors of FE simulations with different mesh sizes for a study of convergence (based on Figure 4-19).

4.3.2 Influence Of Damage Model On Strain Analysis

The damage model in FE investigation does not affect the occurrence of localization. On the other hand, the use of damage model enables the termination of forming process once the localization has occurred. Implementation of damage model also facilitates the post-processing of strain history by quickly identifying the element in the localized site. A large value of damage strain was given in the model so that the material could attain large deformation well beyond localized necking. However, since the physical meaning of strain rate, strain acceleration has been investigated and the termination of a forming process has been located at $(\ddot{\epsilon}_1)_{\max}$, the record beyond this stage is generally irrelevant and invalid (Figure 4-21). Only the valid portion of strain history has been identified and extracted for strain analysis to obtain the inflection in strain rate, e.g. the onset of localization.

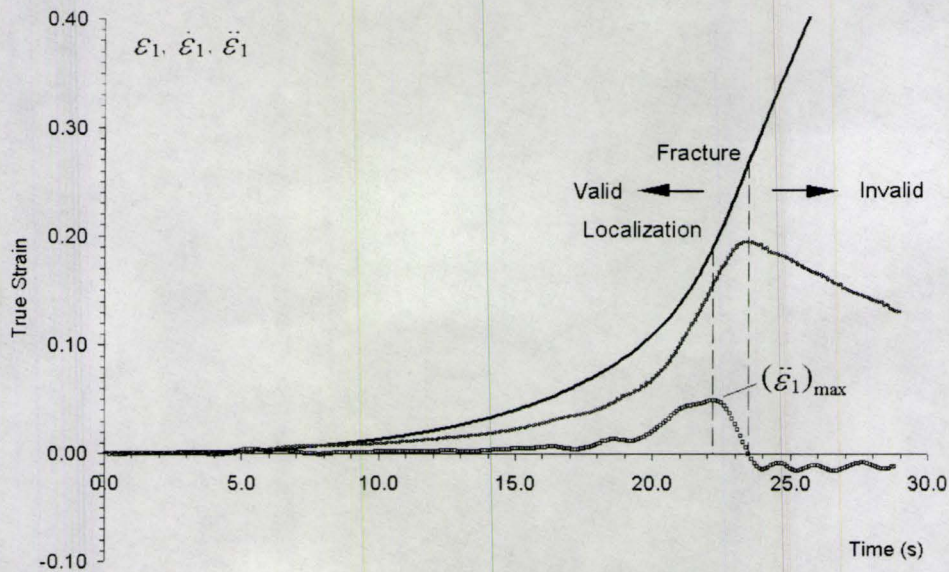


FIGURE 4-21. Application of damage model in FE modelling.

4.4 Validation of Formability Characteristics

The deformation of the random speckles over the surface of the specimens in the punch tests was captured by the ARAMIS online strain imaging system. After post-processing of the on-line data, both the field and history of strain contours can be obtained from which the limit strains were further calculated.

When the localized neck site is located, the strain history from the element inside the neck can be extracted for the analysis to seek the inflection point, $(\dot{\epsilon}_I)_{\max}$, in the major strain rate curve as the limit strain. Also, from the strain histories of the damaged member and its neighbors, a traditional approach to seek the limit strain, $(\epsilon_I)_{cr}$, was utilized and compared with the proposed approach based on $(\dot{\epsilon}_I)_{\max}$ criterion.

The predicted FLDs were also validated with ARGUS 3D imaging system based on electrochemically etched periodic grids. This technique utilizes a method similar to the traditional method to measure the strain of the deformed grids from 360° spatial views. ARGUS only captures the end stage of the specimen but not the strain development as a continuous process as in ARAMIS, although visual check of necking zone and manual strain measurements are not necessarily required. The limit strains from ARGUS tests were obtained from interpolation of data across a deep neck or fracture using Bragard criterion ϵ_{Br} . Thus, a comparison of FLDs obtained from $(\dot{\epsilon}_I)_{\max}$, $(\epsilon_I)_{cr}$ and ϵ_{Br} as criteria could be made.

The role of ARAMIS strain imaging system was only for validation, although with the technique of online imaging, the strain history and contour can be quickly

obtained. Also, since this device is very expensive and requires considerable training for its operation, it is still not commonly used in industry. The ultimate goal of this research is not to use the ARAMIS system, and in fact avoid the use of any strain measurement, and focus on the experimental load-displacement curves and FE analysis as a means to obtain FLDs.

Chapter 5

Optimization Of Material And Friction Input Data For FE Simulations Of Forming Tests

FE modelling with material input directly from uniaxial tensile test can already produce limit strains for certain paths. However, the simulated process may not agree with the experimental load versus displacement curve. An arbitrary selection or variation in the input parameters in the model to match the model and experimental load curves may lead to too many attempts at simulations. Therefore, an optimization procedure was developed for calibrating FE based load-displacement curves with the experimental curves to minimize the number of tests. In this chapter, the optimization methodology is first presented for biaxial tensile strain path with no frictional contact. This is followed by the cases involving biaxial tensile strain paths with friction as well as cases involving strain paths on the tension-compression side.

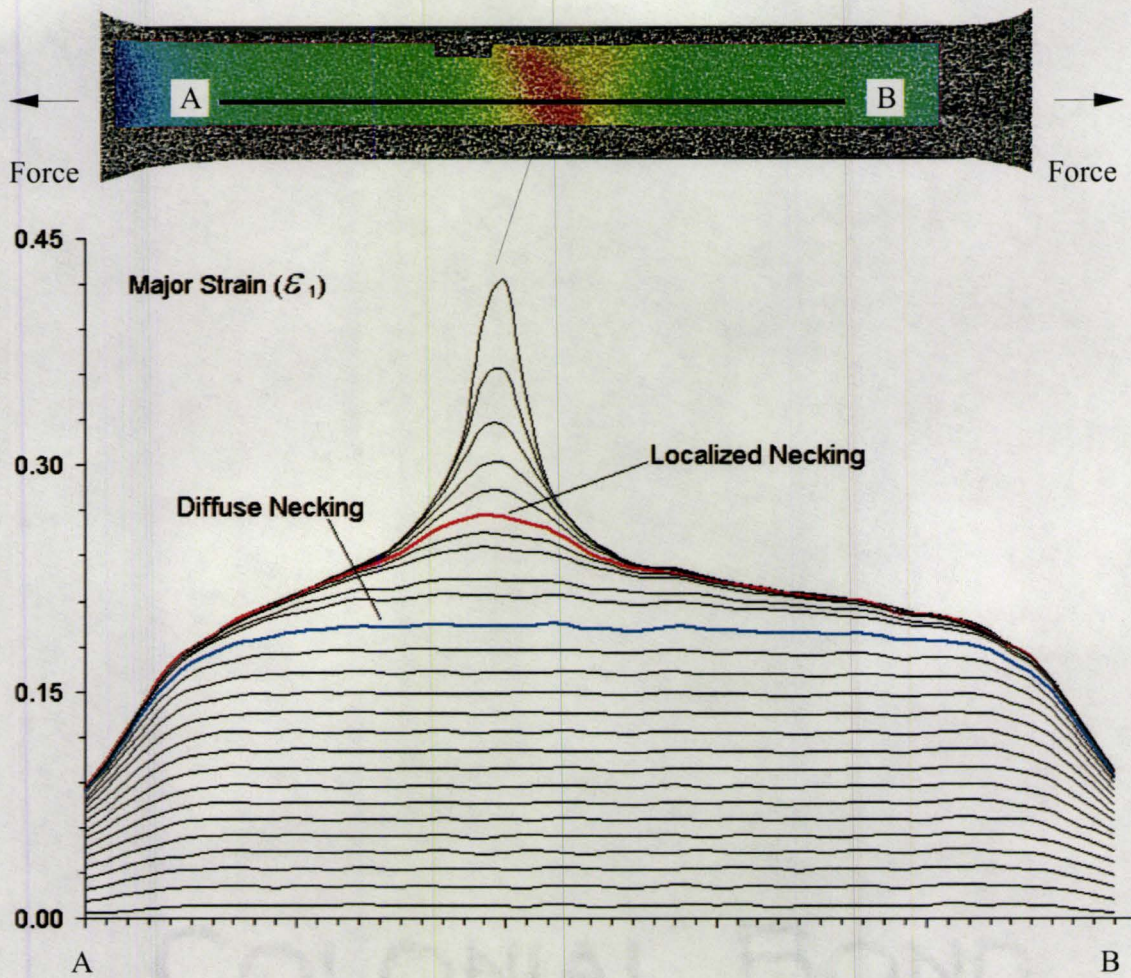


FIGURE 5-1. Strain history from ARAMIS indicating diffuse necking and localized necking for a 0.5" wide uniaxial tensile test specimen (AA6111-T4, 1 mm thickness).

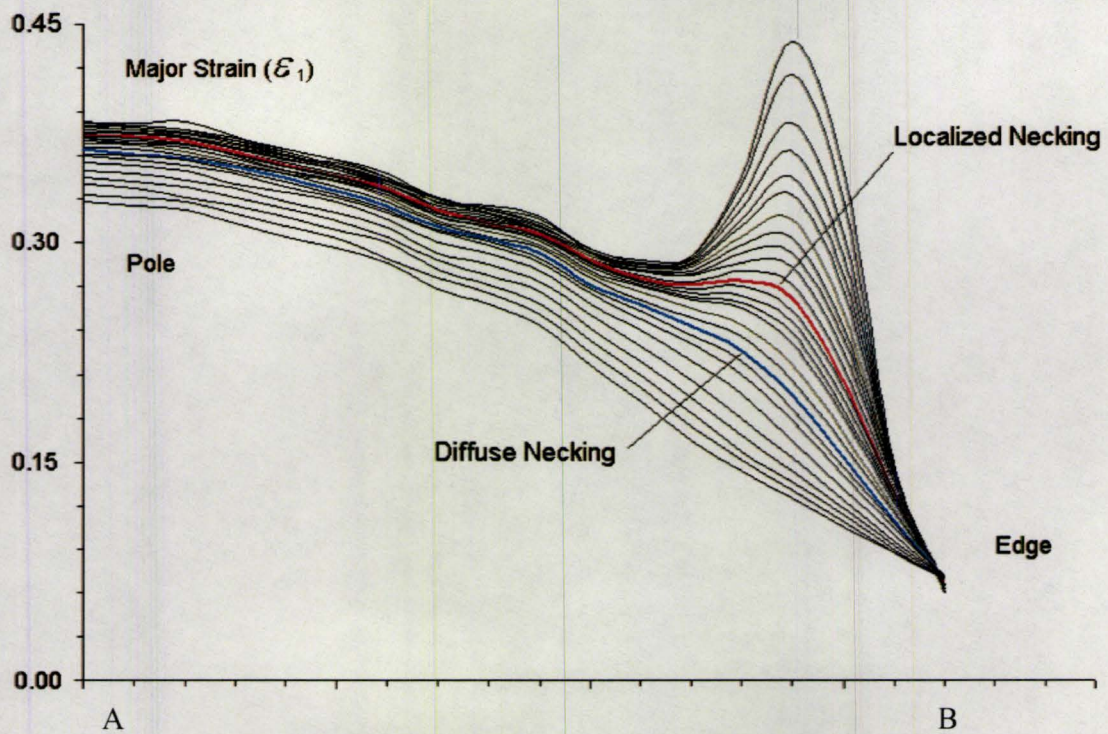
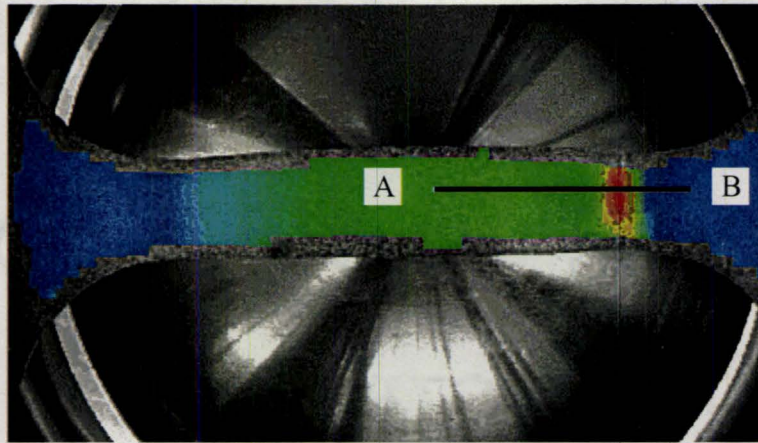


FIGURE 5-2. Strain history from ARAMIS indicating diffuse necking and localized necking for a 0.5" wide punch test specimen (AA6111-T4, 1 mm thickness, 2" diameter punch).

The stress-strain relationship obtained from uniaxial tensile test was not used directly for FE simulations since the material may behave differently for different loading paths (Figures 5-1 and 5-2). A trial-and-error procedure was utilized to determine the $\sigma - \epsilon$ curve input for different biaxial loading paths. Also, to obtain various strain paths in the tension-tension region (i.e. right side of FLD), only the lubrication conditions were varied, keeping the same geometry of specimen. Therefore, to simplify the optimization work, first the case of biaxial loading without friction was considered. A weight function was established to relate the two commonly used hardening laws, namely power law and Voce law to obtain a close agreement with experimental load versus displacement curve. Further, once the stress-strain relationship at large strains was established, friction coefficient between the sheet and punch was varied for the other biaxial tensile loading paths. A similar methodology by using weight function was employed to establish the friction function in term of time. The stress-strain relationship obtained from uniaxial tensile test was directly utilized for the tension-compression side (i.e., the left side of FLD) along with the weight function for friction.

A characteristic fracture strain value, ϵ_f , was also established for the different strain paths to terminate the simulations.

5.1 Optimization Of $\sigma - \epsilon$ Input For AA6111-T4

As mentioned earlier, two hardening laws, power law and Voce law, were considered in the extrapolation of stress-strain curves for AA6111-T4 sheet of 1 mm

thickness (Figure 5-3). A fit to the experimental uniaxial true stress-true strain data $\sigma - \epsilon$ to the power law ($\sigma = K\epsilon^n$) for the two material constants resulted in $K = 550$ and $n = 0.215$. Similarly, a fit of experimental data to Voce law ($\sigma = B - (B - A)e^{m\epsilon}$) resulted in $A = 200$, $B = 435$ and $m = -8.2$.

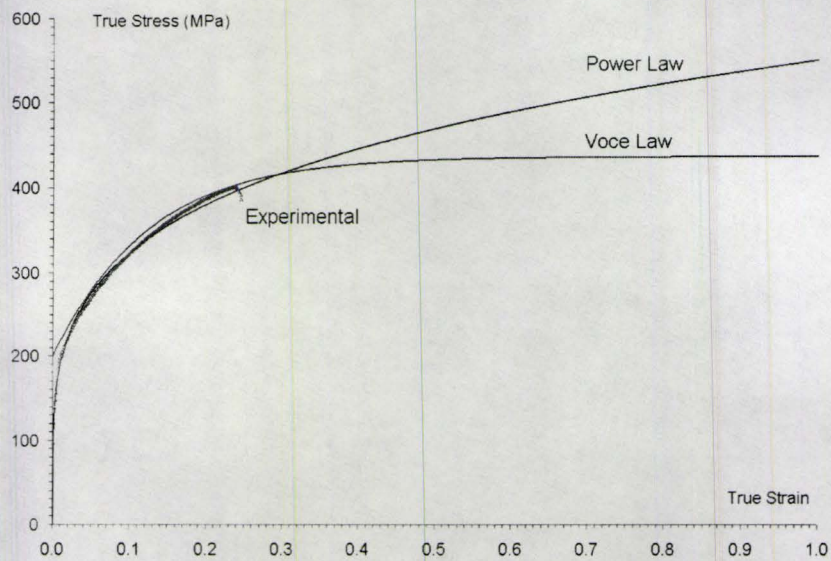


FIGURE 5-3. Stress-strain relationship of 1 mm thickness specimen of AA6111-T4 (1 mm thickness) from uniaxial tensile test and fitted with power law and Voce law.

The experimental data of stress-strain relationship from uniaxial tensile tests show that the variation in the magnitude of true stress is within $\pm 2\%$ in the range of the fit (Figure 5-4). In terms of parameters of power law, namely K , n , and those of Voce law, A , B and m , a 2% variation was applied to each parameter to evaluate the range of possible combinations. Also, these parameters needed to be examined with Considère criterion to ensure the extrapolation of stress-strain relationship complies with the instability conditions.

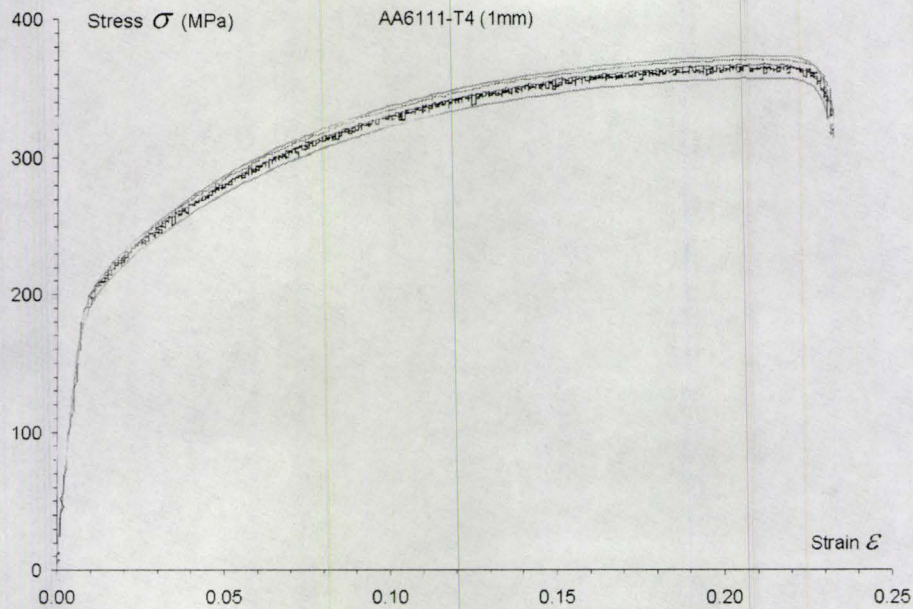


FIGURE 5-4. True stress – true strain relationship of AA6111-T4 specimen showing a band of $\pm 2\%$ variation (1 mm thickness, test speed 0.25 mm/s).

The extrapolation was first carried out with the power law because of fewer parameters and its simpler form. The influence of K is proportional to the stress, when n -value is kept constant. As the K value increases, the magnitude of stress increases in the range $0 < \epsilon < 1$. However, the effect of n over the stress-strain curve is to change its slope or curvature. As the n value increases the slope of stress-strain curve decreases. However, when associating the Considère criterion with instability, there is no influence from the K value, whereas the influence of the n value is linear as expressed below.

$$\frac{1}{\sigma} \frac{d\sigma}{d\epsilon} = \frac{1}{K\epsilon^n} \frac{d(K\epsilon^n)}{d\epsilon} = \frac{Kn\epsilon^{n-1}}{K\epsilon^n} = \frac{n}{\epsilon} \quad (\text{Eq 5-1})$$

The strains at instability are obtained as:

for diffuse necking, $\frac{1}{\sigma} \frac{d\sigma}{d\varepsilon} = 1$, or, $\varepsilon = n$ (Eq 5-2)

and for localized necking, $\frac{1}{\sigma} \frac{d\sigma}{d\varepsilon} = \frac{1}{2}$, or, $\varepsilon = 2n$ (Eq 5-3)

Equations (5-2) and (5-3) indicate that by changing K value, the stress changes proportionally, but the K value does not affect the instability.

Two extreme conditions, upper bound and lower bound, and the mean value of K and n were preliminarily tested via FE simulations to ensure the inputs produced a band of load curves that covered experimental load trace, as well as the deviations in the load-displacement curves between the upper / lower bounds and the mean value. The corresponding parameters are shown in Table 5-1:

TABLE 5-1. Power law parameters for trial-and-error tests in FE simulation (AA6111-T4, 1 mm thickness, 2" diameter punch, low friction). The symbols K_0 and n_0 refer to the experimentally measured K and n values mentioned earlier.

Upper bound	$K = 1.02 K_0$	$n = 0.98 n_0$
Lower bound	$K = 0.98 K_0$	$n = 1.02 n_0$
Middle	$K = 1.00 K_0$	$n = 1.00 n_0$
Reference value	$K_0 = 550$	$n_0 = 0.215$

The two bounds of the input data from power law produced the two limits of the load curves shown in Figure 5-5. The middle part of the experimental data (up to about 17 mm of punch displacement) basically falls into the band of regular 100% and 98% lower bound, although the end part of the FE load curve approaches the experimental

load curve with the mean input. However, none of the input data could produce a good agreement for the initial part of the curve. No matter how the parameters were varied between 98% and 102%, they could not produce a close agreement with the experimental data. This means a lower magnitude of stress has been utilized in the range of low strain and needed reconsideration with a higher value. However, the power law seems to be limited in attaining a significant increase in the initial stage of stress-strain curve. Therefore, a Voce law hardening behaviour was considered to improve the extrapolation.

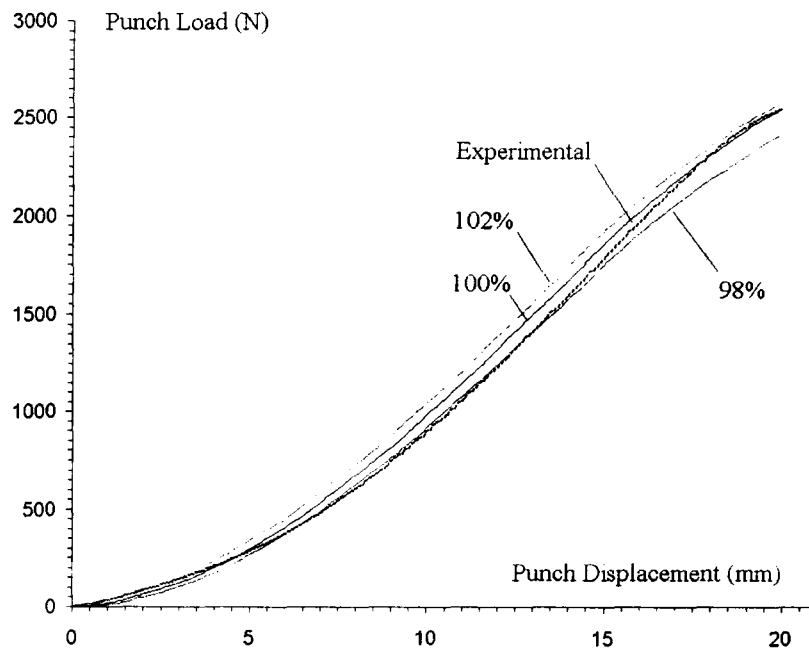


FIGURE 5-5. A comparison of experimental load-displacement data and those based on power law in the FE simulation (AA6111-T4, 1 mm thickness, 2" diameter punch, balanced biaxial, $\mu = 0$).

Among the three variables in the Voce law, the parameter A influences the initial value of stress, whereas the parameter B influences the saturation of stress, and the parameter m influences the curvature. Increasing the A , B and m value will also increase

the initial stress, saturated stress and curvature and vice versa. Once again, upper and lower bounds in $\sigma - \epsilon$ curves were utilized as well as “mean” $\sigma - \epsilon$ curve to obtain three corresponding load-displacement curves via tentative FE simulations. The corresponding parameters are shown in Table 5-2:

TABLE 5-2. Voce law parameters for trial-and-error tests in FE simulation (AA6111-T4, 1 mm thickness, 2” diameter punch, low friction). The symbols A_0 , B_0 and m_0 refer to the experimentally measured A , B and m values mentioned earlier.

Upper bound	$A = 1.02 A_0$	$B = 1.02 B_0$	$m = 1.02 m_0$
Lower bound	$A = 0.98 A_0$	$B = 0.98 B_0$	$m = 0.98 m_0$
Middle	$A = 1.00 A_0$	$B = 1.00 B_0$	$m = 1.00 m_0$
Reference value	$A_0 = 200$	$B_0 = 435$	$m_0 = -8.2$

The material modelling with Voce law produced good agreement in the initial stage of the load curves, as well as in the middle part. However, the later stage of the FE results deviated significantly from the experimental data. Although the input $\sigma - \epsilon$ curve for upper bound produced the highest load curve, it is still lower than the experimental data (Figure 5-6). This indicates that only with variation in the Voce law parameters, it is difficult to achieve good agreement between the FE and experimental load curves.

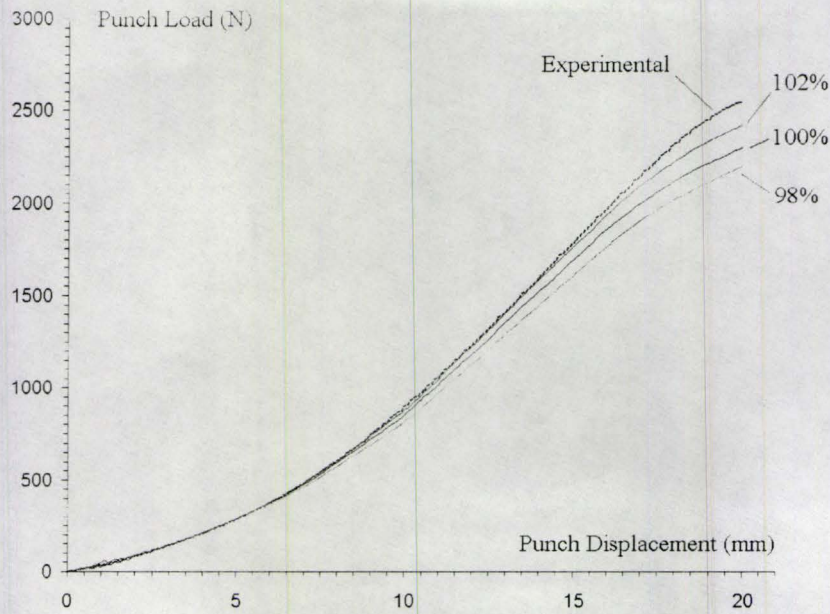


FIGURE 5-6. A comparison of experimental load-displacement curve and those based on Voce law in the FE simulation (AA6111-T4, 1 mm thickness, 2" diameter punch, balanced biaxial, $\mu = 0$).

Further investigation of parameter sensitivity was focused on the Considère criterion.

$$\frac{d\sigma}{d\varepsilon} = \frac{d(B - (B - A)\exp(m\varepsilon))}{d\varepsilon} = -m(B - A)\exp(m\varepsilon) \quad (\text{Eq 5-4})$$

$$\begin{aligned} \frac{1}{\sigma} \frac{d\sigma}{d\varepsilon} &= \frac{-m(B - A)\exp(m\varepsilon)}{B - (B - A)\exp(m\varepsilon)} = \frac{mB - m(B - A)\exp(m\varepsilon) - mB}{B - (B - A)\exp(m\varepsilon)} \\ &= m \left[1 - \frac{B}{B - (B - A)\exp(m\varepsilon)} \right] = m \left[1 - \frac{1}{1 - (1 - \frac{A}{B})\exp(m\varepsilon)} \right] \quad (\text{Eq 5-5}) \end{aligned}$$

Expressing the right hand side of Equation (5-5) by a new parameter, p , one obtains

$$\frac{1}{\sigma} \frac{d\sigma}{d\varepsilon} = p, \text{ or, } m \left[1 - \frac{1}{1 - \left(1 - \frac{A}{B}\right) \exp(m\varepsilon)} \right] = p. \text{ One can express the strain at instability}$$

as:

$$\varepsilon = \frac{1}{m} \log \left(\frac{\frac{p}{p-m}}{1 - \frac{A}{B}} \right). \quad (\text{Eq 5-6})$$

$$\text{For diffuse necking, } \frac{1}{\sigma} \frac{d\sigma}{d\varepsilon} = 1, (p=1), \text{ or, } \varepsilon = \frac{1}{m} \log \left(\frac{\frac{p}{p-m}}{1 - \frac{A}{B}} \right) = \frac{1}{m} \log \left(\frac{1}{1 - \frac{A}{B}} \right)$$

(Eq 5-7)

$$\text{For localized necking, } \frac{1}{\sigma} \frac{d\sigma}{d\varepsilon} = \frac{1}{2}, (p = \frac{1}{2}), \text{ or, } \varepsilon = \frac{1}{m} \log \left(\frac{\frac{p}{p-m}}{1 - \frac{A}{B}} \right) = \frac{1}{m} \log \left(\frac{1}{1 - \frac{A}{B}} \right)$$

(Eq 5-8)

As evident from Equation (5-8), the strain at instability is influenced by the parameters A , B and m . A sensitivity check for each of the Voce law parameters was carried out. The influence of A on the hardening behaviour is that as A increases the curve in $\frac{1}{\sigma} \frac{d\sigma}{d\varepsilon}$ plot decreases monotonically (Figure 5-7) and the strains at diffuse necking ε_D and localized necking ε_L decrease accordingly.

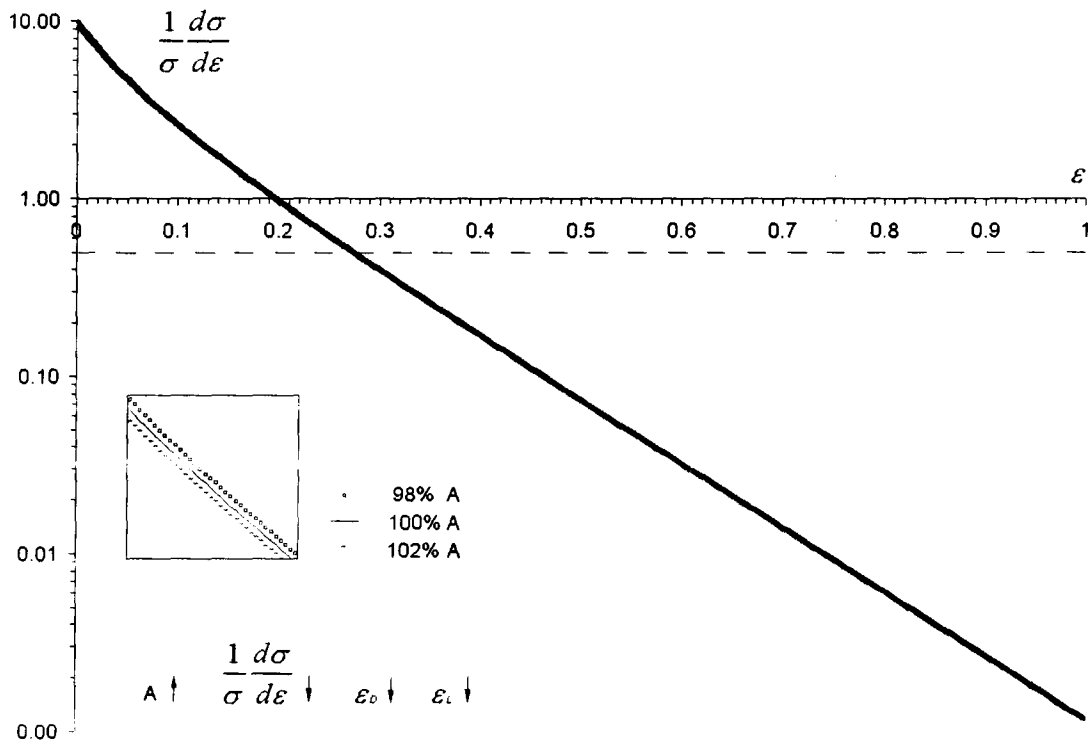


FIGURE 5-7. Influence of Voce law parameter A on the hardening behaviour shown in $\frac{1}{\sigma} \frac{d\sigma}{d\varepsilon}$ versus ε curve (horizontal dashed line indicating localized necking).

The influence of B on the hardening behaviour is that as B increases the curve in Considère plot increases monotonically and the strains at diffuse necking ε_D and localized necking ε_L increase correspondingly (Figure 5-8).

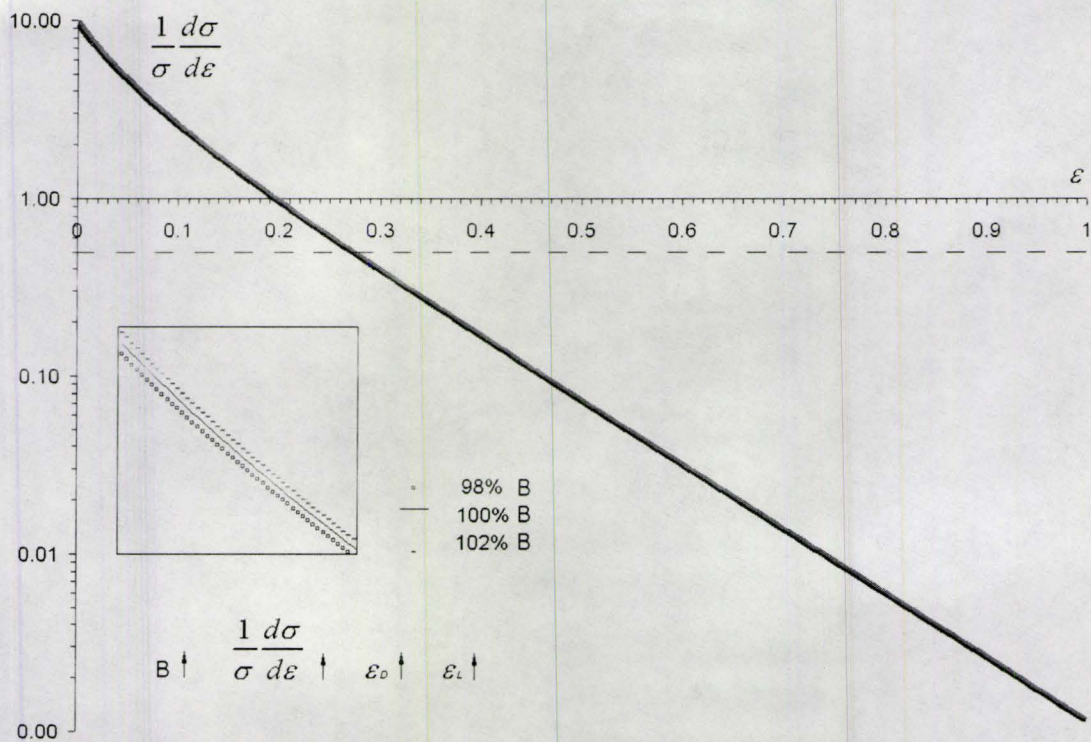


FIGURE 5-8. Influence of Voce law parameter B on the hardening behaviour shown in $\frac{1}{\sigma} \frac{d\sigma}{d\varepsilon}$ versus ε curve (horizontal dashed line indicating localized necking).

The influence of m to the hardening behaviour is no longer monotonic, as shown in Figure 5-9. At small strains ($\varepsilon < 0.10$), the increase of m makes the Considère curves rise, whereas at strains greater than 0.10, the increase of m makes the Considère curves drop. Accordingly, the strains at instability decrease. However, the change in the magnitude is not significant.

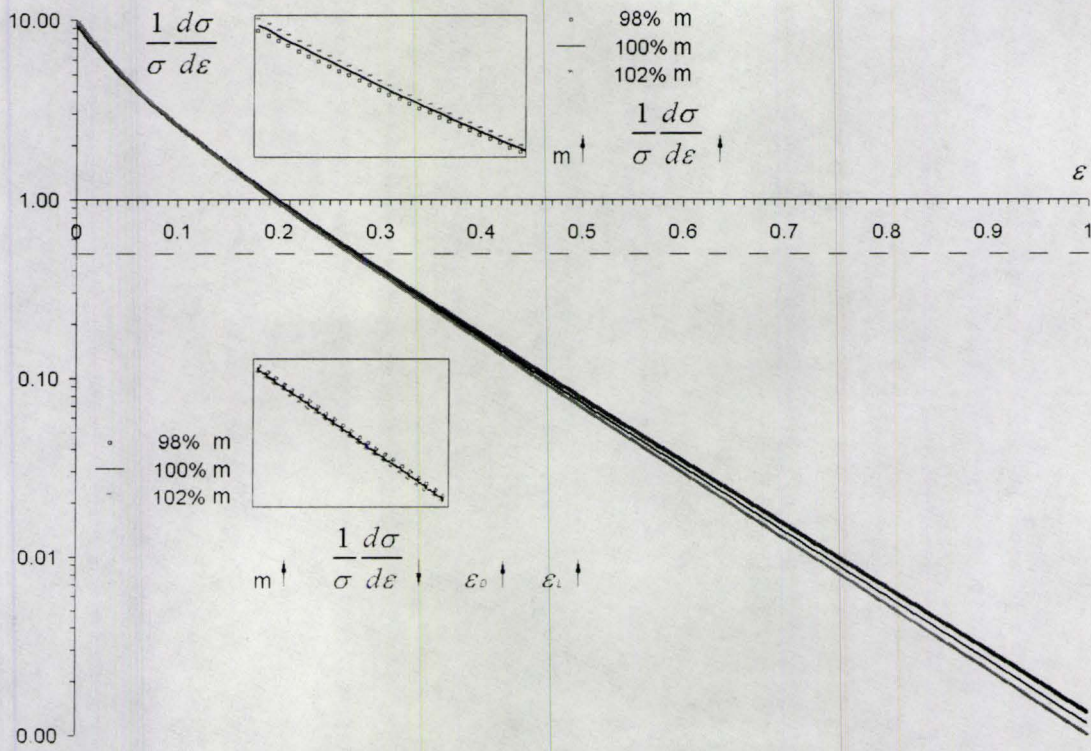


FIGURE 5-9. Influence of Voce law parameter m on the hardening behaviour shown in $\frac{1}{\sigma \frac{d\sigma}{d\epsilon}}$ versus ϵ curve (horizontal dashed line indicating localized necking).

A summary of the influence of various parameters of both power law and Voce law is given in Table 5-3. The arrows pointing upwards and downwards indicate an increase or decrease in the values of the parameters shown in the table.

TABLE 5-3. Influence of power law and Voce law parameters on the hardening behaviour in Considère curve.

Power Law	Variable	Considère $\frac{1}{\sigma} \frac{d\sigma}{d\varepsilon}$, or $\frac{n}{\varepsilon}$	Strain at Diffuse $\frac{1}{\sigma} \frac{d\sigma}{d\varepsilon} = 1$, or $\varepsilon_D = n$	Strain at Localization $\frac{1}{\sigma} \frac{d\sigma}{d\varepsilon} = \frac{1}{2}$, or $\varepsilon_L = 2n$
	K	---	---	---
	$n \uparrow$	$\frac{1}{\sigma} \frac{d\sigma}{d\varepsilon} \uparrow$	$\varepsilon_D \uparrow$	$\varepsilon_L \uparrow$
Voce Law	Variable	Considère $\frac{1}{\sigma} \frac{d\sigma}{d\varepsilon}$, or $m \left[1 - \frac{1}{1 - (1 - \frac{A}{B}) \exp(m\varepsilon)} \right]$	Strain at Diffuse $\frac{1}{\sigma} \frac{d\sigma}{d\varepsilon} = 1$, or $\varepsilon_D = \frac{1}{m} \log \left(\frac{1}{1 - \frac{A}{B}} \right)$	Strain at Localization $\frac{1}{\sigma} \frac{d\sigma}{d\varepsilon} = \frac{1}{2}$, or $\varepsilon_L = \frac{1}{m} \log \left(\frac{1}{1 - \frac{A}{B}} \right)$
	$A \uparrow$	$\frac{1}{\sigma} \frac{d\sigma}{d\varepsilon} \downarrow$	$\varepsilon_D \downarrow$	$\varepsilon_L \downarrow$
	$B \uparrow$	$\frac{1}{\sigma} \frac{d\sigma}{d\varepsilon} \uparrow$	$\varepsilon_D \uparrow$	$\varepsilon_L \uparrow$
	$m \uparrow$	$\frac{1}{\sigma} \frac{d\sigma}{d\varepsilon}$ (varies)	$\varepsilon_D \uparrow$	$\varepsilon_L \uparrow$

Although the parameters of power law and Voce have been investigated, the sensitivity does not necessarily influence the stress-strain relationship and further the instability significantly, but the “type” of hardening law does.

From the preliminary FE simulation of the material input with the power law and the Voce law, the task for optimization was to link the two laws, since the power law worked well for the large strain and the Voce law worked well for the small strain regime.

Therefore, a hybrid of the two hardening laws was considered. As a first step, a linear relationship was utilized to combine the two laws for the extrapolation.

A hybrid law (1) was proposed as $\sigma_{H1} = \varepsilon\sigma_p + (1 - \varepsilon)\sigma_v$, where ε is the strain, a unit weight function in range of $0 \leq \varepsilon \leq 1$. Since the Voce law works fine in the initial part, more weight is given to Voce law in the beginning. At large strains, however, more weight is given to the power law since it worked fine in the final stage. Hybrid law (2) was proposed as $\sigma_{H2} = (\sigma_p + \sigma_v)/2$. This can be regarded as a special case of an “equal” weight function. The four curves of stress-strain relationship are plotted in the Figure 5-10.

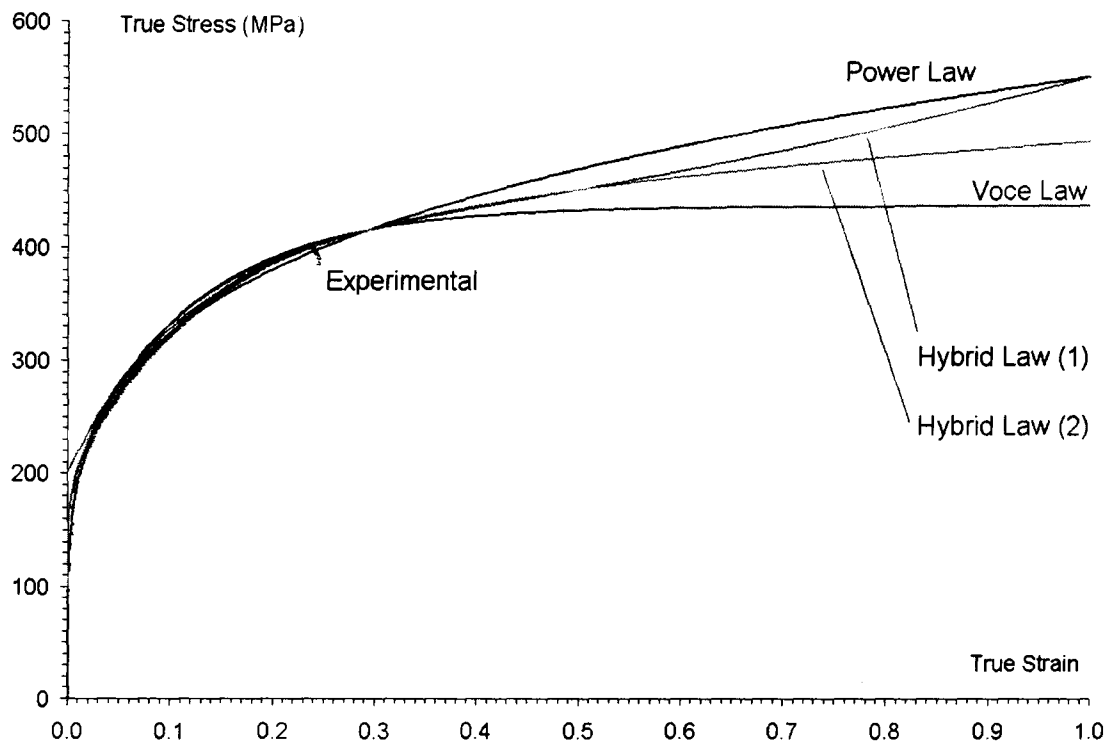


FIGURE 5-10. Stress-strain curves for different hardening laws (power, Voce, hybrid 1 & 2, AA6111-T4, 1 mm thickness).

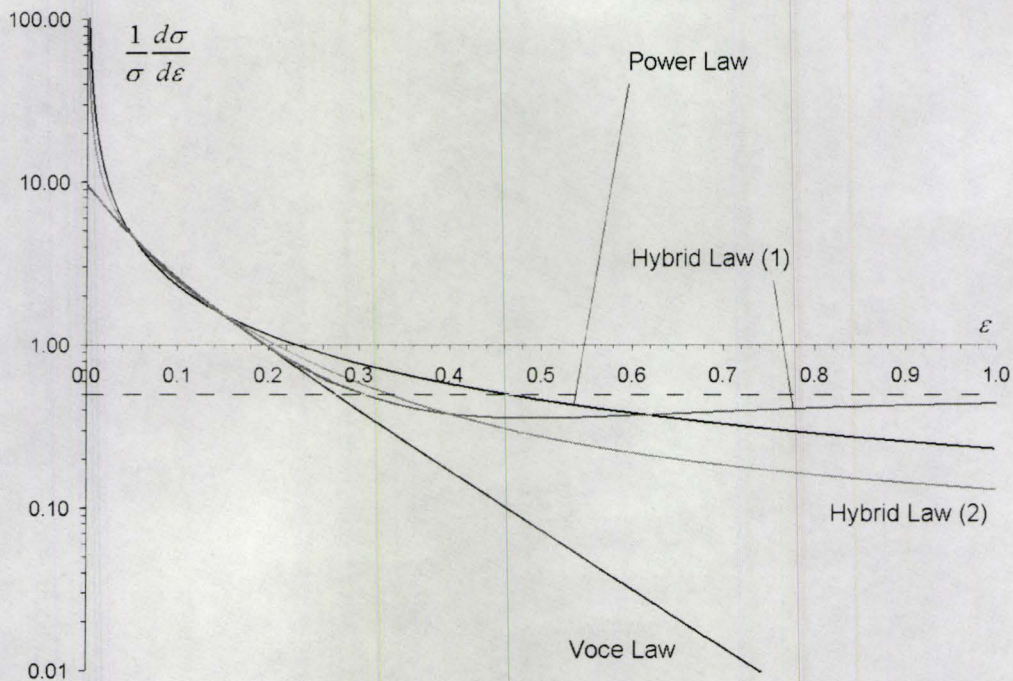


FIGURE 5-11. Hardening behaviour as per Considère criterion of four laws (power, Voce, hybrid (1) and (2), horizontally dashed line indicating localized necking, AA6111-T4, 1 mm thickness).

On applying Considère criterion to all the four laws discussed earlier resulted in a plot shown in Figure 5-11.

If the material behaviour in the real situation functions similar to the Voce law initially and approaches to power law at large strains, it should appear as a curve between the curves of power law and Voce law. However, the hybrid law (1) seems to saturates much too earlier. Also, it diverges from the power law curve. Therefore, the hybrid law (1) does not seem to produce a good fit, at least for the large strains, although it agrees with the Voce law in the initial part very well. The hybrid law (2) approaches the power law at large strain, but the initial part is far from the Voce law curve.

Further interpolation was carried out between the hybrid law (1) and (2). Weight functions were used to interpolate the two hybrid laws. Observation of Considère plot of power law, Voce law and hybrid laws (1) and (2) showed that the curves of four laws intersect at strain around ($0 < \varepsilon < 0.20$). In order to have a continuous weight function, a break point for a bi-linear function of the hybrid law (3) is used. Before this point, the weight function evolves along hybrid law (1). However, after this point the weight function develops linearly to the average of law (1) and (2) at $\varepsilon = 1$, namely 0.75 for contribution of power law and 0.25 for Voce law.

To simplify the numerical process for break point, the power law and Voce law were chosen since Considère expressions ($\frac{1}{\sigma} \frac{d\sigma}{d\varepsilon}$) have been obtained for the two laws as

shown below.

$$\left(\frac{1}{\sigma} \frac{d\sigma}{d\varepsilon} \right)_p = \frac{n}{\varepsilon} \quad (\text{Eq 5-9})$$

$$\left(\frac{1}{\sigma} \frac{d\sigma}{d\varepsilon} \right)_v = m \left[1 - \frac{1}{1 - \left(1 - \frac{A}{B}\right) \exp(m\varepsilon)} \right] \quad (\text{Eq 5-10})$$

By equating the two Considère expressions (Eq 5-9) and (Eq 5-10), i.e.

$$\left(\frac{1}{\sigma} \frac{d\sigma}{d\varepsilon} \right)_p = \left(\frac{1}{\sigma} \frac{d\sigma}{d\varepsilon} \right)_v, \text{ one obtains}$$

$$m \left[1 - \frac{1}{1 - \left(1 - \frac{A}{B}\right) \exp(m\varepsilon)} \right] = \frac{n}{\varepsilon} \quad (\text{Eq 5-11})$$

Numerical solution produces two results for intersection at $\epsilon_{S1} = 0.050$ and $\epsilon_{S2} = 0.150$. The first one was neglected due to too small a value of strain.

Therefore, the weight function of the third proposed law starts along the hybrid law (1) when the value of strain is small ($\epsilon < \epsilon_{S2}, 0.15$) evolves linearly and lies between the hybrid law (1) and (2) as shown in Figures 5-12 and 5-13.

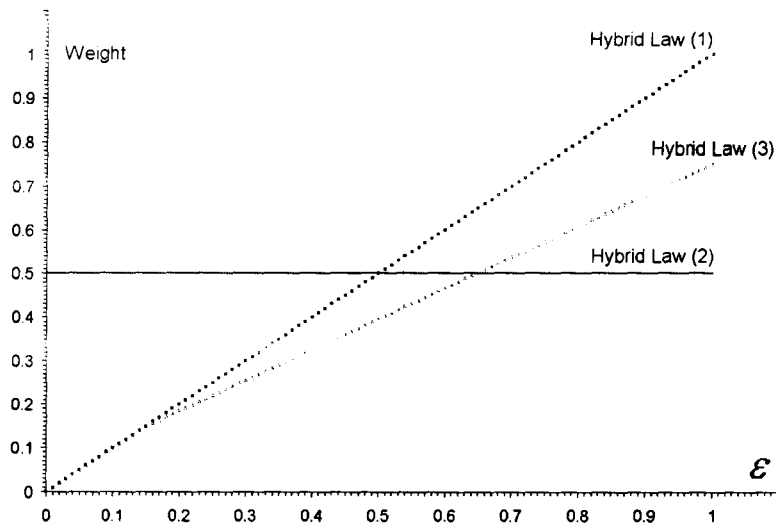


FIGURE 5-12. Weight functions for power law part of hybrid laws (1), (2) and (3).

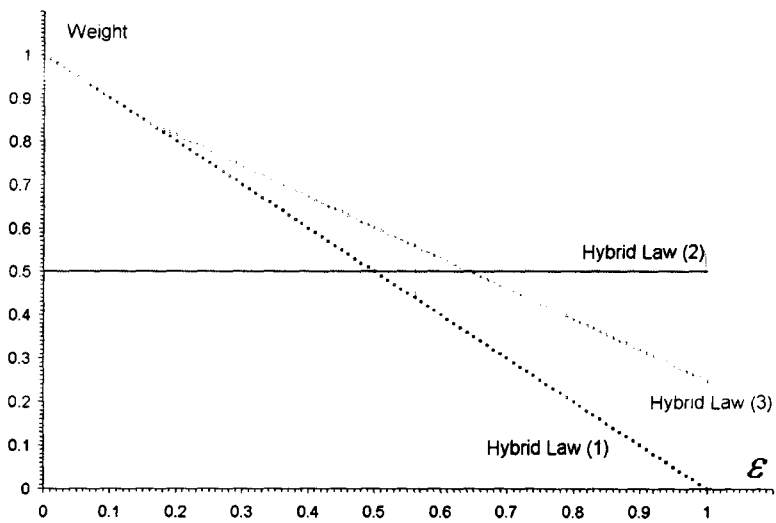


FIGURE 5-13. Weight functions for Voce law part of hybrid laws (1), (2) and (3).

Weight functions for the three proposed hybrid laws are shown in Table 5-4:

TABLE 5-4. Weight functions for proposed hybrid laws.

Law		Weight function	Condition
Hybrid law (1)	Power law	ϵ	$0 \leq \epsilon \leq 1$
	Voce law	$1 - \epsilon$	$0 \leq \epsilon \leq 1$
Hybrid law (2)	Power law	0.5	$0 \leq \epsilon \leq 1$
	Voce law	0.5	$0 \leq \epsilon \leq 1$
Hybrid law (3)	Power law	ϵ	$0 \leq \epsilon \leq \epsilon_{S2}$
		$\frac{0.75 - \epsilon_{S2}}{1 - \epsilon_{S2}} (\epsilon - \epsilon_{S2}) + \epsilon_{S2}$ $= \frac{0.75 - \epsilon_{S2}}{1 - \epsilon_{S2}} \epsilon + \frac{0.25 \epsilon_{S2}}{1 - \epsilon_{S2}}$	$\epsilon_{S2} \leq \epsilon \leq 1$
	Voce law	$1 - \epsilon$	$0 \leq \epsilon \leq \epsilon_{S2}$
		$1 - \left[\frac{0.75 - \epsilon_{S2}}{1 - \epsilon_{S2}} (\epsilon - \epsilon_{S2}) + \epsilon_{S2} \right]$ $= -\frac{0.75 - \epsilon_{S2}}{1 - \epsilon_{S2}} \epsilon + \frac{1 - 1.25 \epsilon_{S2}}{1 - \epsilon_{S2}}$	$\epsilon_{S2} \leq \epsilon \leq 1$

Incorporating $\epsilon_{S2} = 0.150$ with the equations for hybrid law (3) in Table 5-4, the weight functions were obtained as:

for power law $0.706\epsilon + 0.044$ (Eq 5-12)

for Voce law $-0.706\epsilon + 0.956$ (Eq 5-13)

Therefore, the hybrid law (3) can be written as:

$$\sigma_{H3} = \varepsilon\sigma_p + (1 - \varepsilon)\sigma_v \quad \text{when } 0 \leq \varepsilon \leq 0.15$$

$$\sigma_{H3} = (0.706\varepsilon + 0.044)\sigma_p + (-0.706\varepsilon + 0.956)\sigma_v \quad \text{when } 0.15 \leq \varepsilon \leq 1$$

(Eq 5-14)

Equation (5-14) represents the simplest solution to interpolate between the power law and Voce law. The corresponding stress-strain relationship is plotted in Figure 5-14.

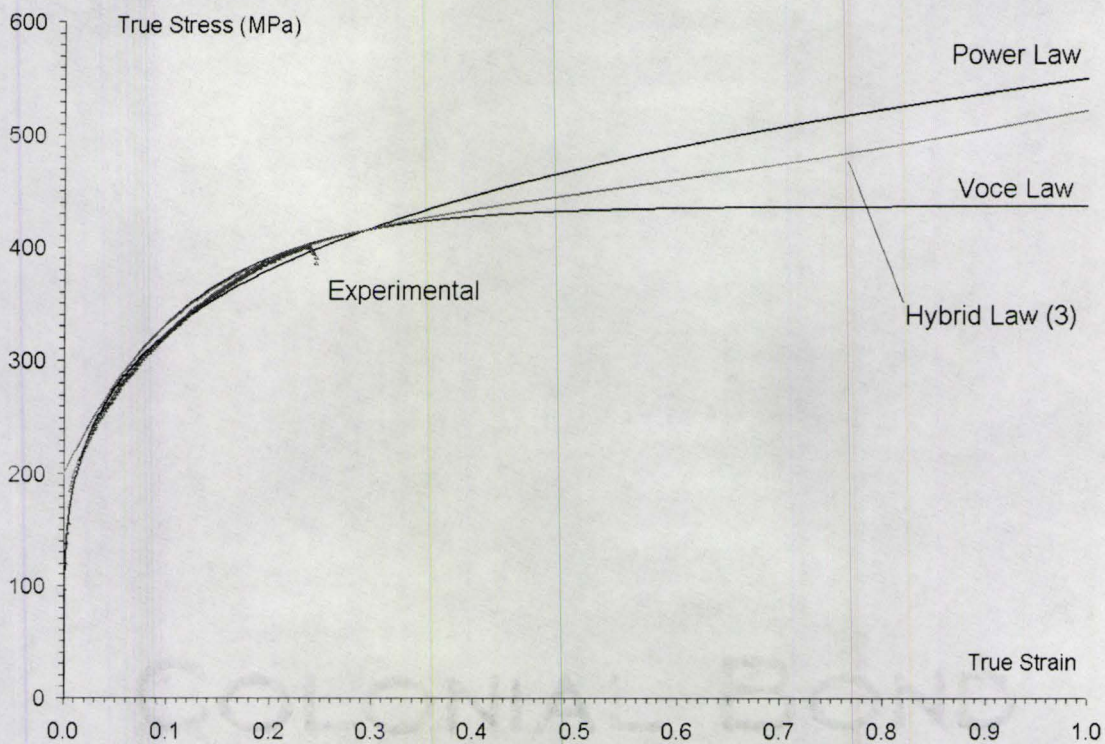


FIGURE 5-14. Stress-strain relationship of 1 mm thickness specimen of AA6111-T4 from uniaxial tensile test and fitted with power law, Voce law and hybrid law (3).

The various proposed hardening laws are once again plotted for AA6111-T4 in terms of Considère criterion in Figure 5-15. Experimental data showed that at fracture of AA6111-T4 sheet of 1 mm, the strain is around a value of 0.70. Examining the deviation

of the hardening curves in Considère plot at this strain, the hybrid law (3) produced smallest deviation with the power law curve.

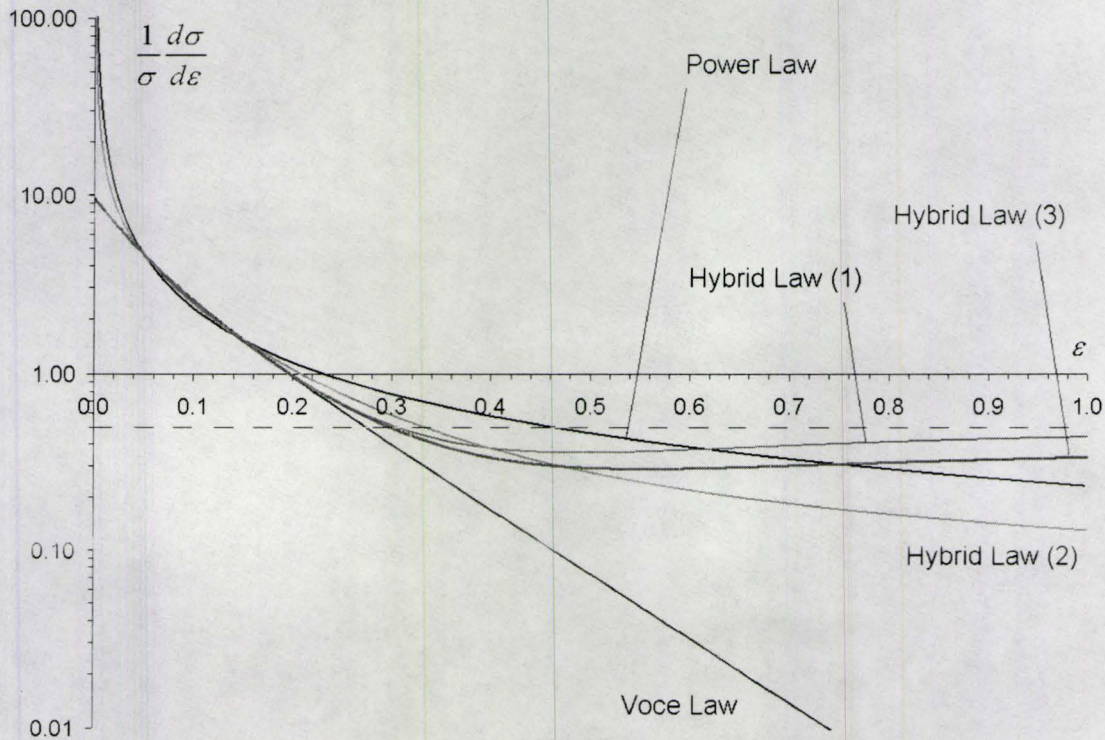


FIGURE 5-15. Hardening behaviour as per Considère criterion of various laws (power, Voce, hybrid (1), (2) and (3), horizontally dashed line indicating localized necking, AA6111-T4, 1 mm thickness).

Overall, an effective optimization process has been developed for material input to obtain a suitable extrapolation of the stress-strain curves. Based on the investigation of the two commonly used hardening laws, power law and Voce law, the influence of the sensitivity of the parameters on the magnitude of the stress-strain curve and instability values is relatively minor. However, the “type” hardening law is more important in the extrapolation.

5.2 Optimization Of μ Input For AA6111-T4

With the above stress-strain relationship, hybrid law (3), for biaxial loading at low friction ($\mu = 0$), friction functions were constructed for other typical paths such as direct punch-sheet contact ($\mu = 0.30 \sim 0.40$) and contact pressure through the Teflon film ($\mu = 0.10 \sim 0.15$). Similar to the methodology used in stress-strain determination, upper and lower bounds and a mean value of friction coefficients were employed for FE simulation with hybrid law (3) for material input. A variation in μ value of ± 0.10 was used to interpolate the friction function. The corresponding load-displacement traces were plotted together with the experimental data for error check.

Also, for tension-compression side of paths (i.e. left side of FLD), the material input is taken as Voce law and the contact condition is mainly direct contact as in the experiment. However, due to the specimen geometry variation, it is not full contact for these specimens. Therefore, the friction functions needed a reconsideration using a similar methodology to biaxial loading side for direct contact, e.g. to test the upper / lower bound and mean value of friction coefficient and then establish a weight function.

The main task of μ optimization is to establish a friction coefficient function in term of time, although the default FE code (ABAQUS explicit) generally treats the friction coefficient as constant through the entire simulation process. Also, the test process is at a constant speed, so there is a direct relationship between time and displacement. Therefore, from the load-displacement curve, the load and friction can be associated through displacement or time.

The optimization procedure is detailed below with the 0.5” width (uniaxial strain path) specimen. By varying the μ values, three load curves were obtained. The experimental curve was in the scatter band of assumed μ input, although none of the three inputs could produce a load curve with overall good agreement over the entire load-displacement regime. Curve with low friction matched the initial part well whereas the medium friction curve fitted well in the middle and the high friction curve approached to the experimental curve in the end (Figure 5-16). It was assumed that the real process is subject to a friction change from low to high. Accordingly, several sections were created for applying discrete values of friction coefficient in the simulations (Figure 5-17). The procedural details for implementation into ABAQUS are given in Appendix 5.

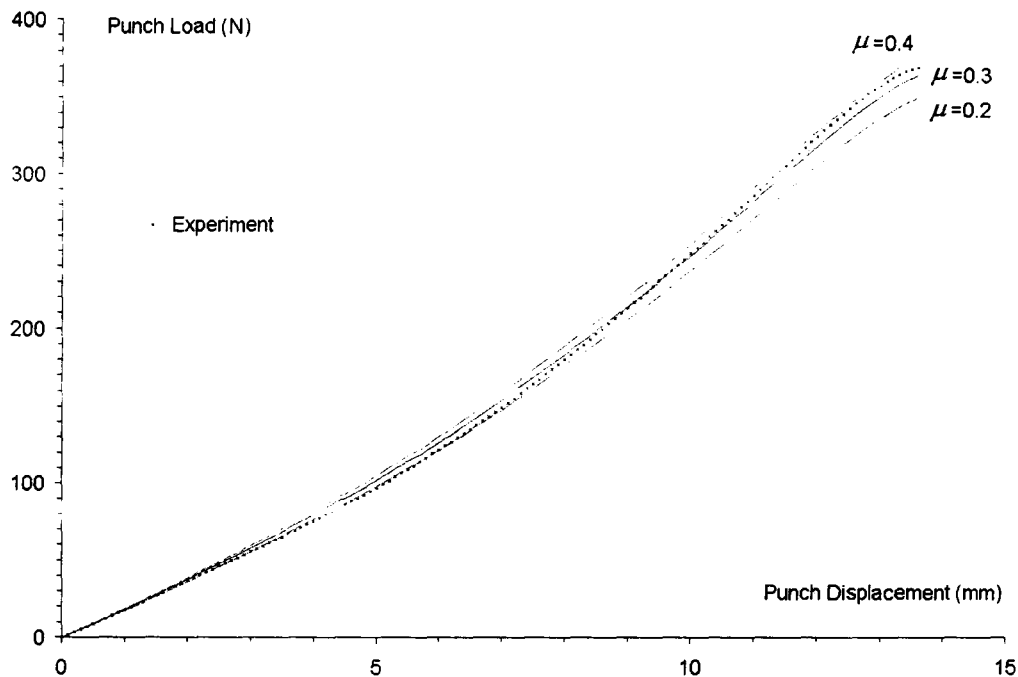


FIGURE 5-16. FE results of load curves with different constant friction inputs (AA6111-T4, 0.5” wide specimen, 1 mm thickness, 2” diameter punch).

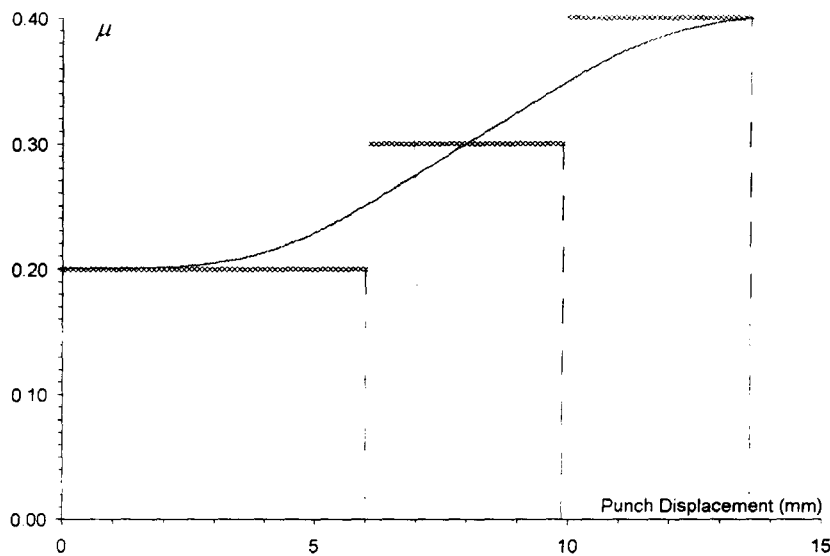


FIGURE 5-17. Friction input as a function of punch displacement (AA6111-T4, 0.5” wide specimen, 1 mm thickness).

In the implementation of the friction function in FE (ABAQUS/Explicit), several interaction properties were defined (in the example below, three are given). In each definition, the frictional coefficient was taken to be constant as shown below.

```

** INTERACTION PROPERTIES
*Surface Interaction, name=Lubrication_01
*Friction
0.2,
*Surface Interaction, name=Lubrication_02
*Friction
0.3,
*Surface Interaction, name=Lubrication_03
*Friction
0.4,
    
```

The process was then divided into three segments related to time or displacement since a constant speed was used. In a certain segment, one of the “interaction properties”

was applied. The first time segment was initialized with one interaction definition, say interaction 1 for duration of 60 steps as shown below.

```
*Step, name=Punch_01
Punch_01
*Dynamic, Explicit
, 60
** Interaction: P-SH
*Contact Pair, interaction=Lubrication_01,
mechanical constraint=KINEMATIC, cpset=P-SH_01
surfcent_01, Punch-1.RigidSurface_
```

As the process proceeds, the friction evolves to another coefficient value. In the next time segment, the contact property is deleted and replaced with the current coefficient, say interaction 2 for duration of 40 steps.

```
*Step, name=Punch_02
Punch_02
*Dynamic, Explicit
, 40
** Interaction: P-SH
*Contact Pair, op=DELETE, cpset=P-SH_01
Punch-1.RigidSurface_, surfcent_01
*Contact Pair, interaction=Lubrication_02,
mechanical constraint=KINEMATIC, cpset=P-SH_02
Punch-1.RigidSurface_, surfcent_01
```

A similar procedure was implemented for the next step. Therefore, the whole simulation process with one constant coefficient could be divided into segments with different coefficients that approach the realistic process.

Also, different weight functions were constructed for Teflon and direct contact conditions in biaxial paths, and for dry contact near-plane-strain paths.

5.3 Further Optimization Of $\sigma - \epsilon$ And μ Input For Other Materials

The optimization procedure described above for 1 mm AA6111-T4 sheet was extended to 2 mm sheet. Both sheet thicknesses were tested at two different strain rates. The data from the optimization work for these materials is presented in Appendix 6.

5.4 General Procedure For Optimization Of $\sigma - \epsilon$ And μ Input

A general optimization procedure is summarized as follows:

- (1) Obtain experimental load curves of different geometries and different specimen lubrication conditions from hemispherical punch tests.
- (2) Obtain experimental uniaxial tensile properties of a given material in the rolling direction. Analyze the $\sigma - \epsilon$ relationship for a variation of $\pm 2\%$ in the parameter values.
- (3) Carry out FE simulations with trial values of upper bound, lower bound and mean values of fitted curve of power law and Voce law, for a balanced biaxial strain path, $\mu = 0$. Make error-check after the three simulations.
- (4) Establish a weight function for the determination of a hybrid law of $\sigma - \epsilon$ relationship. Simulate with FE and make error-check to compare the FE result based on hybrid law with experimental load-displacement curves. Apply the proposed localized necking criterion to obtain limit strain for balanced biaxial.

- (5) For a different path of biaxial tension and $\mu \neq 0$, apply the determined hybrid law using varied μ with upper and lower bounds and mean value (± 0.10 variation).
- (6) Based on the error-check from (5) for the three FE simulations to determine the friction function of μ , create a tabular function of μ in term of time as an input of FE modelling for contact definition. Use localized necking criterion for the given strain path.
- (7) Repeat (5) - (6) for any other strain path of biaxial tension of interest.
- (8) Use the uniaxial tensile raw data for the simulation of uniaxial tensile path and make the error-check. Similar to (5) - (6), determine if weight function is necessary.
- (9) Repeat (8) for plane strain path or other strain paths.

In summary, although the sensitivity of parameters from power law and Voce law was extensively investigated, the sensitivity of the parameters does not affect the extrapolation significantly. However, the type of hardening law chosen for extrapolation has a strong bearing on the quality of fit between the experimental and model load-displacement curves.

In the construction of weight functions, priority was given to linear weight function for interpolation. The quality of proposed hardening law was examined with Considère criterion. The proposed hardening laws (material input) and friction functions were employed in FE simulations for AA6111-T4 test specimens at 1 mm and 2 mm sheet thickness and different test speeds.

Chapter 6

Results

This chapter presents the predicted and experimentally obtained FLDs for AA6111-T4 and AA6181-T4 aluminum alloys and DP600 dual phase steel sheet. The predictions are based on (i) proposed localized necking criterion presented earlier in Chapter 3, (ii) experimental-numerical methodology presented in Chapter 4, and (iii) an optimization procedure for FE simulation input data presented in Chapter 5. The results are arranged as follows: material properties from uniaxial tensile test (AA6111-T4 of 1 mm and 2 mm thickness), experimentally obtained and FE results of load-displacement traces, FE predicted FLDs and comparison with ARAMIS/ARGUS results, and examinations of additional strain paths and strain rate and sheet thickness on proposed necking criterion and FLD.

6.1 Material Properties From Uniaxial Tensile Tests

The stress-strain relationship obtained from uniaxial tensile tests for AA6111-T4 of 1 mm and 2 mm thickness are plotted in Figure 6-1. Material properties such as yield strength, ultimate tensile strength, elongation, material parameters for power law and Voce law are presented in Table 6-1. Each stress-strain curve and examination with Considère criterion are presented in Appendix 7.

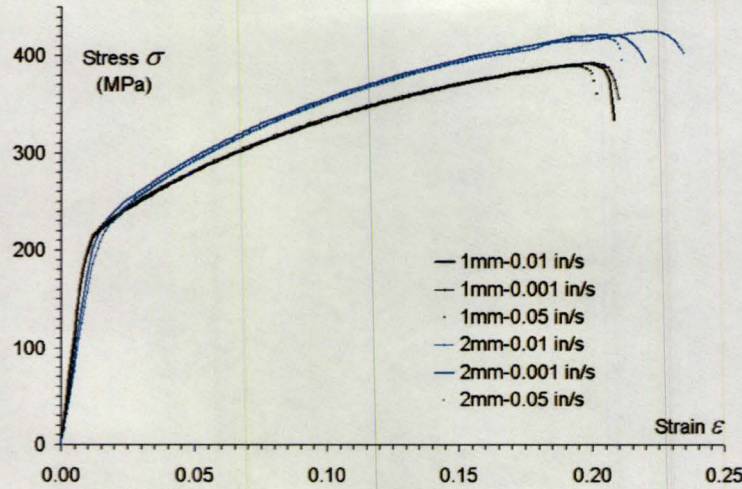


FIGURE 6-1. True stress – true strain relationship of AA6111-T4 sheets in 1 mm and 2 mm thickness at different test speeds.

TABLE 6-1. Uniaxial tensile material parameters in the longitudinal direction (with respect to rolling) for AA6111-T4 at different sheet thickness and test speeds.

Tests	Yield Stress (MPa)	Ultimate Strength (MPa)	Elongatio n	Power law		Voce law		
				K (MPa)	n	A (MPa)	B (MPa)	m
1mm, 0.25 mm/s	148.00	381.00	0.200	550	0.215	200.00	435.00	-8.20
1mm, 0.025 mm/s	148.00	380.00	0.203	555	0.220	200.00	435.00	-8.30
1mm, 1.25 mm/s	147.00	379.00	0.198	555	0.214	200.00	440.00	-8.20
2mm, 0.25 mm/s	157.00	426.00	0.227	620	0.240	190.00	460.00	-9.20
2mm, 0.025 mm/s	158.00	421.00	0.210	605	0.230	187.00	460.00	-10.00
2mm, 1.25 mm/s	154.00	420.00	0.206	620	0.220	190.00	460.00	-9.50

These data were further utilized in the optimization work for material input in FE simulations as discussed earlier in Chapter 5.

6.2 Characteristics Of Load Curve From Experiments

Experimental punch load versus displacement curves were processed using running average method in MATLAB, with which the noise in the data was smoothed (refer to Appendix 2). Smoothed experimental load traces from AA6111-T4 specimens with various geometries indicating inflection (diffuse necking, based on a maximum in the load rate) are shown in Figure 6-2.

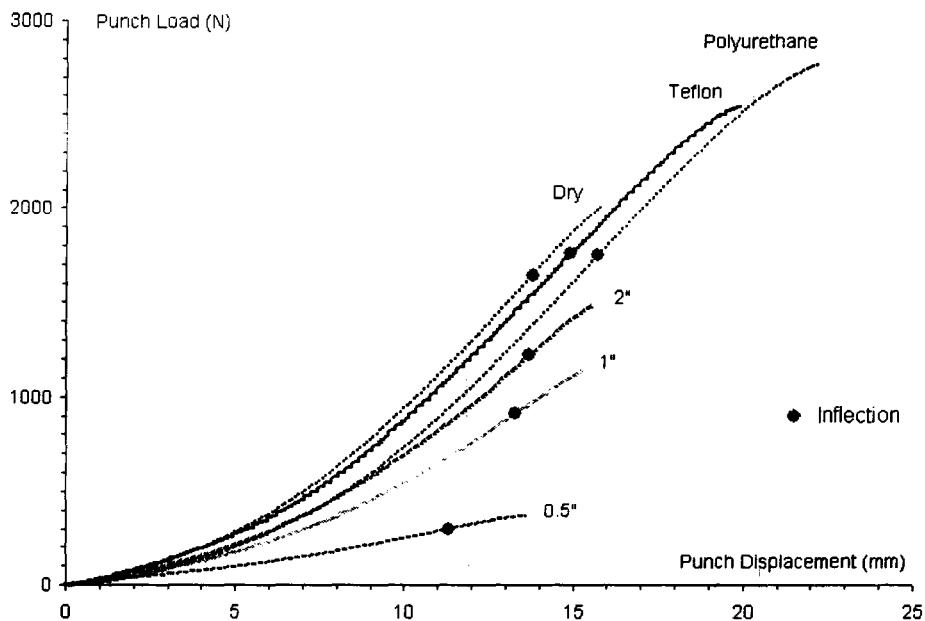


FIGURE 6-2. Experimental punch load versus displacement curves from hemispherical punch tests. Solid circles indicate inflection points (material: AA6111-T4, 1 mm thickness, 2" diameter punch).

The observation of load curves from experiments shows that as the specimen width increases, and consequently the strain path is changed from left side to the right side of FLD space, the dome height and the load amplitude increases up to the plane strain condition. For the right side of FLD space, the load drop and fracture occurs at a

later stage with a decrease in friction (or an increase in the strain ratio towards unity). Accordingly, the inflection points shift upwards as specimens get wider or as the friction is reduced.

Figure 6-3 presents the load rate (derivative of the load with displacement) versus punch displacement curves for the data presented in Figure 6-2. An observation of the load-rate curves shows that a characteristic point is exhibited by each specimen geometry. As discussed earlier in Chapter 4 and in Appendix 1, the peak represents the onset of diffuse instability. A rapid drop in the load rate after the peak is reached representing the development of localized necking. However, it was not possible to accurately determine the onset of localized necking from the shape of the load or load rate curves.

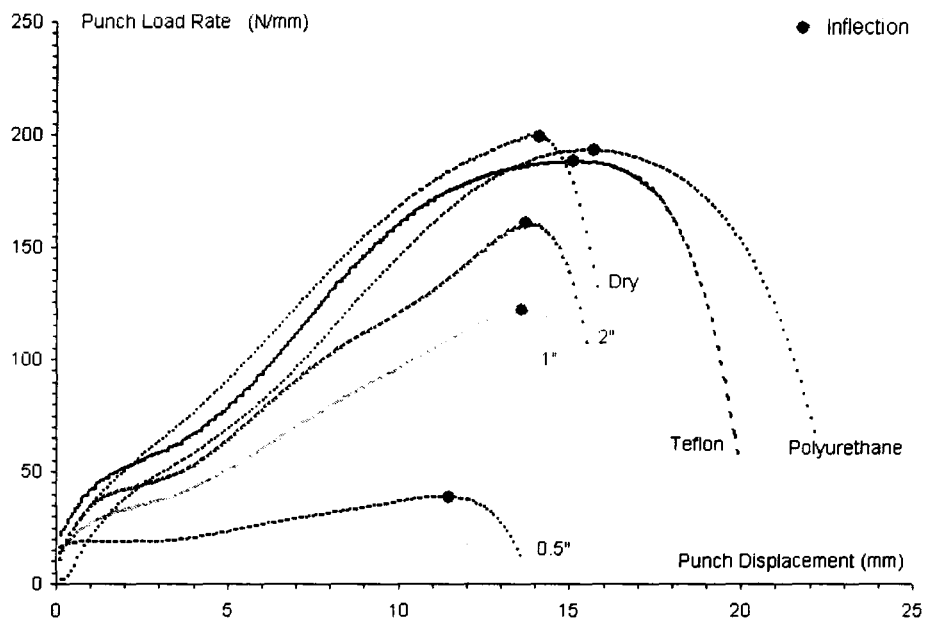


FIGURE 6-3. Inflection points in processed experimental load versus displacement curves, 1st order of derivative of load curve, or, the load rate dF/dh versus punch displacement for AA6111-T4, 1 mm thickness, 2” diameter.

The analysis of the load curves resulted in dome height corresponding to maximum load and the location of inflection point for each specimen geometry and lubrication condition. These values were utilized in the calibration of FE based load-displacement curves, as described earlier in Chapter 5.

6.3 FE Output Of Load Curves

Figures 6-4 to 6-6 show AA6111-T4 punch load versus displacement curves for 3 different strain paths from FE simulations. These simulations utilize optimized stress-strain curves (hybrid law 3) and friction data as described in Chapter 5. An error check was carried out to verify if the limit dome height, load magnitude and location of inflection point are in good agreement with the experimental data. A tolerance of 5% in the load and displacement values was considered adequate in the evaluation of the quality of fit between the experimental and model load-displacement curves. As shown, acceptable result within 5% tolerance has been achieved for each of the cases. This has provided a good basis for further analysis of the strain history to obtain the limit strains from the FE simulations.

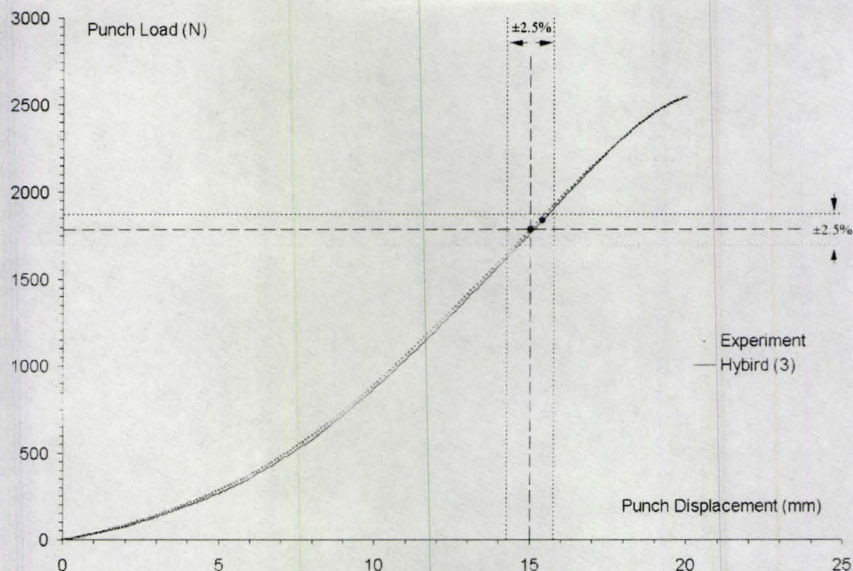


FIGURE 6-4. Comparison of FE and experimental load traces for AA6111-T4 (sheet thickness of 1 mm, 5'' wide specimen, polyurethane lubrication between the punch and sheet). Dashed lines showing scatter band of 5% tolerance. The inflection point lies within the regular region arising from the 5% tolerance bands.

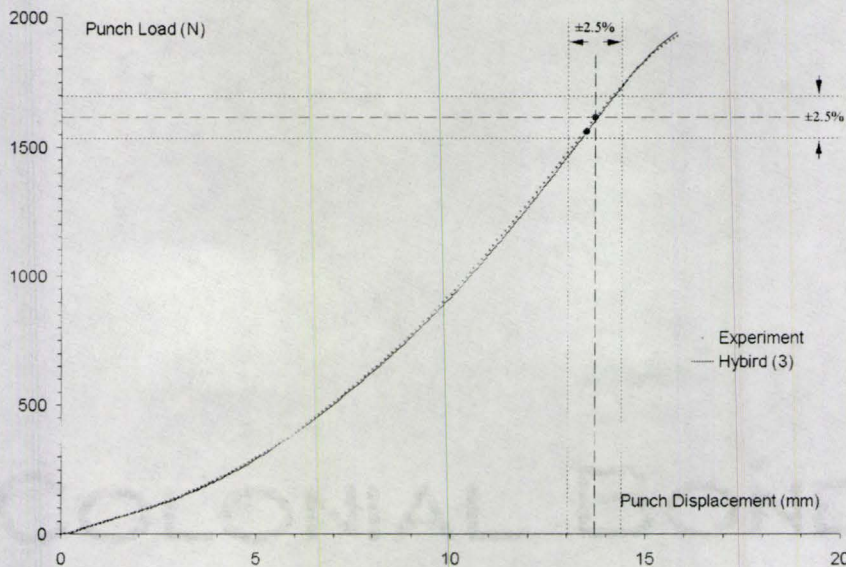


FIGURE 6-5. Comparison of FE and experimental load traces for AA6111-T4 (sheet thickness of 1 mm, 5'' wide specimen, direct dry contact). Dashed lines showing scatter band of 5% tolerance. The inflection point lies within the regular region arising from the 5% tolerance bands.

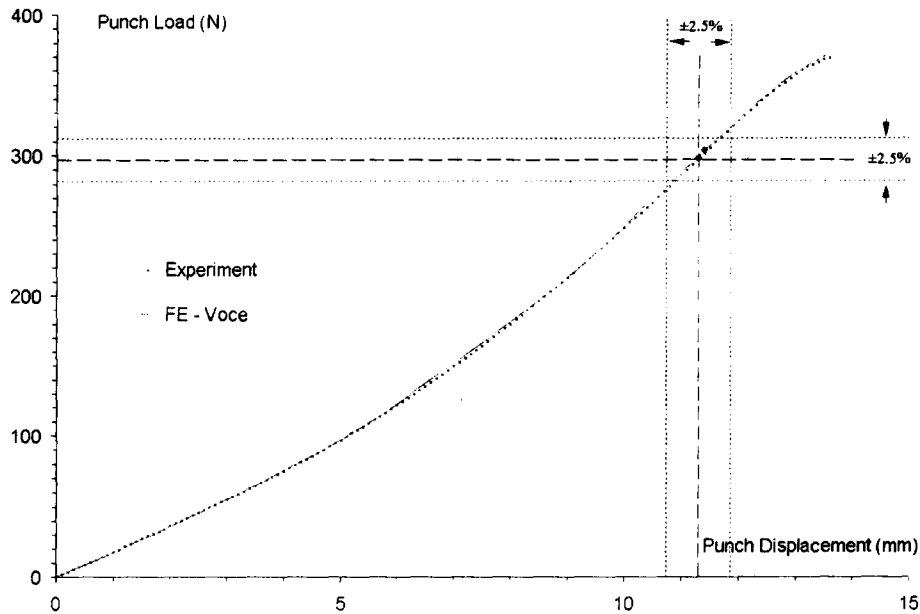
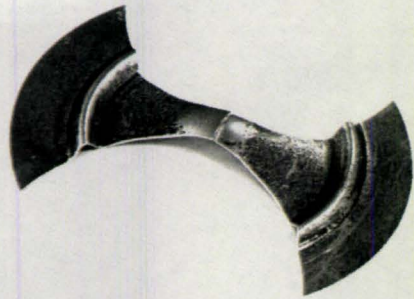


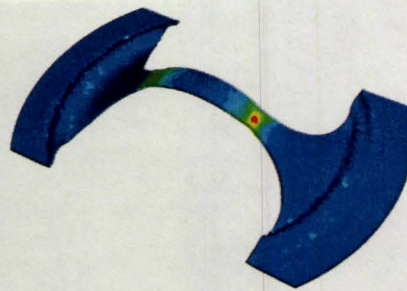
FIGURE 6-6. Comparison of FE and experimental load traces for AA6111-T4 (sheet thickness of 1 mm, 0.5" wide specimen, direct dry contact). Dashed lines showing scatter band of 5% tolerance. The inflection point lies within the regular region arising from the 5% tolerance bands.

6.4 Using FE Results Of Strain History To Obtain FLD

Deformed specimens from the FE simulations are shown in Figure 6-7. The strain contours reveal that the localized necking was captured in the FE models. The limit strains were obtained by processing the strain histories as described earlier in Chapter 3 (Section 3.1).



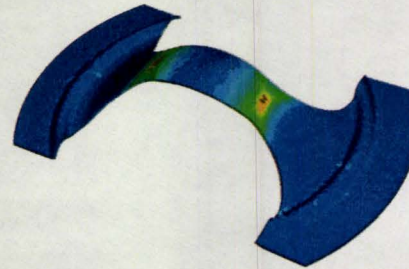
a. 0.5" wide specimen (Experimental)



b. 0.5" wide specimen (FE)



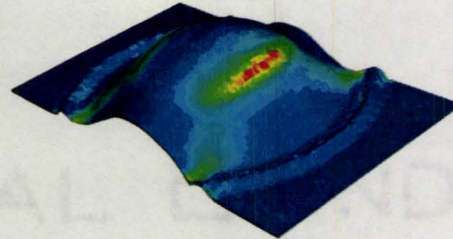
c. 1" wide specimen (Experimental)



d. 1" wide specimen (FE)



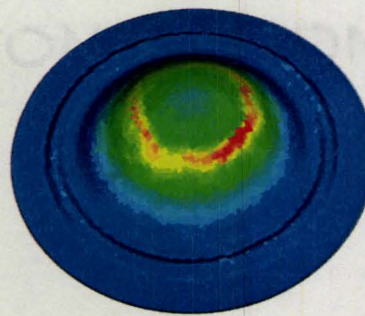
e. 2" wide specimen (Experimental)



f. 2" wide specimen (FE)



g. 5" wide specimen (Experimental, dry).



h. 5" wide specimen (FE, dry).

FIGURE 6-7. Typical deformed specimen shapes (a, c, e, g) and corresponding FE results (b, d, f, h) showing localized necking (AA6111-T4, 1 mm thickness, 2" diameter punch).

The strain histories of principal strains of all elements in a selected band from the pole to the edge of the deformed dome specimen containing the localized zone was extracted from the FE output, specifically the element inside the neck where damage occurred was identified and its strain history was tracked. The derivatives of major and minor strains in terms of time were then obtained resulting in spatial and temporal strain rate and “strain acceleration” data (magnitude only). The onset of localized necking was defined as the inflection point in the major strain rate curve or a maximum in the major strain acceleration, as discussed earlier.

These plots show a common characteristic that the curves of major strain rate $\dot{\epsilon}$, for the draw side (0.5” wide specimen, Figure 6-8) and stretch side (5” wide specimen, Figure 6-9) show an inflection point and reach the maximum at the end when fracture occurs. The corresponding strain accelerations attain maximum $(\ddot{\epsilon}_1)_{\max}$ values at the occurrence of localized necking and a near zero value at fracture ($\ddot{\epsilon}_1 \approx 0$).

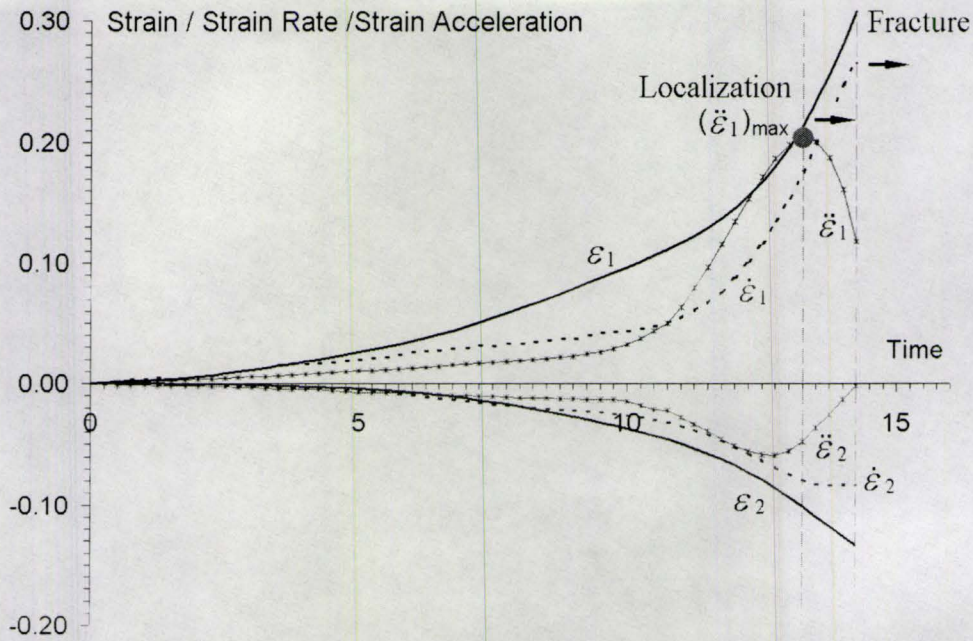


FIGURE 6-8. Histories of major/minor strain, strain rate and strain acceleration of 0.5" wide specimen of AA6111-T4 (1 mm thickness, 2" diameter punch).

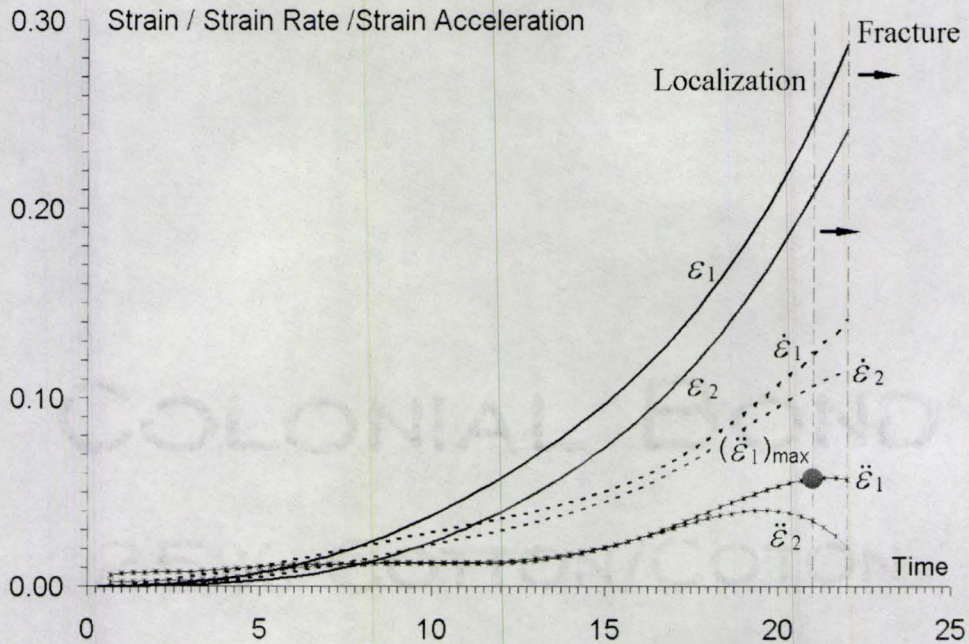


FIGURE 6-9. Histories of major/minor strain, strain rate and strain acceleration of 5" wide specimen (dry contact) of AA6111-T4 (1 mm thickness, 2" diameter punch).

The limit strains from various test simulations were assembled to construct the FLD of AA6111-T4 at 1 mm sheet thickness as shown in Figure 6-10.

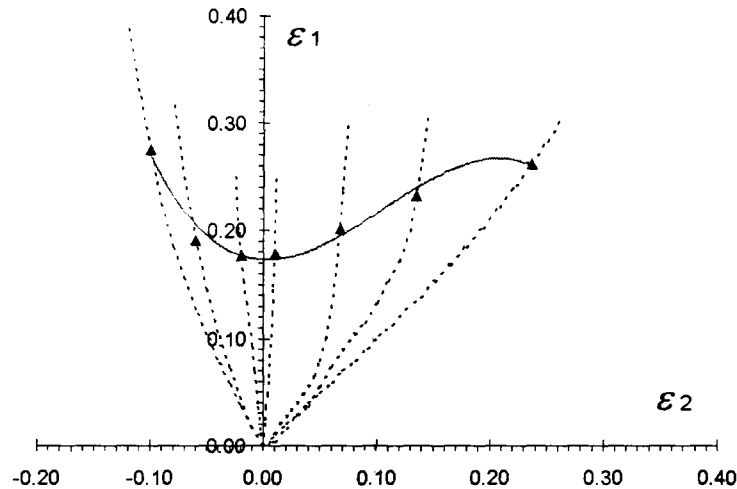


FIGURE 6-10. FE prediction of FLD for AA6111-T4 (1 mm thickness, 2" diameter punch).

The predicted FLDs based on the incorporated experimental load curves and FE simulations have been examined with ARAMIS / ARGUS strain imaging systems. The comparison is presented in the next section.

6.5 Experimental Data From ARAMIS / ARGUS Systems

The on-line strain imaging system ARAMIS provided the spatial and temporal strains similar to the FE analysis to obtain the limits strains for sheet materials of AA6111-T4 and AA6181-T4.

6.5.1 ARAMIS Results For AA6111-T4

ARAMIS strain imaging system provided temporal and spatial strain results for AA6111-T4 of 1 mm thickness as shown in Figures 6-11 to 6-16. In these figures, images for different strain paths corresponding to the onset of localized necking as per the proposed localization criterion, are presented.

The 0.5" wide specimen exhibits a strain path similar to uniaxial tensile loading. This is a far left strain path in the tension-compression region of FLD. A localized neck was observed although it was located away from the center of symmetry of the specimen (Figure 6-11).

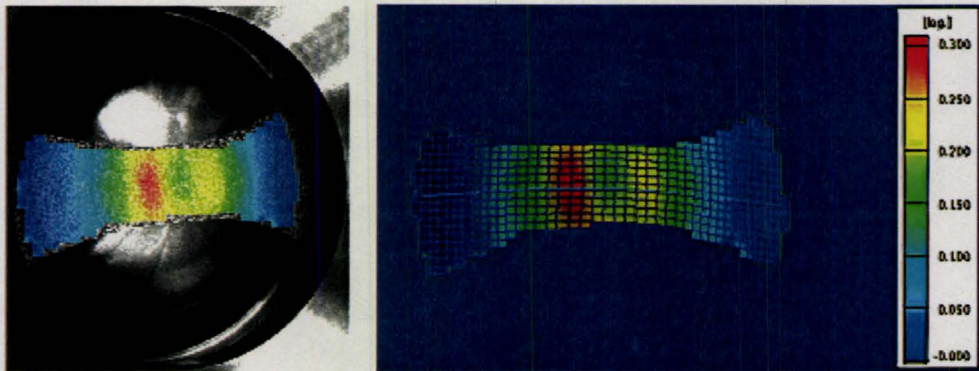


FIGURE 6-11. Typical test specimen with corresponding major strain map for AA6111-T4 over the specimen surface from ARAMIS strain measurement system (0.5" wide specimen).

By increasing the specimen width, as expected, the strain paths moved towards the plane strain path (Figure 6-12). Two symmetric areas of high strain values, equal distance from the pole, were observed. One of these areas, was identified as a localized region as per the proposed criterion.

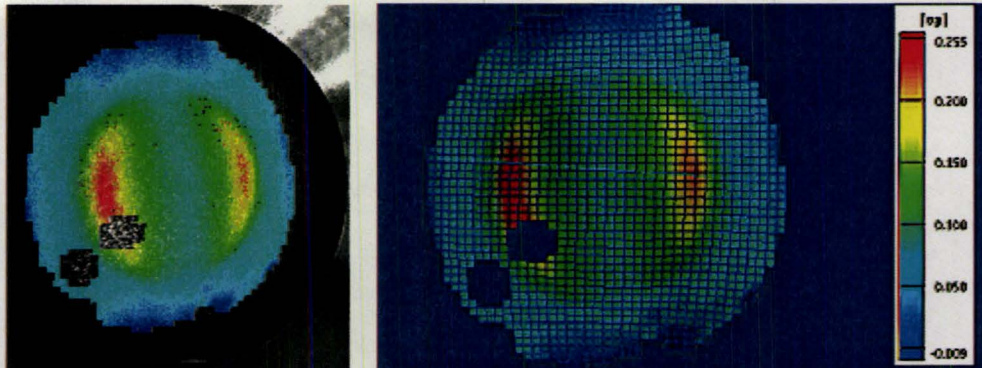


FIGURE 6-12. Typical test specimen with corresponding major strain map for AA6111-T4 over the specimen surface from ARAMIS strain measurement system (2'' wide specimen).

The result of a fully clamped specimen with dry contact condition is presented in Figure 6-13. An almost continuous ring pattern of high strain values was observed for these specimens.

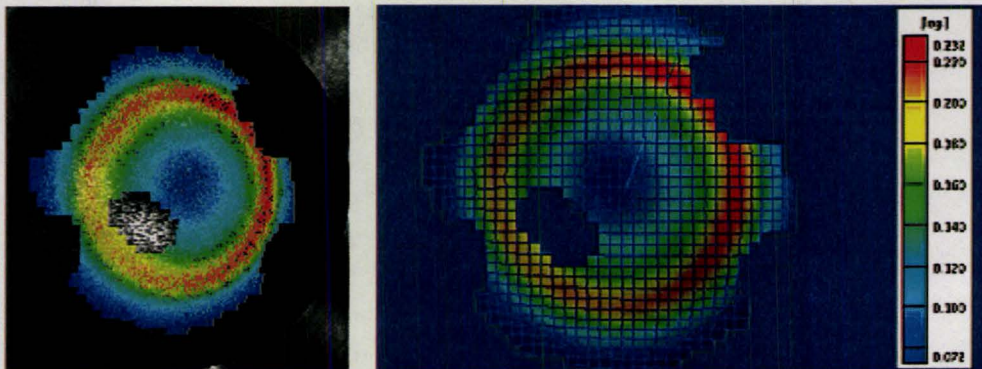


FIGURE 6-13. Typical test specimen with corresponding major strain map for AA6111-T4 over the specimen surface from ARAMIS strain measurement system (5'' wide specimen, direct dry contact between punch and sheet).

Figure 6-14 shows the result of a fully clamped specimen with a sand paper placed between punch and sheet interface. A strain path close to plane strain, but slightly on the tension-tension side, was obtained. Compared to dry contact, a lower dome height

was achieved due mainly to a higher friction condition at the punch-sheet interface. However, the major strain values were higher than those of plane strain case.

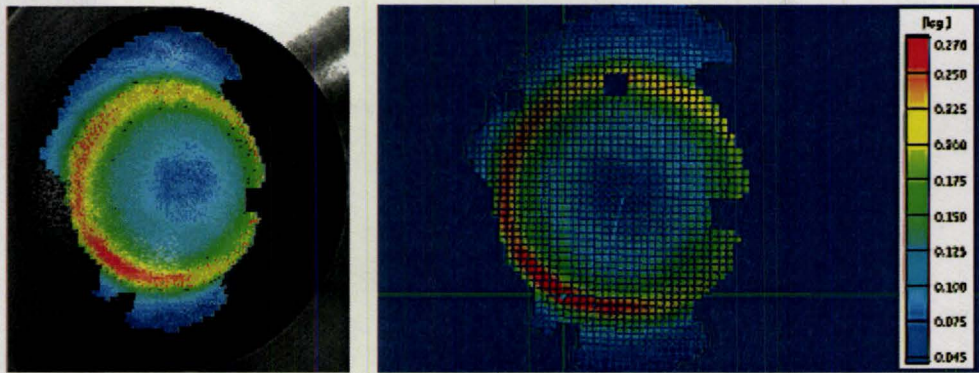


FIGURE 6-14. Typical test specimen with corresponding major strain map for AA6111-T4 over the specimen surface from ARAMIS strain measurement system (5'' wide specimen, sand paper interface between punch and sheet).

It is to be noted that there is close relation between the location of neck and the lubrication condition. As the friction reduces, such as the test condition with Teflon shown in Figure 6-15, the region showing high values of strain moves towards the pole.

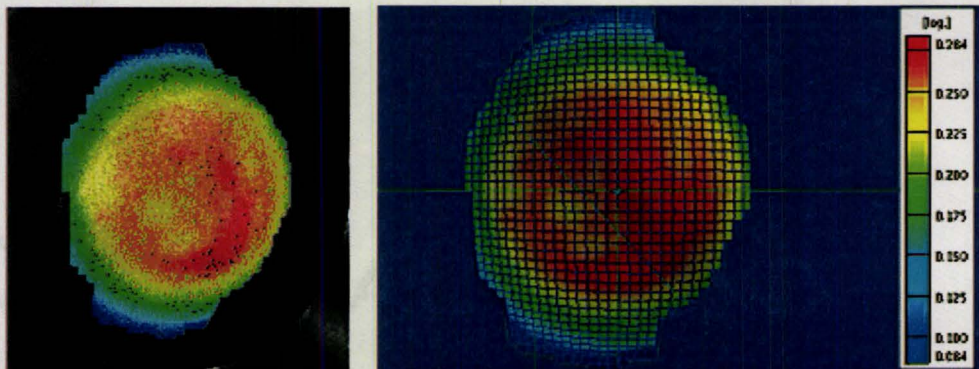


FIGURE 6-15. Typical test specimen with corresponding major strain map for AA6111-T4 over the specimen surface from ARAMIS strain measurement system (5'' wide specimen, Teflon film between punch and sheet).

For tests with a Polyurethane pad, the location of neck was found to be in the pole area of the specimen and this represents a balanced biaxial strain path as shown in Figure 6-16.

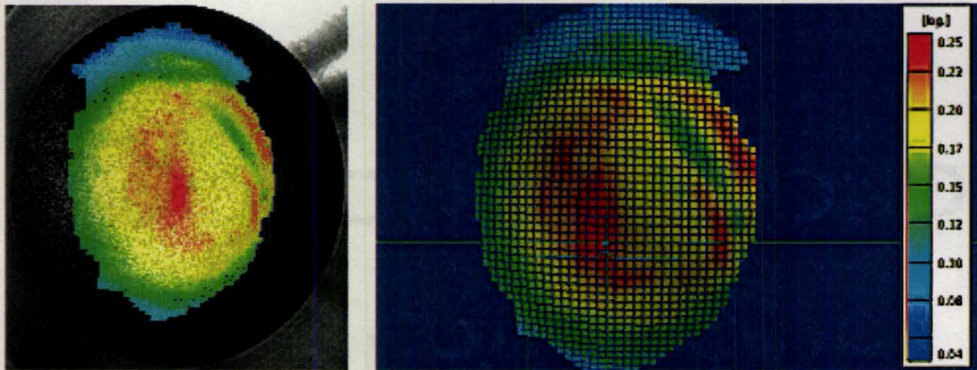


FIGURE 6-16. Typical test specimen with corresponding major strain map for AA6111-T4 over the specimen surface from ARAMIS strain measurement system (5" wide specimen, Polyurethane pad between punch and sheet).

Two of the strain paths corresponding to 2" and 5" wide specimen (dry contact) are presented to demonstrate the examination of proposed necking criterion of $(\ddot{\epsilon}_1)_{\max}$ with ARAMIS data (Figures 6-17 and 6-18). The results provide confirmation that the major strain acceleration, $(\ddot{\epsilon}_1)_{\max}$, exhibits a peak in the strain history approaching the end of deformation (fracture), which can be used as the onset of localized necking.

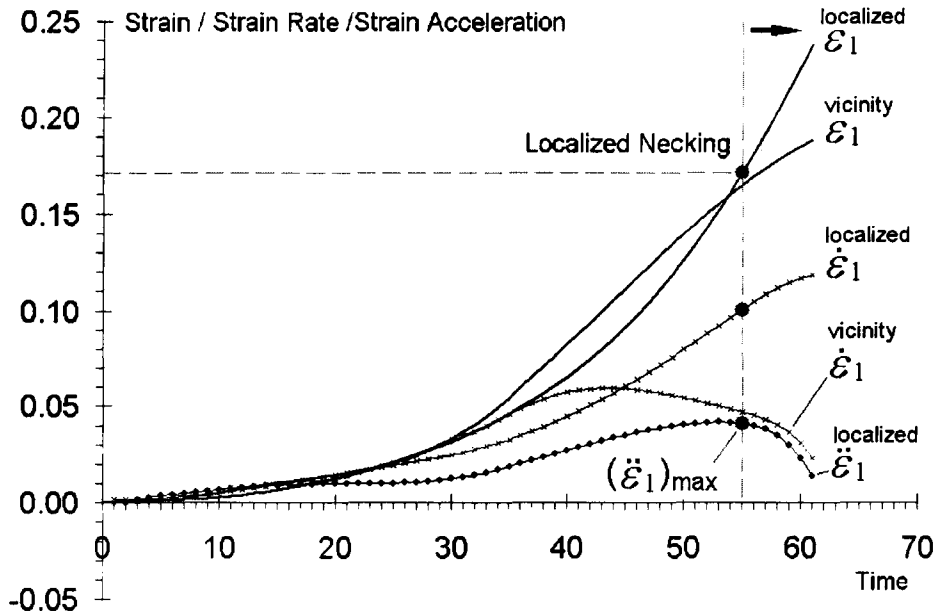


FIGURE 6-17. Analysis of strain history showing evolution of strain, strain rate and strain acceleration at the localization and its vicinity for 2" wide specimen (AA6111-T4, 1 mm thickness, 2" diameter punch).

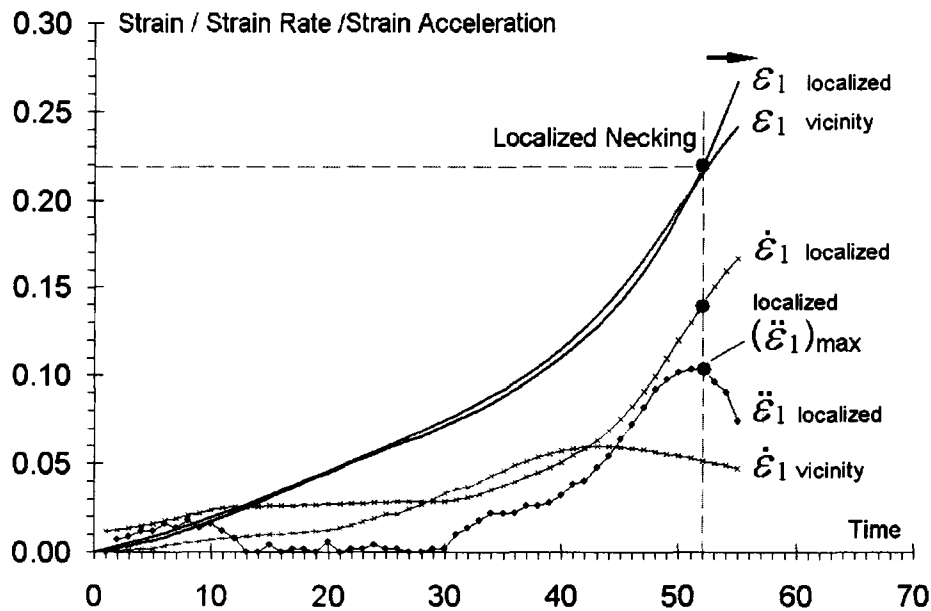


FIGURE 6-18. Analysis of strain history showing evolution of strain, strain rate and strain acceleration at the localization and its vicinity for 5" wide specimen (AA6111-T4, 1 mm thickness, dry contact, 2" diameter punch).

FLDs obtained from earlier FE simulations (Figure 6-10) and from ARAMIS experimental data using criterion of $(\dot{\epsilon}_1)_{\max}$ are plotted together in Figure 6-19. Good agreement was achieved. Also, FLDs from FE simulations with two different criteria, namely maximum major strain acceleration $(\dot{\epsilon}_1)_{\max}$ and critical major strain $(\epsilon_1)_{cr}$ are compared in Figure 6-20. As explained in Chapter 3, Section 3.3, the limit strains from $(\epsilon_1)_{cr}$ are generally underestimated.

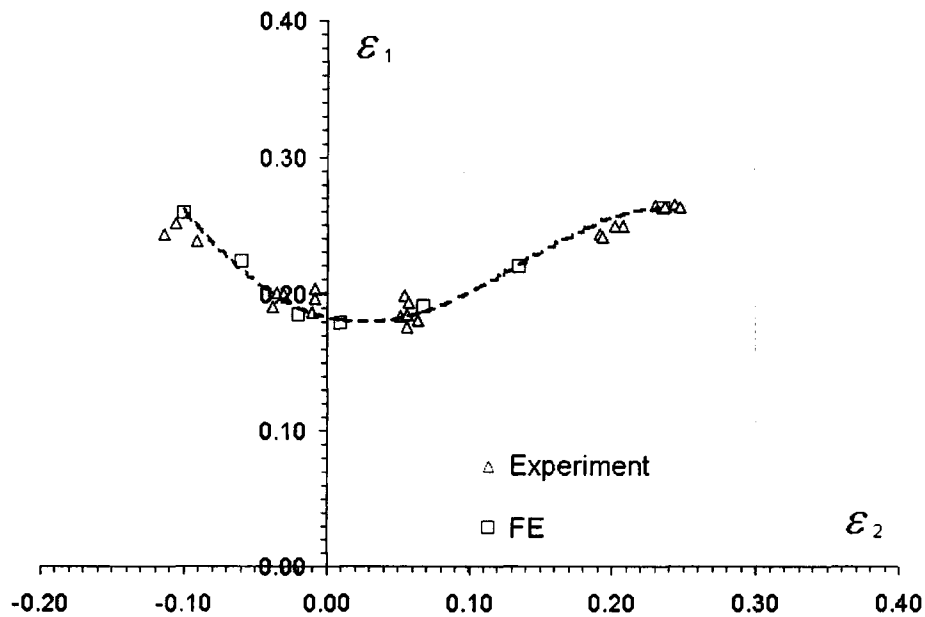


FIGURE 6-19. FLDs obtained from FE simulation using $(\dot{\epsilon}_1)_{\max}$ criterion compared with experimental values from ARAMIS for AA6111-T4 (1 mm thickness, 2" diameter punch).

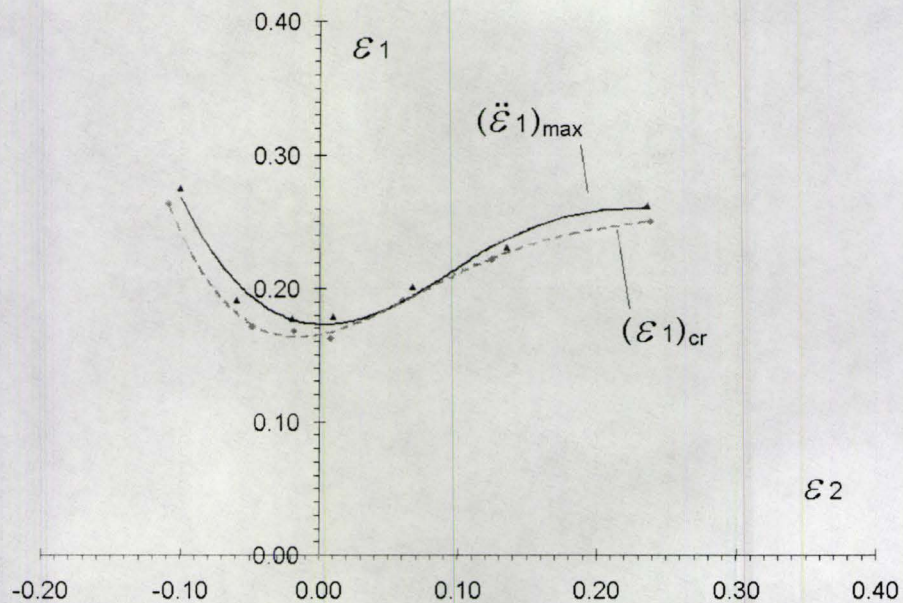


FIGURE 6-20. FLDs from FE results using $(\ddot{\epsilon}_1)_{\max}$ and $(\epsilon_1)_{cr}$ criteria for AA6111-T4 (1 mm thickness, 2" diameter punch).

6.5.2 ARAMIS And ARGUS Results For AA6181-T4

ARAMIS for 0.5" and 7" wide specimens of AA6181-T4 are presented in Figures 6-21 and 6-22 separately. The 0.5" wide specimen provided a path close to the uniaxial tensile path, whereas the 7" wide specimen with polyurethane pad interface provided a balanced biaxial tension path. The results of Figures 6-21 and 6-22 demonstrate once again the existence of a peak in major strain acceleration. Therefore, the proposed necking criterion of $(\ddot{\epsilon}_1)_{\max}$ was utilized to determine of the limit strains.

Figure 6-21 also shows a comparison of the different behaviour of material inside the localized neck and its vicinity. The strain history of the material inside the neck exhibits a rapid increase. The corresponding strain rate also increases monotonically

until fracture. The inflection point in the rate curve presents as a peak in the acceleration curve, i.e. $(\dot{\epsilon}_1)_{\max}$. It is to be noted that the strain in the material in the vicinity of the neck demonstrates a trend towards saturation. Strain rate curve of the material in the vicinity of the neck drops much earlier than the one inside the neck. This result for AA6181-T4 has provided further experimental support to the criterion of maximum strain acceleration as the onset of localized necking.

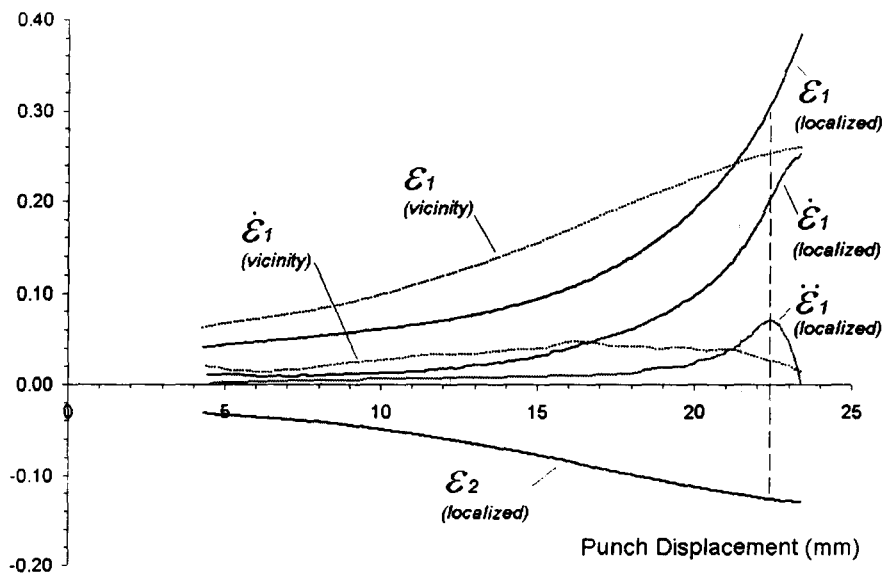


FIGURE 6-21. Strain history from ARAMIS result indicating localized necking at $(\dot{\epsilon}_1)_{\max}$ for 0.5" wide specimen (AA6181-T4, 1 mm thickness, 4" diameter punch).

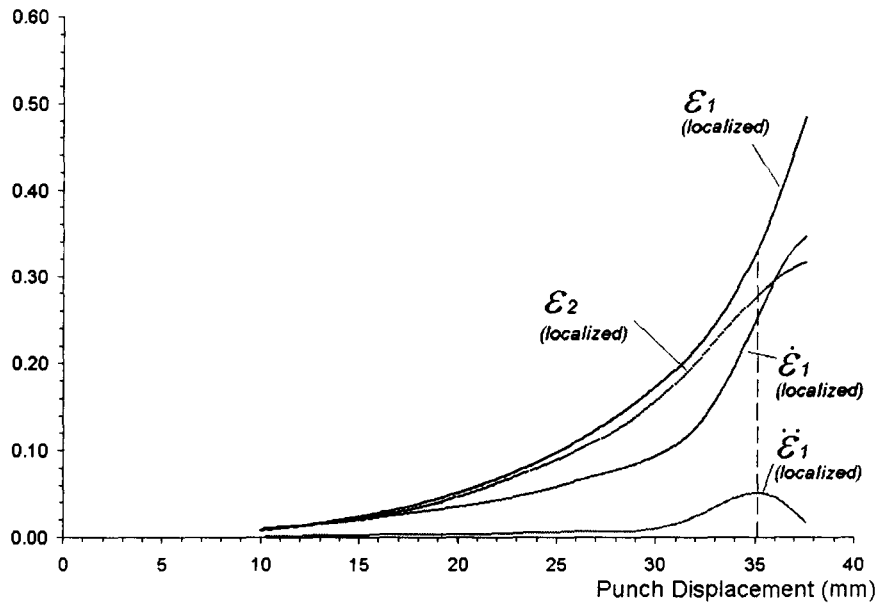


FIGURE 6-22. Strain history from ARAMIS result indicating localized necking at $(\dot{\epsilon}_1)_{\max}$ for 7" wide specimen (AA6181-T4, 1 mm thickness, 4" diameter punch, Polyurethane pad interface).

The ARGUS system provides a post-test strain map of the deformed specimens. Bragard criterion is commonly utilized in post-test strain analysis of deformed specimens in order to construct a FLD. However, this traditional approach of strain evolution considers plane strain condition as the onset of localization and this aspect needs a closer examination. Therefore, the limit strains from periodic grids after the test for deformed AA6181-T4 specimens were obtained with Bragard criterion using the strain measurement system ARGUS 3D. For this purpose, a second order polynomial was utilized as an interpolating function for measurement of limit strains in the vicinity of the localized neck region (Figure 6-23).

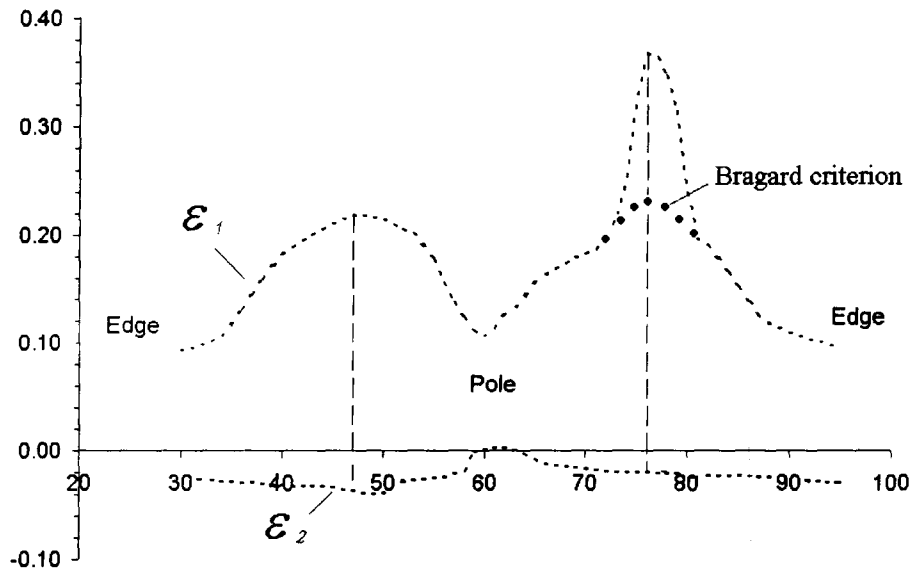


FIGURE 6-23. Post-test strain assessment with ARGUS 3D for 4" wide specimen using Bragard criterion (AA6181-T4, 4" diameter punch).

The resulting FLDs of AA6181-T4 using critical major strain $(\epsilon_1)_{cr}$ (using ARAMIS with stochastic pattern on the specimen) and Bragard criterion (using ARGUS defined grid pattern) are compared with the maximum strain acceleration $(\ddot{\epsilon}_1)_{max}$ (using ARAMIS with stochastic pattern) in Figure (6-24). Clearly, $(\ddot{\epsilon}_1)_{max}$ provides a higher FLD curve compared to the other two localization criteria. This is further discussed in the next chapter.

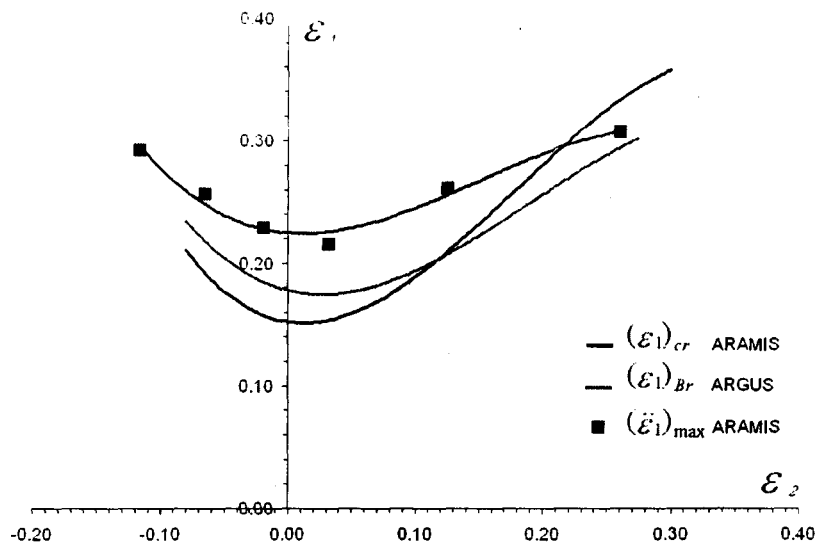


FIGURE 6-24. Comparison of limit strains of AA6181-T4 using various criteria.

This research has presented a novel approach to utilize the routinely obtained punch load-displacement traces from tests. The material properties from uniaxial tensile tests are incorporated in an optimization procedure to extrapolate the stress-strain curves for FE simulation. The above methodology along with the proposed necking criterion offers a rapid determination of FLD via the FE method.

An assessment of the proposed $(\dot{\epsilon}_1)_{\max}$ criterion with other methods, further expansion of the concept of inflection point and further consideration of optimization work are discussed in the next chapter.

6.6 Further Experimental Examinations Of The Proposed Localized Necking Criterion

Three additional strain paths beyond the traditional FLD paths were experimentally studied to further assess the applicability of the proposed necking criterion.

In order to assess the validity of the proposed necking criterion for material of different thickness and strain rate sensitivity, AA6111-T4 was also tested at 2 mm and at two different speeds. DP600 steel sheets at 1.88 mm thickness were tested at two different speeds. Additional strain paths, obtained by employing specimens with a hole in the centre, and specimens with non-symmetric notches were also tested. These results are presented in the following sub-sections.

6.6.1 Thickness And Strain Rate Effects

The influence of strain rate was investigated in AA6111-T4 by changing the punch speed. The specimens were tested with punch speeds of 0.25 mm/s (regular speed), 1.25 mm/s (system maximum limit) and 0.025 mm/s (low speed). For each test at different speeds, both dry condition and polyurethane pad between punch and sheet were utilized. This test was carried out for 1 mm and 2 mm thick biaxial tensile specimens. The result of 1 mm tests is given in Figure 6-25. As the punch speed increases, there is a slight reduction in the magnitude of the force. This can be attributed to slightly negative strain rate sensitivity (or m -value) for AA6111-T4 as reported in the literature. As the

strain rate increases, the stress decreases, which leads to a drop in the punch load. Similar results were obtained for 2 mm AA6111-T4 sheet as shown in Figure 6-26.

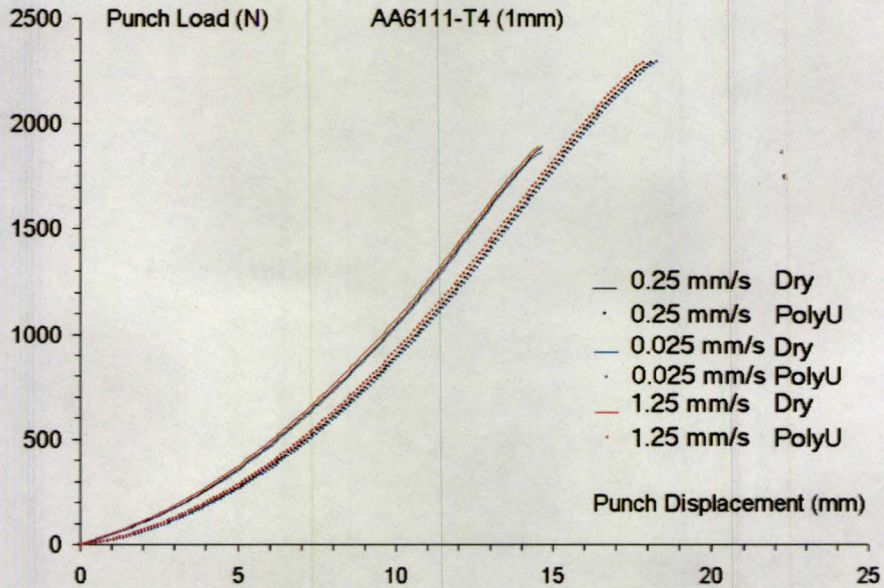


FIGURE 6-25. Load versus displacement curves for 1 mm sheets of AA6111-T4 at different speeds with different lubrication conditions (biaxial tension cases).

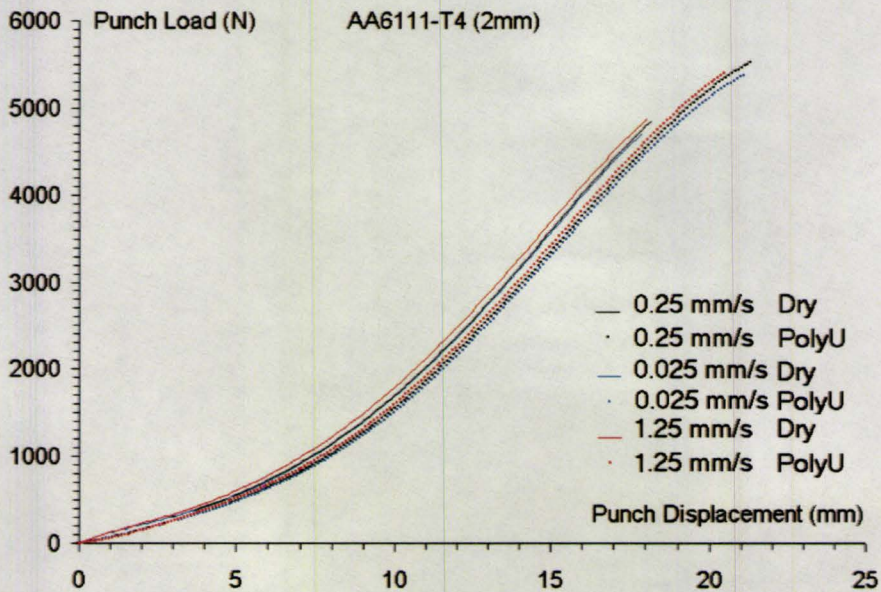


FIGURE 6-26. Load versus displacement curves for 2 mm sheets of AA6111-T4 at different speeds with different lubrication conditions (biaxial tension).

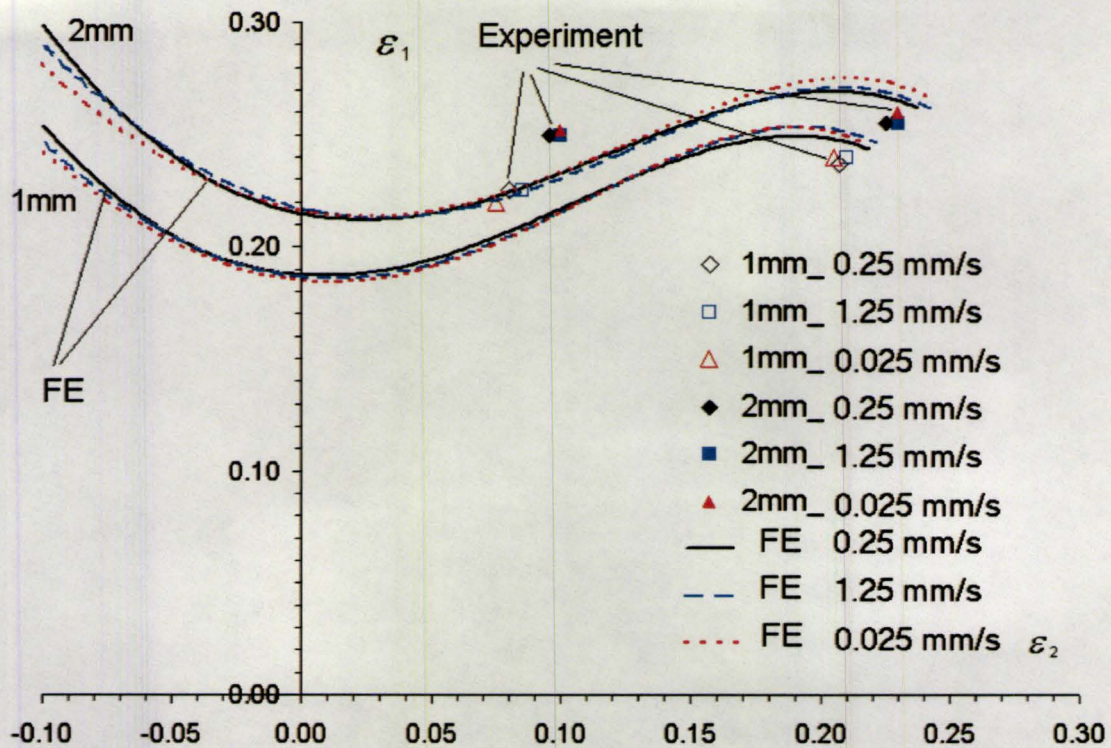


FIGURE 6-28. Comparison of FLDs of 1 mm and 2 mm sheets of AA6111-T4 at different speeds.

It is to be noted that, in the determination of the two sets of FLDs shown above, $(\ddot{\epsilon}_1)_{\max}$ localized necking criterion was utilized in the analysis of strain history data obtained from ARAMIS strain imaging system.

The influence of the strain rate (or punch speed) on the proposed criterion was also investigated with DP600 steel, a material known to have a positive strain rate sensitivity [Thomson, 2006]. The load curves marked with inflection points are plotted in Figure 6-29. As the test speed increases, the magnitude of loads and maximum dome heights increase for DP600 confirming its positive strain rate sensitivity. The inflection point also moves to a larger punch displacement indicating a later occurrence of

instability. The FLD for this material at two different punch velocities is shown in Figure 6-30. The effect of strain rate (and indirectly m) on FLD is clearly captured by the proposed pseudo strain acceleration criterion employed in the processing of ARAMIS based strain history data.

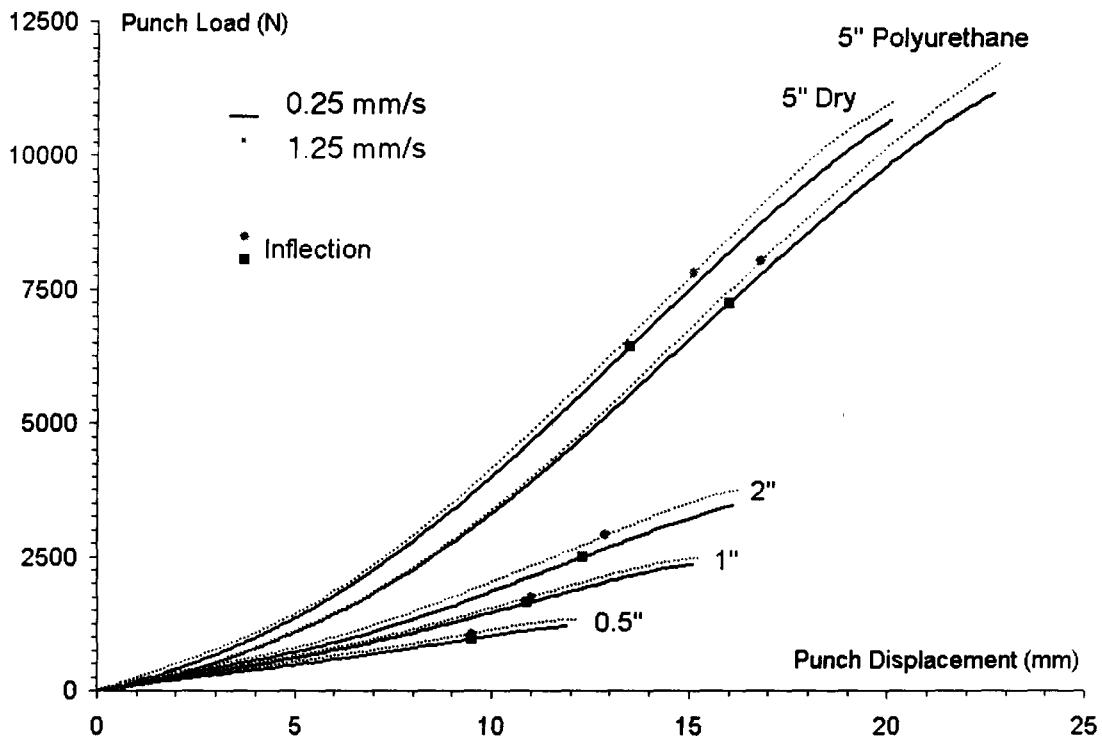


FIGURE 6-29. Experimental load versus displacement curves at different punch speeds for DP600, 1.88 mm sheet. The inflection points are marked on each of the load curves.

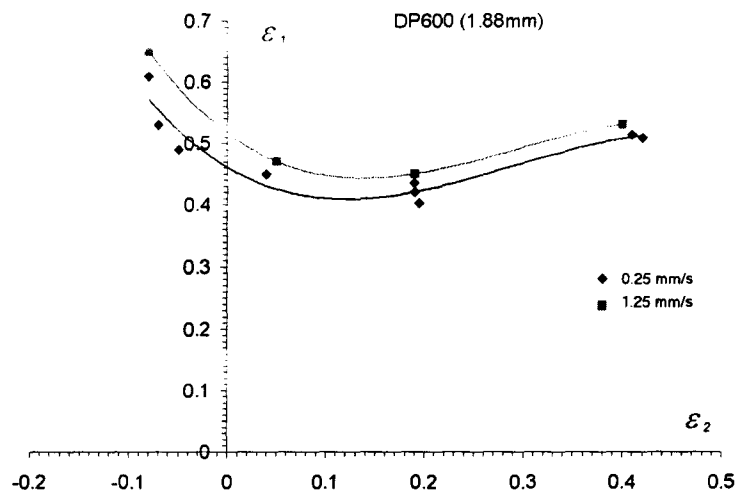


FIGURE 6-30. A comparison of experimental FLDs of 1.88 mm sheets of DP600 steel at two different punch speeds.

Figures 6-28 and 6-30 show that strain rate and thickness effect are captured by the proposed criterion, which further prove the validity of the methodology. The set of hemispherical punch tests could be rapidly conducted at high speeds to fracture to save time. Recorded punch-displacement curves along with the proposed methodology can then be applied to rapidly obtain the FLDs using the FE method.

6.6.2 Additional Strain Paths

6.6.2.1 High Friction Interface Characteristics

Punch load-displacement curve for a rather atypical lubrication condition was compared with the others to study the influence of friction. A sand paper with grit-200 was placed between punch and sheet to create a high friction contact condition and the resulting load-displacement curve is shown in Figure 6-31. As the lubrication condition

worsens, the load shows a higher magnitude at the same punch displacement value due to the higher friction and also an earlier fracture.

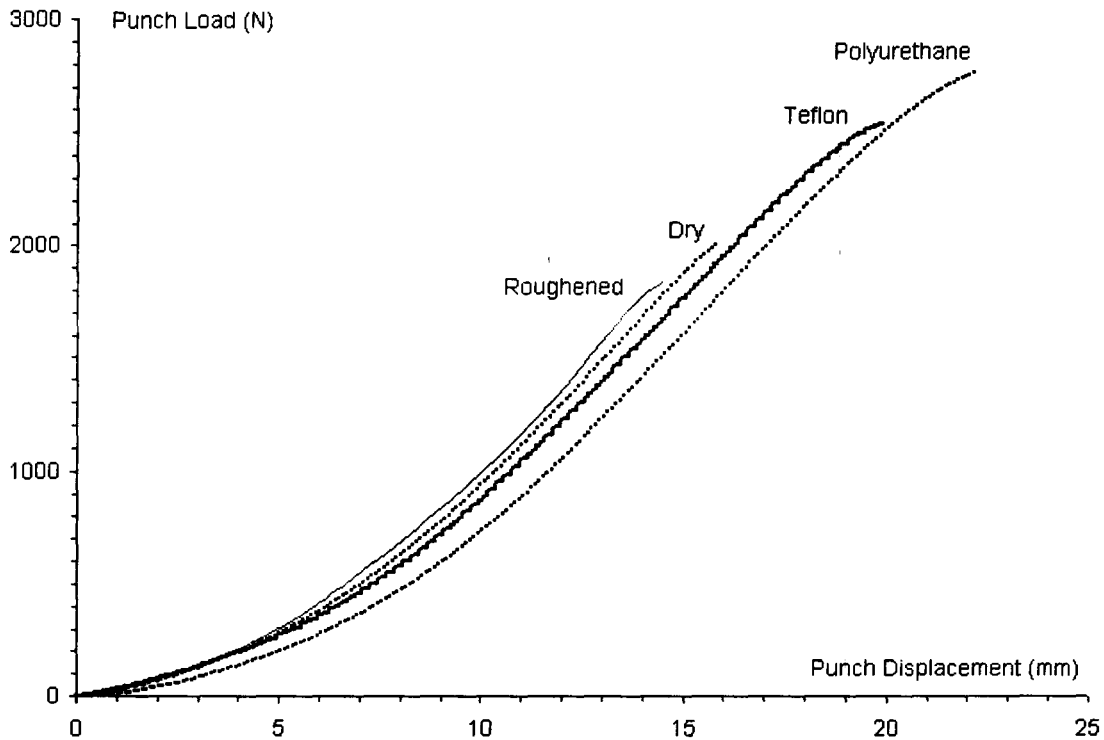


FIGURE 6-31. Punch load-displacement curves under various lubrication conditions (sand paper, dry contact, Teflon, polyurethane, material: AA6111-T4, 1 mm thickness, 2” diameter punch).

The results of strain map and strain history were calculated in the ARAMIS system for further analysis of limit strains. Only the major strain data of sand paper interface between the punch and sheet is shown here for brevity (Figure 6-32).

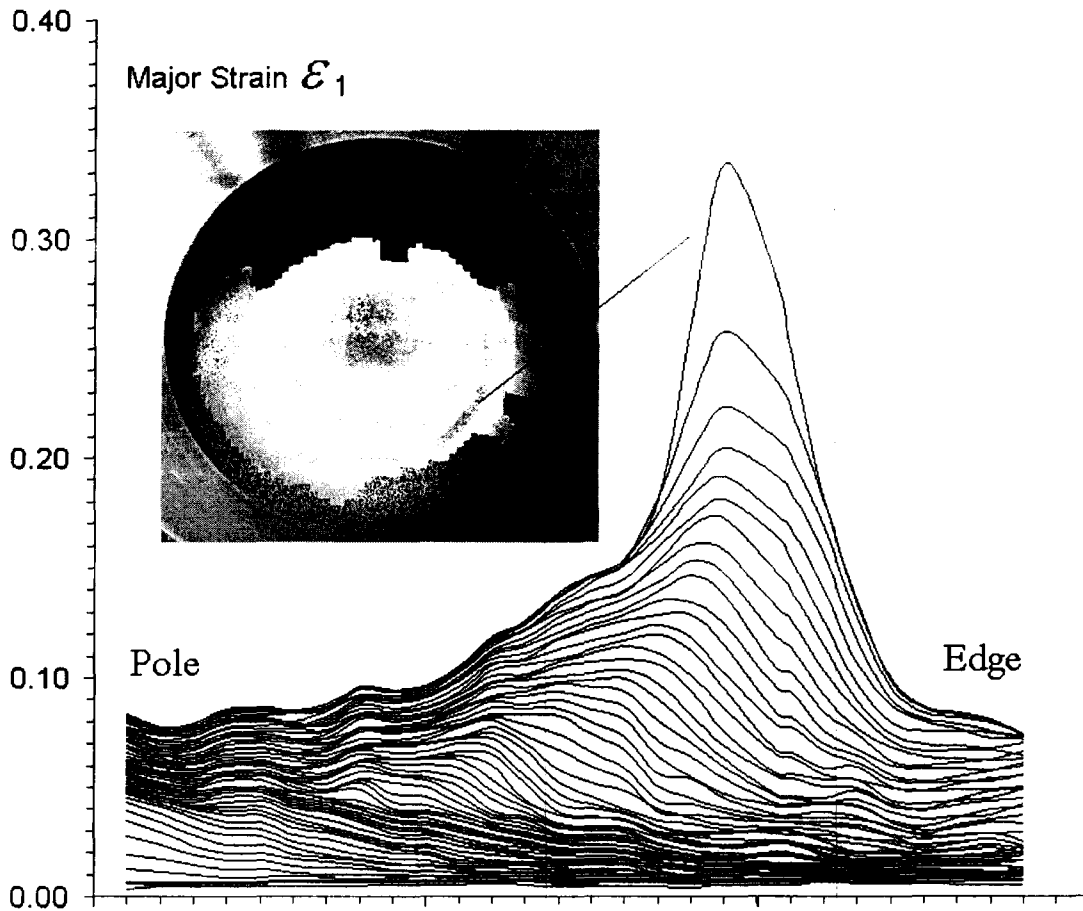


FIGURE 6-32. Strain map and strain history of test with sand paper interface between the punch and sheet.

The proposed criterion, e.g., to seek the inflection point in the major strain history, or a peak in the curve of second derivative, $(\dot{\epsilon}_1)_{\max}$, was utilized to determine the limit strain. The characteristic point was located and employed as the limit strain. Using this criterion, the limit strains of various strain paths were obtained and plotted in Figure 6-33. The proposed approach produced good results for conventional paths of dry contact, Teflon and polyurethane conditions, and also filled the gap between plane strain and dry

condition with the results of sand paper interface between the punch and sheet. This can be observed from a comparison of Figure 6-19 and Figure 6-33.

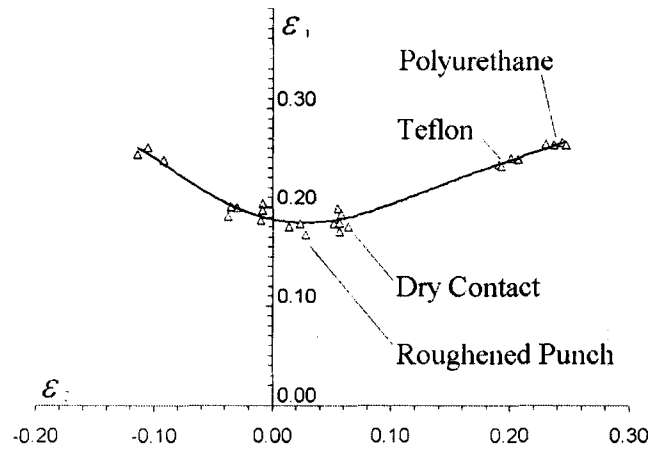


FIGURE 6-33. FLD of AA6111-T4 obtained with $(\dot{\epsilon}_1)_{\max}$ criterion.

The load displacement for sand paper interface between the punch and sheet and dry condition are close together (Figure 6-31). However, the FLD (Figure 6-33) shows that this path is much closer to plane strain than the direct dry condition.

6.6.2.2 Specimen With A Central Hole

Specimens with a machined hole in the centre, in a range of diameters, were also used to obtain additional strain paths and to assess the applicability of the proposed necking criterion. The specimens with central hole were tested in both the Nakajima and Marciniak punch systems since they were assumed to behave differently due to the out-of-plane and in-plane deformations that occur in these two tests respectively. Utilizing the same criterion, i.e., seeking $(\dot{\epsilon}_1)_{\max}$ in major strain rate curve, the strain history of a

given path was processed. The result of a Nakajima test for a 5 mm inner diameter is plotted in Figure 6-34.

The deformation of a specimen with a central hole produces many remarkably different strain paths from different regions of the specimen. By varying the hole size, paths from right-hand-side to left-hand-side can be obtained. The strain path from the very edge of the circle initially evolved along a shear path but turned towards and finally failed near uniaxial tensile path. The strain path of the pattern next to the edge moved towards the plane strain direction but remained in the safe zone. Further away from the edge, the strain path shifted to the right-hand side as shown in Figure 6-34.

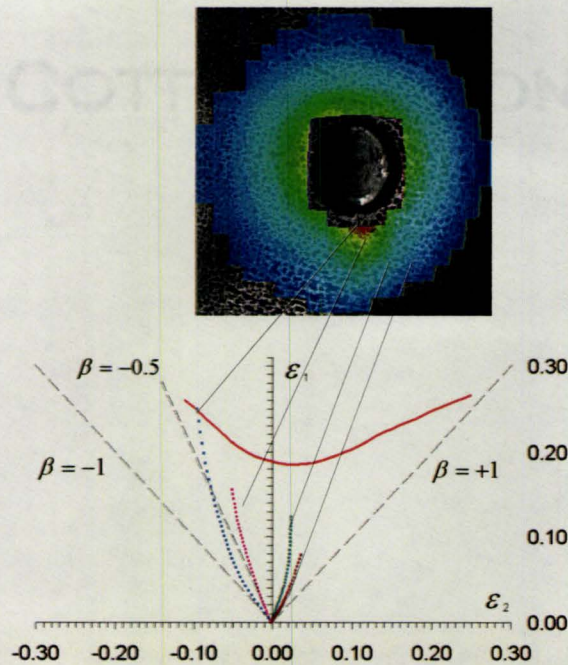


FIGURE 6-34. Strain map of specimen and strain paths from different locations along the edge of the specimen with central hole in Nakajima test ($r = 5$ mm).

A similarity was found in the tension-compression side strain paths obtained from Nakajima and Marciniak tests (Figures 6-34 and 6-35). However, there was a clear strain path change in the tension-tension side strain path for Marciniak test. It evolved initially in tension-tension side of FLD but eventually turned towards to tension-compression side.

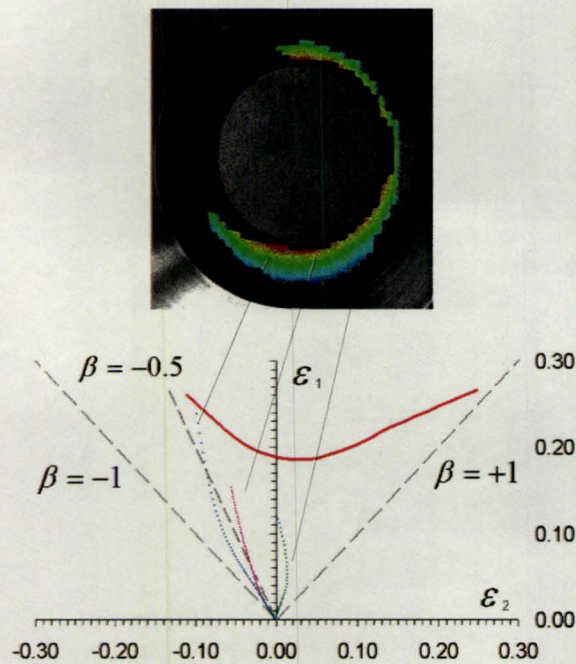


FIGURE 6-35. Strain map of specimen and strain paths from different locations along the edge of the specimen with central hole in Marciniak test ($r = 12.5$ mm).

The strain paths in the specimen with central hole may vary from right-hand-side to left-hand-side. However, a generalization of the results from the two types of punch tests seems to indicate a convergence towards a uniaxial tensile path. By changing the hole size, although initially one may attain a strain path between shear and uniaxial tensile, the specimen with central hole can not produce a final strain path left of the uniaxial tension strain path as shown by a comparison of earlier Figure 6-19 and a new Figure 6-36.

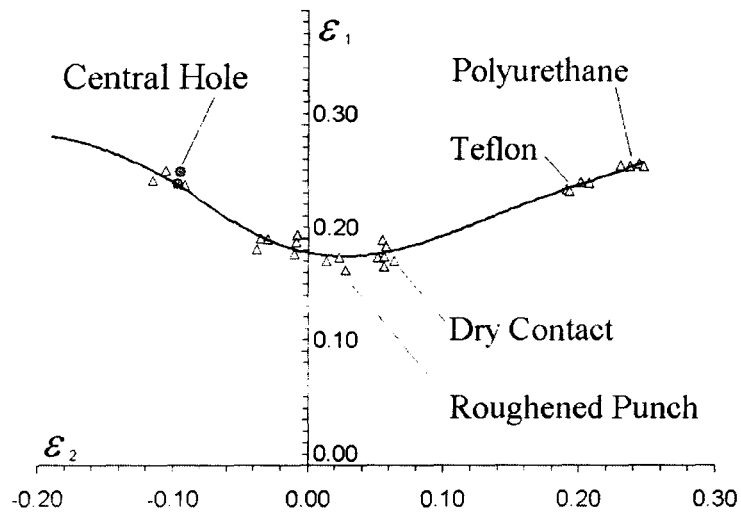


FIGURE 6-36. FLD of AA6111-T4 obtained with $(\epsilon_1)_{\max}$ criterion.

6.6.2.3 In-plane Shear Tests

In-plane shear tests, without the use of a punch, were conducted to obtain a wider range of strain paths that are close to the pure shear path. The specimen dimensions were presented earlier in Chapter 4 (Section 4.2.1, Figure 4-15). The results show that specimens with a large clearance C produced a path closer to pure shear than those with a smaller clearance. At a given clearance, as the notch spacing decreases, the strain ratio β decreases, and approaches a value of -1 (pure shear).

The strain paths resulting from two different notch configurations are shown in Figure 6-37. The left image shows that the tip of the crack lies in a neck cavity in the middle of the notch width. The right image, on the other hand, indicates that the crack path propagates in the shear bands to form a curvilinear trajectory, indicating an occurrence of shearing process. ARAMIS strain history data is plotted to show the

different strain paths. Analysis of ARAMIS data, similar to the two previous cases, was carried out using the proposed localized necking criterion.

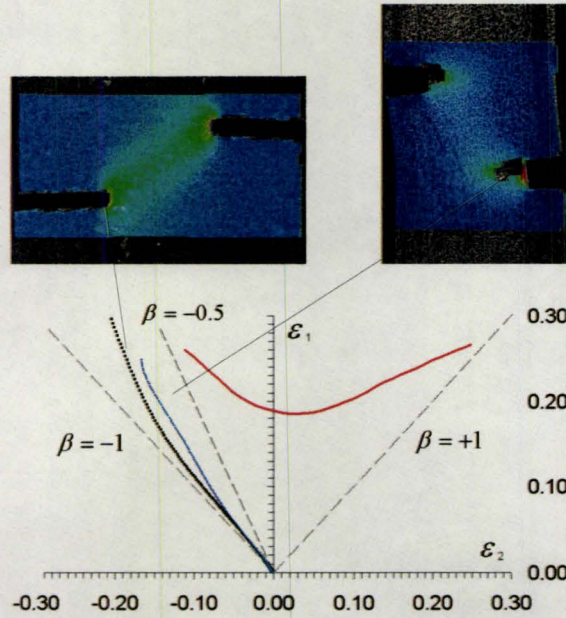


FIGURE 6-37. Strain paths of shear specimens with non-symmetric notches.

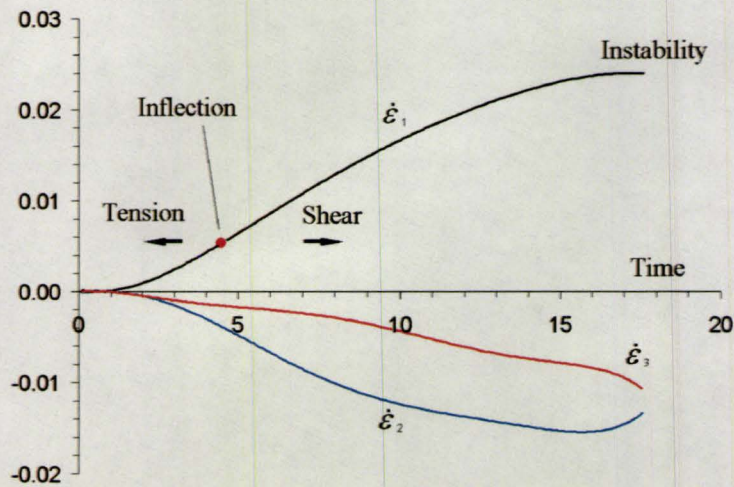


FIGURE 6-38. Curves of strain rate from a notched specimen showing inflection point as onset of shearing process.

An inflection point was observed when the gradient of the major strain history was plotted (Figure 6-38). This inflection point has been defined in the case of punch stretching as the onset of localized necking. However, the presence of inflection point in the shear process requires a more general definition, which will be discussed in the next chapter.

Chapter 7

Discussion

In this research an attempt has been made to integrate experimental specimen-scale punch load and displacement response of the sheet material with FE based simulations of the specific experiments, and resulting strain development in the simulated specimen, to obtain forming limits. Two key developments associated with this integration involve a new and superior localized necking criterion and an optimization scheme for calibrating the experimental and FE based punch load versus displacement curves. Localized necking criterion is shown to work well with the strain output data from FE simulations as well as with the continuously measured strain data from the ARAMIS system. The original proposal of Hecker and Ghosh regarding the existence of an inflection point in the load-displacement curves is exploited during the calibration of the punch load versus punch displacements from the experiments and FE models. A similar inflection in the major strain rate is numerically and experimentally observed for a range of strain paths and geometric conditions. The criterion has been adapted to extract the spatial and temporal strain data obtained independently from the FE simulations and on-line strain measurement system to obtain the limit strains and their locus in terms of a FLD.

The discussion is arranged as follows. First, an assessment of the proposed localized necking criterion is made with respect to the other more established criteria.

This is followed by a further exploration of the inflection point in shearing process. Thirdly, aspects of the optimization work are given further consideration by analyzing local stress-strain behaviour in uniaxial tension with the ARAMIS system.

7.1 Strain Evaluation In And Around Neck Region And Validity Of Bragard Criterion

In-depth investigation of the concept of strain evolution through traditional approach was carried out with AA6181-T4 sheet material. Observations that the attainment of plane strain state may not necessarily lead to localized necking has been presented in Figures 3-7 and 3-13. The fact that the minor strain keeps varying to some extent as the neck grows was examined through conventional post-test approach such as ARGUS, which further supports the concept proposed in this research.

Different paths (Figure 7-1) chosen to verify the concept of strain evolution for typical geometries such as a 4” wide specimen (near plane strain path) include path A-A (across the centre of specimen in transverse direction, pole area), path C-C (across the centre of specimen in longitudinal direction containing two localized zones) and paths B-B and D-D (near localization sites).

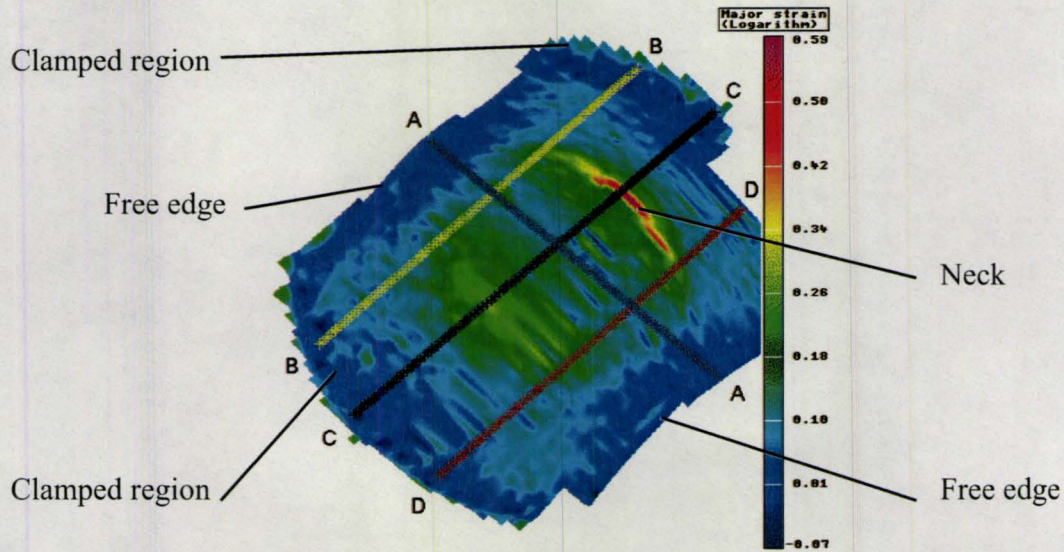


FIGURE 7-1. Strain contours for 4" wide specimen from ARGUS 3D post-processing (AA6181-T4, 1 mm thickness).

The results showed that a near plane strain state has occurred for path A-A (Figure 7-2). However, plane strain condition does not lead to the onset of localization. Also, no localization was observed along paths B-B or D-D (path D-D is shown in Figure 7-3). The path C-C along the longitudinal direction, which contains two seemingly symmetrical zones of deformation, was studied to determine why only one of the two exhibited the localization (Figure 7-3).

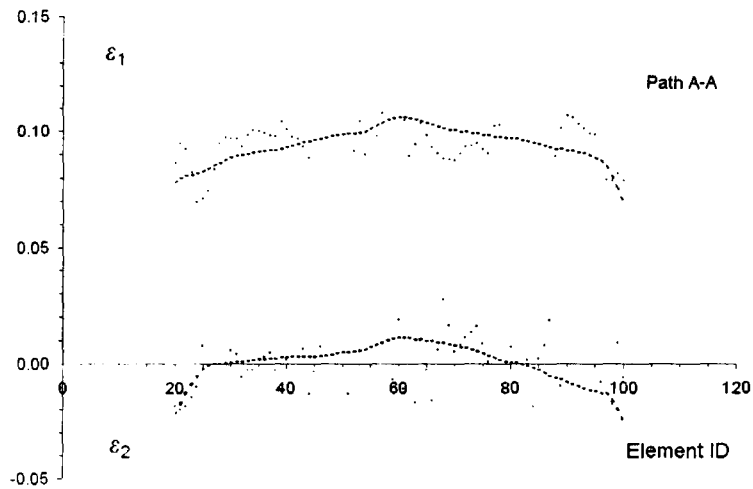


FIGURE 7-2. Strain path A-A from Figure 7-1.

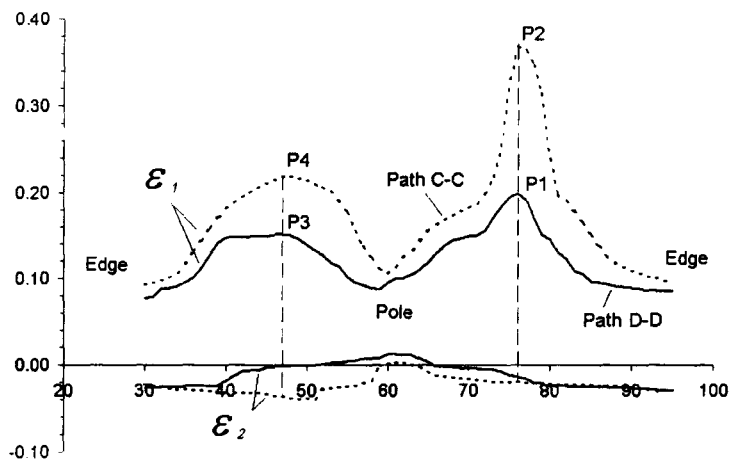


FIGURE 7-3. Strain paths C-C, D-D from Figure 7-1 (see Figure 7-4 for points marked P1 ~ P4 in current figure).

To clarify this question, path C-C was compared to path D-D, since C-C can be assumed to be the subsequent stage of D-D. The result shows that after the onset of localization, the minor strain does continue to evolve, although at slower rate compared to the rapid growth in major strain. The points P1-P4 from Figure 7-3 are re-plotted in Figure 7-4.

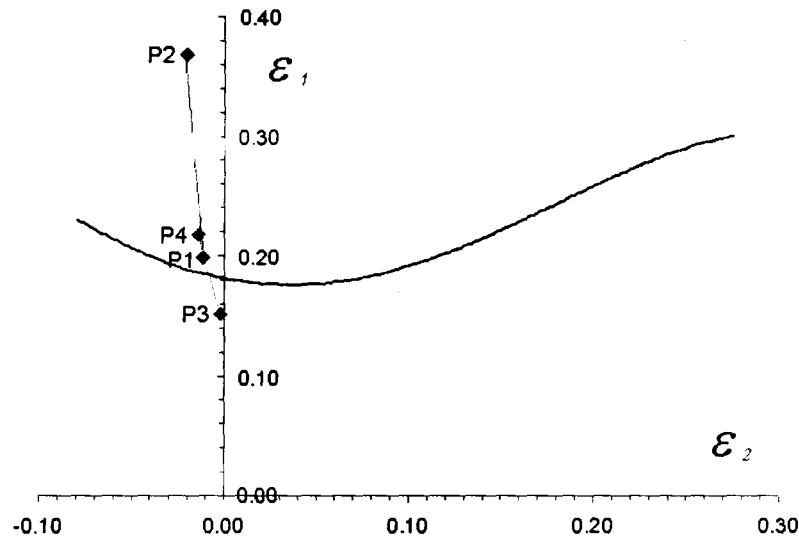


FIGURE 7-4. Using the post-test strains to trace the strain evolution from ARGUS 3D post-processing (points P1 ~ P4 from Figure 7-3).

As shown in Figure 7-4, the evolution of minor strain continues after localized necking. On the other hand, considering the incompressibility (or constancy of volume) when the localization occurs, the major strain increment, $\Delta\epsilon_1$, is ever increasing in the positive direction and has a value much greater than that of minor strain increment, $\Delta\epsilon_2$, which results in an ever-increasing value (on the negative value) of the thickness strain increment, $\Delta\epsilon_3$. Whether the increment of minor strain $\Delta\epsilon_2$ is positive or negative has no significant influence. This reduction in the thickness does not necessarily require the reduction in the minor strain. This can be expressed in an equation form as follows (the up and down arrows indicate increase and decrease in the three principal strain components):

$$\Delta \varepsilon_1 \nearrow + \Delta \varepsilon_2 \nearrow + \Delta \varepsilon_3 \searrow = 0 \quad (|\Delta \varepsilon_1| < |\Delta \varepsilon_3|, \text{ RHS}) \quad (\text{Eq 7-1})$$

$$\Delta \varepsilon_1 \nearrow + \Delta \varepsilon_2 \searrow + \Delta \varepsilon_3 \searrow = 0 \quad (|\Delta \varepsilon_1| > |\Delta \varepsilon_3|, \text{ LHS}) \quad (\text{Eq 7-2})$$

It can be assumed that the strain paths in two symmetric neck positions along line C-C evolve differently as shown in Figure 7-3. Material inhomogeneity may also be attributed to the different strain evolution in the two neck regions.

The results analyzed here using Bragard criterion and, as shown in Figure 7-4, clearly demonstrate that the minor strain continues to evolve in the neck region (for example, strain paths $P_1 \rightarrow P_2$, $P_3 \rightarrow P_4$). This result further confirms the earlier assertion that attainment of plane strain state is not a condition for localized necking.

7.2 Assessment Of Various Localized Necking Criteria To Determine The Limit Strains

An important source of variability in FLD, for the same material, arises from the selection of a criterion for strain localization. Figure 6-24 earlier showed a comparison of FLDs of AA6181 produced by using three different strain localization criteria, namely, critical major strain criterion $(\varepsilon_1)_{cr}$, Bragard criterion ε_{Br} and the proposed maximum major strain acceleration criterion $(\ddot{\varepsilon}_1)_{max}$.

Overall, critical major strain criterion $(\varepsilon_1)_{cr}$ produced the lowest values whereas the maximum strain acceleration $(\ddot{\varepsilon}_1)_{max}$ produced the highest. The limit strains obtained using $(\varepsilon_1)_{cr}$ is generally less than that interpolated by Bragard criterion since $(\varepsilon_1)_{cr}$ is

from the vicinity of a localized site. Bragard criterion produces a “virtual” value that cannot be experimentally measured and is generally slightly greater than the strain in the vicinity.

The obvious advantage of the first two criteria $(\epsilon_1)_{cr}$ and ϵ_{Br} is the direct observation and fast estimation. However, the “onset” of localization from these criteria is influenced by the grid or speckle size since observation and comparison of elements next to the localized element are required. Also, subjectivity exists since different selection of measured points may produce errors in the shape and position of the resulting limit curves. Neither of the two can give a clear definition of the “onset” of localization. Further, by tracking the magnitude of major strain with respect to the neighbour element may simply mislead to an earlier stage ahead of localization (Figure 3-13).

The basis of the proposed maximum major strain acceleration criterion $(\dot{\epsilon}_1)_{max}$ is that the material in the neck region has a higher acceleration than its neighbour and eventually reaches a maximum. The strain rate increases to a maximum at a reducing rate, whereas the strain still keeps increasing until fracture occurs. The reduction in strain acceleration from the maximum to zero represents the process of localization. This demonstrates the broad characteristics of the major strain acceleration and these remain independent of the strain path, material constitutive law and its material parameters, and whether the deformation occurs in the plane or out-of-the plane of the sheet.

The proposed criterion appears to be useful and practical. The bifurcation phenomenon of localization was studied and explained utilizing the concept of strain evolution. A case study was made by employing all the regions around a localized site

(Figure 3-7). Region *A* in the site of strain localization and region *B* in the vicinity of localization (neighbor of *A* on the pole side) exhibit significant difference in both the strain and strain rate (Figure 7-5). The region *A* shows an increasing trend in the strain and increasing trend with a peak in strain rate when fracture occurs. The neighbor *B*, on the other hand, shows saturation in the strain and a drop in strain rate after localization. Despite the mesh dependency problem, the bifurcation phenomenon of localization was explained utilizing the concept of strain evolution with reasonable interpretation. The bifurcation presents itself first in the strain rate but not strain. As mesh size changes, this difference may appear in the strain from the two regions. Obviously when localization occurs, only a very narrow area of material shows a rapid growth in the major strain. The strain development in the neighboring region contributes little to the overall deformation.

It is to be noted that the strain rate in the localized region, instead of strain, showing a maximum value at the very end of forming process maintains the ever-increasing trend in the strain. Otherwise, according to the relationship of integral or derivative, if the strain reaches a maximum, the corresponding strain rate at fracture must be zero. This appears contradictory to the fast and transient process of fracture. Experimental results from the ARAMIS system also demonstrate the validity of a maximum in the major strain acceleration (Figure 7-5).

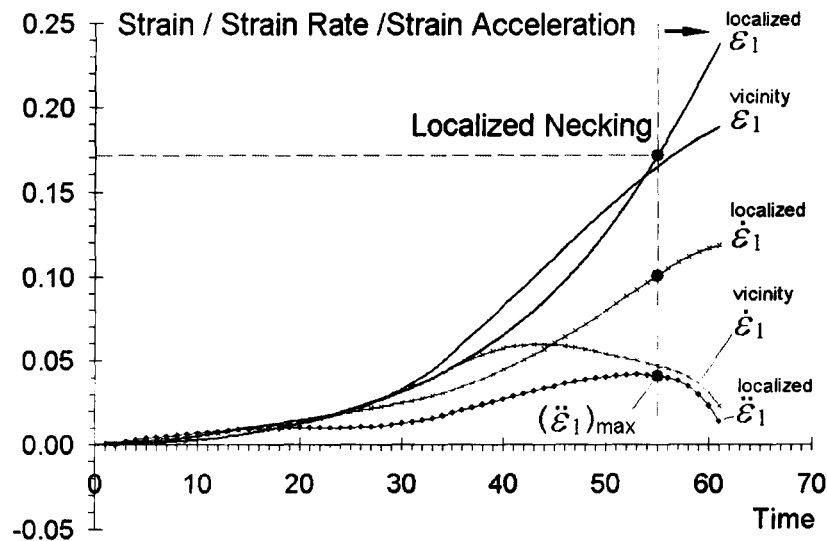


FIGURE 7-5. Bifurcation behaviour of major strain (ARAMIS results of AA6111-T4, 1 mm thickness, 2" diameter punch).

The advantages of the proposed criterion over the other two mentioned earlier are in terms of a definite physical meaning and less subjectivity in the determination of limit strains. Also, this method is less mesh dependent than the critical strain criterion. The inflection in major strain rate can be easily calculated once the strain histories are obtained.

The proposed necking criterion exhibits definite advantages over the criteria of Kocks et al., Greiger et al. and Pepelnjak et al. The analytical model of Kocks et al. was an idealized model although defects of geometric defect, prestrain and microstructural defect have been taken into account, which could not represent the localized necking behaviour at large strain, even an inflection point was observed initially.

The method of Greiger et al., as reviewed in the Chapter 2, is a comparison of the gradient between the localized neck and the vicinity. It is fundamentally the critical major

strain criterion, $(\epsilon_1)_{cr}$, although a gradient was employed to demonstrate the different behaviour of material inside and outside the neck. Also, as analyzed earlier, the advantage of strain history recorded by the strain imaging system was not fully utilized. No reason or criterion was presented as to why a spatial result of strains at a certain instance was selected for analysis. Therefore, this method does not reveal the development of localization behaviour.

Pepelnjak et al. proposed a method using the second derivative of thickness strain, which is similar to this research. As analyzed earlier, the thickness strain cannot be obtained directly from experiment, although the thickness reduction is closely related to the forming limit. Also, the physical meaning of the second order of derivative in thickness strain was not explained. In this research the different behaviour of major and minor strain has been extensively studied. For evaluation purpose, the thickness strain is also analyzed in Figures 7-6 and 7-7. Figure 7-6 shows the strain histories of major, minor strains obtained directly from experiment, whereas the thickness strain is calculated as per plastic incompressibility.

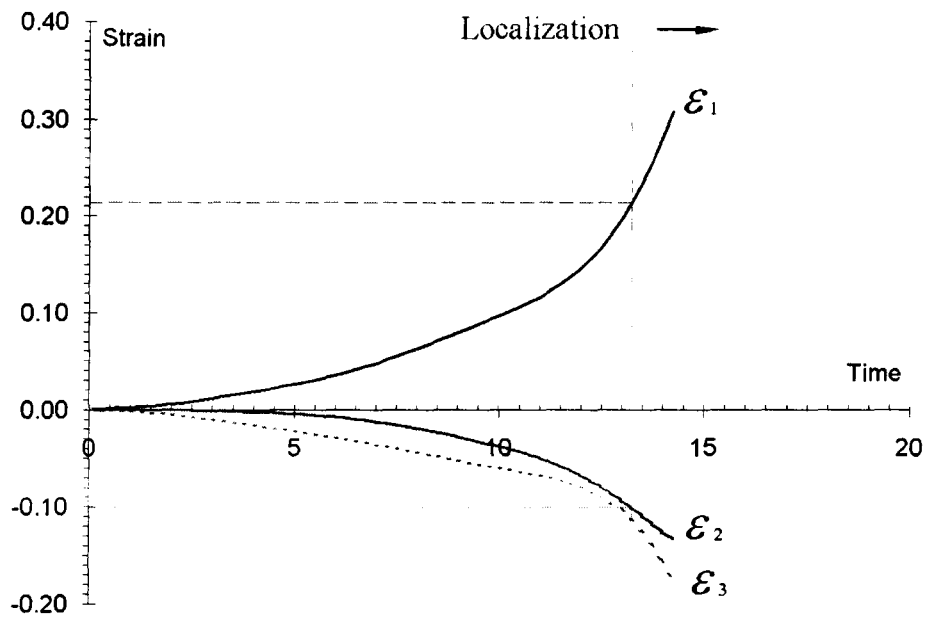


FIGURE 7-6. Strain histories of major, minor and thickness for 0.5” wide specimen of AA6111-T4 in 2” diameter punch test (major and minor strains obtained experimentally).

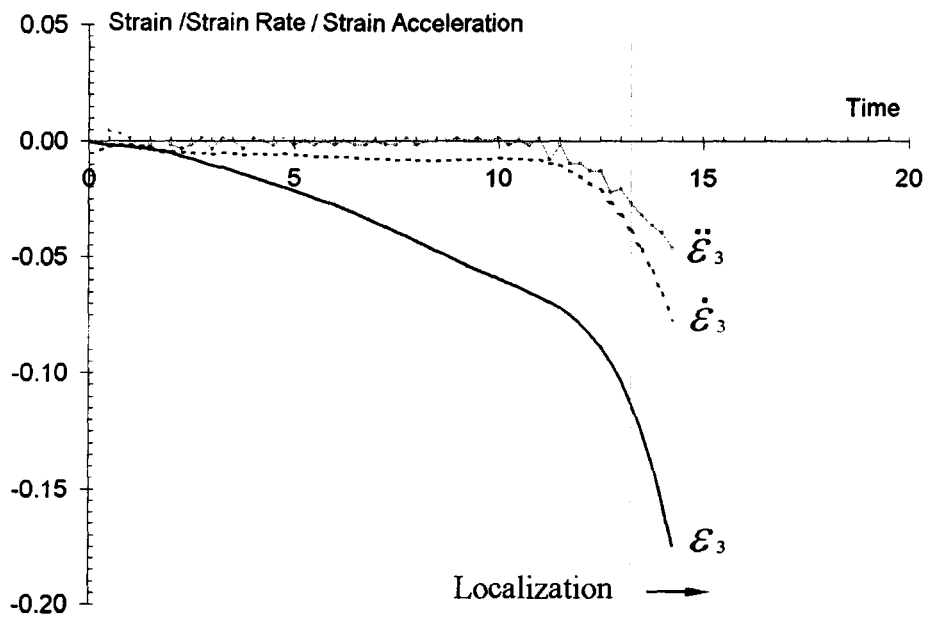


FIGURE 7-7. Strain history, rate and acceleration of thickness strain for Figure 7-6 specimen.

Figure 7-7 shows the strain history, rate and acceleration curves in terms of time. The trend of thickness strain history in the work of Pepelnjak et al. (Figure 2-10) is not observed in this research. Both the rate and acceleration curves demonstrate a monotonically decreasing trend, in which no characteristic points have been observed.

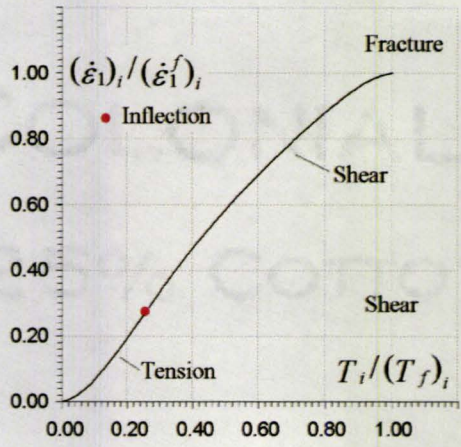
Based on the results from both FE prediction and experiment of this research, the proposed criterion of $(\dot{\epsilon}_i)_{\max}$ to seek the inflection point in major strain rate as the onset of localized necking is more reasonable than the criterion to locate inflection point in thickness strain and other criteria.

7.3 General Definition Of Inflection Point In Forming Process

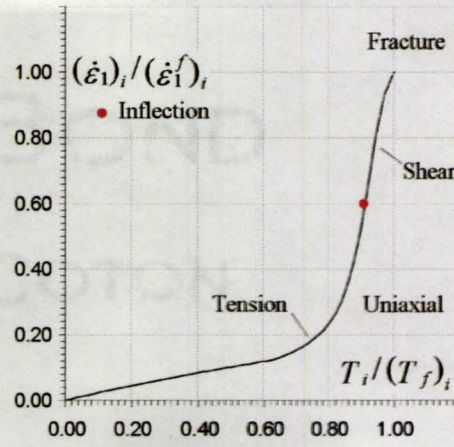
Experimental results from in-plane shear tests when plotted in terms of strain rate exhibit an inflection point (Figure 6-38). This can be expanded as follows. In a pure shear process, there is generally no localized necking behaviour although thickness reduction is indeed observed. One could possibly consider that the inflection point shrinks to the very start of the process. In this case, the curvature of the major strain gradient should show a monotonically increasing trend of a convex shape. Therefore, it can be assumed that, for a shear process, the strain rate curve has a convex shape. Similarly, a concave shape in the strain rate curve represents a tension process. With these two assumptions, the major forming processes during punch stretching can be re-evaluated.

The deformation process of specimen with notches showed that the sheet was subjected to tension initially and then a shearing process took over until the onset of instability (Figure 6-38, top curve).

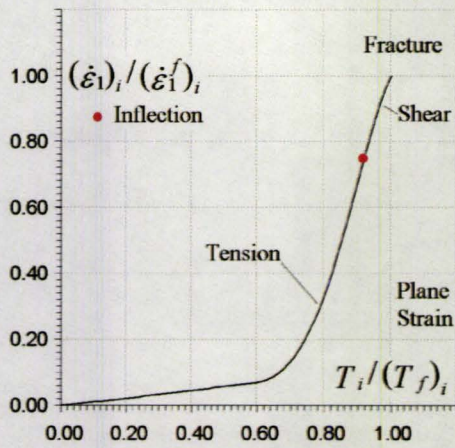
For this purpose, the representative curves of major strain gradient, including uniaxial tensile, plane strain, biaxial tensile and shearing, were normalized and re-plotted to demonstrate the shift in the inflection point as a function of strain path (Figure 7-8). For each curve, the x-coordinate is time step divided by the corresponding final time, resulting in a final value of 1. The y-coordinate is major strain gradient divided by corresponding values at fracture, which also produces a value of 1 in the end. Therefore, the various curves have been normalized for consideration of curve shapes only. All the processes start from zero and end at fracture. The shift in the inflection points reveals the characteristics of these processes. In a sequence of strain ratio from -1 (shear) to $+1$ (balanced biaxial tension), i.e., $-1 < \beta < +1$, the inflection point moves from start of the process to the end, showing that the processes are changing from increasing tension to a final shear mode (Figure 7-8f).



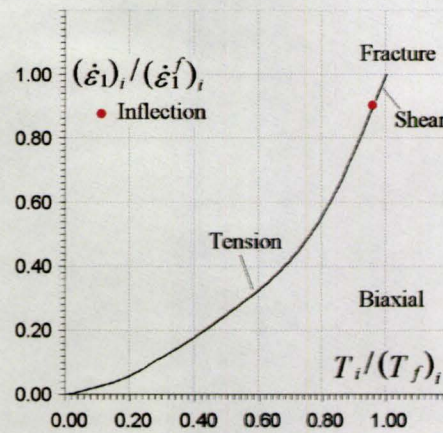
a. Notched shear samples



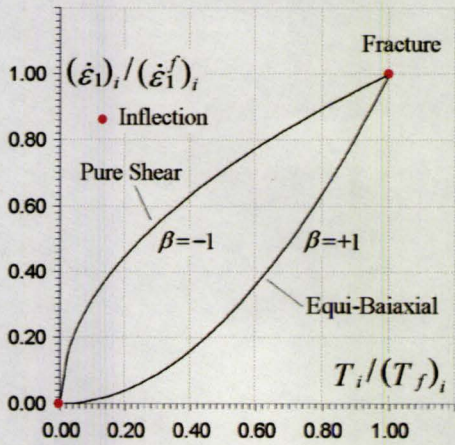
b. Uniaxial



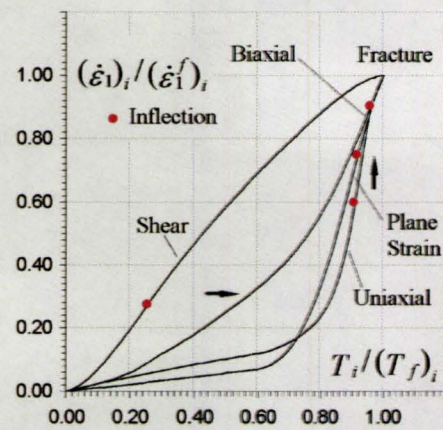
c. Plane strain



d. Biaxial



e. Pure shear and equi-biaxial



f. Assembly of various paths

FIGURE 7-8. Major strain rate curves of various paths showing inflection point and different curvature.

In uniaxial tensile or near plane strain process, the specimens are subjected to tension and finally transient shearing process. The shapes of the gradient of strain curves are concave initially and convex at the later stage. Inflection points can be obtained for these processes. In a biaxial tensile process, the shape of major strain gradient curve is primarily concave and may exhibit an inflection point if there is friction in the forming process. If the process is close to balanced biaxial, the shape of major strain gradient curve is monotonically increasing in a concave shape. The inflection point may not appear. This explains why fracture is often observed without obvious localized necking in equi-biaxial loading path.

7.4 Physical Significance Of The Proposed Localized Necking Criterion

The proposed localized necking criterion of $(\dot{\epsilon}_1)_{\max}$ was implemented to obtain the limit strains from the FE simulations of various tests. The results for 0.5” wide specimens under in-plane and out-of-plane deformation conditions were given earlier in Figures 3-11 and 3-12 respectively. The curves of second derivative of strain versus time, i.e., the “acceleration” curves of each test condition, are normalized with respect to time and plotted in Figure 7-9. As shown, the acceleration curve of in-plane test exhibits a sharp increase leading to a sharp peak in $\ddot{\epsilon}_1$ value. However, for out-of-plane test, the acceleration curve increases more gradually to a shallow peak in $\ddot{\epsilon}_1$ value. The different shapes of acceleration curves for the same geometry and similar strain paths are related to

the different local deformation conditions for the two cases. For the in-plane test, there is no contact with punch in the vicinity of strain localization. As a result, the strain localization process, a single macroscopic shear band type instability, is likely to be less constrained and more prone to a rapid development. Consequently rapid development of strain and strain acceleration at the macroscopic shear band is expected. On the other hand, for out-of-plane deformation, the presence of a punch in the vicinity of strain localization has a stabilizing influence on the initiation and growth of macroscopic shear bands. It is likely that the shear band propagation through the thickness is reduced in this case which would lead to a more “diffuse” development of strain, and correspondingly the strain acceleration, at the neck.

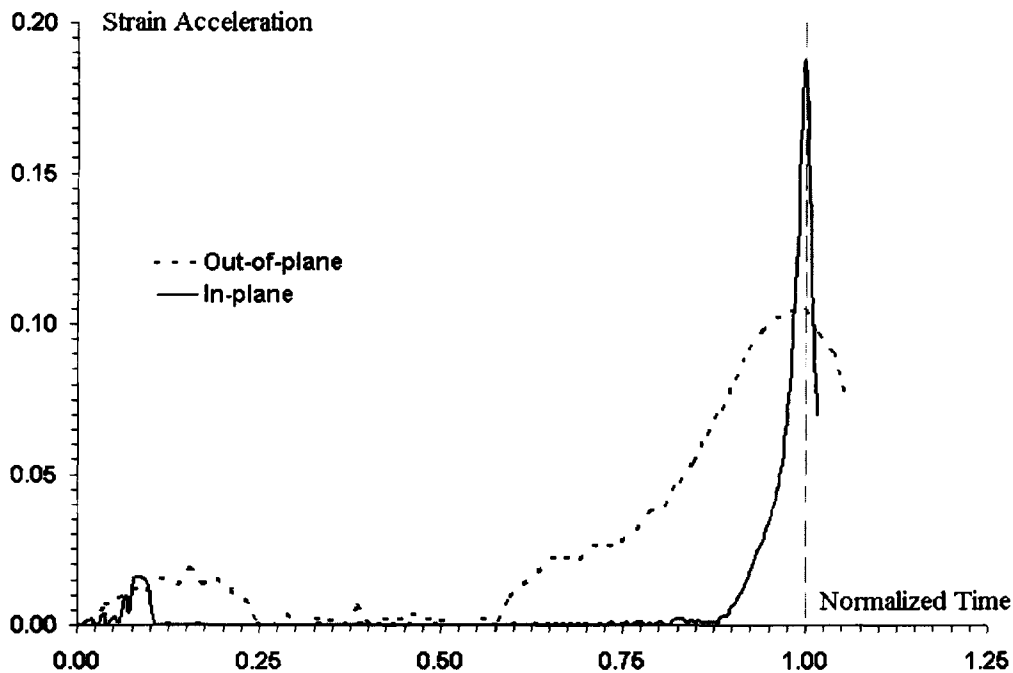


FIGURE 7-9. Comparison strain acceleration curves of in-plane and out-of-plane test.

7.5 Punch Size Effect On Prediction Of FLD

Two different punch sizes were used in this research, namely 4” for AA6181-T4 and 2” for AA6111-T4 sheets. Various punch sizes generally cause increased strain at the neck due to additional bending effect. The bending strain can be calculated from simple bending theory as shown below (Eq 7-3).

$$\varepsilon_B = \frac{t}{R} \quad (\text{Eq 7-3})$$

where the ε_B is the strain caused by bending over a radius R and sheet thickness t . As shown, the smaller is the punch size, the larger is the bending strain. For sheet thickness of 1 mm, 4” punch diameter, the strain caused by bending is 1/50.8, or 0.02 approximately whereas for a 2” punch diameter, the strain is roughly 1/25.4, or 0.04. These factors are clearly significant for FLD usage in stamping analysis. However, the intention of the present work was to assess the overall methodology, as proposed in this work, towards FLD prediction and not directly address the issue of bending related effect on FLD. In other words, a one-to-one correlation was made between the experimental punch and sheet geometry, and the corresponding FE simulations, to assess the validity of the proposed methodology.

7.6 Expanding Optimization Work

The necessity to conduct the optimization work with the input $\sigma - \varepsilon$ is largely because of the limitation of conventional uniaxial test strain range. Stress-strain relation

needs to be extrapolated to large strain to account for the range of strains that occur for the entire range of strain paths in punch tests. However, an arbitrary extrapolation may not lead to results that are in good agreement with the punch load versus displacement data. Therefore, the optimization work is about how to determine an appropriate stress-strain relation at large strain. The calibration in terms of actual “shapes” of the load-displacement curves from experiments and FE output is perhaps less significant. As discussed earlier, the inflection point in the two curves is utilized for this purpose along with the other parameters. This ensures that the two curves are equivalent.

In a conventional approach, to obtain the strain-stress relationship of certain material, uniaxial tensile test is employed, in which generally a strain gauge (extensometer) is utilized. The gauge measures the extension of the specimen that can be converted into strain. The load cell outputs the load that can be converted into stress.

On-line strain measurement systems such as the ARAMIS system provide continuous sample-scale strain evolution data from the gauge region of a uniaxial tensile sample as shown earlier in Chapter 5. This type of data can be processed to obtain an extended true-stress-true strain curve from a high strain localized region of the specimen where local width and thickness data is available from the respective strains. Such a procedure was utilized with AA6111-T4 uniaxial tensile data from the ARAMIS system resulting in Figure 7-10. This figure shows the dimensionless curves of thickness, width and area calculated from ARAMIS experimental data for an AA6111-T4 uniaxial tensile specimen.

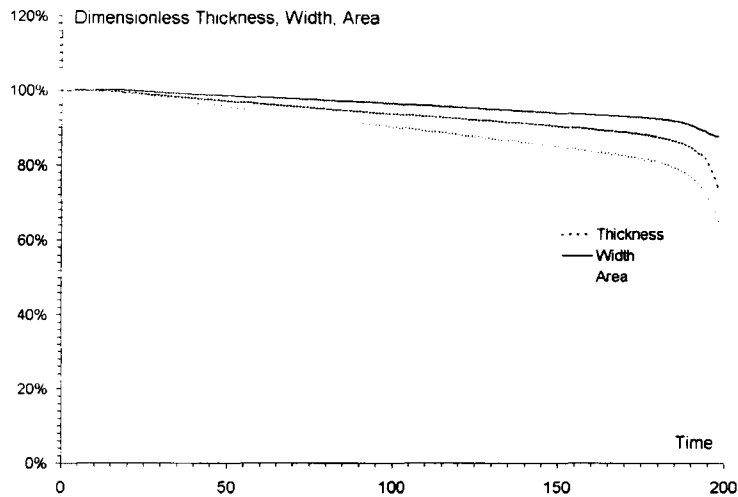


FIGURE 7-10. Ratios of thickness, width and area with respect to the original values obtained from strain imaging system (AA6111-T4, 1 mm thickness).

Instantaneous width and thickness data in Figure 7-10 were further processed to obtain the extended true stress-true strain curve. This curve is shown in Figure 7-11 along with the conventional engineering and true stress-strain curves.

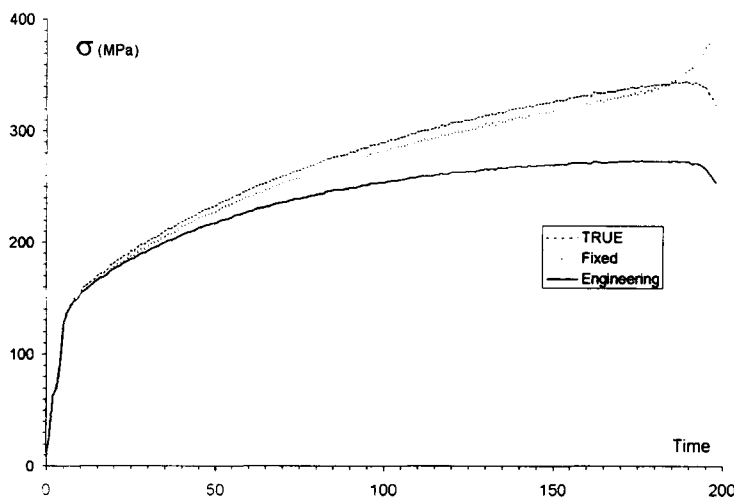


FIGURE 7-11. Stress versus time curves for uniaxial tests on AA6111-T4 sheet (Three curves correspond to conventional engineering, true stresses and true stresses from the ARAMIS system based on local width and length strain measurements).

As shown, the ARAMIS based stress curves in terms of time does not drop as the conventional engineering or true stress-strain curve, but increases when the cross-section of the sample is reduced in the last stage of the test. The above relationship is re-plotted in terms of stress versus strain curves in Figure 7-12. Clearly an extended true stress-strain curve is possible with the use of the ARAMIS system and therefore better than the conventional determination of true stress-true strain curves using a clip-on extensometer.

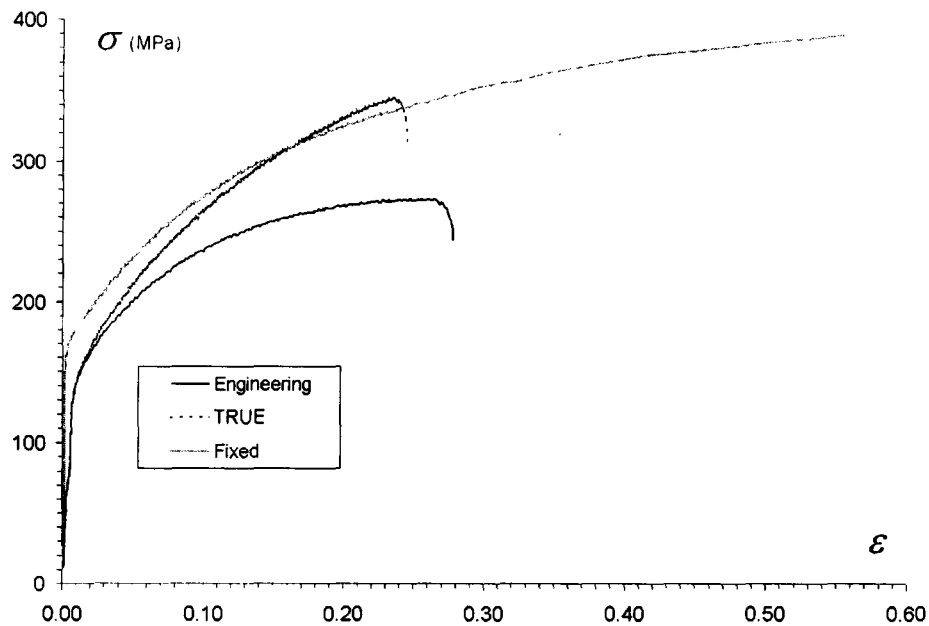


FIGURE 7-12. Engineering stress-strain curve and two different corresponding true stress-strain curves from (i) conventional method, and (ii) based on local strain measurements (AA6111-T4, 1 mm thickness, test speed 0.25 mm/s).

A comparison of the stress normalized work hardening rate as a function of strain from the previous figure is shown in Figure 7-13. Also, added is a curve based on hybrid law (3) from the earlier optimization work. The results reveal that the hybrid law follows the ARAMIS based extended curve rather well up to the experimental true strains of 0.55.

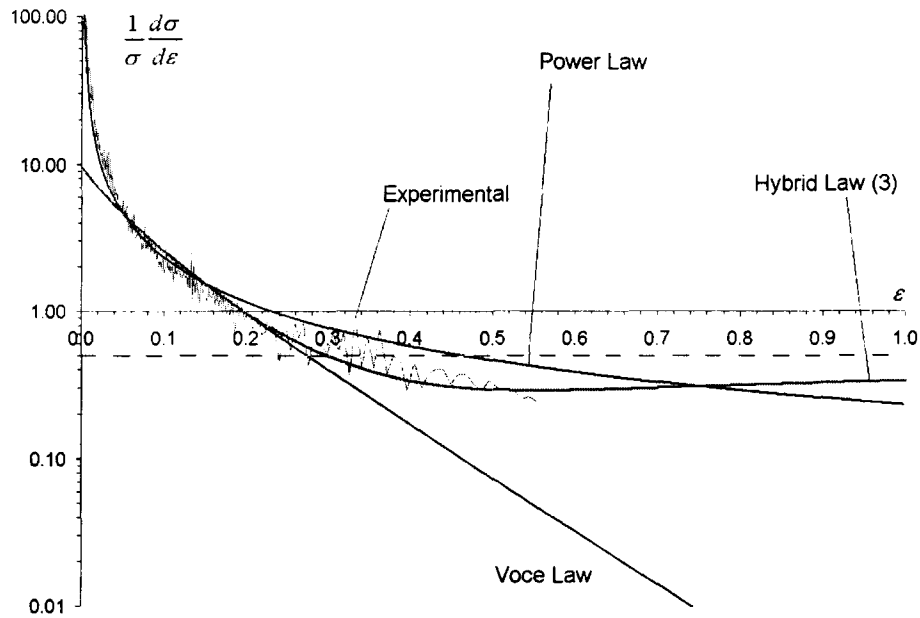


FIGURE 7-13. Plot of hardening behaviour with various hardening laws (power, Voce, hybrid 3 and experimental, horizontally dashed line indicating localized necking, AA6111-T4, 1 mm thickness, test speed 0.25 mm/s).

The purpose of this analysis was to obtain a direction for the curve fitting in the optimization procedure. The value of present investigation is that it can effectively minimize the number of tests. However, the optimization procedure developed in this work does not rely on the measurement of stress-strain curves using such sophisticated tools as the ARAMIS system which are not available in typical mechanical or formability testing laboratories and yet it provides results of comparable quality.

Chapter 8

Conclusions

Many aspects of forming limit prediction have been addressed in this research leading to the development of a unified and robust methodology for rapid determination of forming limit diagrams of sheet materials that does not rely on experimental strain measurements. The methodology has been verified for a range of materials, gauges, strain rates, specimen geometry and other test conditions. The developments in this research include (1) a proposed localized necking criterion and its adaptations to experimental and numerical spatial and temporal strain data, (2) analysis of punch load traces for a characteristic point (3) detailed examination of the traditional strain paths with various specimen geometries and lubrication conditions in conjunction with the proposed localized necking criterion, (4) investigation of some unconventional strain paths to extend the strain range for forming limits, (5) validation of the proposed criterion for material thickness and rate effects, (6) optimization of material and friction input for FE modeling, and finally (7) validation of final predicted forming limits using the proposed approach with independent experimentally obtained FLDs.

The main conclusions can be stated as follows:

1. An inflection point in the punch load versus displacement trace from the hemispherical punch test, indicative of the onset of diffuse necking, can be

utilized effectively in calibrating the FE based load displacement curves with those from the experiments.

2. A similar inflection point exists in the strain rate history of the critical region of the deforming sheet material. This inflection point corresponds to the onset of localized necking and can be easily obtained by plotting the strain history in terms of the major strain acceleration. This major strain acceleration criterion can be used to obtain forming limit along any specific strain path and subsequently the forming limit diagram.
3. The major strain acceleration criterion, $(\dot{\epsilon}_1)_{\max}$, rather than the critical major strain, $(\epsilon_1)_{cr}$, or the Bragrad criterion, ϵ_{Br} , exhibits a more definite physical meaning.
4. Experimental results of strain evolution indicate that minor strain continues to evolve even after a localized neck has been established.
5. The inflection point in the curves of major strain rate for various strain paths can be generalized as a transition from tension to shear.
6. An optimization method for improving the quality and consistency of the material and friction input data for the FE simulations of the experiments has been developed. A hybrid hardening law, based on a combination of Hollomon law and Voce law, has been proposed and is shown to yield good results when calibrating the experimental and numerical stress-strain curves. This law has also been validated with extrapolated stress-strain curves from on-line, sample-scale strain measurements from uniaxial tension tests.

7. Predicted forming limit diagrams using the proposed experimental-numerical methodology are in good agreement with those obtained by the use of the proposed experimental procedure for aluminum sheet materials AA6111-T4, AA6181-T4 and for steel sheet, DP600.

The proposed criterion to obtain the formability characteristics of automotive sheet materials produced good results and reasonable agreement with experiments. This approach provides a rapid determination of limit strains to construct the FLD with little subjectivity and in an efficient manner.

References

- Barata da Rocha, A., Barlat, F., Jalinier, J.M., *Prediction Of The Forming Limit Diagrams Of Anisotropic Sheets In Linear And Non-Linear Loading*, Material Science Engineering, vol. 68, p. 151 – 164, 1984.
- Barata Da Rocha, A., Jalinier, J.M., *Plastic Instability Of Sheet Metals Under Simple And Complex Strain Paths*, Transaction of Iron and Steel Institute, Japan, vol. 24, no.2, p.132 – 140, 1984.
- Barata da Rocha, A., in: *Forming Limit Diagrams: Concepts, Methods and Applications*, Wagoner, R.H., Chan, K.S., Keeler, S.P. (eds.), The Minerals, Metals & Materials Society (TMS), p. 183 – 202, 1989.
- Barlat, F., *Crystallographic Texture, Anisotropic Yield Surfaces And Forming Limits Of Sheet Metals*, Materials Science and Engineering, 91, p. 55 – 72, 1987.
- Barlat, F., *Forming Limit Diagrams - Predictions Based On Some Microstructural Aspects Of Materials*, The Minerals, Metals & Materials Society, p. 275 – 301, 1989.
- Barlat, F., Lian, J., *Plastic Behaviour And Stretchability Of Sheet Metals, Part I: A Yield Function For Orthotropic Sheets Under Plane Stress Conditions*, International Journal of Plasticity, 5, p. 51 – 66, 1989.
- Barlat, F., Lege, D.J., Brem, C., *A Six-Component Yield Function For Anisotropic Materials*, International Journal of Plasticity, vol.7, p. 693 – 712, 1991.

- Barlat, F., Becker, R.C., Brem, J.C., Lege, D.J., Murtha, S.J., Hayashida, Y., Maeda, Y., Yanagawa, M., Chung, K., Matsui, K., Hattori, S., *Yielding Description For Solution Strengthened Aluminum Alloys*, International Journal of Plasticity, vol. 13, no. 4, p. 385 – 401, 1997.
- Barlat, F., Lazov, M.V., Brem, J.C., Lege, D.J., *Strain And Strain Rate Hardening Modelling For Aluminum Alloys*, Plasticity'02, Khan, A., Lopez-Pamies, O. (editors), Neat Press, p. 690 – 692, 2002.
- Bassani, J.L., *Yield Characterization Of Metals With Transversely Isotropic Plastic Properties*, International Journal of Mechanical Sciences, 19, p. 651 – 670, 1977.
- Bate, P., Wilson, D.V., *Strain localization in biaxially stretched sheets containing compact defects II: Analysis using a finite element model*, International Journal of Mechanical Sciences, vol. 26 no. 5, p. 363 – 372, 1984.
- Bishop, J.F.W., Hill, R., *A Theory Of The Plastic Distortion Of A Polycrystalline Aggregate Under Combined Stresses*, Philosophical Magazine, vol. 42, p. 414 – 427, 1951.
- Burford D.A., Wagoner, R.H., *A More Realistic Method For Predicting The Forming Limits Of Metal Sheets*, Forming Limit Diagram: Concepts, Methods, and Applications, Wagoner, R.H., Chan, K.S., Keeler, S.P. (Editors), The Minerals, Metals and Materials Society (TMS), 1989.
- Boogaard, A.H. van den, *Thermally Enhanced Forming of Aluminum Sheet (Modelling and experiments)*, Dissertation, University of Twente, The Netherlands, 2002.

- Bragard, A., Baret, J.C., Bonnarens, H., *A Simplified Method To Determine The FLD Onset Of Localized Necking*, Liège, Rapport Centre de Recherche de la métallurgie, vol. 35, 33, 1972.
- Chow, C.L., Jie, M., Hu, S.J., *Forming Limit Analysis Of Sheet Metals Based On A Generalized Deformation Theory*, Journal of Engineering Materials and Technology, vol. 125, iss. 3, p. 260 – 265, 2001.
- Chu, C.C., *On The Effect Of Strain Path On The Formability Of Sheet Metal*, in Experimental Verification of Process Models, American Society for Metals, p. 278 – 287, 1983.
- Cockroft, M.G., Latham, D.J., *Ductility And The Workability Of Metals*, Journal of Institute of Metals, vol. 96, p. 33 – 39, 1968.
- Considère, A., *Mémoire sur l'emploi du fer et de l'acier dans les constructions*, Annales des Ponts et Chaussées, 9, 574, 1985.
- Drucker, D. C., *A More Fundamental Approach To Plastic Stress-Strain Relations*, Proceedings of First US National Congress of Applied Mechanics, vol. 1, p. 487 – 491, 1951.
- Ferron, G., Touati, M.M., *Determination Of The Forming Limits In Planar-isotropic And Temperature-sensitive Sheet Metals*, International Journal of Mechanical Sciences, vol. 27, no.3, p. 121 – 133, 1985.
- Freudenthal, A.M., *The Plastic Behaviour Of Engineering Materials And Structures*, New York, Wiley Inc., 1950.

- Galanulis, K., Hofmann, A., *Determination Of Forming Limit Diagram Using An Optical Measurement System*, Proceedings of the SheMet'99, p. 245 – 252, 1999.
- Geiger, M., Merklein, M., *Determination of Forming Limit Diagrams – A New Analysis Method For Characterization of Materials' Formability*, CIRP Annals, STC F, 52/1/2003, p. 213 – 216, 2003.
- Ghosh, A. K., *A Method For Determining The Coefficient Of Friction In Punch Stretching Of Sheet Metals*, International Journal of Mechanical Sciences, vol. 19, p. 457 – 470, 1977.
- Goglio, L., Belinardi, G., *Improving Computational And Experimental Results Matching In Sheet Metal Forming*, Numiform 89, Thompson et al. (Editors), 1989.
- Goodwin, G.M., *Application Of Strain Analysis To Sheet Metal Forming Problems In The Press Shop*, Metall. Ital. vol. 8, p. 767 – 774, 1968.
- Gotoh, M., *A Theory Of Plastic Anisotropy Based On A Yield Function Of Fourth Order*, International Journal of Mechanical Sciences, 19, p. 505 – 520, 1977.
- Gotoh, M., *Effect Of Out-Of-Plane Stress On The Forming Limit Of Sheet Metals*, International Journal J.S.M.E., Series A 38(1), p.123 – 132, 1995.
- Graf, A.F., Hosford, W.F., *Effect Of Changing Strain Paths On Forming Limit Diagrams Of Al2008-T4*, Metallurgical and Materials Transactions, 24A, p. 2497 – 2512, 1993.
- Gurson, A., *Continuum Theory Of Ductile Rupture By Void Nucleation And Growth: Part I - Yield Criteria And Flow Rules Of Porous Ductile Media*, Journal of Engineering Material Technology, vol. 99, p. 2 – 15, 1977.

- Hart, E.W., *Theory Of The Tensile Test*, Acta Metallurgica, 15, p. 351 – 355, 1967.
- Hecker, S.S., *A Simple Forming Limit Curve Technique And Results On Aluminum Alloys*, Sheet Metal Forming and Formability, Proceedings of The 7th International Deep Drawing Research Group (IDDRG) Congress, Amsterdam, 51 – 58, 1972.
- Hecker, S.S., *Experimental Studies Of Yield Phenomena In Biaxially Loaded Metals*, in Constitutive Equations in Viscoplasticity: Computational and Engineering Aspects. ASME, Yew York, p. 1 – 33, 1976.
- Hecker, S.S., *Experimental Studies of Sheet Stretchability*, Proceeding of Formability, Analysis, Modelling and Experimentation, Illinois, October 24 and 25, 1977.
- Hill, R., *A Theory Of The Yielding And Plastic Flow Of Anisotropic Metals*, Proceedings of the Royal Society of London, Series A, vol. 193, p. 281 – 297, 1948.
- Hill, R., Hutchinson, J.W., *Bifurcation Phenomena In The Plane Tension Test*, Journal of Mechanics and Physics of Solids, 23, p. 239 – 264, 1975.
- Hill, R., *Theoretical Plasticity Of Textured Aggregates*, Mathematical Proceedings of the Cambridge Philosophical Society, vol. 85, p. 179 – 191, 1979.
- Horsetemeyer, M.F., Chiesa, M.L., Bammann D.J., *Predicting Forming Limit Diagrams With Explicit And Implicit Finite Element Codes*, SAE Technical Paper 940749, 1994.
- Hosford, W.F., 7th North American Metalworking Conference S.M.E. Dearborn, MI, USA, p. 191 – 200, 1979.
- Hosford, W.F., Caddell, R. M., *Metal Forming—Mechanics and Metallurgy*, 2nd edition, Englewood Cliff, NJ: Prentice Hall, p. 309, 1993.

- Hosford, W.F., Duncan, J.L., *Sheet Metal Forming: A Review*, JOM, vol. 51, no. 11, p. 39 – 44, 1999.
- Inal, K., Wu, P.D., Neale, K.W., *Simulation Of Earing In Textured Aluminum Sheets*, International Journal of Plasticity, 16, p. 635 – 648, 2000.
- Jain, M.K., Allin, J., *Analysis Of Experimental Variability Of Forming Limit Diagrams*, Proceedings of 39th SAMPE Symposium, Anaheim, CA, April 11 – 14, vol. 39, II, p.2564 – 2577, 1994.
- Jain, M.K., Lloyd, D.J., MacEwen, S.R., *Hardening Laws, Surface Roughness And Biaxial Tensile Limit Strains Of Sheet Aluminum Alloys*, International Journal of Mechanical Sciences, vol. 38 no.2, p. 219 – 232, 1996.
- Jones, S.E., Gillis, P.P., *A Generalized Quadratic Flow Law for Sheet Metals*, Metallurgical Transactions A, 15, p. 129 – 137, 1984.
- Kang, J., Wilkinson, D.S., Jain, M.K., Mishra, R.K., *Three-dimensional Structure Of Portevin-Le Chatelier Bands And Shear Bands In Strip Cast AA5754 Sheets Using Digital Image Correlation*, SAE International, 07M-301, 2007.
- Keeler, S.P., Backofen, W.A., *Plastic Instability And Fracture In Sheets Stretched Over Rigid Punches*, Transaction of ASM, vol. 56, p. 25 – 48, 1963.
- Kim, Y., Park, C., *A Numerical And Experimental Study Of Deformation Characteristics Of The Plane Strain Punch Stretching Test*, Metallurgical And Materials Transactions A, vol. 28A, p. 1653 – 1659, 1997.

- Kocks, U.F., Jonas, J.J., Mecking, H., *The Development Of Strain-Rate Gradients*, Symposium of “Formability, Analysis and Experimentation”, Chicago, AIME, 1977.
- Karafilis, A.P., Boyce, M.C., *A General Anisotropic Yield Criterion Using Bounds And A Transformation Weighting Tensor*, Journal of Mechanic and Physics of Solids 41, p. 1859 – 1886, 1993.
- Lian, J., Zhou, D., *Diffuse Necking And Localized Necking Under Plane Stress*, Material Science Engineering, A111, p. 1 – 7, 1989.
- Lin, T.H. *Physical Theory of Plasticity*, Advances In Applied Mechanics, vol. 11, editor Chia-Shun Yih, Academic Press New York, p. 256 – 311, 1971.
- Lloyd, D.J., *The Work Hardening Of Some Commercial Al Alloys*, Materials Science Forum, vol.519 – 521, p. 55 – 61, 2006.
- Logan, R.W., Hosford, W.F., *Upper-Bound Anisotropic Yield Locus Calculations Assuming 111-Pencil Glide*, International Journal of Mechanical Sciences, vol. 22, iss. 7, p. 419 – 430, 1980.
- Lovella, M., Higgsb, C.F., Deshmukha, P., Mobleya, A., *Increasing Formability In Sheet Metal Stamping Operations Using Environmentally Friendly Lubricants*, Journal of Materials Processing Technology, vol. 177, iss. 1 – 3, p. 87 – 90, 2006.
- Makinde, A., Thibodeau, L., Neale. K.W., *Development Of An Apparatus For Biaxial Testing Using Cruciform Specimens*, Experimental Mechanics, vol. 32, 2, p. 138 – 144, 1992.

- Marciniak, Z., Kuczynski, K., *Limit Strains In The Process Of Stretch-Forming Sheet Metal*, International Journal of Mechanical Sciences, vol. 9, p. 609 – 620, 1967.
- Marciniak, Z., Kuczynski, K., Pokora, T., *Influence Of The Plastic Properties Of A Material On The Forming Limit Diagram For Sheet Metal In Tension*, International Journal of Mechanical Sciences, vol. 15, p. 789 – 805, 1973.
- Marciniak, Z., Kuczynski, K., *The Forming Limit Curve For Bending Processes*, International Journal of Mechanical Sciences, vol. 21 no. 10, p. 609 – 621, 1979.
- McClintock, F.A., *A Criterion For Ductile Fracture By The Growth Of Holes Subjected To Multiaxial Stress States*, Journal of Applied Mechanics, vol. 35, p. 363 – 371, 1968.
- Miyauchi, K., *Some Interesting Behaviour Of Prestrained Sheet Metals In Press Forming*, IDDRG Working Group Meetings, 1985
- Montheillet, F., Gilormini, P., Jonas, J.J., *Relation Between Axial Stresses And Texture Development During Torsion Testing: A Simplified Theory*, Acta Metallurgica, 33, p. 705 – 717, 1985.
- Müschelborn, W., Sonne, H.M., *Einfluß des Formänderungsweges auf die Grenzformänderungen des Feinglechs*, Archiv für das Eisenhüttenwesen, vol. 46, no.9, p. 597 – 602, 1975.
- Needleman, A., Tvergaard, V., *An Analysis Of Ductile Rupture In Notched Bars*, Journal of Mechanical Physics of Solids, vol. 32, no. 6, 1984.

- Nie, Q.Q., Lee, D., Mater, J., *The Effect Of Rate Sensitivity On History Dependent Forming Limits Of Anisotropic Sheet Metals*, Journal of Material Shaping Technology, vol. 9, p. 233 – 240, 1991.
- Oyane, M., Sato, T., Okimoto, K., Shima, S., *Criteria For Ductile Fracture And Their Applications*, Journal of Mechanical Working Technology, vol. 4, p. 65 – 81, 1980.
- Parmar, A., Mellor, P.B., Chakrabarty, J., *A New Model For The Prediction Of Instability And Limit Strains In Thin Sheet Metal*, International Journal of Mechanical Sciences, vol. 19 no. 7, p. 389 – 398, 1977.
- Pearce, R., *Some Aspects Of Anisotropic Plasticity In Sheet Metals*, International Journal of Mechanical Sciences, vol. 10, p. 995 – 1004, 1968.
- Pepelnjak, T., Petek, A., Kuzman, K., *Analysis Of The Forming Limit Diagram In Digital Environment*, Advanced Materials Research, vol. 6 – 8, p. 697 – 704, 2005.
- Rasmussen, S.N., *Effect Of Rounded Vertices In The Yield Surface On Localized Necking In Biaxially Stretched Sheets*, International Journal of Mechanical Sciences, vol. 24, p. 729 – 739, 1982.
- Rice, J.R., Tracey, D., *On The Ductile Enlargement Of Voids In Triaxial Stress Fields*, Journal of Mechanics and Physics of Solids, vol. 17, p. 201 – 217, 1969.
- Samuel, M., *FEM Simulations And Experimental Analysis Of Parameters Of Influence In The Blanking Process*, Journal of Material Processing Technology, vol. 84, p. 97 – 116, 1998.

- Schey, J.A., Fischer, R.F., *Effects Of Clamp Force In Limiting Dome Height (LDH) Test*, Journal of material Shaping Technology, 9, 85 – 88, 1991.
- Smith, L.M., Averill, R.C., Lucas, J.P., Stoughton, T.B., Matin, P.H., *Influence Of Transverse Normal Stress On Sheet Metal Formability*, International Journal of Plasticity, 19, p. 1567 – 1583, 2003.
- Situ, Q., Bruhis, M., Jain, M.K., *Obtaining Formability Characteristics Of Automotive Materials Using On-line Strain Imaging System*, The 6th International Conference and Workshop on Numerical Simulation of 3D Sheet Forming Processes, Detroit, Michigan, USA, August 15th – 19th, Proceeding p. 131 – 135, 2005.
- Situ, Q., Bruhis, M., Jain, M.K., *A Suitable Criterion For Precise Determination Of Incipient Necking In Sheet Materials*, Materials Science Forum, vol. 519 – 521, p. 111 – 116, 2006.
- Savoie, J, Jain, M., Wu, P.D., Tugcu, P., Neale, K.W., *Assessment Of Various Yield Criteria For Prediction Of Forming Limit Strains In An Aluminum Sheet*, The Minerals, Metals & Materials Society (TMS), October, 1988.
- Storen, S., Rice, J.R., *Localized Necking In Thin Sheets*, Journal of the Mechanics and Physics of Solids, 24, p. 421 – 441, 1975.
- Story, J.M., *Variables Affecting Dome Test Results*, Journal of Applied Metalworking, vol. 2, no. 2, p. 119 – 125, 1982.
- Swift, H.W., *Plastic Instability Under Plane Stress*, Journal of the Mechanics and Physics of Solids, vol. 1, p.1 – 18, 1952.

- Takuda, H., Tanaka, Y., Hatta, N., *Finite Element Analysis of Forming Limit In Bore Expanding of Aluminum Alloy Sheets*, Applied Mechanics, 68, p. 566 – 576, 1998.
- Taylor, G.I., *Plastic Strains In Metals*, Journal of Institute Metals, 62, p. 307 – 324, 1938.
- Thomson, A., *High Strain Rate Characterization of Advanced High Strength Steels*, Thesis of Master of Applied Science in Mechanical Engineering, University of Waterloo, 2006.
- Toh, C.H., Shiau, Y.C., Kobayashi, S., *Analysis Of A Test Method OF Sheet metal Formability Using The Finite Element Method*, Journal of Engineering for Industry, vol. 108, p. 3 – 8, 1986.
- Toth, L., Hirsch, J., Houtte, P., *On the role of texture development in the forming limits of sheet metals*, International Journal of Mechanical Sciences, vol. 38, p. 1117 – 1126, 1996.
- Tresca, H., *Sur l'écoulement des Corps. solides soumis a`des fortes pressions*. Compt. Rend. Acad., Sci. Paris, 59, p. 754 – 756, 1964.
- Voce, E., *The Relationship Between Stress And Strain For Homogeneous Deformation*, Journal of Institute Metals, vol. 74, p. 537 – 562, 1948.
- Voce, E., *A Practical Strain Hardening Function*, Metallurgia, p. 219 – 226, 1955.
- von Mises, R., Angew, R., *Mechanik der plastischen Formiinderung von Kristallen*, Mathematik Und Mechanik, 8, p. 161 – 185, 1928.
- Wagoner, R.H., *A Technique For Measuring Strain-Rate Sensitivity*, American Society For Metals And The Metallurgical Society Of AIME, vol. 12A, January, 1981.

- Wilson, D.V., Roberts, W.T., Rodrigues, P.M.B., *Effect Of Grain Anisotropy On Limit Strains In Biaxial Stretching-Part 1*, Metallurgy Transaction A, 12A, p. 1595 – 1611, 1982.
- Wilson, D.V., Mirshams, A.R., Roberts, W. T., *An Experimental Study Of The Effect Of Sheet Thickness And Grain Size On Limit-Strains In Biaxial Stretching*, International Journal of Mechanical Sciences, vol. 25, p. 859 – 870, 1983.
- Yamada, Y., Koide, M., *Analysis Of The Bore-Expanding Test By The Incremental Theory Of Plasticity*, International Journal Of Mechanical Sciences, vol. 10, p. 1 – 4, 1968.
- Yang, T.S., Hsu, T.C., *Forming Limit Analysis Of Hemispherical-Punch Stretch Forming*, Journal of Materials Processing Technology, vol. 117, no.1 – 2, p. 32 – 36, 2001.
- Zhao, L., Sowerby, R., Sklad, M.P., *The Influence Of Strain Path And Material Properties On Forming Limit Diagrams*, Proceedings of AEPA '96, Hong Kong, p. 709 – 714, 1996.
- Zhou, Y., Neale, K.W., *Texture Evolution During The Biaxial Stretching Of f.c.c. Sheet Metals*, Textures and Microstructures, 22, p. 87, 1993.
- Zhu, X., Weinmann, K., Chandra, A., *A Unified Bifurcation Analysis Of Sheet Metal Forming Limits*. Journal of Engineering Materials and Technique, 3, 329 – 333, 2001.

Appendices

Appendix 1. Analytical Model Of Hemispherical Punch Test

An analytical model is established to reveal the instability characteristics of the load versus displacement curve from a punch-based test. The geometry of the deformed specimen (full dome) and punch test rig (punch and die) is analyzed for the hemispherical punch stretching process (Figure A1-1).

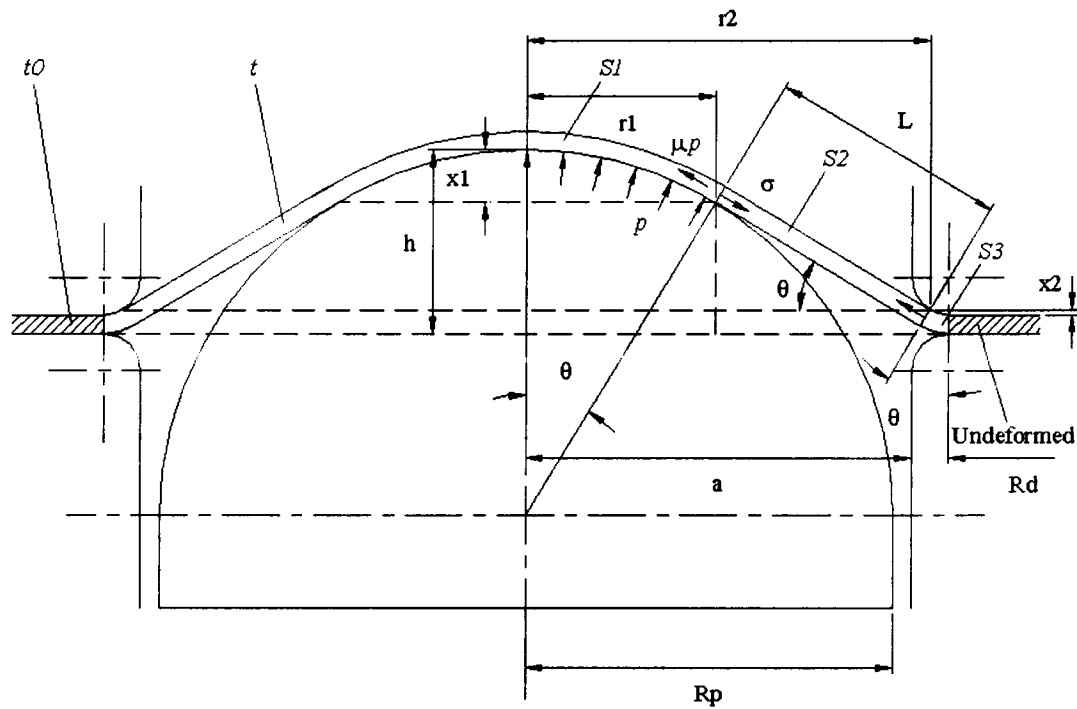


FIGURE A1-1. Schematic of full dome specimen with rigs.

Nomenclature of symbols used in above figure:

R_p	punch radius
R_d	die edge radius
a	inner radius of die
h	punch height
θ	contact angle
r_1	contact radius of punch (to punch axis)
r_2	contact radius of die (to punch axis)
x_1	contact height of punch
x_2	contact height of die
S_1	surface area of contact in punch
S_2	surface area of straight section
S_3	surface area of contact in die

The following assumptions are made:

- the sheet is subjected to uniform deformation;
- the deformation of the sheet is within the edge of the die, the material outside the edge is considered undeformed;
- the instantaneous deformed sheet is considered to contain three parts: spherical section over the punch (S_1), the spherical section over the die (S_3), and stretched straight section tangential to the punch and die (S_2);
- the pressure exerted over the contact area of the punch is considered uniform;
- the friction is considered uniform (and neglected in the final equations);

- the thickness of the sheet is negligible compared to tool size, or represented by the middle of the sheet

The following geometric relationships of the instantaneous parameters to the punch height can be obtained:

$$r_1 = R_p \sin \theta \quad (\text{Eq A-1})$$

$$x_1 = R_p (1 - \cos \theta) \quad (\text{Eq A-2})$$

$$r_2 = a + R_d (1 - \sin \theta) \quad (\text{Eq A-3})$$

$$x_2 = R_d (1 - \cos \theta) \quad (\text{Eq A-4})$$

$$L = \frac{r_2 - r_1}{\cos \theta} \quad (\text{Eq A-5})$$

$$h = L \sin \theta + (x_1 + x_2) = (r_2 - r_1) \tan \theta + (x_1 + x_2) \quad (\text{Eq A-6})$$

Since the punch height h is the main parameter of interest and is increasing constantly during the test, the other parameters are converted to functions of the punch height. The relationship between contact radius r_1 and punch height h is the most important.

Incorporating Equations (A-1), (A-2), (A-3), (A-4) into (A-6), one can obtain:

$$\begin{aligned} h &= (r_2 - r_1) \tan \theta + (x_1 + x_2) \\ &= [a + R_d (1 - \sin \theta) - R_p \sin \theta] \tan \theta + [R_p (1 - \cos \theta) + R_d (1 - \cos \theta)] \\ &= [(a + R_d) - (R_d + R_p) \sin \theta] \tan \theta + [(R_d + R_p) (1 - \cos \theta)] \end{aligned}$$

Multiplying both sides with $\cos\theta$, one can obtain:

$$h \cos\theta = [(a + R_d) - (R_d + R_p) \sin\theta] \sin\theta + [(R_d + R_p)(1 - \cos\theta)] \cos\theta$$

$$h \cos\theta = (a + R_d) \sin\theta - (R_d + R_p) \sin^2\theta + (R_d + R_p)(\cos\theta - \cos^2\theta)$$

$$h \cos\theta = (a + R_d) \sin\theta - (R_d + R_p) \sin^2\theta + (R_d + R_p) \cos\theta - (R_d + R_p) \cos^2\theta$$

$$h \cos\theta = (a + R_d) \sin\theta + (R_d + R_p) \cos\theta - (R_d + R_p)$$

Moving $(R_d + R_p) \cos\theta$ to left side and combine with $h \cos\theta$, one can obtain:

$$(h - R_d - R_p) \cos\theta = (a + R_d) \sin\theta - (R_d + R_p)$$

$$(h - R_d - R_p) \sqrt{1 - \sin^2\theta} = (a + R_d) \sin\theta - (R_d + R_p)$$

Taking square of both sides, one can obtain:

$$(h - R_d - R_p)^2 (1 - \sin^2\theta) = [(a + R_d) \sin\theta - (R_d + R_p)]^2$$

$$(h - R_d - R_p)^2 (1 - \sin^2\theta) = (a + R_d)^2 \sin^2\theta + (R_d + R_p)^2 - 2(a + R_d)(R_d + R_p) \sin\theta$$

$$[(a + R_d)^2 + (h - R_d - R_p)^2] \sin^2\theta - 2(a + R_d)(R_d + R_p) \sin\theta + [(R_d + R_p)^2 - (h - R_d - R_p)^2] = 0$$

(Eq A-7)

Solutions of Eq (A-7) in term of $\sin\theta$ are obtained as:

$$\sin\theta = \frac{[2(a + R_d)(R_d + R_p)] \pm \sqrt{[2(a + R_d)(R_d + R_p)]^2 - 4[(a + R_d)^2 + (h - R_d - R_p)^2][(R_d + R_p)^2 - (h - R_d - R_p)^2]}}{2[(a + R_d)^2 + (h - R_d - R_p)^2]}$$

This is further simplified as Eq (A-8):

$$\sin\theta = \frac{[(a + R_d)(R_d + R_p)] \pm [(a + R_d)(R_d + R_p)] \sqrt{1 - [1 + \frac{(h - R_d - R_p)^2}{(a + R_d)^2}][1 - \frac{(h - R_d - R_p)^2}{(R_d + R_p)^2}]}{(a + R_d)^2 [1 + \frac{(h - R_d - R_p)^2}{(a + R_d)^2}]}$$

$$= \frac{R_d + R_p}{a + R_d} \frac{1 \pm \sqrt{1 - \left[1 + \left(\frac{R_d + R_p}{a + R_d} \right)^2 \left(1 - \frac{h}{R_d + R_p} \right)^2 \right] \left[1 - \left(1 - \frac{h}{R_d + R_p} \right)^2 \right]}}{\left[1 + \left(\frac{R_d + R_p}{a + R_d} \right)^2 \left(1 - \frac{h}{R_d + R_p} \right)^2 \right]}$$

(Eq A-8)

There are two solutions of Eq (A-8) as below:

$$\sin \theta|_1 = \frac{R_d + R_p}{a + R_d} \frac{1 + \sqrt{1 - \left[1 + \left(\frac{R_d + R_p}{a + R_d} \right)^2 \left(1 - \frac{h}{R_d + R_p} \right)^2 \right] \left[1 - \left(1 - \frac{h}{R_d + R_p} \right)^2 \right]}}{\left[1 + \left(\frac{R_d + R_p}{a + R_d} \right)^2 \left(1 - \frac{h}{R_d + R_p} \right)^2 \right]}$$

$$\sin \theta|_2 = \frac{R_d + R_p}{a + R_d} \frac{1 - \sqrt{1 - \left[1 + \left(\frac{R_d + R_p}{a + R_d} \right)^2 \left(1 - \frac{h}{R_d + R_p} \right)^2 \right] \left[1 - \left(1 - \frac{h}{R_d + R_p} \right)^2 \right]}}{\left[1 + \left(\frac{R_d + R_p}{a + R_d} \right)^2 \left(1 - \frac{h}{R_d + R_p} \right)^2 \right]}$$

Solution 1 is for $\pi/2 \leq \theta \leq \pi$, which is not the expected range. Solution 2 is for $0 \leq \theta \leq \pi/2$, which is further studied. Incorporating Eq (A-1) into (A-8), one can obtain:

$$\sin \theta = \frac{R_d + R_p}{a + R_d} \frac{1 - \sqrt{1 - \left[1 + \left(\frac{R_d + R_p}{a + R_d} \right)^2 \left(1 - \frac{h}{R_d + R_p} \right)^2 \right] \left[1 - \left(1 - \frac{h}{R_d + R_p} \right)^2 \right]}}{\left[1 + \left(\frac{R_d + R_p}{a + R_d} \right)^2 \left(1 - \frac{h}{R_d + R_p} \right)^2 \right]} = \frac{r_1}{R_p}$$

(Eq A-9)

The expressions for contact radius r_1 and contact angle θ of punch are shown below:

$$r_1 = \frac{R_d + R_p}{a + R_d} \frac{1 - \sqrt{1 - \left[1 + \left(\frac{R_d + R_p}{a + R_d}\right)^2 \left(1 - \frac{h}{R_d + R_p}\right)^2\right] \left[1 - \left(1 - \frac{h}{R_d + R_p}\right)^2\right]}}{\left[1 + \left(\frac{R_d + R_p}{a + R_d}\right)^2 \left(1 - \frac{h}{R_d + R_p}\right)^2\right]} R_p \quad (\text{Eq A-10})$$

$$\theta = \arcsin\left(\frac{r_1}{R_p}\right) \quad (\text{Eq A-11})$$

Above equations show that the contact radius (r_1) is a function of tool dimensions (R_p , R_d , a) and punch displacement or dome height (h), regardless of material parameter. This has been experimentally established by Ghosh [Ghosh, 1977]. Other parameters, x_1 , x_2 , r_2 , L can be obtained from above values of contact radius (r_1) and contact angle of punch (θ).

Due to the plastic incompressibility (constant volume of material), the instantaneous sheet thickness can be obtained as:

$$V = \pi(a + R_d)^2 t_0 = (S_1 + S_2 + S_3) t \quad (\text{Eq A-12})$$

where the surface areas of S_1 , S_2 and S_3 are punch contact, die contact and straightened part.

S_1 is the surface area of the crown formed by the punch, which can be obtained as:

$$S_1 = \int_0^\theta (2\pi R_p \sin \theta) (R_p d\theta) = 2\pi R_p^2 \int_0^\theta \sin \theta d\theta = 2\pi R_p^2 (1 - \cos \theta) = 2\pi R_p x_1 \quad (\text{Eq A-13})$$

S_2 is the side surface area of a truncated cone, or frustum. An expansion of the side surface of the frustum is given in Figure A1-2.

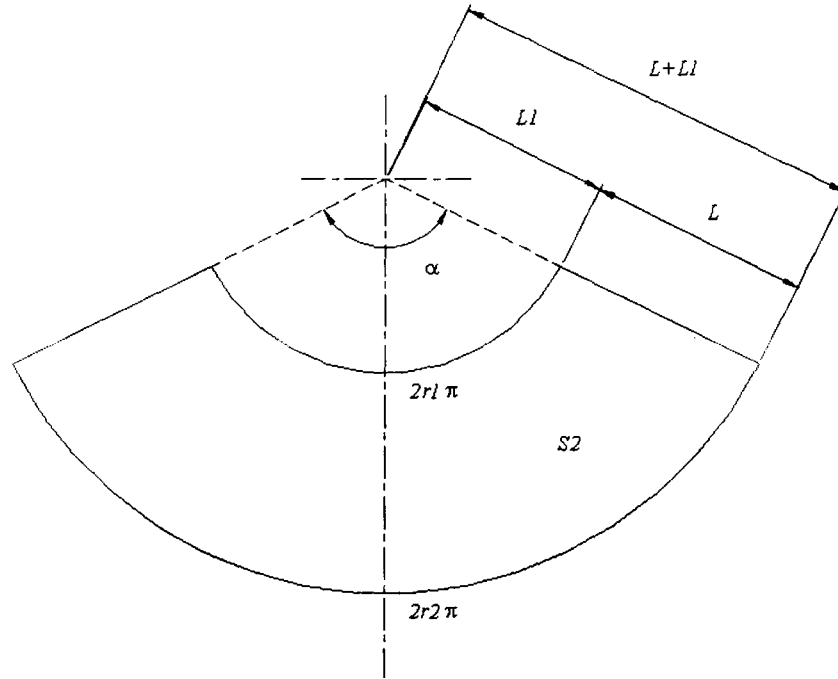


FIGURE A1-2. Expanded surface of truncated cone of area S_2 .

The geometric relationship of the top surface (r_1 circle) and base surface (r_2 circle) produces:

$$\alpha = \frac{2\pi r_1}{L_1} = \frac{2\pi r_2}{L_1 + L} = \frac{2\pi r_2 + 2\pi r_1}{L_1 + L + L_1} = \frac{2\pi(r_2 + r_1)}{2L_1 + L} \quad (\text{Eq A-14})$$

where α , L_1 and L are the expansion angle, inner radius and slant height respectively.

$$S_2 = \pi(L_1 + L)^2 \frac{\alpha}{2\pi} - \pi(L_1)^2 \frac{\alpha}{2\pi} = \frac{\alpha}{2} [(L_1 + L)^2 - (L_1)^2] = \frac{\alpha}{2} (2L_1 + L)L = \pi(r_2 + r_1)L \quad (\text{Eq A-15})$$

S_3 is the surface area of the crown formed by the die, which can be obtained as:

$$\begin{aligned}
 S_3 &= \int_0^\theta 2\pi [a + R_d(1 - \sin \theta)] (R_d d\theta) = 2\pi R_d (a + R_d) \int_0^\theta d\theta - 2\pi R_d^2 \int_0^\theta \sin \theta d\theta \\
 &= 2\pi R_d (a + R_d) \theta - 2\pi R_d^2 (1 - \cos \theta) = 2\pi R_d (a + R_d) \theta - 2\pi R_d x_2
 \end{aligned}$$

(Eq A-16)

The current thickness t (initial thickness t_0) is obtained as:

$$\begin{aligned}
 \frac{t_0}{t} &= \frac{S_1 + S_2 + S_3}{(a + R_d)^2} = \frac{2R_p x_1 + (r_1 + r_2)L + 2R_d(a + R_d)\theta - 2R_d x_2}{(a + R_d)^2} \\
 &= \frac{R_p^2 - R_d^2}{(a + R_d)^2} \left(2 - \cos \theta - \frac{1}{\cos \theta} \right) + \frac{R_d}{a + R_d} (2\theta - 2 \tan \theta) + \frac{1}{\cos \theta}
 \end{aligned}$$

(Eq A-17)

The thickness strain is then obtained as:

$$-\varepsilon_t = \ln \left(\frac{t_0}{t} \right) = \ln \left[\frac{R_p^2 - R_d^2}{(a + R_d)^2} \left(2 - \cos \theta - \frac{1}{\cos \theta} \right) + \frac{R_d}{a + R_d} (2\theta - 2 \tan \theta) + \frac{1}{\cos \theta} \right]$$

(Eq A-18)

Considering the plastic incompressibility ($\varepsilon_1 + \varepsilon_2 + \varepsilon_3 = 0$) for balanced biaxial loading ($\varepsilon_1 = \varepsilon_2$), the thickness strain is obtained as $\varepsilon_3 = -2\varepsilon_1 = \varepsilon_t$. The effective strain can be obtained as:

$$\bar{\varepsilon} = \frac{\sqrt{2}}{3} \sqrt{(\varepsilon_1 - \varepsilon_2)^2 + (\varepsilon_2 - \varepsilon_3)^2 + (\varepsilon_3 - \varepsilon_1)^2} = 2\varepsilon_1 = -\varepsilon_3 = -\varepsilon_t$$

(Eq A-19)

$$\text{or, } \bar{\varepsilon} = \ln \left[\frac{R_p^2 - R_d^2}{(a + R_d)^2} \left(2 - \cos \theta - \frac{1}{\cos \theta} \right) + \frac{R_d}{a + R_d} (2\theta - 2 \tan \theta) + \frac{1}{\cos \theta} \right]$$

(Eq A-20)

The instantaneous sheet thickness can then be obtained as:

$$t = t_0 \exp(-\bar{\varepsilon})$$

(Eq A-21)

Since the geometry is axisymmetric, the horizontal component of punch force (at the punch contact periphery) along the circumference is balanced and cancelled. The vertical component of punch force is obtained as:

$$\begin{aligned}
 F &= \int_0^\theta (p \cos \theta + \mu p \sin \theta)(2\pi R_p \sin \theta)(R_p d\theta) = \pi p R_p^2 \int_0^\theta 2(\cos \theta + \mu \sin \theta) \sin \theta d\theta \\
 &= \pi p R_p^2 \int_0^\theta (2 \cos \theta \sin \theta + 2\mu \sin^2 \theta) d\theta = \pi p R_p^2 \int_0^\theta [\sin 2\theta + \mu(1 - \cos 2\theta)] d\theta \\
 &= \frac{1}{2} \pi p R_p^2 [-\cos 2\theta + \mu(2\theta - \sin 2\theta)]_0^\theta = \frac{1}{2} \pi p R_p^2 [-\cos 2\theta + \mu(2\theta - \sin 2\theta) + 1] \\
 &= \pi p R_p^2 [\sin^2 \theta + \mu(\theta - \sin \theta \cos \theta)]
 \end{aligned}$$

(Eq A-22)

The force in the straight section (S_2 in Figure A-1) gives:

$$F = \sigma_1 (2\pi R_p \sin \theta t) \sin \theta \quad \text{(Eq A-23)}$$

Therefore, the relationship between pressure and stress is obtained as:

$$F = \pi p R_p^2 [\sin^2 \theta + \mu(\theta - \sin \theta \cos \theta)] = \sigma_1 (2\pi R_p \sin \theta t) \sin \theta \quad \text{(Eq A-24)}$$

The pressure can then be obtained as:

$$p = \sigma_1 \frac{2t \sin^2 \theta}{R_p [\sin^2 \theta + \mu(\theta - \sin \theta \cos \theta)]} \quad \text{(Eq A-25)}$$

Considering a balanced biaxial loading, $\sigma_1 = \sigma_2$, $\sigma_3 = 0$, Mises effective stress is expressed as:

$$\bar{\sigma} = \frac{1}{\sqrt{2}} \sqrt{(\sigma_1 - \sigma_2)^2 + (\sigma_2 - \sigma_3)^2 + (\sigma_3 - \sigma_1)^2} = \sigma_1 \quad \text{(Eq A-26)}$$

For a material following power law, $\bar{\sigma} = K\bar{\epsilon}^n$, the pressure can be obtained as:

$$\begin{aligned}
 p &= K\bar{\epsilon}^n \frac{2t_0 \exp(-\bar{\epsilon})}{R_p} \frac{\sin^2\theta}{\sin^2\theta + \mu(\theta - \sin\theta \cos\theta)} \\
 &= \frac{2Kt_0}{R_p} \bar{\epsilon}^n \exp(-\bar{\epsilon}) \frac{\sin^2\theta}{\sin^2\theta + \mu(\theta - \sin\theta \cos\theta)} \quad (\text{Eq A-27})
 \end{aligned}$$

Neglecting the friction, or, $\mu = 0$, the pressure can be re-written as:

$$p = \frac{2Kt_0}{R_p} \bar{\epsilon}^n \exp(-\bar{\epsilon}) \quad (\text{Eq A-28})$$

Instability (diffuse necking) occurs when $dp = 0$, On differentiating (Eq A-27) and on substituting this instability condition, one produces:

$$dp = \frac{2Kt_0}{R_p} \bar{\epsilon}^n \exp(-\bar{\epsilon}) \left(\frac{n}{\bar{\epsilon}} - 1 \right) d\bar{\epsilon} = 0, \text{ or, } \frac{n}{\bar{\epsilon}} - 1 = 0, \text{ e.g., } \bar{\epsilon} = n. \quad (\text{Eq A-29})$$

This exactly complies with the theoretical prediction of Hill and Swift. This condition further leads to following specific conditions:

$$\frac{dp}{dh} = \frac{dp}{d\bar{\epsilon}} \frac{d\bar{\epsilon}}{dh} = \frac{dp}{d\bar{\epsilon}} \frac{d\bar{\epsilon}}{v dt} = \frac{1}{v} \frac{dp}{d\bar{\epsilon}} \frac{d\bar{\epsilon}}{dt} = 0, \quad \text{where} \quad \frac{d\bar{\epsilon}}{dt} \neq 0 \quad (\text{Eq A-30})$$

$$\frac{dp}{dr_1} = \frac{dp}{dh} \frac{dh}{dr_1} = \frac{dp}{dh} \frac{1}{\left(\frac{dr_1}{dh} \right)} = 0, \quad \text{where} \quad \frac{dr_1}{dh} \neq 0 \quad (\text{Eq A-31})$$

$$\frac{dp}{d\theta} = \frac{dp}{dh} \frac{dh}{d\theta} = \frac{dp}{dh} \frac{1}{\left(\frac{d\theta}{dh} \right)} = 0, \quad \text{where} \quad \frac{d\theta}{dh} \neq 0 \quad (\text{Eq A-32})$$

Accordingly, when instability occurs, $\bar{\epsilon} = n$, $\frac{dp}{d\bar{\epsilon}} = 0$, $\frac{dp}{dh} = 0$, $\frac{dp}{dr_1} = 0$ and $\frac{dp}{d\theta} = 0$

from equations (Eq A-30) - (Eq A-32).

Incorporating pressure from Eq A-28 into the punch force Eq A-22 (neglecting the friction), one obtains:

$$F = \pi p R_p^2 \sin^2 \theta = (2\pi K_{t_0} R_p) \bar{\epsilon}^n \exp(-\bar{\epsilon}) \sin^2 \theta \quad (\text{Eq A-33})$$

Numerical calculation using Eq A-28 and Eq A-33 are made to obtain punch force F and the inflection (dF/dh) as a function of punch displacement, h . Both of the equations are further processed to have dimensionless form as Eq (A-34) and (A-35).

$$p / \frac{2K_{t_0}}{R_p} = \bar{\epsilon}^n \exp(-\bar{\epsilon}) \quad (\text{Eq A-34})$$

$$F / 2\pi K_{t_0} R_p = \bar{\epsilon}^n \exp(-\bar{\epsilon}) \sin^2 \theta \quad (\text{Eq A-35})$$

At maximum pressure ($dp/dh = 0$), $(dF/dh)_{max}$ is obtained, in other words, inflection in the force versus displacement curves occurs at maximum pressure (Figure A1-3). Alternatively, the onset of instability leads to an inflection in the curve of punch force. Further, the inflection in punch force is associated with $\bar{\epsilon} = n$, the occurrence of instability corresponding to diffuse necking.

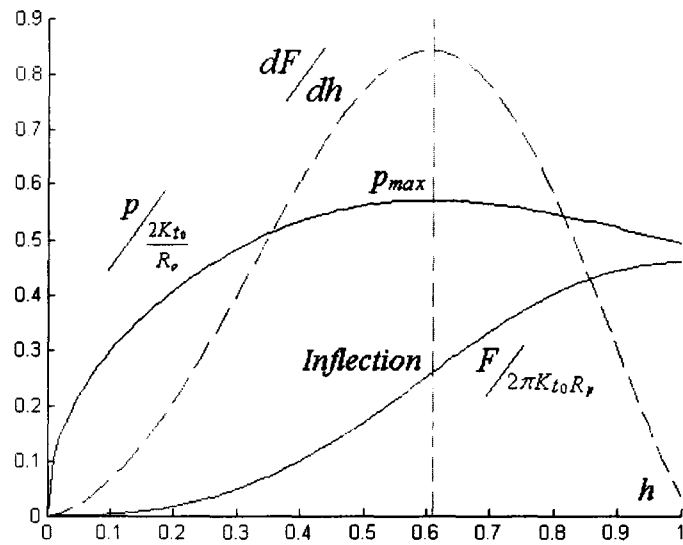


FIGURE A1-3. Analytical model to obtain characteristic points in load curve.

This simplified model agrees with not only the theoretical predictions of Hill and Swift for in-plane deformation but also with the experimental observations of Hecker and Ghosh [Ghosh, 1977] for hemispherical punch tests.

Appendix 2. MATLAB Code For Re-sample Process

(Runs In MATLAB 6)

```

clear all

x0=load('c:\temp\x0.txt');
y0=load('c:\temp\y0.txt');

n0=length(x0);
prec=1E+1;

for p=(x0(1)*prec+1):1:(x0(n0)*prec+1)

kn=0; yk=0; ya=0;
m=(p-1)/prec;

for j=1:1:n0

if x0(j)==m
kn=kn+1; yk=yk+y0(j); ya=yk/kn;
end

end

xm(p)=m;
ym(p)=ya;

end

xm1=xm';
ym1=ym';

hold on
plot(x0, y0, 'b')
plot(xm1, ym1, 'r')

```

Appendix 3. MATLAB Code For Moving Average Method

(Runs In MATLAB 6)

```
clear all
```

```
x=[ ..... ];
m=length(x);
w=n;
```

(number of elements)

(window size)

```
for i=1:1:w
sigma=0;
for s=-(i-1):1:i-1
sigma=sigma+x(i+s);
end
xm(i)=sigma/(2*i-1);
end
```

(average within window)

```
for i=w+1:1:m-w
sigma=0;
for s=-w:1:w
sigma=sigma+x(i+s);
end
xm(i)=sigma/(2*w+1);
end
```

(window moving)

(average within new window)

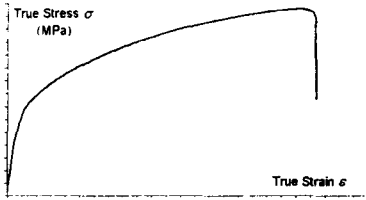
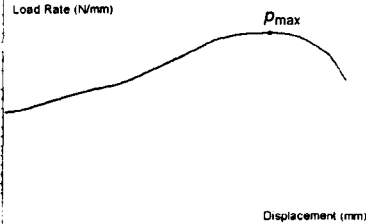
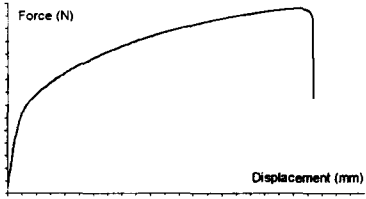
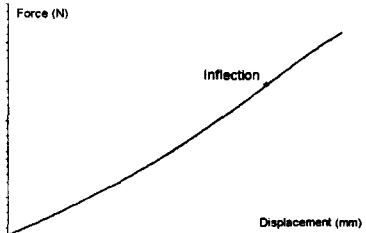
```
i=1:m;
j=1:m-w;
grid
hold;
plot(i,x,'-')
plot(j,xm,'red')
legend('Raw-Data', 'Average',4);
xlabel('Indentation');
ylabel('Reaction Force');
```

(output processed data)

Appendix 4. Instability Criteria Of Uniaxial And Biaxial Tensile Tests

The instability criteria for biaxial loading condition are compared with established criteria for uniaxial tension in Table A4-1. The stress-strain curve in uniaxial tensile test demonstrates a similar shape to force-displacement curve since the sectional area is generally considered as constant. However, in the punch test, both the pressure and the contact area of the dome surface are functions of punch stroke. The attainment of maximum pressure as described earlier corresponds to the occurrence of material instability in the form of diffuse necking. The contact area on the other hand is ever increasing. Therefore, an increasing trend of force is maintained. The instance when maximum pressure is achieved corresponds to the inflection point in the load trace, which indicates the onset of diffuse necking.

TABLE A4-1. Comparison of criteria to determine instability of uniaxial tensile and biaxial tensile.

	Uniaxial Tensile	Biaxial Tensile
Force	$F = \sigma A$	$F = \int p ds$
Instability condition		
Diffuse necking (contact) area	$\mathcal{E} = n$ A constant	$\mathcal{E} = n$ $S = \pi r^2$ (r contact radius)
	<p>Maximum force</p> 	<p>Inflection</p> 
Instability determination	F_{max}	$(dF/dh)_{max}$

Appendix 5. FE Code For Uniaxial Tensile Path

(Runs In ABAQUS 6.4)

```

*Heading
** Job name: Job-1 Model name: Model-1
*Preprint, echo=NO, model=NO, history=NO, contact=NO
**
** PARTS
**
*Part, name=DB
*Node
  1,    0.,   -25.,    0.
*Nset, nset=DB-RefPt_, internal
1,
*Surface, type=REVOLUTION, name=RigidSurface_, internal
START,    27.5,   -5.5
LINE,    27.5,   -4.5
CIRCL,    30.,   -2.,    30.,   -4.5
LINE, 34.457,   -2.
CIRCL, 35.296, -1.545, 34.457,   -1.
LINE, 36.004, -0.455
CIRCL, 36.843,    0., 36.843,   -1.
LINE, 38.157,    0.
CIRCL, 38.996, -0.455, 38.157,   -1.
LINE, 39.704, -1.545
CIRCL, 40.543,   -2., 40.543,   -1.
LINE,    50.,   -2.
*Rigid Body, ref node=DB-RefPt_, analytical surface=RigidSurface_
*End Part
**
*Part, name=DU
*Node
  1,    0.,    25.,    0.
*Nset, nset=DU-RefPt_, internal
1,
*Surface, type=REVOLUTION, name=RigidSurface_, internal
START,    50., 1
LINE, 41.974,    1.
CIRCL, 40.161, 2.154, 41.974,    3.
LINE, 39.839, 2.846
CIRCL, 38.026,    4., 38.026,    2.
LINE, 36.974,    4.

```

```

CIRCL, 35.161, 2.846, 36.974, 2.
LINE, 34.839, 2.154
CIRCL, 33.026, 1., 33.026, 3.
LINE, 30., 1.
CIRCL, 27.5, 3.5, 30., 3.5
LINE, 27.5, 4.5
*Rigid Body, ref node=DU-RefPt_, analytical surface=RigidSurface_
*End Part
**
*Part, name=Dome
*Node
1, 0., 75., 0.
*Nset, nset=Dome-RefPt_, internal
1,
*Surface, type=REVOLUTION, name=RigidSurface_, internal
START, 25., 50.
CIRCL, 0., 25., 0., 50.
*Rigid Body, ref node=Dome-RefPt_, analytical surface=RigidSurface_
*End Part
**
*Part, name=Punch
*Node
1, 0., -50., 0.
*Nset, nset=Punch-RefPt_, internal
1,
*Surface, type=REVOLUTION, name=RigidSurface_, internal
START, 0., 0.
CIRCL, 25., -25., 0., -25.
*Rigid Body, ref node=Punch-RefPt_, analytical surface=RigidSurface_
*End Part
**
*Part, name=Sheet
*Node
*Element, type=C3D8R
**
** Region: (AL:Picked)
*Elset, elset=_PickedSet300, internal, generate
** Section: AL
*Solid Section, elset=_PickedSet300, material=AL
1.,
**
*End Part
**
** ASSEMBLY

```

```

**
*Assembly, name=Assembly
**
*Instance, name=Punch-1, part=Punch
    0.,    -5.,    0.
*End Instance
**
*Instance, name=DB-1, part=DB
*End Instance
**
*Instance, name=DU-1, part=DU
*End Instance
**
*Instance, name=Sheet-1, part=Sheet
    0.,    0.,    0.
    0.,    0.,    0.,    -1.,    0.,    0., 90
*End Instance
**
*Nset, nset=RF-P, instance=Punch-1
1,
*Nset, nset=RF-DU, instance=DU-1
1,
*Nset, nset=RF-DB, instance=DB-1
1,
**
*Nset, nset=Cent, instance=Sheet-1, generate
1, , 1
*Elset, elset=Cent, instance=Sheet-1, generate
1, , 1
*Surface, TYPE=NODE, name=surfcent_01
Cent
**
*Nset, nset=_PickedSet183, internal, instance=DU-1
1,
*Nset, nset=_PickedSet184, internal, instance=DB-1
1,
*Nset, nset=_PickedSet185, internal, instance=Punch-1
1,
**
*End Assembly
**
** MATERIALS
**
*Material, name=AL

```

*Density

2.7,

*Elastic

69000, 0.33

*Plastic

200.01, 0.000

201.95, 0.001

203.87, 0.002

205.77, 0.003

207.66, 0.004

209.54, 0.005

211.39, 0.006

213.24, 0.007

215.06, 0.008

216.88, 0.009

218.68, 0.010

235.87, 0.020

251.70, 0.030

266.27, 0.040

279.70, 0.050

292.06, 0.060

303.45, 0.070

313.93, 0.080

323.59, 0.090

332.48, 0.100

340.67, 0.110

348.21, 0.120

355.15, 0.130

361.55, 0.140

367.43, 0.150

372.86, 0.160

377.85, 0.170

382.45, 0.180

386.69, 0.190

390.59, 0.200

394.18, 0.210

397.49, 0.220

400.53, 0.230

403.34, 0.240

405.92, 0.250

408.30, 0.260

410.49, 0.270

412.51, 0.280

414.37, 0.290

416.08, 0.300
427.26, 0.400
432.17, 0.500
434.32, 0.600
435.26, 0.700
435.68, 0.800
435.86, 0.900
435.94, 1.000
**
*Shear Failure, Element Deletion=yes
0.70
**
** INTERACTION PROPERTIES
**
*Surface Interaction, name=Friction
*Friction
0.3,
*Surface Interaction, name=Lubrication_01
*Friction
0.2,
*Surface Interaction, name=Lubrication_02
*Friction
0.3,
*Surface Interaction, name=Lubrication_03
*Friction
0.4,
**
** STEP: Clamping
**
*Step, name=Clamping
Clamping
*Dynamic, Explicit
, 20
*Bulk Viscosity
0.06, 1.2
** Mass Scaling: Semi-Automatic
** Whole Model
** *Fixed Mass Scaling, factor=100
**
** BOUNDARY CONDITIONS
**
** Name: DB Type: Displacement/Rotation
*Boundary
_PickedSet184, 1, 1

```

_PickedSet184, 2, 2
_PickedSet184, 3, 3
_PickedSet184, 4, 4
_PickedSet184, 5, 5
_PickedSet184, 6, 6
**
** Name: DU-Clamp Type: Velocity/Angular velocity
*Boundary, type=VELOCITY
_PickedSet183, 1, 1
_PickedSet183, 2, 2, -0.1
_PickedSet183, 3, 3
_PickedSet183, 4, 4
_PickedSet183, 5, 5
_PickedSet183, 6, 6
**
** Name: P-Clamp Type: Displacement/Rotation
*Boundary
_PickedSet185, 1, 1
_PickedSet185, 2, 2
_PickedSet185, 3, 3
_PickedSet185, 4, 4
_PickedSet185, 5, 5
_PickedSet185, 6, 6
**
** INTERACTIONS
**
** Interaction: DB-SH
*Contact Pair, interaction=Friction, mechanical constraint=KINEMATIC, cpset=DB-SH
surfcent_01, DB-1.RigidSurface_
**
** Interaction: DU-SH
*Contact Pair, interaction=Friction, mechanical constraint=KINEMATIC, cpset=DU-SH
surfcent_01, DU-1.RigidSurface_
**
** Interaction: P-SH
*Contact Pair, interaction=Lubrication_01, mechanical constraint=KINEMATIC,
cpset=P-SH
surfcent_01, Punch-1.RigidSurface_
**
** OUTPUT REQUESTS
**
*Restart, write, number interval=20, time marks=NO
**
** FIELD OUTPUT: F-Output-1

```

```

**
*Output, field, number interval=20
**
*Node Output
RF, U
**
*Element Output, directions=YES
LE, PEEQ, S, STATUS
**
** *Output, history, frequency=0
**
*End Step
**
** STEP: Punch
**
*Step, name=Punch_01
Punch_01
*Dynamic, Explicit
, 60
*Bulk Viscosity
0.06, 1.2
** Mass Scaling: Semi-Automatic
** Whole Model
** *Fixed Mass Scaling, factor=100
**
** BOUNDARY CONDITIONS
**
** Name: DB Type: Displacement/Rotation
*Boundary, op=NEW
_PickedSet184, 1, 1
_PickedSet184, 2, 2
_PickedSet184, 3, 3
_PickedSet184, 4, 4
_PickedSet184, 5, 5
_PickedSet184, 6, 6
**
** Name: DU-Punch Type: Displacement/Rotation
*Boundary, op=NEW
*Boundary, op=NEW
_PickedSet183, 1, 1
_PickedSet183, 2, 2
_PickedSet183, 3, 3
_PickedSet183, 4, 4
_PickedSet183, 5, 5

```

```

_PickedSet183, 6, 6
**
** Name: P-Punch Type: Velocity/Angular velocity
*Boundary, op=NEW
*Boundary, op=NEW, type=VELOCITY
_PickedSet185, 1, 1
_PickedSet185, 2, 2, 0.1
_PickedSet185, 3, 3
_PickedSet185, 4, 4
_PickedSet185, 5, 5
_PickedSet185, 6, 6
**
** OUTPUT REQUESTS
**
*Restart, write, number interval=80, time marks=NO
**
** FIELD OUTPUT: F-Output-1
**
*Output, field, number interval=80
**
*Node Output
RF, U
**
*Element Output, directions=YES
LE, PEEQ, S, STATUS
**
** HISTORY OUTPUT: H-Output-1
**
*Output, history, time interval=1
*Node Output, nset=RF-P
RF2,
*End Step
**
** STEP: Punch
**
*Step, name=Punch_02
Punch_02
*Dynamic, Explicit
, 40
*Bulk Viscosity
0.06, 1.2
** Mass Scaling: Semi-Automatic
** Whole Model
** *Fixed Mass Scaling, factor=100

```

```

**
** BOUNDARY CONDITIONS
**
** Name: DB Type: Displacement/Rotation
*Boundary, op=NEW
_PickedSet184, 1, 1
_PickedSet184, 2, 2
_PickedSet184, 3, 3
_PickedSet184, 4, 4
_PickedSet184, 5, 5
_PickedSet184, 6, 6
**
** Name: DU-Punch Type: Displacement/Rotation
*Boundary, op=NEW
*Boundary, op=NEW
_PickedSet183, 1, 1
_PickedSet183, 2, 2
_PickedSet183, 3, 3
_PickedSet183, 4, 4
_PickedSet183, 5, 5
_PickedSet183, 6, 6
**
** Name: P-Punch Type: Velocity/Angular velocity
*Boundary, op=NEW
*Boundary, op=NEW, type=VELOCITY
_PickedSet185, 1, 1
_PickedSet185, 2, 2, 0.1
_PickedSet185, 3, 3
_PickedSet185, 4, 4
_PickedSet185, 5, 5
_PickedSet185, 6, 6
**
** INTERACTIONS
**
** Interaction: DB-SH
*Contact Pair, op=DELETE, cpset=DB-SH_01
DB-1.RigidSurface_, surfcent_01
*Contact Pair, interaction=Lubrication_02, mechanical constraint=KINEMATIC,
cpset=DB-SH_02
DB-1.RigidSurface_, surfcent_01
**
** Interaction: DU-SH
*Contact Pair, op=DELETE, cpset=DU-SH_01
DU-1.RigidSurface_, surfcent_01

```

```

*Contact Pair, interaction=Lubrication_02, mechanical constraint=KINEMATIC,
cpset=DU-SH_02
DU-1.RigidSurface_, surfcent_01
**
** Interaction: P-SH
*Contact Pair, op=DELETE, cpset=P-SH_01
Punch-1.RigidSurface_, surfcent_01
*Contact Pair, interaction=Lubrication_02, mechanical constraint=KINEMATIC,
cpset=P-SH_02
Punch-1.RigidSurface_, surfcent_01
**
** OUTPUT REQUESTS
**
*Restart, write, number interval=80, time marks=NO
**
** FIELD OUTPUT: F-Output-1
**
*Output, field, number interval=80
**
*Node Output
RF, U
**
*Element Output, directions=YES
LE, PEEQ, S, STATUS
**
** HISTORY OUTPUT: H-Output-1
**
*Output, history, time interval=1
*Node Output, nset=RF-P
RF2,
*End Step
**
** STEP: Punch
**
*Step, name=Punch_03
Punch_03
*Dynamic, Explicit
, 50
*Bulk Viscosity
0.06, 1.2
** Mass Scaling: Semi-Automatic
** Whole Model
** *Fixed Mass Scaling, factor=100
**

```

```

** BOUNDARY CONDITIONS
**
** Name: DB Type: Displacement/Rotation
*Boundary, op=NEW
    _PickedSet184, 1, 1
    _PickedSet184, 2, 2
    _PickedSet184, 3, 3
    _PickedSet184, 4, 4
    _PickedSet184, 5, 5
    _PickedSet184, 6, 6
**
** Name: DU-Punch Type: Displacement/Rotation
*Boundary, op=NEW
*Boundary, op=NEW
    _PickedSet183, 1, 1
    _PickedSet183, 2, 2
    _PickedSet183, 3, 3
    _PickedSet183, 4, 4
    _PickedSet183, 5, 5
    _PickedSet183, 6, 6
**
** Name: P-Punch Type: Velocity/Angular velocity
*Boundary, op=NEW
*Boundary, op=NEW, type=VELOCITY
    _PickedSet185, 1, 1
    _PickedSet185, 2, 2, 0.1
    _PickedSet185, 3, 3
    _PickedSet185, 4, 4
    _PickedSet185, 5, 5
    _PickedSet185, 6, 6
**
** INTERACTIONS
**
** Interaction: DB-SH
*Contact Pair, op=DELETE, cpset=DB-SH_01
    DB-1.RigidSurface_, surfcent_01
*Contact Pair, interaction=Lubrication_03, mechanical constraint=KINEMATIC,
cpset=DB-SH_02
    DB-1.RigidSurface_, surfcent_01
**
** Interaction: DU-SH
*Contact Pair, op=DELETE, cpset=DU-SH_01
    DU-1.RigidSurface_, surfcent_01

```

```
*Contact Pair, interaction=Lubrication_03, mechanical constraint=KINEMATIC,
cpset=DU-SH_02
DU-1.RigidSurface_, surfcent_01
**
** Interaction: P-SH
*Contact Pair, op=DELETE, cpset=P-SH_01
Punch-1.RigidSurface_, surfcent_01
*Contact Pair, interaction=Lubrication_03, mechanical constraint=KINEMATIC,
cpset=P-SH_02
Punch-1.RigidSurface_, surfcent_01
**
** OUTPUT REQUESTS
**
*Restart, write, number interval=80, time marks=NO
**
** FIELD OUTPUT: F-Output-1
**
*Output, field, number interval=80
**
*Node Output
RF, U
**
*Element Output, directions=YES
LE, PEEQ, S, STATUS
**
** HISTORY OUTPUT: H-Output-1
**
*Output, history, time interval=1
*Node Output, nset=RF-P
RF2,
*End Step
```

Appendix 6. Optimized Material Input For AA6111-T4 Of 1 mm And 2 mm Sheet Thickness

[1] 1 mm thickness, 0.25 mm/s test speed

$$\sigma_p = K\varepsilon^n, \sigma_H = B - (B - A)e^{-m\varepsilon},$$

$$K = 550, n = 0.215, A = 200, B = 435, m = 8.2$$

Optimized stress-strain input is:

$$\sigma_H = \varepsilon\sigma_p + (1 - \varepsilon)\sigma_v \quad \text{when } 0 \leq \varepsilon \leq 0.150$$

$$\sigma_H = (0.706\varepsilon + 0.044)\sigma_p + (-0.706\varepsilon + 0.956)\sigma_v \quad \text{when } 0.150 \leq \varepsilon \leq 1$$

(Eq A6-1)

[2] 1 mm thickness, 0.025 mm/s test speed

$$\sigma_p = K\varepsilon^n, \sigma_H = B - (B - A)e^{-m\varepsilon},$$

$$K = 555, n = 0.220, A = 200, B = 435, m = 8.3$$

Optimized stress-strain input is:

$$\sigma_H = \varepsilon\sigma_p + (1 - \varepsilon)\sigma_v \quad \text{when } 0 \leq \varepsilon \leq 0.153$$

$$\sigma_H = (0.705\varepsilon + 0.045)\sigma_p + (-0.705\varepsilon + 0.955)\sigma_v \quad \text{when } 0.153 \leq \varepsilon \leq 1$$

(Eq A6-2)

[3] 1 mm thickness, 1.25 mm/s test speed

$$\sigma_p = K\varepsilon^n, \sigma_H = B - (B - A)e^{-m\varepsilon},$$

$$K = 555, n = 0.214, A = 200, B = 440, m = 8.2$$

Optimized stress-strain input is:

$$\sigma_H = \varepsilon\sigma_p + (1 - \varepsilon)\sigma_v \quad \text{when } 0 \leq \varepsilon \leq 0.155$$

$$\sigma_H = (0.704\varepsilon + 0.046)\sigma_p + (-0.704\varepsilon + 0.954)\sigma_v \quad \text{when } 0.155 \leq \varepsilon \leq 1$$

(Eq A6-3)

[4] 2 mm thickness, 0.25 mm/s test speed

$$\sigma_p = K\varepsilon^n, \sigma_H = B - (B - A)e^{-m\varepsilon},$$

$$K = 620, n = 0.240, A = 190, B = 460, m = 9.2$$

Optimized stress-strain input is:

$$\sigma_H = \varepsilon\sigma_p + (1 - \varepsilon)\sigma_v \quad \text{when } 0 \leq \varepsilon \leq 0.160$$

$$\sigma_H = (0.643\varepsilon + 0.057)\sigma_p + (-0.643\varepsilon + 0.943)\sigma_v \quad \text{when } 0.160 \leq \varepsilon \leq 1$$

(Eq A6-4)

[5] 2 mm thickness, 0.025 mm/s test speed

$$\sigma_p = K\varepsilon^n, \sigma_H = B - (B - A)e^{-m\varepsilon},$$

$$K = 605, n = 0.230, A = 187, B = 460, m = 10$$

Optimized stress-strain input is:

$$\sigma_H = \varepsilon\sigma_p + (1 - \varepsilon)\sigma_v \quad \text{when } 0 \leq \varepsilon \leq 0.165$$

$$\sigma_H = (0.641\varepsilon + 0.059)\sigma_p + (-0.641\varepsilon + 0.941)\sigma_v \quad \text{when } 0.165 \leq \varepsilon \leq 1$$

(Eq A6-5)

[6] 2 mm thickness, 1.25 mm/s test speed

$$\sigma_p = K\varepsilon^n, \sigma_H = B - (B - A)e^{-m\varepsilon},$$

$$K = 620, n = 0.220, A = 190, B = 460, m = 9.5$$

Optimized stress-strain input is:

$$\sigma_H = \varepsilon\sigma_p + (1 - \varepsilon)\sigma_v \quad \text{when } 0 \leq \varepsilon \leq 0.160$$

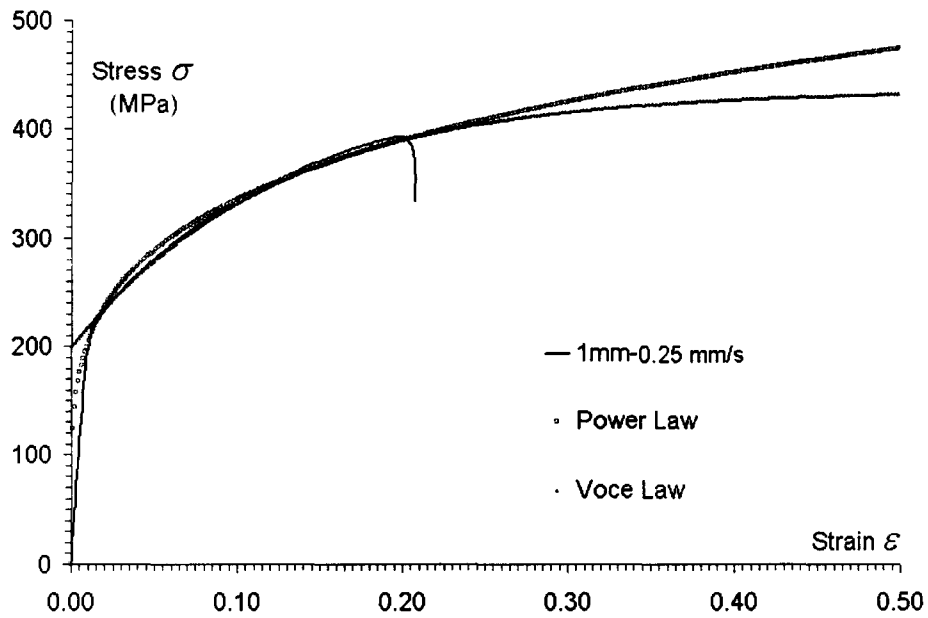
$$\sigma_H = (0.643\varepsilon + 0.057)\sigma_p + (-0.643\varepsilon + 0.943)\sigma_v \quad \text{when } 0.160 \leq \varepsilon \leq 1$$

(Eq A6-6)

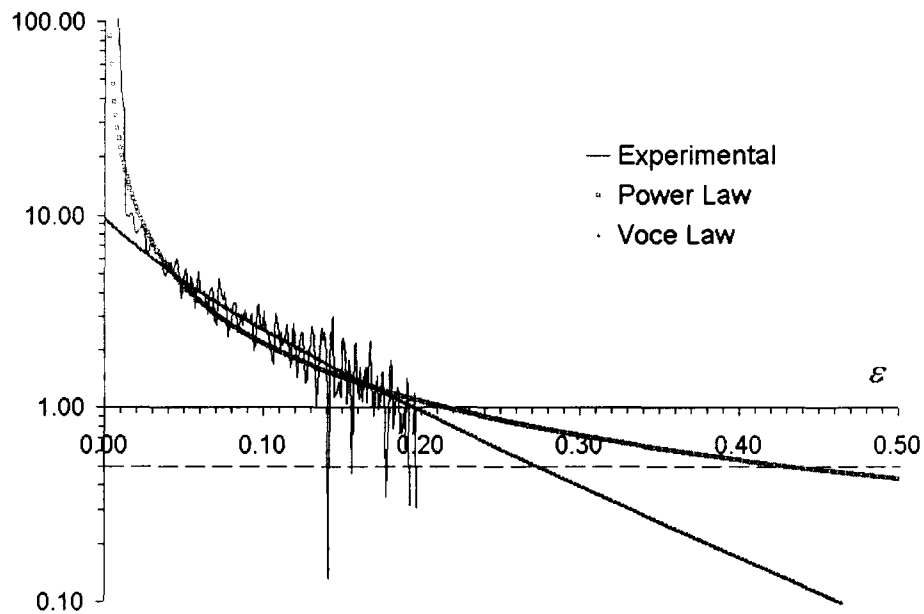
Appendix 7. Material Properties From Uniaxial Tensile Tests Of AA6111-T4 Of 1 mm And 2 mm Sheet Thickness

The parameters for stress-strain relationship of various curves are based on the Table 6-1.

For both 1 mm and 2 mm thickness sheets of AA6111-T4, uniaxial tensile tests were carried out at different test speeds, 0.25 mm/s, 0.025 mm/s and 1.25 mm/s respectively. Hardening laws of power law and Voce law have been utilized in the extrapolation of stress-strain curves. Considère criterion has been employed to examine the quality of parameter fitting. The results are presented in Figures A7-1 to A7-6.

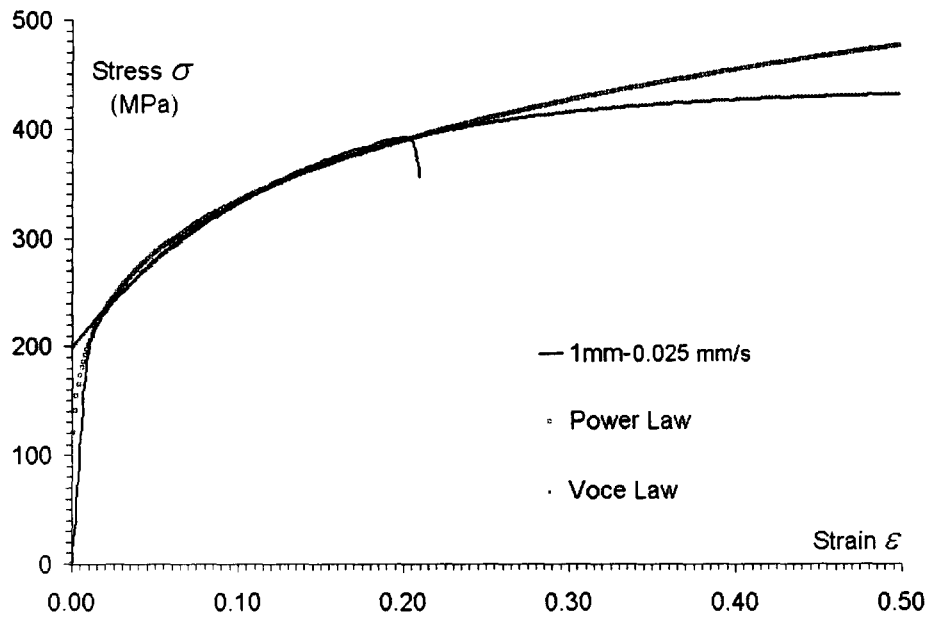


a. Stress-strain relationship (experimental, power law, Voce law).

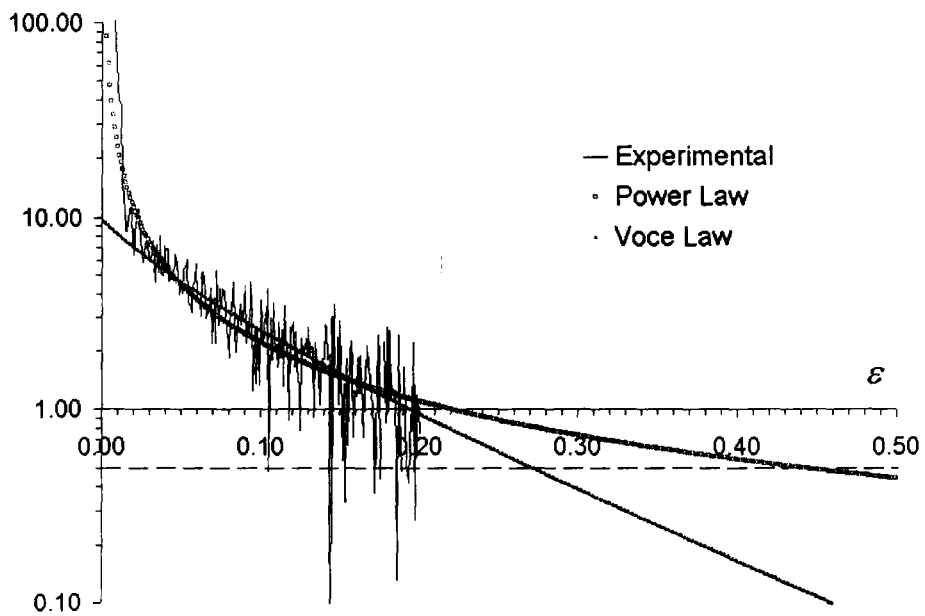


b. Hardening behaviour (experimental, power law, Voce law).

FIGURE A7-1. Proposed curve fitting for AA6111-T4, 1 mm thickness, 0.25 mm/s test speed.

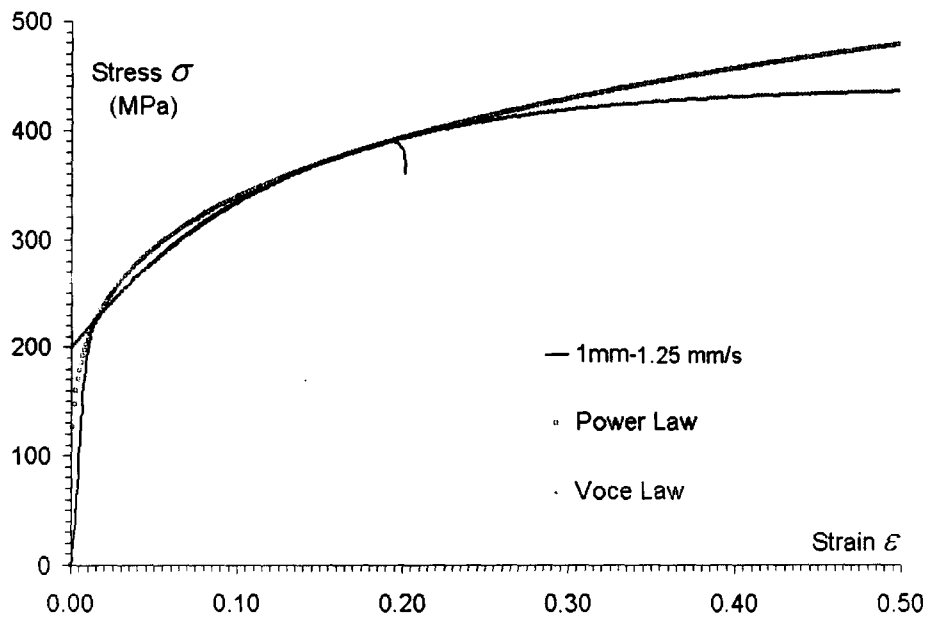


a. Stress-strain relationship (experimental, power law, Voce law).

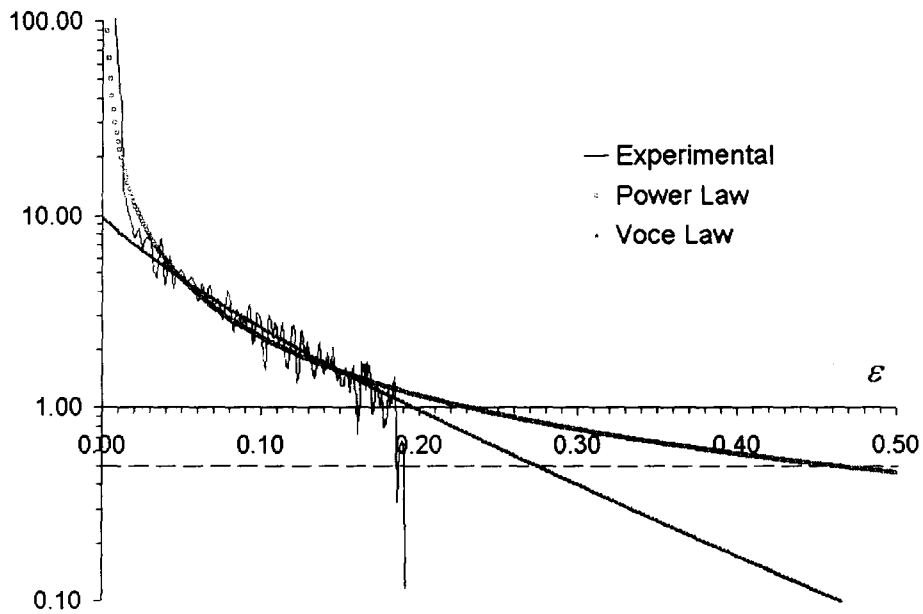


b. Hardening behaviour (experimental, power law, Voce law).

FIGURE A7-2. Proposed curve fitting for AA6111-T4, 1 mm thickness, 0.025 mm/s test speed.

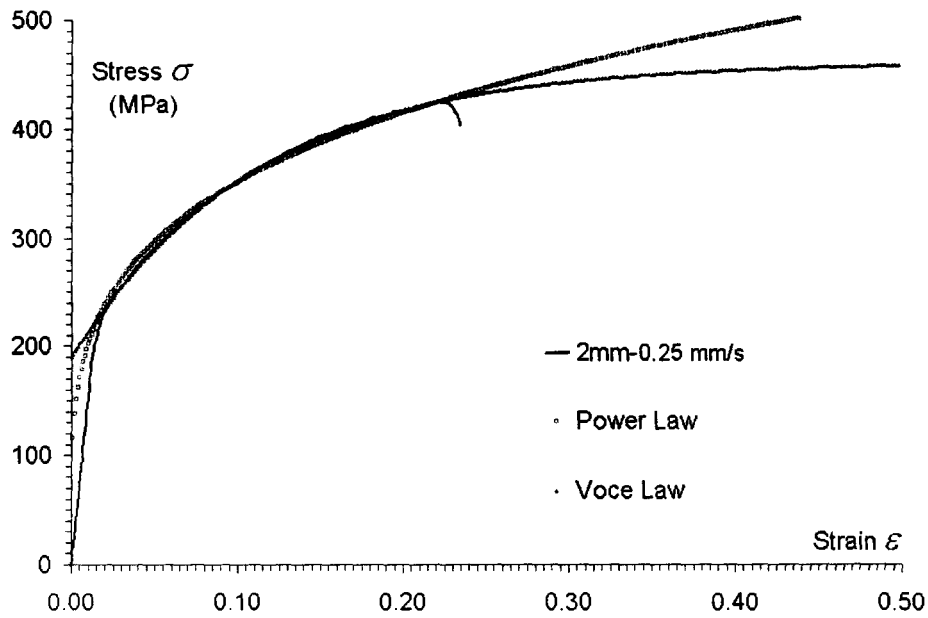


a. Stress-strain relationship (experimental, power law, Voce law).

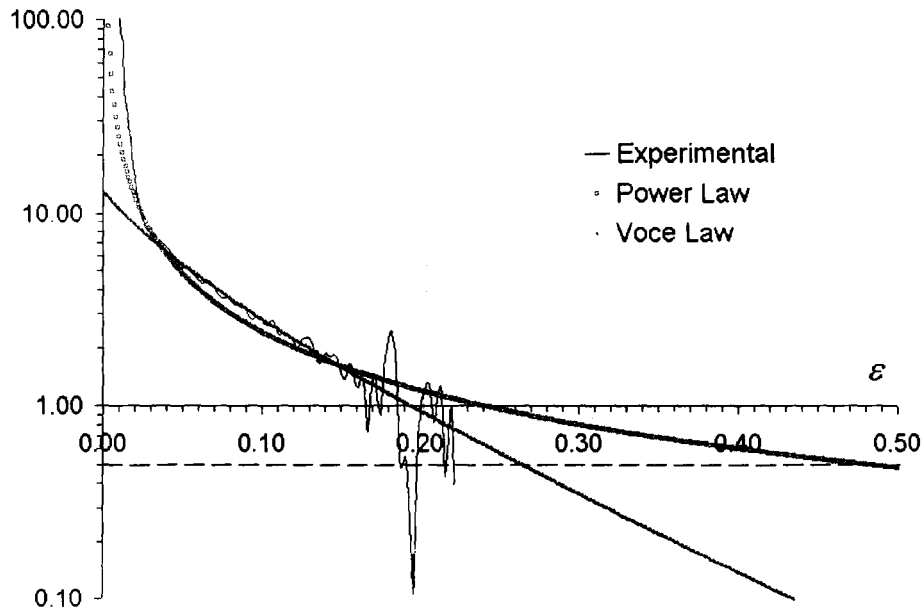


b. Hardening behaviour (experimental, power law, Voce law).

FIGURE A7-3. Proposed curve fitting for AA6111-T4, 1 mm thickness, 1.25 mm/s test speed.

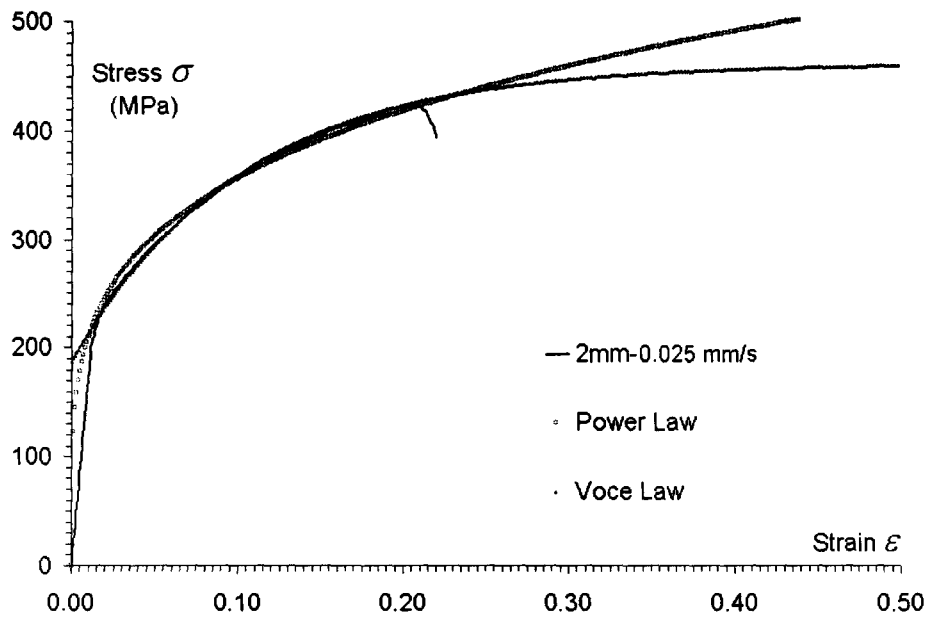


a. Stress-strain relationship (experimental, power law, Voce law).

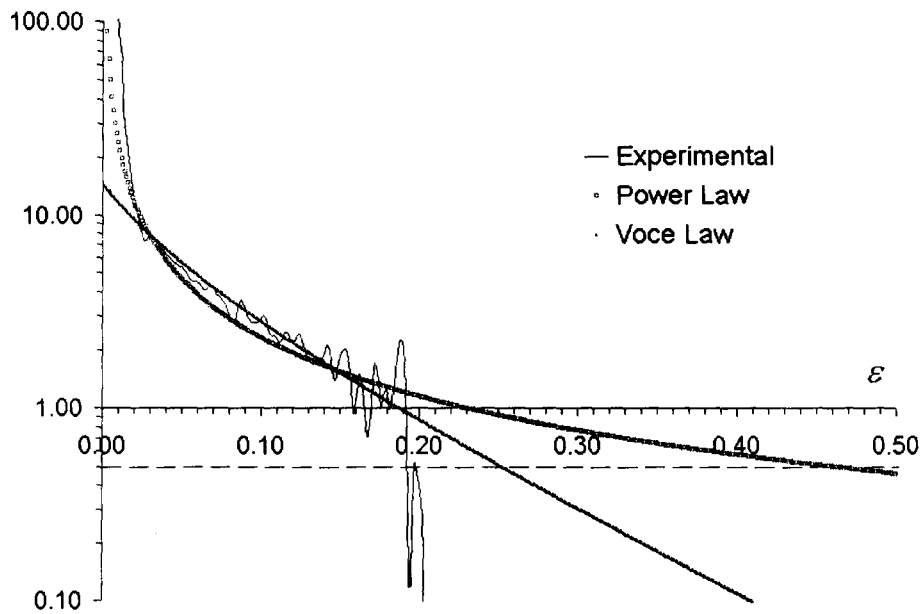


b. Hardening behaviour (experimental, power law, Voce law).

FIGURE A7-4. Proposed curve fitting for AA6111-T4, 2 mm thickness, 0.25 mm/s test speed.

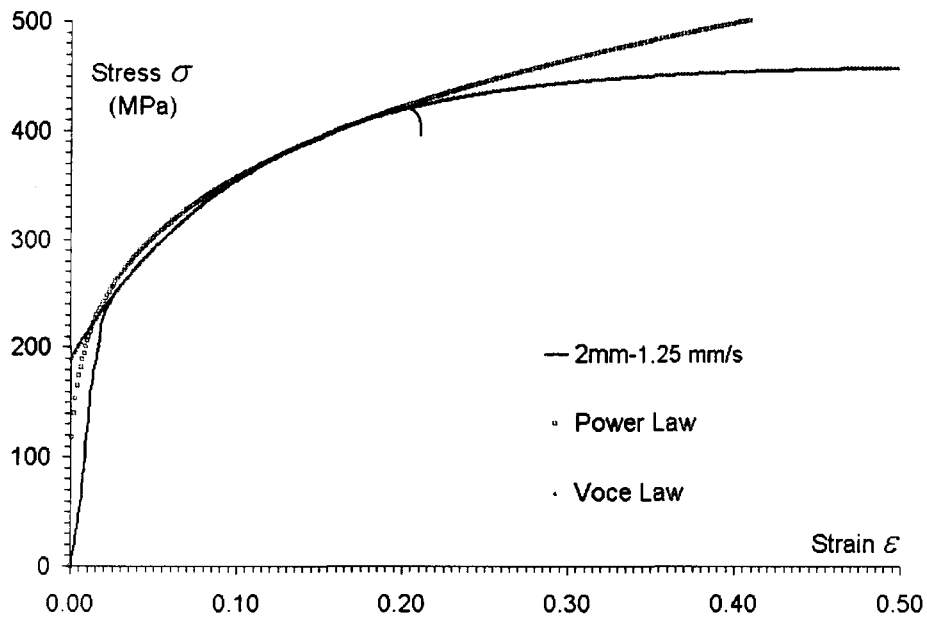


a. Stress-strain relationship (experimental, power law, Voce law).

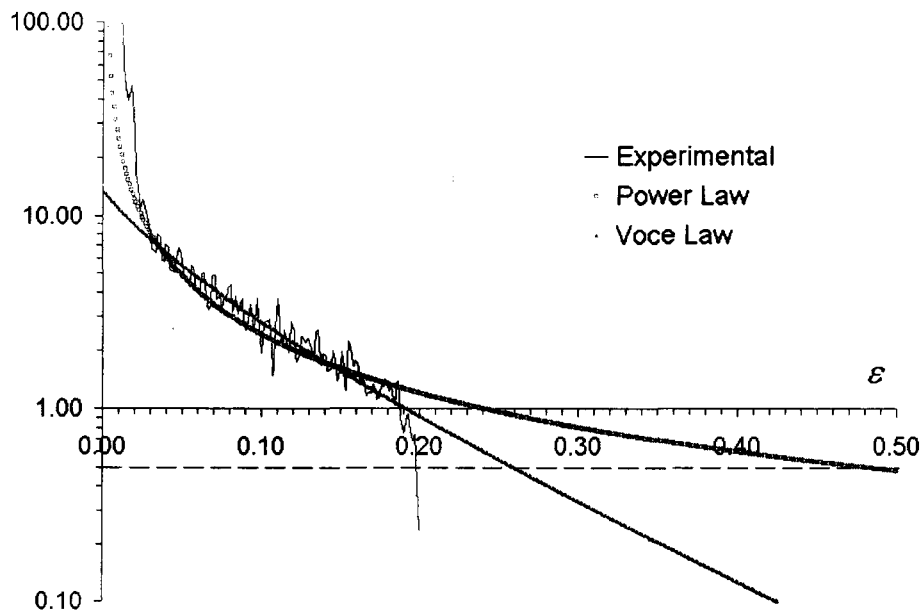


b. Hardening behaviour (experimental, power law, Voce law).

FIGURE A7-5. Proposed curve fitting for AA6111-T4, 2 mm thickness, 0.025 mm/s test speed.



a. Stress-strain relationship (experimental, power law, Voce law).



b. Hardening behaviour (experimental, power law, Voce law).

FIGURE A7-6. Proposed curve fitting for AA6111-T4, 2 mm thickness, 1.25 mm/s test speed.